

# **Bicomponent Co-assembled Molecular Gels: Design, Synthesis and Application in Biocatalysis**

**Ph.D. Thesis**

By  
**SAGAR BISWAS**



**DISCIPLINE OF CHEMISTRY  
INDIAN INSTITUTE OF TECHNOLOGY INDORE  
JANUARY 2019**



# **Bicomponent Co-assembled Molecular Gels: Design, Synthesis and Application in Biocatalysis**

**A THESIS**

*Submitted in partial fulfillment of the  
requirements for the award of the degree*

*of*

**DOCTOR OF PHILOSOPHY**

*by*

**SAGAR BISWAS**



**DISCIPLINE OF CHEMISTRY  
INDIAN INSTITUTE OF TECHNOLOGY INDORE  
JANUARY 2019**





# INDIAN INSTITUTE OF TECHNOLOGY INDORE

## CANDIDATE'S DECLARATION

I hereby certify that the work which is being presented in the thesis entitled **Bicomponent Co-assembled Molecular Gels: Design, Synthesis and Application in Biocatalysis** in the partial fulfillment of the requirements for the award of the degree of **DOCTOR OF PHILOSOPHY** and submitted in the **DISCIPLINE OF CHEMISTRY, Indian Institute of Technology Indore**, is an authentic record of my own work carried out during the time period from November 2013 to December 2018 under the supervision of **Dr. APURBA K. DAS**, Associate professor, Discipline of Chemistry.

The matter presented in this thesis has not been submitted by me for the award of any other degree of this or any other institute.

**SAGAR BISWAS**

-----  
This is to certify that the above statement made by the candidate is correct to the best of my/our knowledge.

**Dr. APURBA K. DAS**

-----  
**SAGAR BISWAS** has successfully given his/her Ph.D. Oral Examination held on  
.....

Signature of Chairperson (OEB)

Date:

Signature of External Examiner

Date:

Signature(s) of Thesis Supervisor(s)

Date:

Signature of PSPC Member #1

Date:

Signature of PSPC Member #2

Date:

Signature of Convener, DPGC

Date:

Signature of Head of Discipline

Date:

-----



## **ACKNOWLEDGEMENTS**

I would like to acknowledge my indebtedness and render my warmest thanks to my supervisor, Dr. Apurba Kumar Das for giving me the opportunity to work on such an exciting research area. I am grateful to him for his support and motivation. His friendly guidance, expert advice, excellent supervision and deep understanding throughout the tenure made this work possible.

I would also like to express my gratitude to Dr. Anjan Chakrobarty, Dr. Amarjeet Nayak and Dr. Manavendra Mahato for extended discussions and valuable suggestions to the improvement of the thesis.

I am pleased to express my sincere gratitude and respect to Prof. Pradeep Mathur (Director, Indian Institute of Technology Indore) for his endless encouragement and availing all the facilities at Indian Institute of Technology Indore.

It is my pleasure to thank Dr. Amarendra Kumar Singh (Head, Discipline of Chemistry, Indian Institute of Technology Indore) for his suggestions and guidance in different purposes. I am also grateful to Dr. Chelvam Venkatesh, Dr. Tridib K. Sarma, Dr. Rajneesh Misra, Dr. Sampak Samanta, Dr. Suman Mukhopadhyay, Dr. Biswarup Pathak, Dr. Sanjay Kumar Singh, Dr. Shaikh M. Mobin and Dr. Satya S. Bulusu for their guidance and help during multiple activities.

Special thanks are due to my group members, Mr. Pramod K. Gavel, Mr. Sayan Maity, Mr. Ankan Biswas, Mr. Rohit J. Gajanan, Mr. Devraj, Mr. Tapas Ghosh, Mr. Deepak and Mithu Roy for their generous co-operation and help to make my work successful.

I am also grateful to all my friends for their generous cooperation and help during my Ph.D. Special thanks to Ms. Madhumita Chatterjee, Mr. Pinaki

Nath and Mr. Hemanta Biswas for their endless help and support during this tenure.

I am glad to thanks to Mr. Kinney Pandey, Mr. Ghanshyam Bhavsar and Mr. Manish Kushwaha for their technical help and support.

The persons with the greatest motivation and support to this work are my lovable mother, Mrs. Rina Biswas, and my lovable father Mr. Subrata Biswas. I would like to express my love and gratitude to them from the deep core of my heart to teach me to be steady on my goal.

I want to express my love to my sister Mrs. Sraboni Biswas and my brother Mr. Santu Biswas for their constant encouragement.

Sagar Biswas

*Dedicated to My Beloved  
Parents*



## Abstract

Self-assembly of amphiphilic molecules holds promise in various applications in the fields of biomedical engineering and nanotechnology. Low molecular weight based amphiphiles, bolaamphiphiles or discotic amphiphiles provide supramolecular architectures. The supramolecular architectures include vesicles, toroids, tubes and other nanostructures. Meanwhile, direct or indirect involvement of a second component induces the co-assembly process of the amphiphiles. To find out an easy approach to control the nanostructures, researchers are inspired to expand multicomponent self-assembled systems. The bicomponent system is the simplest multicomponent systems to achieve controlled co-assembly and gelation. Over the last decade, several bicomponent co-assembled systems were developed and studied thoroughly. Still, there is a wide interest to develop nanoarchitected bicomponent systems which could be used for various applications.

The main objectives of the present study are:

- To synthesize Amoc (9-anthracenemethyloxycarbonyl) capped amino acid-based amphiphilic molecules and to study the influence of graphene quantum dots in the co-assembled systems.
- To control chiral nanostructures of synthesized leucine-based bolaamphiphiles in the co-assembled hydrogel.
- To develop bicomponent co-assembled supramolecular organic frameworks (SOFs) with a controlled pore size in gel state using discotic trifunctional amphiphile for the use of lipase-catalyzed inclusion of gastrodigenin.
- To evolve small amphiphilic based bicomponent co-assembled hydrogel to produce L-DOPA in the gel medium using tyrosinase.

## **1 Blue light emitting self-healable graphene quantum dot embedded hydrogels**

Chapter 3 describes structural and morphological studies of designed small molecular weight amphiphiles (compounds **1** and **2**). Graphene quantum dot (GQDs) was synthesized and embedded into Amoc-F/Amoc-Y (10 mM) amphiphiles in aqueous environments (pH 7.4), which exhibit blue light emitting self-healable hydrogels **1**, **2**. The GQDs tune the mechanical and optical property of the hydrogels. A variable amount of GQDs were incorporated into Amoc-F/Amoc-Y solutions. The optimum concentrations of the GQDs were found  $0.5 \text{ mg mL}^{-1}$  to acquire maximum self-healing property from the amphiphiles **1**, **2**. These Amoc-capped amino acid/GQD assemblies in hydrogel states encourage blue light emission under UV irradiation at a wavelength of 365 nm. The quenching in emission spectra reveals strong  $\pi$ - $\pi$  stacking interactions within aromatic GQDs and Amoc-capped amino acids. Higher the amount of GQDs used greater the quenching was observed. The fluorescence spectra confirm the stabilization of GQDs on fibrils, and electron microscopy images depict the distribution of GQDs on the nanofibrillar 3D networks. The inclusion of GQDs can tune the self-healing properties or thixotropic nature of the hydrogels **1**, **2**.

## **2 Tuning the Handedness: Role of Chiral Component in Peptide-appended Bolaamphiphile-based Co-assembled Hydrogels**

Chapter 4 describes the synthesis and chiral nanostructural investigation of synthesized bolaamphiphiles (**3-11**). Chirality is the intrinsic property of a molecule which can be tuned by the change in chirality of the molecule or by the addition of a chiral component as an external stimulus. An L-leucine based dipeptide appended succinic acid based bolaamphiphile co-assembled with D-tartaric acid to form a supramolecular right-handed nanostructured hydrogel **3** whereas L-tartaric acid co-assembled to form supramolecular left handed nanostructured hydrogel **4**. SEM and TEM experiments revealed the right and left-handed helical nanofibers, which

are responsible for the formation of supramolecular nanostructured hydrogels. The synergistic chiral effect of L-leucine in peptide bolaamphiphile and D/L-tartaric acid plays a significant role in bicomponent gelation with helical nanofibers. The first two amino acids attached to both the sides of succinic acid moiety act as a tuning button for supramolecular chirality of amino acids/peptides. The CD spectroscopy reveals that the second amino acids play a role to modulate supramolecular chirality if the first two amino acids act neutrally to the chirality of bolaamphiphiles.

### **3 Construction of Porous Organic Nanostructures Using Cooperative Self-Assembly for Lipase-Catalyzed Inclusion of Gastrodigenin**

Chapter 5 describes the synthesis and bicomponent co-assembly study of pyridyl amphiphiles (compounds **12** and **13**). The discotic pyridyl amphiphile was found to co-assemble with complementary 1,3,5-benzenetricarboxylic acid and 1,4-benzenedicarboxylic acid to form emulsion gels **6**, **7** with porous architecture. Bifunctional amphiphile was also self-assembled but unable to form emulsion gel. Cooperative self-assembly between amphiphilic pyridyl derivatives and complementary acids was established by several spectroscopic techniques (FT-IR, UV-Vis, PXRD and SAXS). The alteration of complementary acids helps to tune the mechanical property of the bicomponent emulsion gels and also leads to nanostructural diversity. The mechanical property was studied by rheological experiment and TEM images confirmed nanostructural diversity. The supramolecular nanostructures formed in emulsion gels **7** with large pores and enhanced surface area exhibit as a template for lipase (from *Candida rugosa*)-catalyzed inclusion of gastrodigenin (p-hydroxybenzyl alcohol) via an esterification reaction. The enzymatic reaction with an excellent conversion (80%) leads the emulsion gel to separate into two phases, which results in recyclability of the pyridyl amphiphiles. The conversion was studied using HPLC.

#### **4. Bicomponent Co-assembled Nanotubular Hydrogel as Template for Selective Enzymatic Generation of DOPA**

Chapter 6 describes the co-assembly of amphiphilic molecule and 1,3,5-benzenetricarboxylic acid which forms self-supporting hydrogel **8**. After alteration of complementary acids, the bicomponent system becomes unstable to co-assemble in the medium and does not form a gel. Small molecular building blocks co-assembled through non-covalent interactions such as hydrogen bonding,  $\pi$ - $\pi$  stacking. Several spectroscopic techniques established the co-assembly mechanism. SEM and TEM images show the insight of the morphology. The bicomponent hydrogel was used for the synthesis of L-DOPA by using tyrosine. The co-assembled hydrogel is strong enough to hold tyrosinase enzyme in between the crosslinked fibrillar network. L-tyrosine and peptide phenylalanine-tyrosine (FY) were immobilized into the hydrogel to obtain L-DOPA and F-(L)-DOPA peptide. HPLC chromatograms show 95% conversion for L-DOPA and 82% for F-(L)-DOPA. Mass spectra confirm the formation of L-DOPA in hydrogel medium. This method is very efficient to produce L-DOPA in the gel medium with an excellent conversion. The enzymatically synthesized L-DOPA and L-DOPA bonded peptide can also be separated from the mixture by easy tuning of bicomponent co-assembly.

## List of Publications:

1. **Biswas S.**, Rasale D. B., Das A. K. (2016) Blue Light Emitting Self-healable Graphene Quantum Dot Embedded Hydrogels, *RSC Adv.*, 6, 54793-54800 (DOI: 10.1039/c6ra06587b). (Impact Factor: 2.93)
2. **Biswas S.**, Jadhav R. G., Das A. K. (2018) Construction of Porous Organic Nanostructures Using Cooperative Self-Assembly for Lipase-Catalyzed Inclusion of Gastrodigenin, *ACS Appl. Nano Mater.*, 1, 175-182 (DOI: 10.1021/acsnm.7b00085). (Impact Factor: Pending)
3. **Biswas S.**, Bhowmik S., Rasale D. B., Das A. K. (2016) A Highly Selective Colorimetric Detection of Hg(II) via Enzymatic Dephosphorylation Reaction, *Macromol. Symp.*, 369, 108-113 (DOI: 10.1002/masy.201600069). (Impact Factor: 0.62)
4. **Biswas S.**, Das A. K. (2019) Tuning the Handedness: Role of Chiral Component in Peptide-appended Bolaamphiphile-based Co-assembled Hydrogels, *Langmuir*, 35, 2383–2391 (DOI: 10.1021/acs.langmuir.8b03651). (Impact Factor: 3.78)
5. Rasale D. B., **Biswas S.**, Konda M., Das A. K. (2015) Exploring Thermodynamically Downhill Nanostructured Peptide Libraries: From Structural to Morphological Insight, *RSC Adv.*, 5, 1529-1537 (DOI: 10.1039/c4ra09490e). (Impact Factor: 2.93)
6. Aaryashree, **Biswas S.**, Sharma P., Awasthi V., Sengar B. S., Das A. K., Mukherjee S. (2016) Photosensitive ZnO-Graphene Quantum Dot Hybrid Nanocomposite for Optoelectronic Applications, *ChemistrySelect*, 1, 1503-1509 (DOI: 10.1002/slct.201600149). (Impact Factor: 1.5)
7. Rasale D. B., Konda M., **Biswas S.**, Das A. K. (2016) Controlling Peptide Self-Assembly through a Native Chemical Ligation/Desulfurization Strategy, *Chem. Asian J.*, 11, 926-935 (DOI : 10.1002/asia.201501458). (Impact Factor: 3.69)

8. Biswas S., Samui S., **Biswas S.**, Das A. K., Naskar J. (2019) Molecular Recognition of Double-stranded DNA by Synthetic, Homoaromatic Tripeptide (YYY): The Spectroscopic and Calorimetric Study, *Int. J. Biol. Macromol.*, 123, 221-227 (DOI: 10.1016/j.ijbiomac.2018.11.012). (Impact Factor: 3.67)
9. Konda M., Bhowmik S., Mobin S., M., **Biswas S.**, Das A. K. (2016) Modulating Hydrogen Bonded Self-assembled Patterns and Morphological Features by a Change in Side Chain of Third Amino Acid of Synthetic  $\gamma$ -Amino Acid Based Tripeptides, *ChemistrySelect*, 1, 2586-2593 (DOI: 10.1002/slct.201600557). (Impact Factor: 1.5)
10. Biswas S., Samui S., Chakraborty A., **Biswas S.**, De D., Ghosh U., Das A. K., Naskar J. (2017) Insight into the Binding of a Non-toxic, Self-assembling Aromatic Tripeptide with ct-DNA: Spectroscopic and Viscositic Studies, *Biochem Biophys Rep.*, 11, 112-118. (DOI: 10.1016/j.bbrep.2017.07.001).

## **Published Book**

1. Apurba K Das and Sagar Biswas. *Molecular Co-assembly: Development and Future Perspective*, LAP LAMBERT Academic Publishing (ISBN 978-620-0-09121-5).

## **Conference Presentation**

1. Biswas S., Das A.K., Development of Solvent Dependent Bicomponent Molecular Self-assembly and Recyclable Enzymatic Esterification in Emulsion-gels. 2<sup>nd</sup> International Conference on SOFT MATERIALS, MNIT Jaipur (12<sup>th</sup> - 16<sup>th</sup> December 2016).
2. Biswas S., Das A.K., Construction of Porous Organic Nanostructures Using Cooperative Self-Assembly for Lipase-Catalyzed Inclusion of Gastrodigenin. 6<sup>th</sup> Industry-Academia Conclave, Indian Institute of Technology Indore (20<sup>th</sup> November, 2018).

# Table of Contents

<b>1. List of Figures</b>	xvii
<b>2. List of Schemes</b>	xxxiii
<b>3. List of Tables</b>	xxxv
<b>4. Acronyms</b>	xxxvii
<b>5. Nomenclature</b>	xxxix
<b>Chapter 1: General Introduction</b>	
1.1. Introduction of Molecular Assembly	3
1.2. Amphiphiles for Self-assembled Nanostructures	5
1.2.1. Self-assembly of Typical Amphiphiles	6
1.2.2. Self-assembly of Bolaamphiphiles	7
1.2.3. Self-assembly of Trifunctional Amphiphiles	8
1.3. Development of Bicomponent System	10
1.3.1. Bicomponent Self-sorting	12
1.3.2. Bicomponent Co-assembly	13
1.3.3. Bicomponent Covalent Conjugation	14
1.4. Carbon-based Material Driven Self-healable Gels	16
1.4.1. Graphene-based Material Driven Self-healable Gels	17
1.5. Chirality developed by Co-assembly	18
1.5.1. Chirality Induction by Chiral Component	20
1.5.2. Chirality Induction by Achiral Component	22
1.5.3. Chiral Memory via Co-assembly	23
1.6. Tuning Bicomponent Co-assembly	24
1.6.1. pH controlled Co-assembly	25
1.6.2. Sonication Induced Co-assembly	26

1.6.3. Photo-triggered Co-assembly	27
1.7. Application of Co-assembled Gels	28
1.7.1. 3D-Cell Culture and Drug Delivery	29
1.7.2. Co-assembled Gels in Catalysis	31
1.8. Organization of Thesis	33
1.9. References	33
<b>Chapter 2: Blue Light Emitting Self-healable Graphene Quantum Dot Embedded Hydrogels</b>	67
2.1. Introduction	69
2.2. Experimental	71
2.2.1. Synthesis of Amoc-F-OH (1)	71
2.2.2. Preparation of Amoc-Tyr-OH (2)	74
2.2.3. Synthesis of graphene quantum dots	76
2.3. Gel Preparation and Characterization Techniques	76
2.3.1. Preparation of hydrogels	76
2.3.1.1. Preparation of Gel-F and Gel-Y	76
2.3.1.2. Preparation of GQD-F and GQD-Y	77
2.3.2. Morphological study	77
2.3.3. UV-Vis spectroscopy	77
2.3.4. Fluorescence spectroscopy	78
2.3.5. Rheological study	78
2.4. Results and Discussion	78
2.4.1. Microscopic Study	80
2.4.2. Photophysical Study	83
2.4.3. Rheological Study	85
2.4.4. Self-healing property	87
2.5. Conclusion	89
2.6. References	89
<b>Chapter 3: Tuning the Handedness: Role of Chiral Component in Peptide appended Bolaamphiphile-based</b>	

<b>Co-assembled Hydrogels</b>	103
3.1. Introduction	105
3.2. Experimental	107
3.2.1. Synthesis of Compound iii	107
3.2.2. Synthesis of Compound 3	108
3.2.3. Synthesis of Compound iv	110
3.2.4. Synthesis of Compound 4	111
3.2.5. Synthesis of Compound v	112
3.2.6. Synthesis of Compound vi	113
3.2.7. Synthesis of Compound 5	114
3.2.8. Synthesis of Compound vii	116
3.2.9. Synthesis of Compound 6	117
3.2.10. Synthesis of Compound viii	118
3.2.11. Synthesis of Compound 7	120
3.2.12. Synthesis of Compound ix	121
3.2.13. Synthesis of Compound 8	122
3.2.14. Synthesis of Compound x	123
3.2.15. Synthesis of Compound 9	125
3.2.16. Synthesis of Compound xi	126
3.2.17. Synthesis of Compound 10	127
3.2.18. Synthesis of Compound xii	128
3.2.19. Synthesis of Compound 11	129
3.3. Gel Preparation and Characterization Techniques	131
3.3.1. Preparation of hydrogels	131
3.3.2. Rheological Experiments	131
3.3.3. Microscopic Techniques	132
3.3.4. FT-IR spectroscopy	132
3.3.5. Wide angle X-ray diffraction	132
3.3.6. Circular Dichroism Spectrometer	133
3.4. Results and Discussion	133

3.4.1. Rheological Study	135
3.4.2. Morphological Investigation	136
3.4.3. FT-IR Spectroscopy	140
3.4.4. Powder X-ray diffraction Study	141
3.4.5. <sup>1</sup> H NMR Study	142
3.4.6. Investigation of Supramolecular Chirality	143
3.5. Conclusions	149
3.6. References	149

**Chapter 4: Construction of Porous Organic Nanostructures  
using Cooperative Self-assembly for Lipase Catalyzed**

**Inclusion of Gastrodigenin** 159

4.1. Introduction	161
4.2. Experimental	163
4.2.1. 1,3,5-tris[2-(4-pyridyl)ethenyl]benzene (12)	163
4.2.2. 1,4-bis[2-(4-pyridyl)ethenyl]benzene (13)	163
4.3. Gel Preparation and Characterization Techniques	165
4.3.1. Preparation of Emulsions Gels	165
4.3.2. Emulsion Gels for Enzymatic Reaction	166
4.3.3. Separation of Product after Esterification	166
4.3.4. Compound Characterization	167
4.3.5. Rheological Study	167
4.3.6. FT-IR Spectroscopy	167
4.3.7. UV-Vis Spectroscopy	168
4.3.8. Wide Angle X-ray Diffraction	168
4.3.9. Small Angle X-ray Scattering Study	168
4.3.10. Thermogravimetric Analysis	168
4.3.11. Gas Adsorption Measurement	168
4.3.12. HPLC Analysis	169
4.4. Results and Discussion	169
4.4.1. Rheological Study	171

4.4.2. Morphological Study	172
4.4.3. Mechanistic Study	174
4.4.4. UV-Vis Spectroscopic Study	176
4.4.5. Powder X-ray Diffraction Study	177
4.4.6. Porosity Study	178
4.4.7. Mechanism of Nanostructure Formation	180
4.4.8. Enzymatic Reaction	182
4.5. Conclusion	187
4.6. References	188

**Chapter 5: Bicomponent Co-assembled Nanotubular Hydrogel as Template for Selective Enzymatic Generation of DOPA**

<b>Chapter 5: Bicomponent Co-assembled Nanotubular Hydrogel as Template for Selective Enzymatic Generation of DOPA</b>	199
5.1. Introduction	201
5.2. Experimental	203
5.2.1. Synthesis of Boc-Phe-OH (xiii)	203
5.2.2. Synthesis of Boc-Phe-Tyr-OMe (xiv)	203
5.2.3. Synthesis of Boc-Phe-Tyr-OH (xv)	204
5.2.4. Synthesis of H <sub>2</sub> N-Phe-Tyr-OH (FY: 14)	205
5.3. Gel Preparation and Characterization Techniques	207
5.3.1. Preparation of hydrogel	207
5.3.2. Preparation of hydrogels for Enzymatic Reaction	207
5.3.3. Separation of Product after Esterification	207
5.3.4. Compound characterization	208
5.3.5. Rheological Study	208
5.3.6. Morphological study	208
5.3.7. FT-IR Spectroscopy	208
5.3.8. UV-Vis Spectroscopy	209
5.3.9. Powder X-ray Diffraction	209
5.3.10. HPLC Analysis	209
5.4. Results and Discussion	210

5.4.1. Rheological Study	212
5.4.2. Photophysical Study	213
5.4.3. Mechanistic Study	214
5.4.4. Microscopic Study	215
5.4.5. Enzymatic reaction	215
5.5. Conclusion	218
5.6. References	219
<b>Chapter 6: General Conclusions and Perspectives</b>	<b>229</b>
6.1. General Conclusions	231
6.2. Perspectives	233
6.3. References	234

## List of Figures

<b>Chapter 1</b>	<b>General Introduction</b>	
<b>Figure 1.1</b>	DNA base pair. Thymine (T) and adenine (A) connected by two hydrogen bonds; three hydrogen bonds connect guanosine (G) and cytosine (C). The anti-parallel alignment of 3' and 5' ends of sugar-phosphate backbones.	4
<b>Figure 1.2</b>	Molecular structure of different types of amphiphiles and their self-assembly pattern to produce distinct nanostructures.	6
<b>Figure 1.3</b>	Fmoc-peptide amphiphile (guest) and (b) discotic aromatic additive as host (c) development of helical nanofiber through co-assembly.	7
<b>Figure 1.4</b>	Naphthalene-diimide derivative self-assembles to produce vesicle. Morphological transition (2D to 1D; vesicle to fiber) was observed after assembly with pyrene.	8
<b>Figure 1.5</b>	The co-assembly of C3-symmetric (Np-Trx) donor molecule, the linear molecule (MV-NDI) which acts as an acceptor, and the CB[8] acts as host-molecule for the formation of the hexagonal superstructure (2D SOF).	9
<b>Figure 1.6</b>	Schematic of the possible assembly of two amphiphiles into fibers. (a) Self-sorting; (b) random co-assembly; (c) specific co-assembly.	11
<b>Figure 1.7</b>	Molecular structures of regioisomeric compounds and the schematic representation of their solvent-dependent self-assembly (left and right), co-assembly and time-dependent self-sorting (center).	12
<b>Figure 1.8</b>	(A) Molecular structures of cyanuric acid and	14

melamine connected through hydrogen bond and the anti-tumor drug MTX. (B) Peptide amphiphile and the cartoon representation of the co-assembly with MTX.

- Figure 1.9** Bicomponent chemical conjugation catalyzes gelator and gel formation. Trishydrazone hydrogelator formed by covalent conjugation of building blocks leads to the formation of a hydrogel. 15
- Figure 1.10** Oxidized sodium hyaluronate (HA-ALD) and carbon dots dynamic crosslinking lead to the formation of a strong hydrogel. 16
- Figure 1.11** Random co-assembly of GO with DNA forms a self-supporting hydrogel upon heating. The hydrogel shows excellent self-healing property. 18
- Figure 1.12** Supramolecular chirality control in bicomponent systems. Small amphiphilic molecule based co-assembled nanomaterials. 19
- Figure 1.13** (a) The molecular structure of the  $C_3$  symmetric amphiphiles. (b) Showing the co-assembly pattern of chiral molecule with a large number of achiral molecules. 21
- Figure 1.14** H-aggregates driven helical inversion of DPDS and J-aggregates control the co-assembly of EDPAz with LCHF (left) or DCHF (right). M: left-handed nanofibers and P: right-handed nanofibers. 22

<b>Figure 1.15</b>	<i>C<sub>3</sub> symmetric building block is showing symmetry breaking after gelation. Co-assembly with chiral solvents leads to chiral induction and persistence of chiral memory.</i>	23
<b>Figure 1.16</b>	Showing the multi-stimuli responsiveness of supramolecular hydrogel.	25
<b>Figure 1.17</b>	pH-controlled transition of vesicle size and doxorubicin release via the generation of AAC-rich channels transmembrane in large vesicles.	26
<b>Figure 1.18</b>	Schematic representation of sonication induced gelation process.	27
<b>Figure 1.19</b>	Mechanism of interactions of light induced assembly and disassembly process of a bicomponent co-assembled hydrogel.	28
<b>Figure 1.20</b>	G4-quadruplex co-assembled with K <sup>+</sup> ions to produce self-supporting hydrogel for the application in 3D printing and cell culture.	29
<b>Figure 1.21</b>	The co-assembly of Fmoc-FF and KGM produces hydrogel. Showing crosslinked fibrillar network formation due to co-assembly and used for docetaxel release.	30
<b>Figure 1.22</b>	The selective catalytic activity of self-sorted vs. co-assembled bicomponent hydrogels.	32
<b>Chapter 2</b>	<b>Blue Light Emitting Self-healable Graphene Quantum Dot Embedded Hydrogels</b>	
<b>Figure 2.1</b>	<sup>1</sup> H NMR spectrum of anthracen-9-ylmethyl(4-nitrophenyl) carbonate ( <b>i</b> ) in CDCl <sub>3</sub> .	72

<b>Figure 2.2</b>	<sup>1</sup> H NMR spectrum of Amoc-Phe-OH ( <b>1</b> ) in DMSO-d <sub>6</sub> .	73
<b>Figure 2.3</b>	<sup>13</sup> C NMR spectrum of Amoc-Phe-OH ( <b>1</b> ) in DMSO-d <sub>6</sub> .	74
<b>Figure 2.4</b>	ESI-MS spectrum of Amoc-F-OH ( <b>1</b> ).	74
<b>Figure 2.5</b>	<sup>1</sup> H NMR spectrum of Amoc-Tyr-OH ( <b>2</b> ) in DMSO-d <sub>6</sub> .	75
<b>Figure 2.6</b>	<sup>13</sup> C NMR spectrum of Amoc-Tyr-OH ( <b>2</b> ) in DMSO-d <sub>6</sub> .	75
<b>Figure 2.7</b>	ESI-MS spectrum of Amoc-Y-OH ( <b>2</b> ).	76
<b>Figure 2.8</b>	Schematic representation of gel nanofibers and GQDs embedded gel nanofibers through non-specific molecular co-assembly.	79
<b>Figure 2.9</b>	(a) SEM and (b) TEM images of GQDs show dots are separated and well distributed.	80
<b>Figure 2.10</b>	SEM image of Gel-F (a) shows nanofibrillar network. (b) SEM image of Gel-Y shows nanofibrillar network. (c) describes the GQDs decorated morphology by the SEM image of GQD-F(10 mM of Amoc-F-OH with 0.5 mg mL <sup>-1</sup> GQDs) and (d) SEM image shows GQDs deposited fiber of GQD-Y (10 mM of Amoc-Y-OH with 0.5 mg mL <sup>-1</sup> GQDs).	81
<b>Figure 2.11</b>	TEM images of (a) GQD-F (10 mM of Amoc-F-OH with 0.5 mg L <sup>-1</sup> GQDs) and (b) GQD-Y (10 mM of Amoc-Y-OH with 0.5 mg L <sup>-1</sup> GQDs) show GQDs decorated nanofibrillar structures. Both images depict uniform distribution of GQDs on the fibrillar networks.	81
<b>Figure 2.12</b>	TEM image of GQD-F (10 mM of Amoc-F-OH with 0.5 mg mL <sup>-1</sup> GQDs) depicts graphene	82

quantum dots are embedded on fibril (a) And at higher magnification it was shown the size of the decorated GQDs are mostly 7-9 nm. (c), (d) TEM images of GQD-Y (10 mM of Amoc-Y-OH with 0.5 mg mL<sup>-1</sup> GQDs) shows random distribution of GQDs on the fibril.

- Figure 2.13** (a) and (b) represent the TEM images at different concentration of GQDs in GQD-F (10 mmol L<sup>-1</sup> of Amoc-F-OH). (a) corresponds to 0.3 mg mL<sup>-1</sup> of GQDs which shows less amount of GQDs are deposited on the fibril whereas (b) shows more number of GQDs are deposited on the fiber with 0.7 mg mL<sup>-1</sup> of GQDs. (c) and (d) shows the TEM images for GQD-Y with 0.3 mg mL<sup>-1</sup> and 0.7 mg mL<sup>-1</sup> of GQDs respectively. (c) and (d) also showed similar observation as like (a) and (b). 83
- Figure 2.14** (a) and (b) show UV-Vis spectra of GQDs, Gel-F, Gel-Y, GQD-F and GQD-Y. Red shift in UV-Vis was observed for both the gels. Fluorescence spectra of (c) Amoc-F-OH (10 mM), GQD-F and (d) Amoc-Y-OH (10 mM), GQD-Y show successive quenching on increasing addition of GQDs. 84
- Figure 2.15** Dynamic frequency sweep experiment: (a) GQD-F becomes 6 times more rigid than Gel-F due to interaction of GQDs. (b) Step strain experiment signifies thixotropic nature and excellent gel recovery of GQD-F. 86
- Figure 2.16** GQD-Y becomes two times rigid than Gel-Y after inclusion of GQDs represented in dynamic frequency sweep experiment. (b) Step strain 86

experiment describes thixotropic nature and self-healing property of the gel GQD-Y.

**Figure 2.17** (a) and (b) are the optical images of GQD-F, GQD-Y respectively under day light. (c) and (d) are the images under UV light irradiation at a wavelength of 365 nm of hydrogels GQD-F and GQD-Y respectively. Optical images (e) to (i) represent the self-healing property of GQD-F. Hydrogel pieces adhere together after keep in contact with each other and regenerate previous shape by crosslinking network by noncovalent interaction. (i), (j) and (k) represent the self-healing property of the gel GQD-Y. 88

### **Chapter 3 Tuning the Handedness: Role of Chiral Component in Peptide appended Bolaamphiphile-based Co-assembled Hydrogels**

<b>Figure 3.1</b>	<sup>1</sup> H NMR spectrum of compound <b>iii</b> in CDCl <sub>3</sub> .	108
<b>Figure 3.2</b>	Mass spectrum of compound <b>iii</b> .	108
<b>Figure 3.3</b>	<sup>1</sup> H NMR spectrum of compound <b>3</b> in DMSO-d <sub>6</sub> .	109
<b>Figure 3.4</b>	<sup>13</sup> C NMR spectrum of compound <b>3</b> in DMSO-d <sub>6</sub> .	109
<b>Figure 3.5</b>	Mass spectrum of compound <b>3</b> .	110
<b>Figure 3.6</b>	<sup>1</sup> H NMR spectrum of compound <b>iv</b> in DMSO-d <sub>6</sub> .	110
<b>Figure 3.7</b>	Mass spectrum of compound <b>iv</b> .	111
<b>Figure 3.8</b>	<sup>1</sup> H NMR spectrum of compound <b>4</b> in DMSO-d <sub>6</sub> .	112
<b>Figure 3.9</b>	<sup>13</sup> C NMR spectrum of compound <b>4</b> in DMSO-d <sub>6</sub> .	112
<b>Figure 3.10</b>	Mass spectrum of compound <b>5</b> .	112
<b>Figure 3.11</b>	<sup>1</sup> H NMR spectrum of compound <b>v</b> in DMSO-d <sub>6</sub> .	113

<b>Figure 3.12</b>	Mass spectrum of compound <b>v</b> .	113
<b>Figure 3.13</b>	$^1\text{H}$ NMR spectrum of compound <b>vi</b> in $\text{DMSO-d}_6$ .	114
<b>Figure 3.14</b>	Mass spectrum of compound <b>vi</b> .	114
<b>Figure 3.15</b>	$^1\text{H}$ NMR spectrum of compound <b>5</b> in $\text{DMSO-d}_6$ .	115
<b>Figure 3.16</b>	$^{13}\text{C}$ NMR spectrum of compound <b>5</b> in $\text{DMSO-d}_6$ .	115
<b>Figure 3.17</b>	Mass spectrum of compound <b>5</b> .	116
<b>Figure 3.18</b>	$^1\text{H}$ NMR spectrum of compound <b>vii</b> in $\text{CDCl}_3$ .	117
<b>Figure 3.19</b>	Mass spectrum of compound <b>vii</b> .	117
<b>Figure 3.20</b>	$^1\text{H}$ NMR spectrum of compound <b>6</b> in $\text{DMSO-d}_6$ .	118
<b>Figure 3.21</b>	$^{13}\text{C}$ NMR spectrum of compound <b>6</b> in $\text{DMSO-d}_6$ .	118
<b>Figure 3.22</b>	Mass spectrum of compound <b>6</b> .	118
<b>Figure 3.23</b>	$^1\text{H}$ NMR spectrum of compound <b>viii</b> in $\text{DMSO-d}_6$ .	119
<b>Figure 3.24</b>	Mass spectrum of compound <b>viii</b> .	119
<b>Figure 3.25</b>	$^1\text{H}$ NMR spectrum of compound <b>7</b> in $\text{DMSO-d}_6$ .	120
<b>Figure 3.26</b>	$^{13}\text{C}$ NMR spectrum of compound <b>7</b> in $\text{DMSO-d}_6$ .	121
<b>Figure 3.27</b>	Mass spectra of compound <b>7</b> .	121
<b>Figure 3.28</b>	$^1\text{H}$ NMR spectrum of compound <b>ix</b> in $\text{CDCl}_3$ .	122
<b>Figure 3.29</b>	Mass spectra of compound <b>ix</b> .	122
<b>Figure 3.30</b>	$^1\text{H}$ NMR spectrum of compound <b>8</b> in $\text{DMSO-d}_6$ .	123
<b>Figure 3.31</b>	$^{13}\text{C}$ NMR spectrum of compound <b>8</b> in $\text{DMSO-d}_6$ .	123

<b>Figure 3.32</b>	Mass spectra of compound <b>8</b> .	123
<b>Figure 3.33</b>	$^1\text{H}$ NMR spectrum of compound <b>x</b> in DMSO- $\text{d}_6$ .	124
<b>Figure 3.34</b>	Mass spectrum of compound <b>x</b> .	124
<b>Figure 3.35</b>	$^1\text{H}$ NMR spectrum of compound <b>9</b> in DMSO- $\text{d}_6$ .	125
<b>Figure 3.36</b>	$^{13}\text{C}$ NMR spectrum of compound <b>9</b> in DMSO- $\text{d}_6$ .	125
<b>Figure 3.37</b>	Mass spectrum of compound <b>9</b> .	126
<b>Figure 3.38</b>	$^1\text{H}$ NMR spectrum of compound <b>xi</b> in DMSO- $\text{d}_6$ .	126
<b>Figure 3.39</b>	Mass spectrum of compound <b>xi</b> .	127
<b>Figure 3.40</b>	$^1\text{H}$ NMR spectrum of compound <b>10</b> in DMSO- $\text{d}_6$ .	128
<b>Figure 3.41</b>	$^{13}\text{C}$ NMR spectrum of compound <b>10</b> in DMSO- $\text{d}_6$ .	128
<b>Figure 3.42</b>	Mass spectrum of compound <b>10</b> .	128
<b>Figure 3.43</b>	$^1\text{H}$ NMR spectrum of compound <b>xii</b> in DMSO- $\text{d}_6$ .	129
<b>Figure 3.44</b>	Mass spectrum of compound <b>xii</b> .	129
<b>Figure 3.45</b>	$^1\text{H}$ NMR spectrum of compound <b>11</b> in DMSO- $\text{d}_6$ .	130
<b>Figure 3.46</b>	$^{13}\text{C}$ NMR spectrum of compound <b>11</b> in DMSO- $\text{d}_6$ .	130
<b>Figure 3.47</b>	Mass spectrum of compound <b>11</b> .	130
<b>Figure 3.48</b>	Images of bolaamphiphiles <b>7-11</b> with D/L-tartaric acid.	135
<b>Figure 3.49</b>	(a), (b) and (c) represent the frequency sweep experiment data of the hydrogels <b>3</b> , <b>4</b> and hydrogel <b>5</b> ( <b>9</b> + MTA) respectively. Both signify rigid hydrogel formation.	136

<b>Figure 3.50</b>	SEM images of bolaamphiphiles <b>3</b> and <b>6-10</b> at pH 6.	137
<b>Figure 3.51</b>	SEM images of co-assembled systems <b>7-10</b> with L/D-tartaric acid and hydrogel <b>5</b> .	137
<b>Figure 3.52</b>	(a), (b) SEM and TEM images of hydrogel <b>3</b> showing right-handed (P-helix) nanofiber and (c), (d) are the SEM and TEM images of hydrogel <b>4</b> showing left-handed (M-helix) nanofiber.	138
<b>Figure 3.53</b>	(a) TEM image of <b>6</b> showing vesicles. (b), (c) Show the TEM images of right handed helical fibers of hydrogel <b>3</b> ( <b>6</b> + DTA). (d) The TEM image of hydrogel <b>4</b> ( <b>6</b> + LTA) showing left-handed helical fibers.	138
<b>Figure 3.54</b>	(a) Showing the formation of spheres comprised with <b>6</b> . The spheres ruptured on interaction with D-tartaric acid and L-tartaric acid. (b) Shows the nucleation of the small helical unit with D-tartaric acid and L-tartaric acid. (c) The growth of right-handed helical fiber with D-tartaric acid and left-handed helical fiber with L-tartaric acid. Higher order self-assembly of right-handed and left-handed chiral nanofibers and resulting formation of crosslinked helical nanofibrous hydrogels <b>3</b> and <b>4</b> .	139
<b>Figure 3.55</b>	(a) DLS spectra of formed spherical aggregates of compound <b>6</b> .	139
<b>Figure 3.56</b>	(a), (b) are the overlaid FTIR spectra of hydrogel <b>3</b> ( <b>6</b> + DTA) and hydrogel <b>4</b> ( <b>6</b> + LTA) respectively.	140
<b>Figure 3.57</b>	(a), (b) are the overlaid powder X-ray diffraction spectra of hydrogel <b>3</b> ( <b>6</b> + DTA) and hydrogel <b>4</b> ( <b>6</b>	141

+ LTA) respectively.

- Figure 3.58** Concentration dependent NMR spectra of hydrogel **3** with different proportion of D-tartaric acid in D<sub>2</sub>O. Concentration dependent NMR spectra of hydrogel **4** with different proportion of L-tartaric acid in D<sub>2</sub>O. 142
- Figure 3.59** Circular dichroism spectra of **3-11** showing positive and negative spectra depending upon the configuration of the amino acids present in peptides. In all the cases, the concentrations of the bolaamphiphiles (**3-11**) were 400 μM. 143
- Figure 3.60** CD spectra in water and buffer solution of bolaamphiphiles **4-12**. In all the cases, the concentrations of the bolaamphiphiles were 400 μM. 144
- Figure 3.61** CD spectra of **3-11** at pH 6 and 7.4. (a) CD spectra of **3, 4**. (b) CD spectra of **6, 7**. (c) CD spectra of **8, 9** and (d) CD spectra of **10, 11**. The concentrations of all compounds were 400 μM. 145
- Figure 3.62** CD spectra of **7** with variable concentration of D/L-tartaric acid. (a) Shows complete inversion of CD spectra after addition of 250 μM of D-tartaric acid (DTA). (b) Shows small change in CD spectra on addition of L-tartaric acid (LTA). In every case, the concentration of the bolaamphiphile **7** was fixed to 250 μM. 146
- Figure 3.63** (a) The concentration dependent CD spectra of bolaamphiphile **6**. (b) Linear dichroism spectra of bolaamphiphile **6**, before and after addition of D/L-tartaric acid. 147

<b>Figure 3.64</b>	(a) CD spectra of D/L-tartaric acid. (b), (c), (d), (e) and (f) are the CD spectra of bolaamphiphiles <b>7-11</b> with D/L-tartaric acid.	148
<b>Chapter 4</b>	<b>Construction of Porous Organic Nanostructures using Cooperative Self-assembly for Lipase Catalyzed Inclusion of Gastrodigenin</b>	
<b>Figure 4.1</b>	<sup>1</sup> H NMR spectrum of 1,3,5-tris[2-(4-pyridyl)ethenyl]benzene ( <b>12</b> ) in DMSO-d <sub>6</sub> .	164
<b>Figure 4.2</b>	<sup>13</sup> C NMR spectrum of 1,3,5-tris[2-(4-pyridyl)ethenyl]benzene ( <b>12</b> ) in DMSO-d <sub>6</sub> .	164
<b>Figure 4.3</b>	<sup>1</sup> H NMR spectrum of 1,4-bis[2-(4-pyridyl)ethenyl]benzene ( <b>13</b> ) in DMSO-d <sub>6</sub> .	165
<b>Figure 4.4</b>	<sup>13</sup> C NMR spectrum of 1,4-bis[2-(4-pyridyl)ethenyl]benzene ( <b>13</b> ) in DMSO-d <sub>6</sub> .	165
<b>Figure 4.5</b>	Optical images of emulsion gels of (a) <b>tpeb-BTC</b> at different pHs show deformation of emulsion-gels to emulsions. Addition of 100 mM NaCl, the emulsion-gel turns into two phases. (b) Optical images of <b>tpeb-BDC</b> also show the deformation of emulsion-gels to emulsions on variation of pH as well as on the treatment with 100 mM NaCl. (c) Optical images of <b>tpeb-BTC</b> and <b>tpeb-BDC</b> in hexane or in water. <b>tpeb-BTC</b> and <b>tpeb-BDC</b> don't produce self-supporting gel in a particular solvent.	171
<b>Figure 4.6</b>	(a) and (b) represent the frequency sweep experiment of <b>tpeb-BTC</b> and <b>tpeb-BDC</b> emulsion gels respectively. Both signify rigid gel formation.	172
<b>Figure 4.7</b>	(a) TEM image of <b>tpeb-BTC</b> shows nanofibrillar network structures and (b) HR-TEM image of	173

**tpeb-BTC** shows the supramolecular arrangement of fibers having diameter of 3 nm. (c) Supramolecular organic nanofibers show parallel alignment in the **tpeb-BDC** and (d) higher magnification on the side by side aligned molecular fibers of **tpeb-BDC** shows the average diameter of 6 nm.

- Figure 4.8** TEM images (a), (b) show fibrillar bundle formation by **tpeb-BTC** and narrow fibers (diameter 25-40 nm) get separated from bundles. (c) TEM image shows nanorod of **bpeb-BTC** and no significant morphology was observed for **bpeb-BDC** (d). 174
- Figure 4.9** (a), (b), (c) and (d) show the overlaid plot of the IR spectra of **tpeb-BTC**, **tpeb-BDC**, **bpeb-BTC** and **bpeb-BDC** emulsions respectively. 175
- Figure 4.10** (a), (b), (c) and (d) describe UV-Vis spectra of **tpeb-BTC**, **tpeb-BDC**, **bpeb-BTC** and **bpeb-BDC** systems. 176
- Figure 4.11** (a), (b), (c) and (d) show the overlaid plot of the XRD patterns of **tpeb-BTC**, **tpeb-BDC**, **bpeb-BTC** and **bpeb-BDC** systems respectively. 178
- Figure 4.12** (a) and (b) are the SAXS spectra of both **tpeb-BTC** and **tpeb-BDC** respectively. Both the data shows the size of the nanostructures formed in the system. (c) and (d) show the pore size distribution obtained from N<sub>2</sub> adsorption of **tpeb-BTC** and **tpeb-BDC** respectively which matches with the calculated data obtained from SAXS. 179

- Figure 4.13** (a) and (b) show the thermogravimetric analysis (TGA) of **tpeb-BTC** and **tpeb-BDC** respectively.  $N_2$  adsorption in (c) **tpeb-BTC** and (d) **tpeb-BDC** system signify the formation of porous supramolecular organic nanostructures. 180
- Figure 4.14** (a) Cartoon representation of molecular complexes of emulsions-gel **tpeb-BTC**, **tpeb-BDC** and emulsions **bpeb-BTC** and **bpeb-BDC**. (b) The molecular complex of **tpeb-BTC** elongated vertically through columnar  $\pi$ - $\pi$  stacking which forms fibril. Then the fibers composed to form nano-fibrillar bundle. (c) Molecular complex of **tpeb-BDC** with large cavity through columnar stacking forms aligned supramolecular organic nanofibrillar structure. (d) The complex of **bpeb-BTC** elongates through  $\pi$ - $\pi$  stacking interactions forms supramolecular rods. 181
- Figure 4.15** (a) Real time images of **tpeb-BDC** emulsion-gel for lipase catalyzed esterification reaction. After 10 hours of enzymatic reaction, **tpeb-BDC** emulsion-gel converted to sol-emulsion. At 16 hours of the reaction, the emulsion-gel converted into two phases. (b) Rheological analysis of emulsion-gel to sol-emulsion transition. (c) HPLC chromatograms at different reaction time and (d) real-time enzymatic conversion of mono-ester, di-ester. The colors in the graph signify different physical states (emulsion-gel, emulsion and separation of two phases). 183

**Figure 4.16** (a) Standardization of enzyme concentration used for esterification of BDC in tpeb-BDC emulsion gel. (b) Rheological analysis of gel to sol transition of tpeb-BTC. (c), (d) are the HPLC chromatograms of different enzymatic esterification cycles and corresponding histogram plot of the formed BDC-diester. (e) shows the overlaid plot of HPLC chromatograms of BTC monoester formation. (f) Plot of conversion of BTC monoester in tpeb-BTC emulsion-gel. 185

**Figure 4.17** Overall enzymatic esterification cycle of **BDC** in emulsion-gel (**tpeb-BDC**). (i) Formation of emulsion-gel with lipase and p-HBA, (ii) phase separation after esterification, (iii) product isolation and (iv) reformation of emulsion-gel after stirring in presence of additional **BDC**. 186

**Figure 4.18** <sup>1</sup>H NMR spectrum of **BDC** diester formed after enzymatic reaction in emulsion-gel **tpeb-BDC**. Peak at  $\delta = 5.23$  signifies the formation of ester. To enhance the solubility, 2:1 CDCl<sub>3</sub> and DMSO-d<sub>6</sub> was used for <sup>1</sup>H NMR analysis. 187

**Chapter 5 Bicomponent Co-assembled Nanotubular Hydrogel as Template for Selective Enzymatic Generation of DOPA**

**Figure 5.1** <sup>1</sup>H NMR spectrum of Boc-Phe-Tyr-OMe (**xiv**) in DMSO-d<sub>6</sub> 204

**Figure 5.2** Mass spectrum of Boc-Phe-Tyr-OMe (**xiv**). 204

**Figure 5.3** <sup>1</sup>H NMR spectrum of Boc-Phe-Tyr-OH (**xv**) in DMSO-d<sub>6</sub> 205

**Figure 5.4** Mass spectra of Boc-Phe-Tyr-OH (**xv**). 205

<b>Figure 5.5</b>	<sup>1</sup> H NMR spectrum of H <sub>2</sub> N-Phe-Tyr-OH ( <b>14</b> ) in DMSO-d <sub>6</sub> .	206
<b>Figure 5.6</b>	<sup>13</sup> C NMR spectrum of H <sub>2</sub> N-Phe-Tyr-OH ( <b>14</b> ) in DMSO-d <sub>6</sub> .	206
<b>Figure 5.7</b>	Mass spectra of H <sub>2</sub> N-Phe-Tyr-OH ( <b>14</b> ).	207
<b>Figure 5.8</b>	Schematic representation of molecular complexes of hydrogel <b>8</b> ( <b>DAN-BTC</b> ). Molecular complex of <b>DAN-BTC</b> elongated vertically through columnar $\pi$ - $\pi$ stacking interaction, which forms a fibril. Then the fibers on going through higher order self-assembly form a nanofibrillar bundle and finally crosslinked fibrillar network was formed.	211
<b>Figure 5.9</b>	Optical imaged of other bicomponent system. DAN: 1,5-diaminonaphthalene, BDC: 1,4-benzenedicarboxylic acid, SA: succinic acid and BCA: Benzene carboxylic acid. All are equimolar mixture 30 mM of <b>DAN</b> and 30 mM of acid.	211
<b>Figure 5.10</b>	(a) Amplitude sweep rheological data showing gel deformation after an applied strain 10%. (b) represents the frequency sweep experiment of hydrogel <b>8</b> which signifies rigid gel formation.	212
<b>Figure 5.11</b>	(a) The comparison of UV-Vis spectra of hydrogel <b>8</b> ( <b>DAN-BTC</b> ). (b) Comparative fluorescence spectra of hydrogel <b>8</b> ( <b>DAN-BTC</b> ).	213
<b>Figure 5.12</b>	(a) The overlaid FT-IR spectra of <b>DAN-BTC</b> showing significant change in peaks. (b) The overlaid PXRD plot of <b>DAN-BTC</b> , <b>DAN</b> and <b>BTC</b> .	214
<b>Figure 5.13</b>	(a) SEM image of hydrogel <b>8</b> showing fibrillar bundle. (b) Fibrillar nanostructures were observed from TEM image of hydrogel <b>8</b> .	215

- Figure 5.14** (a) showing the substrate chosen for the tyrosinase catalyzed DOPA formation. (b) shows the detailed mechanistic aspect of tyrosinase enzyme activity on tyrosine functionalized peptide. Which shows dopaquinone formation and further oligomerization occurs to form melanin. (c) Tyrosinase selectively forms L-DOPA functionalized peptide and no further oxidation occurs to form dopaquinone in hydrogel **8**. 216
- Figure 5.15** (a) Shows optical images of Y in buffer before (colourless) and after the reaction (dark brown). (b) Optical images of **DAN-BTC** hydrogel showing no color change before and after the conversion of L-DOPA from tyrosine. (c) Conversion of L-DOPA from tyrosine in hydrogel observed by HPLC chromatogram. (d) Optical images of FY in buffer solution before and after the reaction showing significant color change due to oxidation and oligomerization of DOPA (e) Optical images of **DAN-BTC** hydrogel showing no color change before and after the conversion of F-(L)-DOPA from FY. (f) Conversion of F-(L)-DOPA from FY in hydrogel observed by HPLC chromatogram. 217
- Figure 5.16** HPLC chromatogram of the formation of L-DOPA in hydrogel. 218
- Figure 5.17** Mass spectrum of L-DOPA synthesized in hydrogel medium. 218
- Figure 5.18** Mass spectrum of F-(L)-DOPA synthesized in hydrogel medium. 218

## List of Schemes

<b>Chapter 2</b>	<b>Blue Light Emitting Self-healable Graphene Quantum Dot Embedded Hydrogels</b>	
<b>Scheme 2.1</b>	Synthetic pathway of Amoc-capped amino acid based amphiphiles	71
<b>Chapter 3</b>	<b>Tuning the Handedness: Role of Chiral Component in Peptide appended Bolaamphiphile-based Co-assembled Hydrogels</b>	
<b>Scheme 3.1</b>	Synthetic scheme of bolaamphiphiles 3-11	107
<b>Chapter 4</b>	<b>Construction of Porous Organic Nanostructures using Cooperative Self-assembly for Lipase Catalyzed Inclusion of Gastrodigenin</b>	
<b>Scheme 4.1</b>	Synthetic scheme of pyridyl amphiphiles 12 and 13	163
<b>Chapter 5</b>	<b>Bicomponent Co-assembled Nanotubular Hydrogel as Template for Selective Enzymatic Generation of DOPA</b>	
<b>Scheme 5.1</b>	Synthetic scheme of compound 14	203



## List of Tables

<b>Chapter 2</b>	<b>Blue Light Emitting Self-healable Graphene Quantum Dot Embedded Hydrogels</b>	
<b>Table 2.1</b>	Preparation of hydrogels with different conc. of gelators and amount of GQDs	79
<b>Chapter 3</b>	<b>Tuning the Handedness: Role of Chiral Component in Peptide appended Bolaamphiphile-based Co-assembled Hydrogels</b>	
<b>Table 3.1</b>	Molecular structure of bolaamphiphiles <b>3-11</b> with absolute configuration of amino acids. CD behavior of <b>3-11</b> and physical appearance of <b>3-11</b> with addition of D-tartaric acid (DTA) and L-tartaric acid (LTA). CD behaviors of bicomponent systems are also presented.	117
<b>Chapter 4</b>	<b>Construction of Porous Organic Nanostructures using Cooperative Self-assembly for Lipase Catalyzed Inclusion of Gastrodigenin</b>	
<b>Table 4.1</b>	Composition of the bicomponent systems and physical appearance	170
<b>Chapter 5</b>	<b>Bicomponent Co-assembled Nanotubular Hydrogel as Template for Selective Enzymatic Generation of DOPA</b>	
<b>Table 5.1</b>	Composition of the bicomponent systems and physical appearance	210



## ACRONYMS

Abbreviations used for amino acids, peptides, derivatives, substituents, reagents, etc. are largely in accordance with the recommendations of the IUPAC-IUB commission on Biochemical Nomenclature, 1974, Pure and Applied Chemistry, 40, 315-331. All amino acids are L-configuration. Standard three letter coding is used for all amino acids. Additional abbreviations used in this thesis are listed below.

Amoc	9-anthracenemethyloxycarbonyl
Amoc-F	Amoc-Phe
Amoc-Y	Amoc-Tyr
Boc	<i>tert</i> -butyloxycarbonyl
BCA	Benzene carboxylic acid
BDC	Benzene dicarboxylic acid
BTC	Benzene tricarboxylic acid
bpeb	1,4-Bis[2-(4-pyridyl)ethenyl]benzene
CD	Circular Dichroism
CRL	Candida Rugosa Lipase
CDCl <sub>3</sub>	Chloroform-d
DAN	1,5-diaminonaphthaline
DCM	Dichloromethane
DCC	Dicyclohexylcarbodiimide
DMSO	Dimethyl sulfoxide
DMF	Dimethyl Formamide
DTA	D-Tartaric acid
EtOAc	Ethyl Acetate
ESI-MS	Electrospray Ionization Mass Spectrometry
FTIR	Fourier Transform Infrared Spectroscopy
F/Phe	Phenylalanine
GQDs	Graphene quantum dots

HOBt	1-Hydroxybenzotriazole
HPLC	High Performance Liquid Chromatography
HCl	Hydrochloric Acid
HBA	4-Hydroxybenzyl Alcohol
L/Leu	Leucine
LD	Linear Dichroism
LTA	L-Tartaric acid
MeOH	Methanol
Me	Methyl
M	Molar
NaCl	Sodium Chloride
NaOH	Sodium Hydroxide
NaHCO <sub>3</sub>	Sodium Hydrogen Carbonate
NMR	Nuclear Magnetic Resonance
Ph	Phenyl
PB	Phosphate Buffer
pH	The negative logarithm hydrogen-ion activity (-log <sub>10</sub> [H <sub>3</sub> O <sup>+</sup> ])
PXRD	Powder X-ray Diffraction
SA	Succinic acid
SAXS	Small Angle X-ray Scattering
SEM	Scanning Electron Microscope
TEM	Transmission Electron Microscope
TFA	Trifluoroacetic acid
THF	Tetrahydrofuran
TLC	Thin Layer Chromatography
TON	Turnover numbers
TOF	Turnover frequency
tpcb	1,3,5-Tris[2-(4-pyridyl)ethenyl]benzene
Tyr/Y	Tyrosine
UV-Vis	UV-Visible Spectroscopy

## NOMENCLATURE

$\theta$	Angle
$\lambda$	Wavelength
$\alpha$	Alfa
$\beta$	Beta
$\text{\AA}$	Angstrom
nm	Nanometer
$\omega$	Angular frequency
$\delta$	delta
$\mu\text{m}$	Micrometer
$\pi$	Pi
$\sigma$	Sigma
$\gamma$	Gamma
$G'$	Storage modulus
$G''$	Loss modulus



# Chapter 1

## General Introduction



## 1.1 Introduction of Molecular Assembly

Nature has mastery at designing life by fabrication of complex system (i.e., cellular machinery).<sup>[1]</sup> These natural systems are constructed by the ordering of small and uncombed molecular building blocks using hydrogen bond,  $\pi$ - $\pi$  stacking, hydrophobic, van der Waals, ionic, and dipole-dipole interactions.<sup>[2]</sup> Such self-sorting of molecules to a defined nanostructure at multiple size scales is termed as self-assembly.<sup>[3]</sup> Therefore, self-assembly relies on spontaneous integration of either single or multiple components which results in the production of either distinct supermolecules or extended polymolecular assemblies.<sup>[4]</sup> In self-assembled systems desired nano-architecture can be more easily assessed by integrating multiple components. Nature has also served as an inspiration for the multicomponent self-assembly to introduce organized building block-based nano-architectures. Therefore, a variety of molecules including amino acids, peptides, proteins, ureas, nucleobases, DNA, and polysaccharides are being used as the foundation for multicomponent self-assembly. Such multiple prebiotic components self-assemble or self-organize to form cellular life in nature and continuously replicate their linear sequence of monomer. Thus self-assembly process operates several cellular functions in nature. DNA, micelles, vesicles and protein aggregation are the noticeable biological self-assembled systems.<sup>[5]</sup>

DNA is a basic example of multicomponent self-assembly in all living things.<sup>[6]</sup> DNA forms by versatile cooperative noncovalent interactions of multiple components. Individual hydrogen bonding of adenine (A) with thymine (T) and guanine (G) with cytosine (C) helps these nucleobases to hold together to construct large self-assembled double helical superstructures (Figure 1.1).<sup>[7]</sup> DNA transfers the genetic information through dynamic and self-replication. Duplicate chromosomes are generated in each cell by the instruction during the transformation of genetic information in cell division to provide a complete set of

chromosomes. The self-assembled DNA performs these entire significant roles. These unique properties of DNA have made it prepossessing substance for scientists and engineers who are intended to develop nanotechnology.<sup>[8-12]</sup>

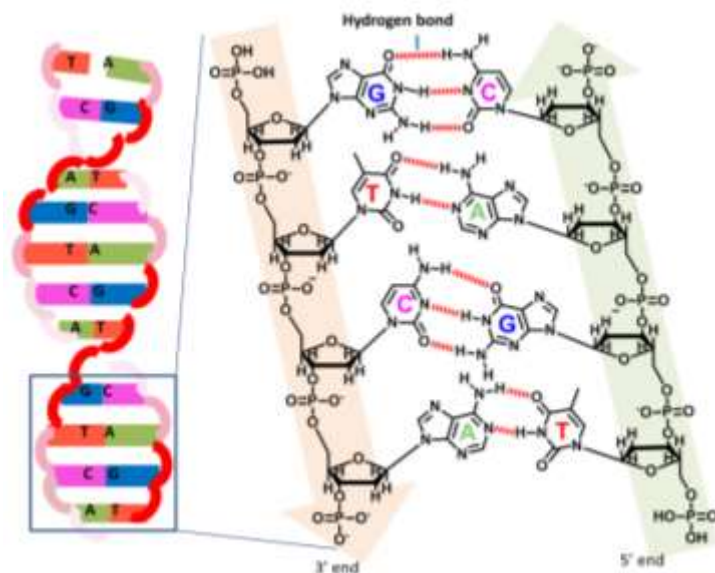


**Figure 1.1.** DNA base pair. Thymine (T) and adenine (A) connected by two hydrogen bonds; three hydrogen bonds connect guanosine (G) and cytosine (C). The anti-parallel alignment of 3' and 5' ends of sugar-phosphate backbones.

The process of self-assembly and disassembly of coat protein in several biological processes helps to transport proteins and lipids.<sup>[13]</sup> Another important example is the formation of a hexameric self-assembled system of insulin which controls the carbohydrate and fat metabolism in the human body. Biocatalysts trigger the integration process of amino acids through peptide bond formation in the living organism. Therefore, self-assembly is found as a powerful approach in the biological pool to function complex machinery. Inspired by such complex machinery, researchers developed various self-assembled systems to understand the biological processes. In chemical biology, the comprehension of the self-assembly process that connects the complementary molecular building blocks through non-covalent interactions,<sup>[14-15]</sup> is the prime concern.

Besides the biomolecular nanostructures, appropriate amphiphilic organic molecules are competent to self-assemble in an organic or aqueous solvent, resulting in a self-supporting gel.<sup>[16-22]</sup> The gel formed in an aqueous medium due to this self-assembly process is termed as a supramolecular hydrogel.<sup>[23-24]</sup> Nowadays supramolecular hydrogel has gained significant attention due to their versatile application in drug delivery,<sup>[25-27]</sup> tissue engineering<sup>[28-30]</sup> biosensing,<sup>[31-32]</sup> wound healing and optoelectronic devices.<sup>[33]</sup> The processes involved in the formation of hydrogel includes chemical synthesis,<sup>[34]</sup> macromolecular assembly, colloidal aggregation<sup>[35-37]</sup> molecular self-assembly<sup>[38]</sup> and multicomponent self-assembly. The self-assembled nanostructures and devices can be achieved through either “top-down” or “bottom-up” approach. The bottom-up approach is more convenient as the molecular building blocks assemble into ordered structures through non-covalent interactions.<sup>[39-40]</sup> The self-assembly process is generally guided by bioactive components or low molecular weight organic molecules or by both of them. These small organic molecular building blocks are developed by tuning the hydrophobic and hydrophilic part of the molecules to construct the controlled self-assembled materials. The molecular building blocks are commonly termed as amphiphiles and these components have a significant impact to exploit the arsenal of self-assembled nanostructured materials.

### 1.2 Amphiphiles for Self-assembled Nanostructures

Amphiphilic molecules are the building blocks to produce unique and novel materials through self-assembly processes for the application in advance nanotechnology.<sup>[41-42]</sup> The integrated actions of such amphiphilic molecules in biosystems allow the act of highly specific cellular functions.<sup>[43-44]</sup> Recent study demonstrates that the thermodynamic incompatibility between the different blocks is the reason for spatial organization into ordered morphologies and this leads to the construction

of nanoscale structural features. Moreover, structural modulation to control the morphology and nanostructured materials has come slowly over the last few decades. The structural modulation leads to the generation of various structural changes in amphiphilic molecules such as monofunctional or typical amphiphile, bifunctional or bolaamphiphiles trifunctional or discotic or  $C_3$  symmetric amphiphiles and also some dendrimeric amphiphiles. This new generation of amphiphiles individually self-assembled to form distinct nanostructure and generally packed differently to produce the unique morphology depending upon its molecular structure (Figure 1.2).<sup>[45]</sup>

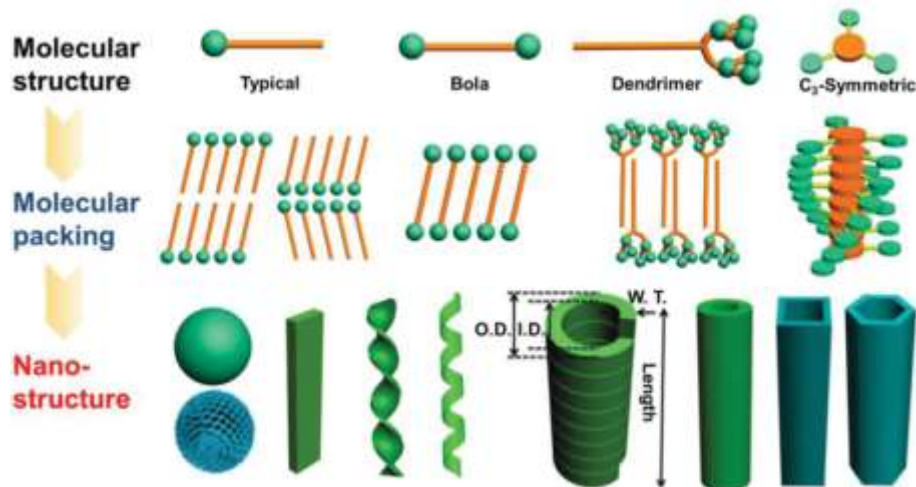


**Figure 1.2.** Molecular structure of different types of amphiphiles and their self-assembly pattern to produce distinct nanostructures.

### 1.2.1 Self-assembly of Typical Amphiphiles

A typical amphiphilic molecule is composed of a hydrophilic head group and a hydrophobic tail as a major moiety.<sup>[42]</sup> Under specific thermodynamic conditions in solution, the amphiphiles self-assemble into nanostructured hydrogel to minimize hydrophobic-tail solvent interactions.<sup>[46]</sup> The nanostructured materials play significant roles in biological membranes, detergency, and drug delivery. Therefore these building blocks were extensively studied over the last few decades.<sup>[47-50]</sup>

N-terminal capped peptide amphiphiles are a significant example of this class of amphiphiles. Banerjee *et al.* showed that the synthesized N-terminally pyrene-conjugated oligopeptide, Py-Phe-Phe-Ala-OMe (Py = pyrene) could form organogel in various organic solvents.<sup>[51]</sup> However, the research works were not only bounded to the self-assembled structures of the amphiphiles. The multicomponent assemblies were also discovered to regulate the nanostructures (Figure 1.3).<sup>[52-53]</sup>

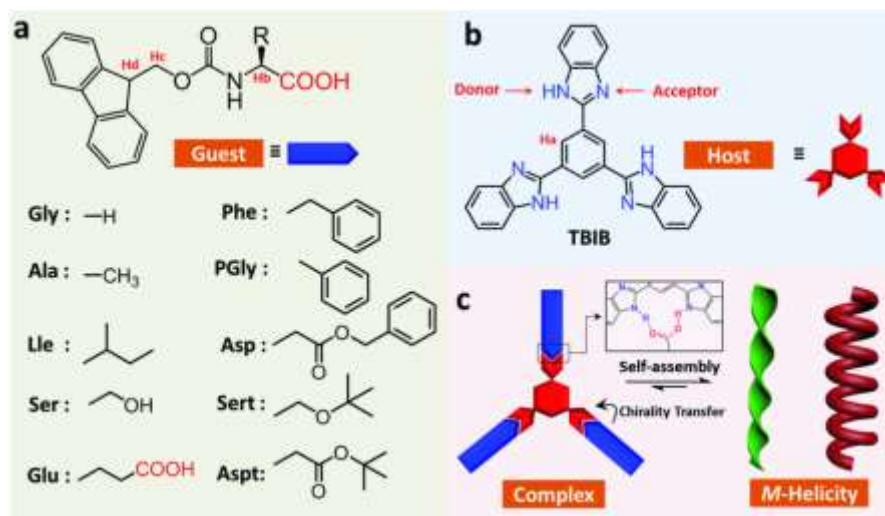


**Figure 1.3.** Fmoc-peptide amphiphile (guest) and (b) discotic aromatic additive as host (c) development of helical nanofiber through co-assembly.

### 1.2.2 Self-assembly of Bolaamphiphiles

Apart from conventional amphiphilic molecules,<sup>[54-55]</sup> an interesting class of two-headed building block known as bolaamphiphile attracted great attention.<sup>[41,56]</sup> A hydrophobic spacer in a bolaamphiphile connects two hydrophilic head groups.<sup>[57]</sup> This bolaamphiphile can self-assemble through non-covalent interactions in water to form a self-supporting hydrogel.<sup>[58]</sup> The formed architecture could be nanotubes with the wall thickness of single molecular-layer distance. Similarly, bolaamphiphile with the methyl ester of histidine also forms single-walled nanotubes. In general, the bolaamphiphiles tend to form nanotubes with single walls. This is due to the presence of two hydrophilic head groups which were

covalently attached with a hydrophobic spacer. The bolaamphiphiles can also produce single layer vesicles without the interference of another component. The multicomponent system helps to tune the nanostructure. The bolaamphiphile produces distinct nanofibers by the multicomponent self-assembly. Ghosh *et. al.* (2014) reported that the naphthalene-diimide-based bolaamphiphile self-assembled to form vesicle without any complementary donor group.<sup>[59]</sup> After inclusion of pyrene donor into the bolaamphiphile, the composite assembles to form 1D-fiber network and finally forms self-supporting hydrogel (Figure 1.4).

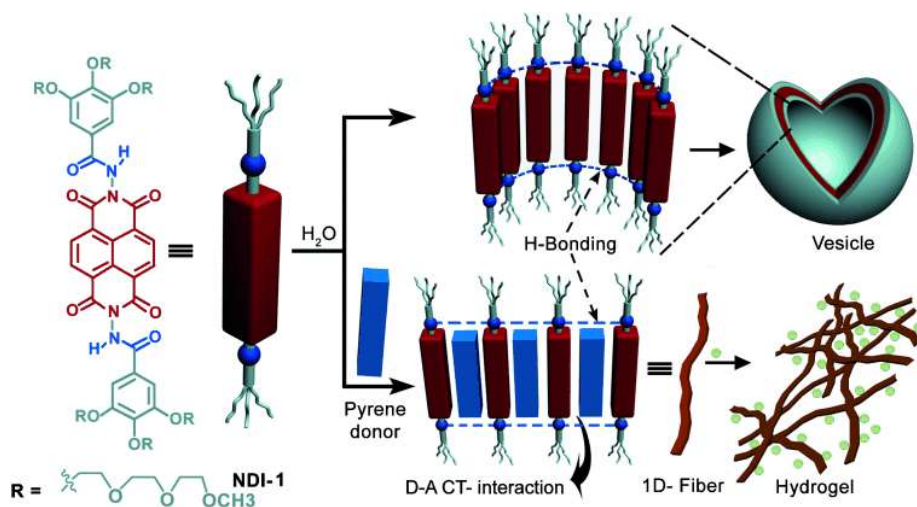


**Figure 1.4.** Naphthalene-diimide derivative self-assembles to produce vesicle. Morphological transition (2D to 1D; vesicle to fiber) was observed after assembly with pyrene.

### 1.2.3 Self-assembly of Trifunctional Amphiphiles

Benzene cored discotic amphiphilic molecules are good gelators as the amphiphiles contain multiple functionalities.<sup>[60-61]</sup> Especially trifunctional amphiphilic molecules were found more significant for the self-assembly as well as gelation.<sup>[62]</sup> The trifunctional amphiphilic molecules serve three sites to interact with complementary amphiphiles. A large number of interactions with complementary building blocks make the development of nanoarchitecture much easier. One of the significant trifunctional

amphiphiles based architecture is porous organic nanostructure. The porous architectures are known for their versatile applications in molecular storage, separation, and catalysis.<sup>[63-68]</sup> The pore sizes of organic frameworks which rely on noncovalent interactions were successfully tuned to avail supramolecular organic frameworks (SOFs).<sup>[69-71]</sup>

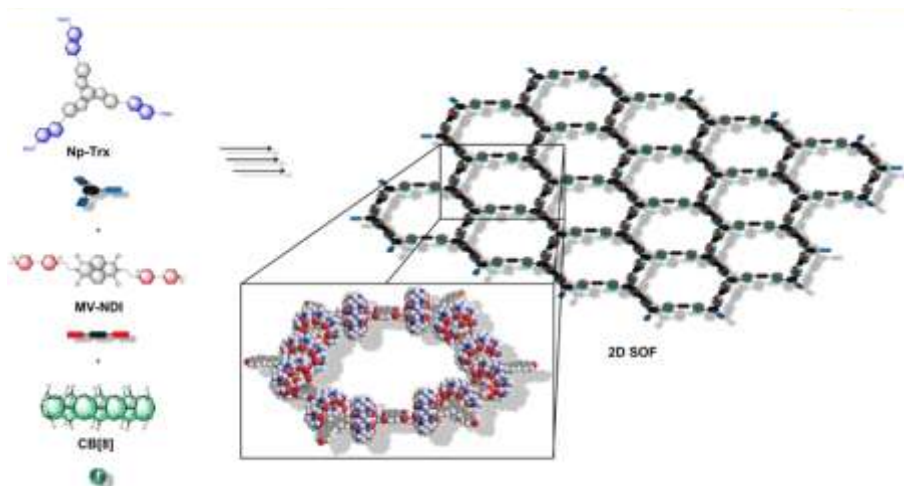


**Figure 1.5.** The co-assembly of C<sub>3</sub>-symmetric (Np-Trx) donor molecule, the linear molecule (MV-NDI) which acts as an acceptor, and the CB[8] acts as host-molecule for the formation of the hexagonal superstructure (2D SOF).

The 2D material exhibits distinct property from those of their bulk counterparts. The two-dimensional SOFs are significant for large surface area. SOF materials are the multicomponent system with porous frameworks as they form through noncovalent interactions using two or more components.<sup>[72-73]</sup> The guest selectivity, flexibility and soft nature make the SOF materials much promising.<sup>[74]</sup> The porosity of SOFs lost by structural deformation upon guest removal and this system was modified by introducing complementary building blocks to achieve a permanent cavity.<sup>[75]</sup> Two-dimensional supramolecular organic frameworks were developed using multicomponent cooperative self-assembly (Figure 1.5). The assembly process enhances donor-acceptor interaction between tris(methoxynaphthyl)-substituted truxene spacer (donor) and a

naphthalene diimide substituted with N-methyl viologenyl moieties (acceptor) in combination with cucurbit[8]uril as host.<sup>[69]</sup>

### 1.3 Development of Bicomponent System

The hydrogel construction method relies on the assembly of multiple components to avail the complete potential of the material in bio-applications.<sup>[76]</sup> This multicomponent or heterotypic hydrogel offers great potentials in bioengineering which is produced by the known approach, i.e., multicomponent self-assembly.<sup>[77]</sup> Bicomponent systems are the humblest multicomponent system to effortlessly direct the self-assembly of the amphiphiles and to grow supramolecular hydrogels.<sup>[78-82]</sup> Two amphiphilic molecules bearing complementary functionality self-organize through noncovalent interaction to form nanostructured gels. Therefore, to attain preferred bicomponent self-assembly, amphiphiles bearing complementary groups were combined.<sup>[83-88]</sup> Cooperative self-assembly between two building blocks changes with altering harmonizing functional groups and the gelation capability of the mixture also rehabilitated.<sup>[89-90]</sup> These cooperative self-assembly depends on supramolecular interactions such as hydrogen-bonding,  $\pi$ - $\pi$  stacking, etc.<sup>[2,91]</sup> Therefore small modification in functional groups causes a significant revolution in the property of the bicomponent system.

Unlike the noncovalent interaction bicomponent system could form a self-supporting hydrogel by covalent conjugation of two components in the system, i.e., covalent bond formation. The co-assembly between two complementary amphiphiles can be tuned very easily. Over the last few years, Adams *et al.* contributed significantly to explore the bicomponent system as a tool for the development of multiple self-assembled materials.<sup>[92,93]</sup> It was also found that spatially resolved bicomponent system can act as a remote control to achieve self-assembled nanostructure.<sup>[94]</sup> Van Eash *et al.* (2009) have reported several

bicomponent systems, which include the addition of different surfactant molecules to the derivatives of 1,3,5-cyclohexyltrisamide hydrogelators.<sup>[95-96]</sup> Generally, gelator molecules autonomously self-assembled into fiber networks. Meanwhile, in a bicomponent system, two molecules can self-sort to form a hydrogel. On the other hand hydrogel can be formed by specific or random co-assembly (Figure 1.6). When the components cooperate to build fibrous nanostructures and the self-assembly is based on a social interaction then this assembly is known as co-operative self-assembly or co-assembly.<sup>[97]</sup>

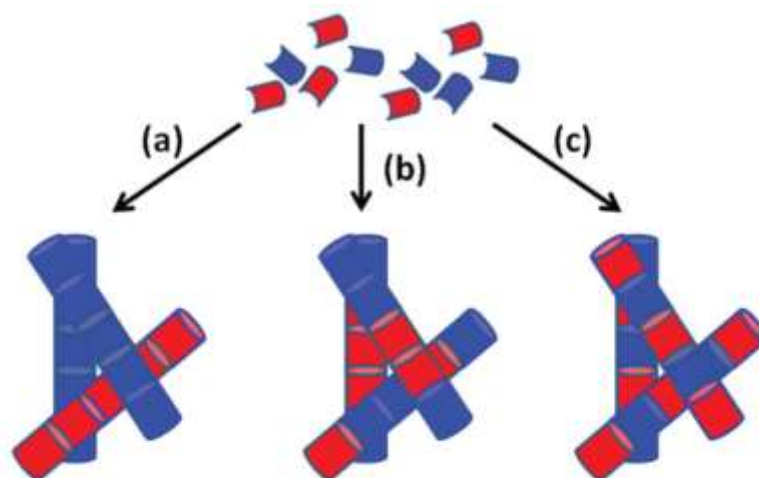


**Figure 1.6.** Schematic of the possible assembly of two amphiphiles into fibers. (a) Self-sorting; (b) random co-assembly; (c) specific co-assembly..

Alternatively, individual amphiphile in a bicomponent system preferably cooperates with themselves which leads to the formation of interpenetrating fibrous networks in the hydrogel. This assembly process is driven by narcissistic interaction and referred as self-sorting.<sup>[98-100]</sup> Sometimes to occur co-assembly in supramolecular gels, two nongelator amphiphiles are essential to complement each other via noncovalent interactions structurally. Therefore, harnessing multiple components for self-assembly is a prime approach in the bottom-up fabrication of bicomponent molecular gels.

### 1.3.1 Bicomponent Self-sorting

Self-sorting depicts the selective recognition of complementary counterparts to produce orthogonal or parallel assembly<sup>[101]</sup> and can be categorized as narcissistic as well as social self-sorting.<sup>[102]</sup> This process could produce abundant aggregates, which leads to the formation of highly organized materials with ordered microscopic structures. Molecular self-sorting is a more adaptable process for low molecular weight building blocks.<sup>[6]</sup> The time-dependent self-sorting of amphiphilic building blocks was also found when the orthogonal noncovalent interactions become operational in a supramolecular assembly (Figure 1.7).<sup>[103]</sup>

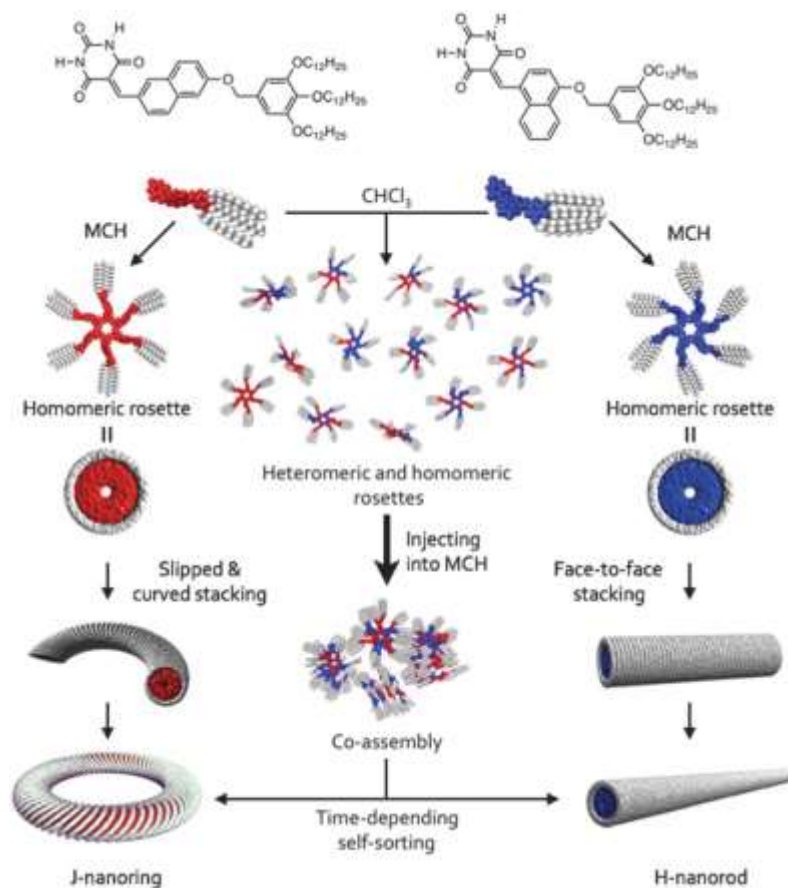


**Figure 1.7.** Molecular structures of regioisomeric compounds and the schematic representation of their solvent-dependent self-assembly (left and right), co-assembly and time-dependent self-sorting (center).

Self or nonself becomes recognizable as the self-sorting process propagates and specificity and directionality of the recognition process helps to distinguish itself from microphase separation.<sup>[104]</sup> The specific nature could be centered on supramolecular interactions,<sup>[105]</sup> comprising hydrogen bonding, ion-dipole interactions and metal-ligand interaction. Self-sorting through a particular supramolecular interaction could play as a substitute of microphase separation in an aqueous medium for the creation of simultaneous aggregates. Therefore, the hydrogen bonding was used in orthogonal self-assembly for the formation of fibers and micelles or vesicles via self-sorting.<sup>[99,106]</sup>

### 1.3.2 Bicomponent Co-assembly

Development of synergistic self-association or co-assembly from multiple components is highly crucial in supramolecular chemistry.<sup>[107]</sup> A molecular-scale integration of amphiphilic materials takes place in co-assembly. The co-assembled system shows significant advantages over physical blend or hybrid at micro/nanoscale developed by self-sorting.<sup>[108]</sup> For example, lipids and polymeric amphiphiles yield liposome and polymersome vesicles via self-assembly which can also harness with bioimaging agents, drugs, and targeting ligands. The co-assembly pathway was found to be more significant for payload loading.<sup>[109]</sup> Additionally, the photophysical property can be harmonized by the co-assembly between electron-poor and electron-rich amphiphiles.<sup>[110]</sup> The molecular packing parameters also control the co-assembly in any dimensional structures and can change the of the dimension the original architecture. For instance, Yan *et al.* (2016) reported that the 1D morphology of phe-phe dipeptide changed to spheres after co-assembly with dianionic porphyrin and showed outstanding photocatalysis properties.<sup>[111]</sup> The suitable approach for the construction of the co-assembled system is the reinforcement of intercomponent interactions including hydrogen bonding,  $\pi$ - $\pi$  stacking, and van der Waals interactions.<sup>[112]</sup> Another much effective

way to achieve the co-assembled system is the integration of structurally similar components.<sup>[113]</sup> Structurally complementary components decrease way of discrimination at the time of assembly process and produce interlocked organization of two components. Recently, two aromatic glutamate-based amphiphiles with strong structural resemblance were harnessed to achieve co-assembled vesicular particles and the  $\pi$ - $\pi$  stacking interaction was found to have a major driving force for the co-assembly between two components (Figure 1.8).<sup>[114]</sup> Small modulation of functionality reduced the possibility of self-sorting and showed significant influence on the molecular arrangement. Biocatalytic reactions also play a crucial role in co-assembly.<sup>[115]</sup>

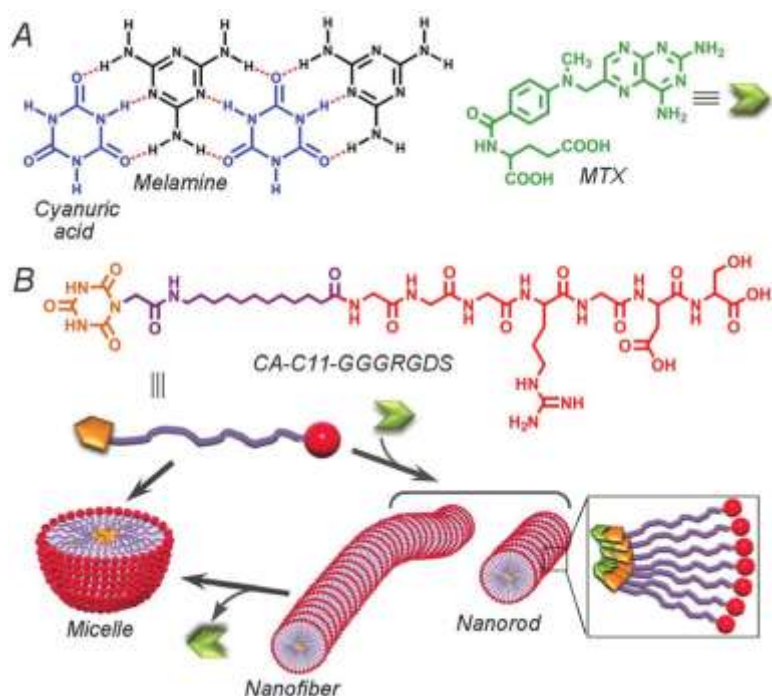


**Figure 1.8.** (A) Molecular structures of cyanuric acid and melamine connected through hydrogen bond and the anti-tumor drug MTX. (B) Peptide amphiphile and the cartoon representation of the co-assembly with MTX.

### 1.3.3 Bicomponent Covalent Conjugation

Unlike the co-assembly processes which rely on noncovalent interaction, two components can also be attached for gelation by covalent

conjugation.<sup>[116]</sup> The covalent bond should be stable, highly selective, specific, bioorthogonal and reversible. This reversible reaction includes hydrazone and imine bond formation, thioether, disulfide bridge formation, and enzyme-mediated transamidation which referred to as dynamic combinatorial chemistry (DCC). The DCC drives the creation of several polymers, peptides, and protein molecules by the combination of two amphiphiles and finally directed to form a hydrogel.<sup>[117]</sup> The bicomponent transient chemical communications enable the assembly and disassembly of the different amphiphiles and produce nanoarchitectures with dynamic properties.<sup>[118]</sup> Hydrazone chemistry is very useful for conjugating biomolecules and stimulates significantly less perturbation in the native form of the peptides or proteins as it possesses small bond distance (Figure 1.9).

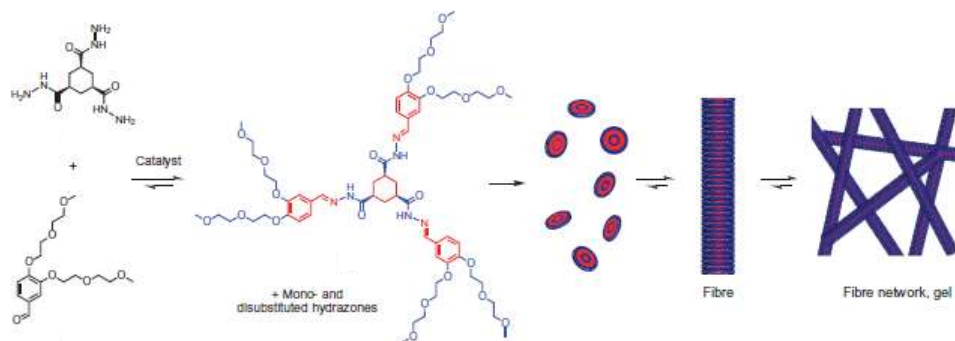


**Figure 1.9.** Bicomponent chemical conjugation catalyzes gelator and gel formation. Trishydrazone hydrogelator formed by covalent conjugation of building blocks leads to the formation of a hydrogel.

Hydrazone chemistry enables quick bond formation due to the high velocity of the reaction under physiological conditions.<sup>[119-120]</sup> Therefore, hydrazone and acyl hydrazone-based functionalities were utilized to develop complex architectures using two different components.<sup>[121]</sup> Disulfide bridge formation is another way to fabricate bicomponent covalent conjugation directed by nature. The cysteine-tagged proteins or peptides undergo oxidation at elevated pH and  $-SH$  groups form a disulfide bridge which can revert to its native form upon reduction due to

redox-active nature of sulfur.<sup>[122]</sup> A multiple dynamic thiol-based disulfide nanostructures were generated with morphology changing capability as an advantage.<sup>[123]</sup> The macrocyclic nanostructures self-replicate which formed by the dynamic combinatorial library of pendant various thiol groups with peptides.<sup>[124]</sup> Enzyme-mediated transamidation as covalent conjugation approach has also attracted significant attention for the construction of multi-component self-assembled nanostructures. The reversible formation of amide bonds between two amphiphilic building blocks leads to the production of gelator molecules to introduce thermodynamically downhill nanostructure.<sup>[125-126]</sup> Several processes were introduced by Ulijn *et al.* (2013) for the induction of self-assembly through enzyme-catalyzed reactions.<sup>[127]</sup> The enzyme catalyzed self-assembly is an efficient way for nanofabrication of complex systems through bottom-up strategy.

#### 1.4 Carbon-based Material Driven Self-healable Gels

Self-healing hydrogels are a class of materials which possess the capability to repair a crack, fracture or after a severe deformation being made on the materials.<sup>[128-133]</sup> The advantages of the self-healable hydrogel are the enhanced useful lifetime with minimal maintenance and the low cost of materials.<sup>[134-136]</sup>

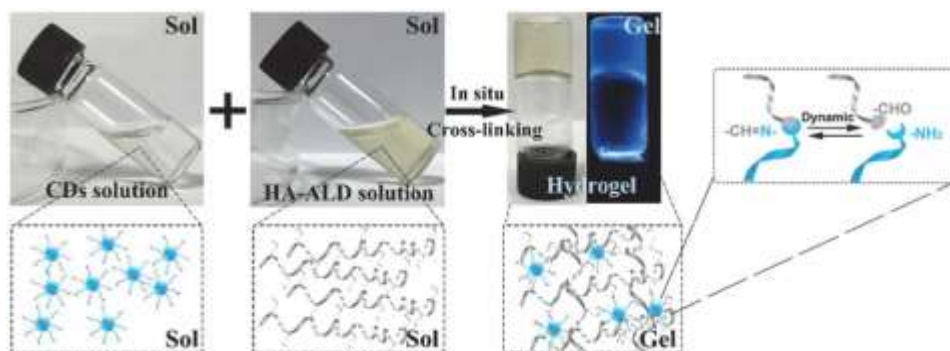


**Figure 1.10.** Oxidized sodium hyaluronate (HA-ALD) and carbon dots dynamic crosslinking lead to the formation of a strong hydrogel.

Several methods were developed over the last few decades to accomplish self-healing materials.<sup>[137-140]</sup> The leading approach used for the renovation of the damaged fiber network comprises dynamic covalent bonds,<sup>[141-142]</sup> or noncovalent interactions such as  $\pi$ - $\pi$  stacking, hydrogen bonding, electrostatic interaction and hydrophobic association.<sup>[143]</sup> It is necessary to remark that incorporation of materials like clay, metallic nanoparticles, carbon nanotubes and graphene to achieve bio-relevant hydrogels was thoroughly studied.<sup>[144]</sup> The small carbon-based materials such as carbon nanotubes, carbon dots, graphene and their other form possess tremendously great interfacial area. Therefore, this material becomes the filler for ideal molecular storage devices as well as for mechanical strengthening of soft materials. Functional carbon-based nanomaterials (CBNs) is essential because of the exceptional chemical and physical properties. Extensive research has done for the fabrication of high-strength materials to exploit these materials in various applications. These advantageous properties of CBNs are also actively investigated in soft materials. CBNs were incorporated into several bio-molecules to achieve strong hydrogels (Figure 1.10).<sup>[145-146]</sup> Multiple stimuli were detected using hydrogel developed by bicomponent covalent conjugation.<sup>[147]</sup>

### 1.4.1 Graphene-based Material Driven Self-healable Gels

Graphene has engrossed much consideration since the time of their isolation<sup>[148]</sup> because of its remarkable mechanical, thermal and electrical properties.<sup>[149-150]</sup> After extensive research, it was found that graphene is substantially biocompatible for adhesion and proliferation of multiple cell lines such as L-929,<sup>[151]</sup> osteoblasts, neuroendocrine PC12 and oligodendroglia.<sup>[152]</sup> Graphene-poly(N-isopropylacrylamide) hydrogel was used in replacing damaged muscle tissue to depict the biocompatibility of the material.<sup>[153]</sup> The unique chemical and physical properties, i.e. electrochemiluminescent,<sup>[154]</sup> optical<sup>[155]</sup> and cytotoxic behavior<sup>[156]</sup> of

functionalized graphene were gained colossal interest. Therefore, the functionalized graphene materials were utilized for several purposes including the enhancement of mechanical property of soft materials and bioimaging.<sup>[157]</sup> Graphene oxide (GO) encapsulated biomolecular hydrogels showed excellent dye degradation in wastewater.<sup>[158]</sup> Recently, Shi *et al.* (2010) produced a GO and poly-vinyl alcohol (PVA) based biocompatible co-assembled hydrogel for selective drug release at physiological pH.<sup>[159]</sup>

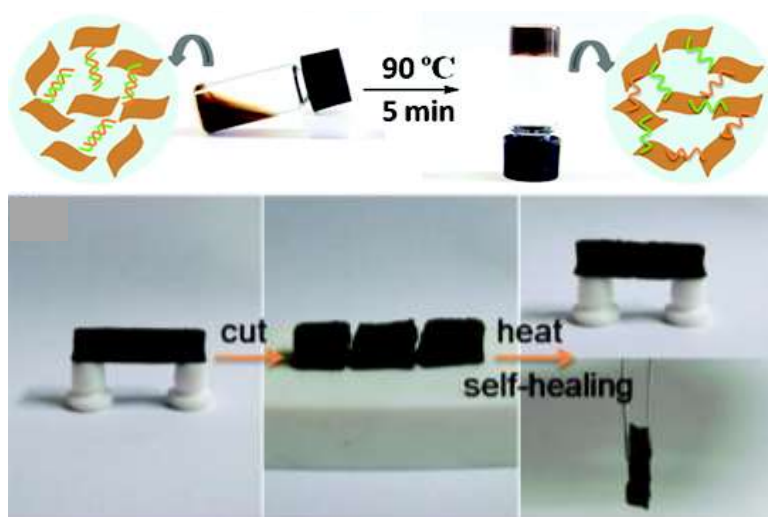


**Figure 1.11.** Random co-assembly of GO with DNA forms a self-supporting hydrogel upon heating. The hydrogel shows excellent self-healing property.

GO also co-assembled with DNA via  $\pi$ - $\pi$  stacking interactions to produce an excellent self-healing hydrogel (Figure 1.11).<sup>[160]</sup> Meanwhile, the unique behavior such as quantum confinement, edge effects, of zero-dimensional graphene quantum dots (GQDs) was also attracted the researchers. Therefore, GQDs was used to produce self-healing hydrogel.<sup>[161]</sup>

## 1.5 Chirality developed by Co-assembly

The chirality in nature including DNA double helix and collagen, the triple helix plays vital functions to provide distinct characteristics to life.<sup>[162]</sup>

Artificial chiral nanostructures were developed to mimic natural chiral systems which have various use in the field of materials science,<sup>[163-164]</sup> chemistry<sup>[165]</sup> and biological systems.<sup>[166]</sup> Raymond *et al.* (2003) developed different kinetically stable supramolecular chiral structures from achiral building blocks utilizing a segmental synthetic pathway.<sup>[167]</sup> The multicomponent self-assembly drives DNA double helix through noncovalent interaction, i.e. hydrogen bonding. Noncovalent interactions possess dynamic property which permits agile control over the self-assembly process and packing parameters of amphiphilic building blocks. The molecular assembly favors an asymmetric packing of amphiphiles via a kinetic or thermodynamic pathway and the autonomously supramolecular level chirality was developed.<sup>[168]</sup> The supramolecular chirality can be generated by chirality amplification, symmetry breaking or bi-component co-assembly of chiral or achiral components.<sup>[169]</sup>

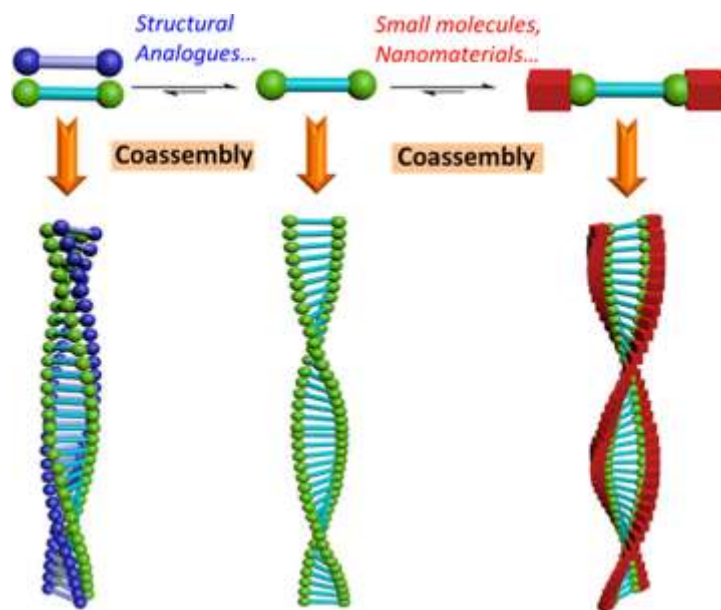


**Figure 1.12.** Supramolecular chirality control in bicomponent systems. Small amphiphilic molecule based co-assembled nanomaterials.

The bicomponent co-assembled systems could reflect biosystems including DNA and proteins which help to understand the natural homochirality for the advancement of chiral materials (Figure 1.12).<sup>[170-</sup>

<sup>171]</sup> Unlike single component system, bicomponent systems exhibit more complexity where different possibilities may arise, i.e. separated self-sorting, co-assembly and heterojunction.<sup>[116,172]</sup> Accordingly, manipulation of homochirality is interesting for the development of assemblies holding multiple components. The development of chiral co-assembled system relates to bioimaging and sensing applications of the materials.

### 1.5.1 Chirality Induced by Chiral Component

In a supramolecular system for the synchronization of chirality using chiral molecule, the sergeant-and-soldier approach is one of the important approaches. The “Majority Rule” and the “Sergeants-and-Soldiers Principle” are the thumb rule to understand principles of chirality introduced by Green *et al.* (1995).<sup>[173]</sup> To regulate the helical nanostructure addition of a minute amount of chiral building blocks (sergeants) to a large number of achiral molecules (soldiers) is sufficient. Using bottom-up approach through noncovalently interactions several low molecular weight systems were developed on the basis of sergeant-and-soldier principle.<sup>[174-175]</sup> All the achiral amphiphiles walk behind the same chiral morphology as a soldier when the chiral amphiphile added to the system as sergeant.<sup>[175]</sup> For instance, in a bicomponent system the optical rotation changes linearly with the proportion of two small enantiomeric amphiphilic molecules present in that system. The induction of chirality was found to be primarily linear or additive.<sup>[176]</sup> Disc-shaped C<sub>3</sub>-symmetric amphiphiles were attracted attention as the permanency of the molecular stacks is assured by multiple secondary interactions.<sup>[177]</sup> This amphiphiles generally co-assembled with the similar structured chiral fraction to produce organized chiral columns to pass the chiral information. At first, Meijer *et al.* reported active sergeants-and-soldiers principle to induce chirality in a dynamic manner using C<sub>3</sub>-symmetric amphiphile (Figure 1.13).<sup>[178]</sup> C<sub>3</sub>-symmetrical amphiphiles usually form helical columnar stacks using cooperative  $\pi$ - $\pi$  stacking, H-bonding

interactions and incorporation of small amount of chiral amphiphilic molecule as sergeant could show sergeant-soldier effects irrespective of the polarity of the solvent.<sup>[179]</sup> Apart from the disc-shaped amphiphiles bolaamphiphiles also actively respond to the sergeant-soldier effect. Recently a study showed that peptide functionalized bolaamphiphiles forms left and right-handed helical morphology upon addition of small amount of chiral bolaamphiphiles.<sup>[180]</sup> Unlike sergeant soldier effect several co-assembled systems with various amphiphiles were reported earlier to control the chiral nanostructure with the addition of chiral components.<sup>[181-182]</sup>

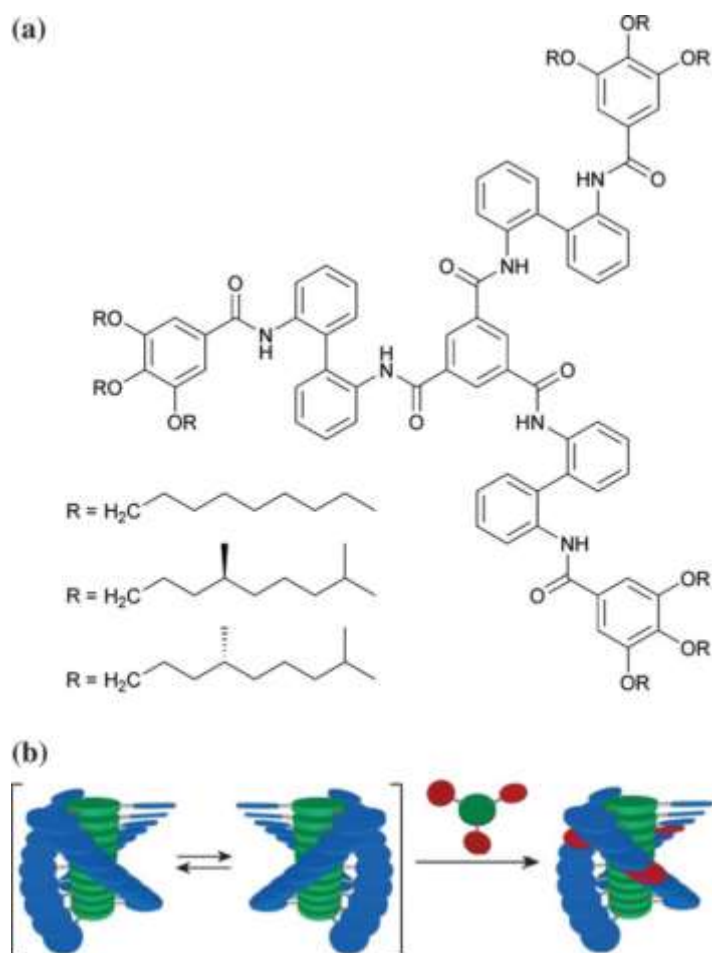


**Figure 1.13.** (a) The molecular structure of the  $C_3$  symmetric amphiphiles. (b) Showing the co-assembly pattern of chiral molecule with a large number of achiral molecules.

### 1.5.2 Chirality Induced by Achiral Component

Bicomponent molecular gels are the perfect tool for superior understanding the riddles of supramolecular chirality in the co-assembled systems. Generally, the supramolecular chiral architectures rely on the inherent chirality of amphiphilic molecules as the chiral building blocks could efficiently produce corresponding helical morphologies.<sup>[183-185]</sup> In different circumstances, upon exposure to external physical or chemical stimuli, achiral building blocks could also produce chiral nanostructures.<sup>[186-187]</sup> The  $\pi$ - $\pi$  stacking between two amphiphiles plays a vital role to develop supramolecular chirality. Therefore several achiral building blocks having aromatic functionality were chosen to induce chirality in the bicomponent co-assembled system to achieve different handedness with unique phenomena.<sup>[188-191]</sup>

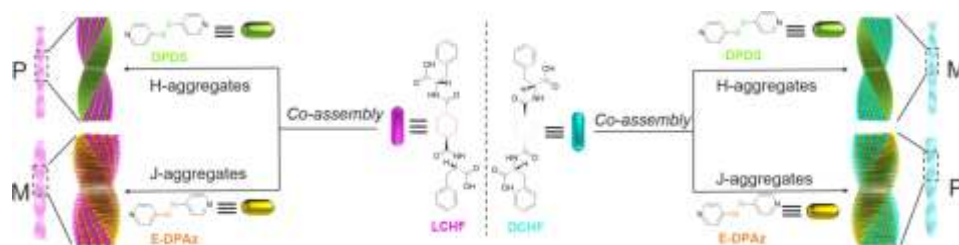


**Figure 1.14.** H-aggregates driven helical inversion of DPDS and J-aggregates control the co-assembly of EDPAz with LCHF (left) or DCHF (right). M: left-handed nanofibers, and P: right-handed nanofibers.

Bicomponent co-assembly using achiral component is, therefore, an important technique to tune the properties of the gels and programmable stimuli responsiveness.<sup>[191]</sup> By the regulation of molecular chirality the handedness of nanostructure into the gels could be finely tuned and three-dimensional arrangement of amphiphiles.<sup>[192]</sup> In the recent year, Zhao *et al.* (2018) have used a similar co-assembly technique to optimize the helicity of the nanostructure by the incorporation of aromatic achiral component (Figure 1.14).<sup>[193]</sup> They have also shown that the helical nature

of the nanostructure is highly dependent on the aggregation pattern (i.e., J or H-aggregates) in the co-assembled hydrogel.

### 1.5.3 Chiral Memory via Co-assembly

An asymmetric orientation of functional groups of an amphiphilic molecule, linked by covalent bonds to the centre, leads to molecular chirality. These bonds are not easily dissociable. On the other hand, an asymmetric organization of molecular building blocks through noncovalent interactions leads to supramolecular chirality.<sup>[194]</sup> The supramolecular system is also easily dissociable and due to dissociation an optically inactive racemic mixture formed from the chiral nanostructure. To prevent the racemates formation supramolecular architecture based chiral template could be used. The supramolecular chirality will not persist if the template bounded form of amphiphiles is thermodynamically stable. On the other hand, kinetic stability of the structure will help to retain the chiral structure for hours, months or even longer even without the chiral template.<sup>[195]</sup> This persistence of chirality after removal of a chiral template is known as ‘Chiral memory’ effect.

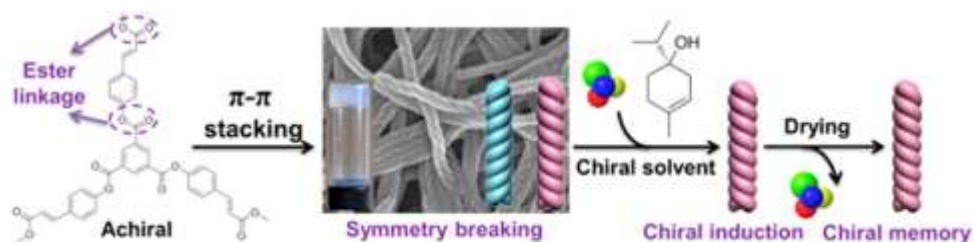


**Figure 1.15.**  $C_3$  symmetric building block is showing symmetry breaking after gelation. Co-assembly with chiral solvents leads to chiral induction and persistence of chiral memory.

The versatility of the chiral memory phenomenon makes them more interesting in the field of supramolecular chirality. To develop the chiral memory by noncovalent interactions bicomponent co-assembly is one of the appropriate tools. Therefore, chiral memory could be used to have

permanent chiral nanostructure by the integration of multiple components having specific functions. Recently, kinetically stable chiral supramolecular polymer with oligo(*p*-phenylenevinylene) was developed which reversibly bind to S-chiral dibenzoyl tartaric acid. New helicity of the supramolecular system was induced due to the reversible co-assembly process. After removal of the S-chiral dibenzoyl tartaric acid the chirality persists as chiral memory.<sup>[196]</sup> Liu *et al.* (2016) also reported the chiral co-assembly of C<sub>3</sub> symmetric gelator with chiral solvent and removal of the solvents leads to the formation of chiral memory (Figure 1.15).<sup>[197]</sup>

### 1.6 Tuning Bicomponent Co-assembly

The term co-assembly itself describes co-operative self-assembly between two different substances that signify co-operation between two complementary functionalized molecules to produce a well-organized microstructure. This co-operation can be tuned very easily as the co-operation relies on noncovalent interactions such as H-bonding,  $\pi$ - $\pi$  stacking and so on. The self-assembly and gelation process is highly influenced by the external stimuli<sup>[198]</sup> (Figure 1.16) and hence the co-assembly process is not far from their boundary. To develop imminent technologies for the control of optical transmission, ion transportation, viscoelasticity, solvent volatility and fluidity, the stimuli-responsive assembly of amphiphiles was thoroughly studied in micelles, vesicles and supramolecular gels.<sup>[199]</sup> Earlier it was found that changing the chemical structure a distinct co-assembled nanostructure can be obtained. Not only tuning the molecular structure but also by changing the conditions of co-assembly by introducing stimuli. Ultra-sonication, pH and Light were exploited to control the molecular aggregations and these physical stimuli have a profound impact on the co-assembly.<sup>[200-202]</sup> The stimuli help externally by providing the appropriate environment to assembly and disassembly process which further enhances the system to rigid gel.



**Figure 1.16.** Showing the multi-stimuli responsiveness of supramolecular hydrogel.

### 1.6.1 pH controlled Co-assembly

Hydrogels prepared from amphiphilic molecules have gained increasing attention.<sup>[203-205]</sup> The amphiphiles co-assemble with another complementary building block to provide hydrogels which are an important class of materials for several bio-applications. In a series of physical stimuli, the pH-responsive hydrogel was attracted a great deal of attention due to the biomedical applications, as the acidity or alkalinity level changes on going from intra and extracellular compartments. In an instance, healthy tissues and tumor tissues possess variable pH.<sup>[206-208]</sup> The pH can tune the mechanical property of the bicomponent hydrogels.<sup>[209]</sup> At elevated pH, two components can merge or persist self-governing whereas at low pH two component could co-assemble or self-sort in the medium. In a recent study, it was reported that the mixture of two N-terminal protected typical peptide amphiphile is complex. Some extent of intermixing was found at high pH and fractional co-assembly between two amphiphiles was noticed at a lower pH.<sup>[210]</sup> The vesicle composed through spontaneous co-assembly of lipid/PEG-containing generates pH-triggered AAc-rich transmembrane channels amphiphile at an elevated pH 8.9 (Figure 1.17). The generation of AAc-rich transmembrane in the co-

assembled vesicles leads to the release of the encapsulated doxorubicin (DOX).<sup>[211]</sup> Therefore, the pH-responsive co-assembled vesicles illustrate potential application of intracellular drug delivery.<sup>[211-212]</sup>

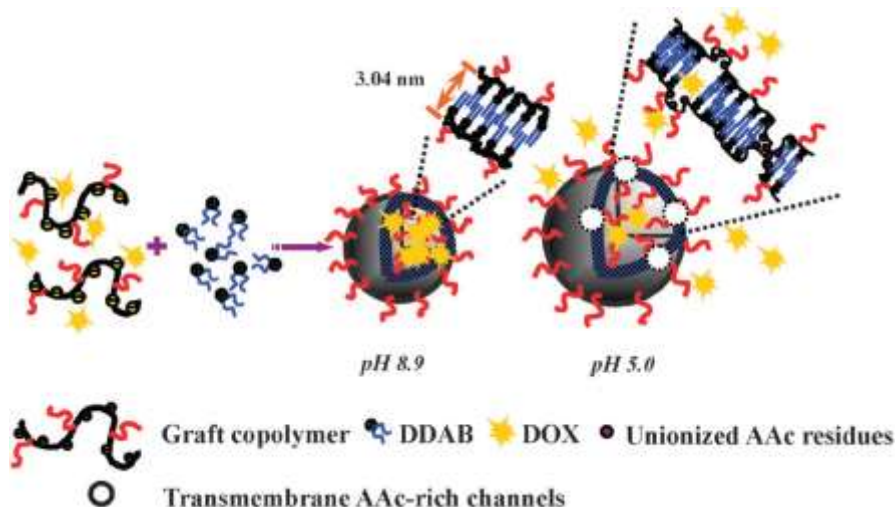


**Figure 1.17.** pH-controlled transition of vesicle size and doxorubicin release via the generation of AAC-rich channels transmembrane in large vesicles.

### 1.6.2 Sonication Induced Co-assembly

Soundwave boosts the translational motion of gelator molecules as a result of which it acts as an important stimulus for molecular switching. Generally, ultrasound or sonication disrupts weak non-covalent interactions between molecules to solubilize the compounds. Therefore, it is extensively utilized for the interruption on aggregations process in food chemistry,<sup>[213]</sup> fundamental research on nanostructure development.<sup>[214]</sup> Apart from disruption sometimes it also pushes the amphiphilic molecules to self-assemble into a controlled nanostructured hydrogel.<sup>[215-216]</sup> Ultrasound provides sufficient energy to break the weak non-covalent interactions. Various self-assembled systems were developed by considering the effect of sonication.<sup>[217-219]</sup> Das *et al.* (2012) reported peptide-appended bolaamphiphile hydrogels which was induced by sonication. These hydrogels can perform as a nanoreactor for in situ generations of platinum (Pt) nanoparticles stabilized by nanofibers.<sup>[220]</sup> The assembly process itself refresh to attain the co-assembly through

reorientation of noncovalent interactions, such as intramolecular hydrogen bonding to intermolecular hydrogen bonding, an elongation of  $\pi$ - $\pi$  stacking interactions and extension of fiber to crosslinked network structures.<sup>[221]</sup> Therefore sonication can control the co-assembly process by providing sufficient energy to achieve a cooperation between two amphiphilic molecules.<sup>[222-223]</sup> A bicomponent -COOH group based gelator interacted with dodecylamine. They form a globular structure in methylmethacrylate through the self-assembly by heating. Whereas a sonication induced fibrillar gel network was found due to the co-assembly of two complementary amphiphilic molecules (Figure 1.18).<sup>[224]</sup>

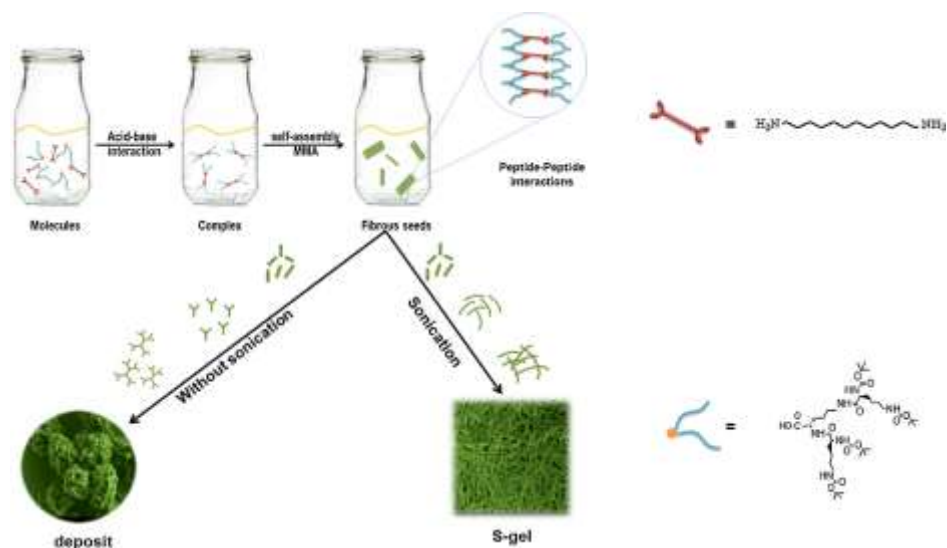


**Figure 1.18.** Schematic representation of sonication induced gelation process.

### 1.6.3 Photo-triggered Co-assembly

Unlike the supramolecular hydrogel, the co-assembled hydrogels are also very much susceptible to the light.<sup>[94,225-226]</sup> The physical stimuli (light) have significantly control on gelation ability and property of gel.<sup>[227]</sup> The turbidity of the hydrogel could be significantly increased with the appearance of macroscopic aggregates within the gel phase. Using the photo responsiveness, molecular aggregation pattern was selectively tuned and spatially resolved hydrogel was developed.<sup>[228]</sup> The photoirradiation could also help to induce supramolecular chirality in the co-assembled

hydrogel.<sup>[6]</sup> The synergistic molecular arrangement in the co-assembled systems are the secrets to the photoresponsive morphological manipulation in gel medium.<sup>[229]</sup> Cholesterol connected naphthalimide and cholesterol conjugated cyanostilbene produce vesicles through co-assembly arrays, whereas both the building blocks response to multiple stimuli. Consequently, exchange of thermoresponsiveness and photosensitiveness occurs between these two building blocks and produces distinct nanostructure.<sup>[6]</sup> The pH-responsive nature was observed due to autonomous co-assembly between two-component in a hydrogel. Oppositely charged cationic surfactant cetyltrimethylammonium bromide was mixed to co-assemble with anionic azobenzene dicarboxylate for improvement of self-sustaining nature of the hydrogel which is also light sensitive (Figure 1.19). The surface coating was repaired by exploiting photoresponsive phase transition of the co-assembled hydrogel and finally, the hydrogel was used as a humidity sensor.<sup>[230]</sup>

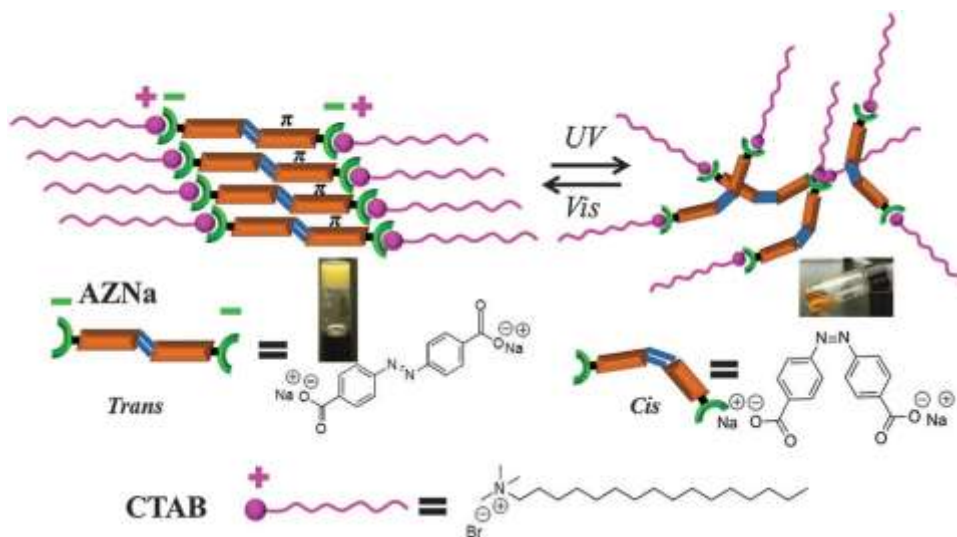


**Figure 1.19.** Mechanism of interactions of light induced assembly and disassembly process of a bicomponent co-assembled hydrogel.

## 1.7 Application of Co-assembled Gel

Supramolecular hydrogels ensuring organized nanoarchitectures are encouraging materials for numerous bioapplications due to their

outstanding biocompatibility.<sup>[203,231-232]</sup> There are many bioapplications such as drug delivery,<sup>[233]</sup> tissue engineering<sup>[234]</sup> cell culture<sup>[235]</sup> and several biocatalytic reactions<sup>[236]</sup> into the supramolecular gels. Such biocompatible gels were also considered for complex 3D-cell culture as matrices.

### 1.7.1 3D-Cell Culture and Drug Delivery

The two dimensional (2D) cell culture systems have some limitation as it does not match with three-dimensional (3D) microenvironments due to the deficiency of structural architecture and gradient.<sup>[237-239]</sup> Although these systems have given the basic idea to interpret complex biological phenomena.<sup>[240-241]</sup> Hydrogel creation was found to be the most significant way to construct 3D cell culture environment as well as 3D bioprinting technology.<sup>[241]</sup>

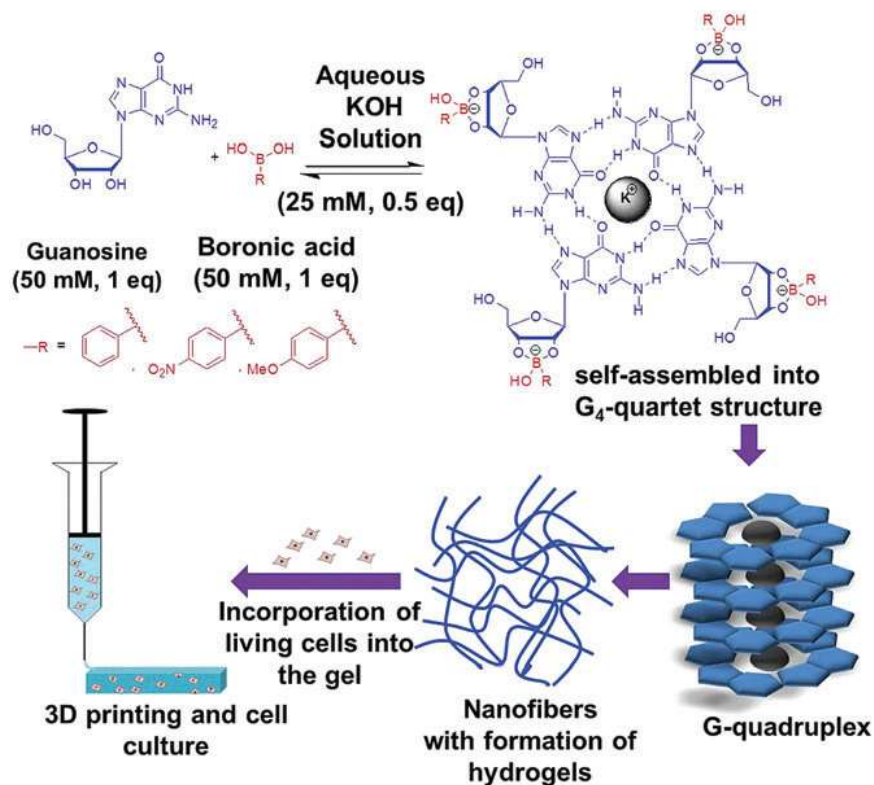


**Figure 1.20.** G<sub>4</sub>-quadruplex co-assembled with K<sup>+</sup> ions to produce self-supporting hydrogel for the application in 3D printing and cell culture.

Till date, some of the developed 3D culture materials were also commercialized for the basic understanding of cell culture study. The polymer-based hydrogels are one of the most commonly used for significant biocompatible properties.<sup>[242-243]</sup> In spite of that direct encapsulation of cells into 3D-cell, culture matrices are still challenging due to the complicated fabricating procedure of the matrices.<sup>[244]</sup> To overcome this problem, bicomponent hydrogels were taken into consideration as it is easy to tune the mechanical property. The injectable and self-healing property of such bicomponent hydrogel are also the prime reason to consider these materials as 3D-cell culture matrices.<sup>[245]</sup> Recently, Das *et al.* (2018) have developed guanosine based bicomponent hydrogel by incorporation of several functionalized boronic acid. The reversible covalent conjugation of the boronic acid with guanosine leads to the formation of G4-quadruplex upon co-assembly with  $K^+$  ions. This hydrogel showed excellent injectable, self-healing property and finally used for excellent 3D-cell culture as well as 3D-bioprinting (Figure 1.20).<sup>[246]</sup>

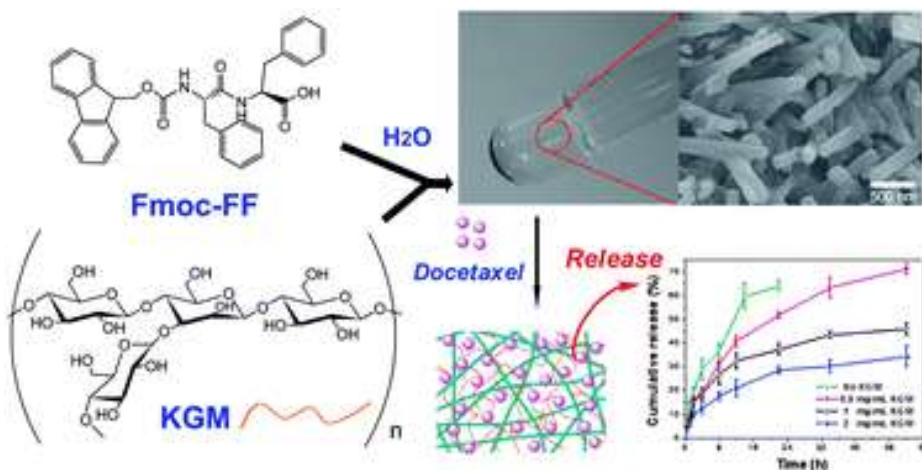


**Figure 1.21.** The co-assembly of Fmoc-FF and KGM produces hydrogel. Showing crosslinked fibrillar network formation due to co-assembly and used for docetaxel release.

Bicomponent hydrogels are not only limited to the cell culture applications. These materials were also found to be applicable in the fields of drug delivery.<sup>[228,247]</sup> In an instance, peptide-polysaccharide (Fmoc-FF/KGM) bicomponent hydrogel was prepared via the co-assembly mechanism. After that, the co-assembled Fmoc-FF/KGM hydrogel was used for drug delivery (Figure 1.21). Docetaxel was immobilized into hydrogel to show in vitro release behavior.<sup>[248]</sup> In a recent study, He *et al.* (2016) have reported Fmoc-FF/Alginate based co-assembled hydrogel triggered by calcium ion which is highly efficient for the drug release application.<sup>[249]</sup>

### **1.7.2 Co-assembled Gels in Catalysis**

Catalysis considered being one of the prime concerns of supramolecular chemistry since it was discovered.<sup>[250]</sup> The cross-linked fiber network of a supramolecular gel permits for mobilization of solvents inside the network. Thus different components could be immobilized inside the fiber network. Moreover, in situ loading of foreign substances inside the gel is also possible all through the gelation process. In one condition the self-assembly mechanism has to remain unharmed after interaction with the substance. Enzymes, efficient and selective bio-catalyst, were considered as the appropriate foreign substance to entrap into the gel network for catalysis.<sup>[251-252]</sup> The approaches to catalysis inside the supramolecular gels were divided into three major parts, i.e. molecular receptors binds with the catalytic centre, two reactants molecule binds with molecular receptors to promote the reaction and construction of catalytic centre using supramolecular interactions.<sup>[252]</sup> Generally, noncovalent interactions were used to construct a catalytic supramolecular gel.<sup>[253]</sup> Peptide amphiphile based bicomponent hydrogel was also found to have catalytically active. Due to the structural differences, amphiphilic building blocks can simultaneously co-assemble and self-sort into the bicomponent gel. Therefore in the same pot, two reactions were carried out due to the

presence of self-sorted network, but in the co-assembled gel network, the reaction did not proceed to the second step (Figure 1.22).<sup>[254]</sup> Moretto *et al.* (2016) prepared co-assembled organogel using terminally protected dipeptide amphiphile and fullerene (C<sub>60</sub>), multiwall carbon nanotubes (MWCNTs).<sup>[255]</sup> The xerogel of C<sub>60</sub> showed important activity for the reduction of azo compounds under UV light mediated by NaBH<sub>4</sub> also for the benzyl alcohol production through reduction of benzoic acid.

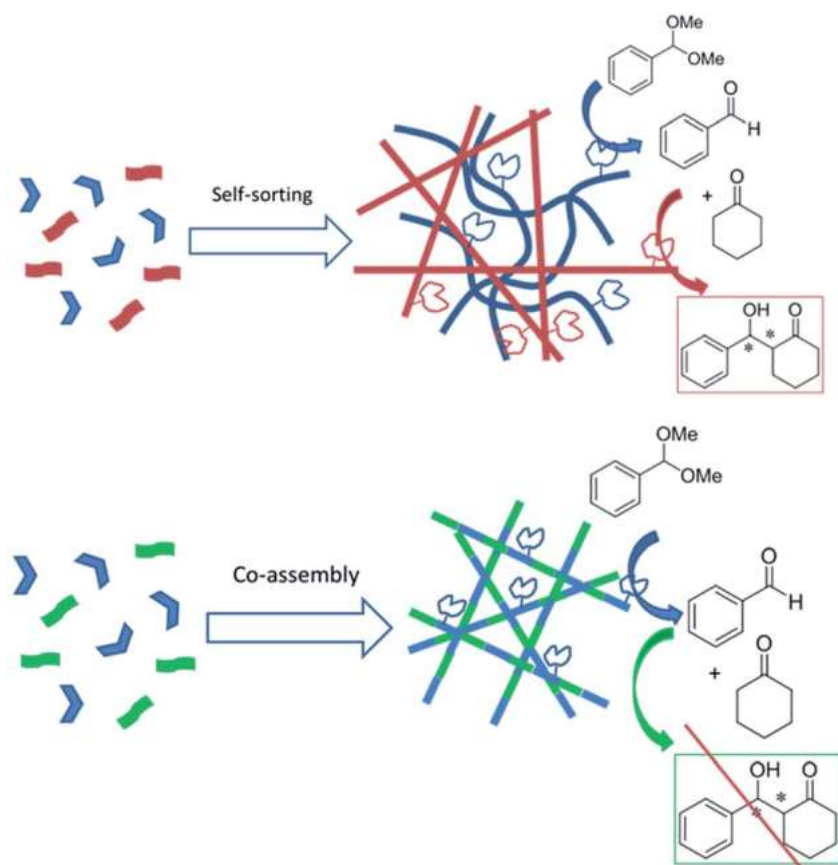


**Figure 1.22.** The selective catalytic activity of self-sorted vs. co-assembled bicomponent hydrogels.

Stupp *et al.* (2007) reported a histidine-based peptide amphiphile which forms organohydrogel. The synthesized supramolecular gel showed esterase enzymes like activity and the substrate 2,4-dinitrophenyl acetate ester readily hydrolyze.<sup>[256]</sup>

## **1.8 Organization of Thesis**

The initial aim of this thesis was to explore different bicomponent co-assembled molecular gels for further applications in biocatalysis. This was achieved by synthesizing various amphiphilic molecules such as Amoc-capped amino acids, bolaamphiphiles and discotic amphiphile. The hydrogelation was achieved by incorporating second components into the medium containing amphiphilic molecules. Further, the supramolecular gels were used for enzymatic inclusion of gastrodigenin and enzymatic generation of DOPA.

Chapter 2: In this chapter, we have exploited Amoc (9-anthracenemethyloxycarbonyl) capped amino acid-based amphiphilic molecules. We intended to exploit the influence of graphene quantum dots in the co-assembled systems to achieve self-healing hydrogels.

Chapter 3: In this chapter, leucine-based bolaamphiphiles were synthesized to control chiral nanostructures in the co-assembled hydrogels.

Chapter 4: In this chapter, we have exploited bicomponent co-assembled supramolecular organic frameworks (SOFs) with a controlled pore size in gel state using discotic trifunctional amphiphile for the use of lipase-catalyzed inclusion of gastrodigenin.

Chapter 5: Exploration of a small amphiphilic based bicomponent co-assembled hydrogel to produce L-DOPA in the gel medium using tyrosinase.

## **1.9 References**

1. Grzybowski B. A., Wilmer C. E., Kim J., Browne K. P., Bishop K. J. M. (2009), Self-assembly: From Crystals to Cells, *Soft Matter*, 5, 1110-1128 (DOI: 10.1039/B819321P).

2. Tu Y., Peng F., Adawy A., Men Y., Abdelmohsen L. K. E. A., Wilson D. A. (2016), Mimicking the Cell: Bio-inspired Functions of Supramolecular Assemblies, *Chem Rev*, 116, 2023-2078 (DOI: 10.1021/acs.chemrev.5b00344).
3. Keizer H. M., Sijbesma R. P. (2005), Hierarchical Self-assembly of Columnar Aggregates, *Chem. Soc. Rev.*, 34, 226-234 (DOI: 10.1039/B312177C).
4. Lehn J.-M. (2002), Toward complex matter: Supramolecular chemistry and self-organization, *Proc. Natl. Acad. Sci. U. S. A.*, 99, 4763–4768 (DOI: 10.1073/pnas.072065599).
5. Conde C., Caceres A. (2009), Microtubule Assembly, Organization and Dynamics in Axons and Dendrites, *Nat. Rev. Neur.*, 10, 319-332 (DOI: 10.1038/nrn2631).
6. Xing P., Tham H. P., Li P., Chen H., Xiang H., Zhao Y. (2018), Environment-Adaptive Coassembly/Self-Sorting and Stimulus-Responsiveness Transfer Based on Cholesterol Building Blocks, *Adv. Sci.*, 5, 1700552 (DOI: 10.1002/advs.201700552).
7. Pray L. (2008), Discovery of DNA structure and function: Watson and Crick. *Nature Education* 1, 100.
8. Seeman N. C. (2003), Double Helix, *Nature*, 421, 427-431 (DOI: 10.1038/nature01406).
9. Seeman N. C. (2007), An Overview of Structural DNA Nanotechnology, *Mol. Biotechnol.*, 37, 246-257 (DOI: 10.1007/s12033-007-0059-4).
10. Aldaye F. A., Palmer A. L., Sleiman H. F. (2008), Assembling Materials with DNA as the Guide, *Science*, 321, 1795-1799 (DOI: 10.1126/science.1154533).
11. Gothelf K. V., LaBean, T. H. (2005), DNA-programmed Assembly of Nanostructures, *Org. Biomol. Chem.*, 3, 4023-4037 (DOI: 10.1039/B510551J).

12. Seeman N. C. (2010), Nanomaterials Based on DNA, *Annu. Rev. Biochem.*, 79, 65-87 (DOI: 10.1146/annurev-biochem-060308-102244).
13. Hernandez-Garcia, A., Kraft, D. J., Janssen, A. F. J., Bomans P. H. H., Sommerdijk N. A. J. M., Thies-Weesie, D. M. E., Favretto M. E., Brock, R., de Wolf F. A., Wertén M. W. T., van der Schoot P., Stuart M. C., de Vries R. (2014), Design and Self-assembly of Simple Coat Proteins for Artificial Viruses, *Nature Nanotechnology*, 9, 698–702 (DOI: 10.1038/nnano.2014.169).
14. Uhlenheuer D. A., Petkau K., Brunsveld L. (2010), Combining Supramolecular Chemistry With Biology, *Chem. Soc. Rev.*, 39, 2817-2826 (DOI: 10.1039/B820283B).
15. Collier J. H. (2008), Modular Self-assembling Biomaterials for Directing Cellular Responses, *Soft Matter*, 4, 2310-2315 (DOI: 10.1039/B805563G).
16. Xu H., Song J., Tian T., Feng R. (2012), Estimation of Organogel Formation and Influence of Solvent Viscosity and Molecular Size on Gel Properties and Aggregate Structures, *Soft Matter*, 8, 3478-3486 (DOI: 10.1039/C2SM07387K).
17. Dunna B., Zink J. (1991), Optical Properties of Sol-gel Glasses Doped with Organic Molecules, *J. Mater. Chem.*, 1, 903-913 (DOI: 10.1039/JM9910100903).
18. Chen Q., Lv Y., Zhang D., Zhang G., Liu C., Zhu D. (2010), Cysteine and pH-responsive Hydrogel Based on a Saccharide Derivative With an Aldehyde Group, *Langmuir*, 26, 3165-3168 (DOI: 10.1021/la903102z).
19. Ajayaghosh A., Praveen V. K., Vijayakumar C. (2008), Organogels as Scaffolds for Excitation Energy Transfer and Light Harvesting, *Chem. Soc. Rev.*, 37, 109-122 (DOI: 10.1039/B704456A).

20. George M., Weiss R. G. (2006), Molecular Organogels Soft Matter Comprised of Low-molecular-mass Organic Gelators and Organic Liquids, *Acc. Chem. Res.*, 39, 489-497 (DOI: 10.1021/ar0500923).
21. Koley P., Pramanik A. (2012), Multilayer Vesicles, Tubes, Various Porous Structures and Organo Gels through the Solvent-assisted Self-assembly of Two Modified Tripeptides and Their Different Applications, *Soft Matter*, 8, 5364-5374 (DOI: 10.1039/C2SM25205H).
22. Adhikari B., Banerjee A. (2011), Short Peptide based Hydrogels: Incorporation of Graphene into the Hydrogel, *Soft Matter*, 7, 9259–9266 (DOI: 10.1039/c1sm06330h).
23. Roy S., Banerjee A. (2011), Amino Acid based Smart Hydrogel: Formation, Characterization and Fluorescence Properties of Silver Nanoclusters within the Hydrogel Matrix, *Soft Matter*, 7, 5300-5308 (DOI: 10.1039/c1sm05034f).
24. Xu H., Das A. K., Horie M., Shaik M. S., Smith A. M., Luo Y., Lu X., Collins R., Liem S. Y., Song A., Popelier P. L. A., Turner M. L., Xiao P., Kinloch I. A., Ulijn R. V. (2010), An Investigation of the Conductivity of Peptide Nanotube Networks Prepared by Enzyme-triggered Self-assembly, *Nanoscale*, 2, 960-966 (DOI: 10.1039/B9NR00233B).
25. Naskar J., Palui G., Banerjee A. (2009), Tetrapeptide-based hydrogels: For encapsulation and slow release of an anticancer drug at physiological pH, *J. Phys. Chem. B*, 113, 11787-11792 (DOI: 10.1021/jp904251j).
26. Koley P., Gayen A., Drew M. G. B., Mukhopadhyay C., Pramanik A. (2012), Design and Self-assembly of a Leucine-enkephalin Analogue in Different Nanostructures: Application of Nanovesicles, *Small*, 8, 984-990 (DOI: 10.1002/sml.201101685).
27. Wada A., Tamaru S., Ikeda M., Hamachi I. (2009), MCM Enzyme-Supramolecular Hydrogel Hybrid as a Fluorescence Sensing Material

- for Polyanions of Biological Significance, *J. Am. Chem. Soc.*, 131, 5321-5330 (DOI: 10.1021/ja900500j).
28. Tsitsilianis C. (2010), Responsive Reversible Hydrogels from Associative “Smart” Macromolecules, *Soft Matter*, 6, 2372-2388 (DOI: 10.1039/B923947B).
  29. Zhao X. B., Pan F., Xu H., Yaseen M., Shan H., Hauser C. A. E., Zhang S., Lu J. R. (2010), Molecular Self-assembly and Applications of Designer Peptide amphiphiles, *Chem. Soc. Rev.*, 39, 3480-3498 (DOI: 10.1039/b915923c).
  30. Li J., Fan C., Pei H., Shi J., Huang Q. (2013), Smart Drug Delivery Nanocarriers with Self-assembled DNA Nanostructures, *Adv. Mater.*, 25, 4386-4396 (DOI: 10.1002/adma.201300875).
  31. Yemini M., Reches M., Rishpon J., Gazit E. (2005), Novel Electrochemical Biosensing Platform Using Self-assembled Peptide Nanotubes, *Nano Lett.*, 5, 183-186 (DOI: 10.1021/nl0484189).
  32. Lee K. Y., Mooney D. J. (2001), Hydrogels for Tissue Engineering, *Chem. Rev.*, 101, 1869-1880 (DOI: 10.1021/cr000108x).
  33. Ma D., Tu K., Zhang L. M. (2010), Bioactive Supramolecular Hydrogel With Controlled Dual Drug Release Characteristics, *Biomacromolecules*, 11, 2204-2212 (DOI: 10.1021/bm100676a).
  34. Zhang S. (2003), Fabrication of Novel Biomaterials through Molecular Self-assembly, *Nat. Biotech.*, 21, 1171-1178 (PMID: 14520402).
  35. Velev O. D., Lenhoff A M. (2000), Colloidal Crystals as Templates for Porous Materials, *Curr. Opin. Colloid Interface Sci.*, 5, 56-63 (DOI: 10.1016/S1359-0294(00)00039-X).
  36. Xia Y., Gates B., Yin Y., Lu Y. (2000), Monodispersed Colloidal Spheres: Old Materials With New Applications, *Adv. Mater.*, 12, 693-713 (DOI: 10.1002/(SICI)1521-4095 (200005) 12:10<693::AID-ADMA693>3.0.CO;2-J)

37. Sajisha V. S., Maitra U. (2013), Multi-component, Self-assembled, Functional Soft Materials, *Chimia*, 67, 44-50 (DOI: 10.2533/chimia.2013.44).
38. Wang Y., Xia Y. (2004), Bottom-up and Top-down Approaches to the Synthesis of Monodispersed Spherical Colloids of Low Meltingpoint Metals, *Nano Lett.*, 4, 2047-2050 (DOI: 10.1021/nl048689j).
39. Ramstrom O., Bunyapaiboonsri T., Lohmann S., Lehn J. M. (2002), Chemical Biology of Dynamic Combinatorial Libraries, *Biochim. Biophys. Acta*, 1572, 178-186 (DOI: 10.1016/S0304-4165(02)00307-0).
40. Mercuri F., Baldoniab M., Sgamellottia A. (2012), Towards Nanoorganic Chemistry: Perspectives for a Bottom-up Approach to the Synthesis of Low-dimensional Carbon Nanostructures, *Nanoscale*, 4, 369-379 (DOI: 10.1039/C1NR11112D).
41. Wang C., Wang Z., Zhang X., (2012) Amphiphilic Building Blocks for Self-Assembly: From Amphiphiles to Supra-amphiphiles, *Acc. Chem. Res.*, 45, 608-618 (DOI: 10.1021/ar200226d).
42. Israelachvili J. N., Mitchell D. J., Ninham B. W. (1976), Theory of Self-assembly of Hydrocarbon Amphiphiles into Micelles and Bilayers, *J. Chem. Soc., Faraday Trans. 2.*, 72, 1525-1568 (DOI: 10.1039/F29767201525).
43. Palivan C. G., Goers R., Najer A., Zhang X., Car A., Meier W. (2016), Bioinspired Polymer Vesicles and Membranes for Biological and Medical Applications, *Chem. Soc. Rev.*, 45, 377-411 (DOI: 10.1039/c5cs00569h).
44. Schrum J. P., Zhu T. F., Szostak J. W. (2010,) The Origins of Cellular Life, *Cold Spring Harbor Perspect. Biol.* 2, No. a002212 (DOI: 10.1101/cshperspect.a002212).
45. Zhang L., Wang X., Wang T., Liu M. (2015), Tuning Soft Nanostructures in Self-assembled Supramolecular Gels: From

- Morphology Control to Morphology-Dependent Functions, *Small*, 11, 1025-38 (DOI: 10.1002/sml.201402075).
46. Fleming S., Ulijn R. V. Design of Nanostructures Based on Aromatic Peptide Amphiphiles. *Chem. Soc. Rev.*, 2014, 43, 8150-8177 (DOI: 10.1039/C4CS00247D).
47. Hwang J. J., Iyer S. N., Li L. S., Claussen R., Harrington D. A., Stupp S. I. (2002), Self-assembling biomaterials: Liquid Crystal Phases of Cholesteryl Oligo(l-lactic acid) and Their Interactions With Cells, *Proc. Natl. Acad. Sci. U. S. A.*, 99, 9662-9667 (DOI: 10.1073/pnas.152667399).
48. Klok H. A., Hwang J. J., Hartgerink J. D., Stupp S. I. (2002), Self-Assembling Biomaterials: L-Lysine-Dendron-Substituted Cholesteryl-(l-lactic acid) $n$ , *Macromolecules*, 35, 6101-6111 (DOI: 10.1021/ma011964t).
49. Hartgerink J. D., Beniash E., Stupp S. I. (2001), Self-assembly and Mineralization of Peptide-amphiphile Nanofibers, *Science*, 294, 1684-1688 (DOI: 10.1126/science.1063187).
50. Hartgerink J. D., Beniash E., Stupp S. I. (2002), Peptide-amphiphile nanofibers: A versatile scaffold for the preparation of self-assembling materials, *Proc. Natl. Acad. Sci. U. S. A.*, 99, 5133-5138 (DOI: 10.1073/pnas.072699999).
51. Adhikari B., Nanda J., Banerjee A. (2011), Pyrene-Containing Peptide-Based Fluorescent Organogels: Inclusion of Graphene into the Organogel, *Chem. Eur. J.*, 17, 11488-11496 (DOI: 10.1002/chem.201101360).
52. B., Adhikari, J., Nanda A. Banerjee (2011), Multicomponent Hydrogels from Enantiomeric Amino Acid Derivatives: Helical Nanofibers, Handedness and Self-sorting, *Soft Matter*, 7, 8913-8922 (DOI: 10.1039/c1sm05907f)

53. Xing P., Phua S. Z. F., Wei X., Zhao Y. (2018), Programmable Multicomponent Self-Assembly Based on Aromatic Amino Acids, *Adv. Mater.*, 30, 1805175 (DOI: 10.1002/adma.201805175).
54. Adamcik J., Castelletto V., Bolisetty S., Hamley I. W., Mezzenga R. (2011), Direct Observation of Time-resolved Polymorphic States in the Self-assembly of End-capped Heptapeptides, *Angew. Chem. Int. Ed.*, 50, 5495-5498 (DOI: 10.1002/anie.201100807).
55. Fry H. C., Garcia J. M., Medina M. J., Ricoy U. M., Gosztola D. J., Nikiforov M. P., Palmer L. C., Stupp S. I. (2012), Self-Assembly of Highly Ordered Peptide Amphiphile Metalloporphyrin Arrays, *J. Am. Chem. Soc.*, 134, 14646-14649 (DOI: 10.1021/ja304674d)
56. Fuhrhop A. H., Wang T. Y. (2004), Bolaamphiphiles, *Chem. Rev.*, 104, 2901-2937 (DOI: 10.1021/cr030602b).
57. Shimizu T. (2002), Bottom-up Synthesis and Structural Properties of Self-assembled High-axial-ratio Nanostructures, *Macromol. Rapid Commun.*, 23, 311-331 (DOI: 10.1002/1521-3927(20020401)23:5/6<311::AID-MARC311>3.0.CO;2-U).
58. Zhan C., Gao P., Liu M. (2005), Self-assembled Helical Spherical nanotubes from an L-Glutamic Acid based Bolaamphiphilic Low Molecular Mass Organogelator, *Chem. Commun.*, 0, 462-464 (DOI: 10.1039/B413259A).
59. Mollaa M. R., Ghosh S. (2014), Aqueous Self-assembly of Chromophore-conjugated Amphiphiles. *Phys. Chem. Chem. Phys.*, 16, 26672-26683 (DOI: 10.1039/C4CP03791J).
60. Yamanaka M. (2016), Development of C<sub>3</sub>-Symmetric Tris-Urea Low-Molecular-Weight Gelators, *Chem Rec.* 16, 768-82 (DOI: 10.1002/tcr.201500282).
61. Prabhu D. D., Aneesh Sivadas P., Das S. (2014), Solvent Assisted Fluorescence Modulation of a C<sub>3</sub>-Symmetric Organogelator, *J. Mater. Chem. C*, 2, 7039-7046 (DOI: 10.1039/C4TC01008F).

62. van Gorp J. J., Vekemans J. A. J. M., Meijer E. W. (2002), C<sub>3</sub>-Symmetrical Supramolecular Architectures: Fibers and Organic Gels from Discotic Trisamides and Trisureas, *J. Am. Chem. Soc.*, 124, 14759-14769 (DOI: 10.1021/ja020984n).
63. Shimomura S., Kitagawa, S. (2011), Soft Porous Crystal Meets TCNQ: Charge Transfer-type Porous Coordination Polymers, *J. Mater. Chem.*, 21, 5537-5546 (DOI: 10.1039/C1JM10208G).
64. Lu J., Perez-Krap C., Suyetin M., Alsmail N. H., Yan Y., Yang S., Lewis W., Bichoutskaia E., Tang C. C., Blake A. J., Cao R., Schröder M. (2014), A Robust Binary Supramolecular Organic Framework (SOF) with High CO<sub>2</sub> Adsorption and Selectivity, *J. Am. Chem. Soc.*, 136, 12828-12831 (DOI: 10.1021/ja506577g).
65. Fu J., Das S., Xing G., Ben T., Valtchev V., Qiu S. (2016), Fabrication of COF-MOF Composite Membranes and Their Highly Selective Separation of H<sub>2</sub>/CO<sub>2</sub>, *J. Am. Chem. Soc.*, 138, 7673-7680 (DOI: 10.1021/jacs.6b03348).
66. Ding S. Y., Gao J., Wang Q., Zhang Y., Song W. G., Su C. Y., Wang W. (2011), Construction of Covalent Organic Framework for Catalysis: Pd/COF-LZU1 in Suzuki-Miyaura Coupling Reaction, *J. Am. Chem. Soc.*, 133, 19816-19822 (DOI: 10.1021/ja206846p).
67. Bhanja P., Mishra S., Manna K., Mallick A., Das Saha K., Bhaumik A. (2017), Covalent Organic Framework Material Bearing Phloroglucinol Building Units as a Potent Anticancer Agent, *ACS Appl. Mater. Interfaces*, 9, 31411-31423 (DOI: 10.1021/acsami.7b07343).
68. Patra B. C., Khilari S., Manna R. N., Mondal S., Pradhan D., Pradhan A., Bhaumik A. (2017), A Metal-Free Covalent Organic Polymer for Electrocatalytic Hydrogen Evolution, *ACS Catal.*, 7, 6120-6127 (DOI: 10.1021/acscatal.7b01067).
69. Pfeiffermann M., Dong R., Graf R., Zajaczkowski W., Gorelik T., Pisula W., Narita A., Müllen K., Feng X. (2015), Free-Standing Monolayer Two-Dimensional Supramolecular Organic Framework

- with Good Internal Order, *J. Am. Chem. Soc.*, 137, 14525-14532 (DOI: 10.1021/jacs.5b09638).
70. Teyssandier J., Feyter S. D., Mali K. S. (2016), Host-Guest Chemistry in Two-Dimensional Supramolecular Networks, *Chem. Commun.*, 52, 11465-11487 (DOI: 10.1039/C6CC05256H).
71. Zhang Y., Zhan T. G., Zhou T. Y., Qi Q. Y., Xu X. N., Zhao X. (2016), Fluorescence Enhancement Through the Formation of a Single-Layer Two-dimensional Supramolecular Organic Framework and Its Application in Highly Selective Recognition of Picric Acid, *Chem. Commun.*, 52, 7588-7591 (DOI: 10.1039/C6CC03631G).
72. Yang W., Greenaway A., Lin X., Matsuda R., Blake A. J., Wilson C., Lewis W., Hubberstey P., Kitagawa S., Champness N. R., Schroder M. (2010), Exceptional Thermal Stability in a Supramolecular Organic Framework: Porosity and Gas Storage, *J. Am. Chem. Soc.*, 132, 14457-14469 (DOI: 10.1021/ja1042935).
73. Tian J., Chen L., Zhang D. W., Liu Y., Li Z. T. (2016), Supramolecular Organic Frameworks: Engineering Periodicity in Water Through Host-Guest Chemistry, *Chem. Commun.*, 52, 6351-6362 (DOI: 10.1039/C6CC02331B).
74. Zhang K. D., Tian J., Hanifi D., Zhang Y., Sue A. C. H., Zhou T. Y., Zhang L., Zhao X., Liu Y., Li Z. T. (2013), Toward a Single-Layer Two-Dimensional Honeycomb Supramolecular Organic Framework in Water, *J. Am. Chem. Soc.*, 135, 17913-17918.
75. Maspoch D., Ruiz-Molina D., Veciana J. (2007), Old Materials With New Tricks: Multifunctional Open-Framework Materials, *Chem. Soc. Rev.*, 36, 770-818 (DOI: 10.1039/B501600M).
76. Collier J. H., Rudra J. S., Gasiorowski J. Z., Jung J. P. (2010), Multi-component extracellular matrices based on peptide self-assembly, *Chem. Soc. Rev.*, 39, 3413-3424 (DOI: 10.1039/B914337H).
77. Yuan D., Xu B. (2016), Heterotypic Supramolecular Hydrogels, *J. Mater. Chem. B*, 4, 5638-5649 (DOI: 10.1039/C6TB01592A).

78. de Loos M., van Esch J., Kellogg R. M., Feringa B. L. (2001), Chiral Recognition in Bis-Urea-Based Aggregates and Organogels through Cooperative Interactions, *Angew. Chem. Int. Ed.*, 40, 613-616 (DOI: 10.1002/1521-3773(20010202)40:3<613::AID-ANIE613>3.0.CO;2-K).
79. Cai W., Wang G.-T., Du P., Wang R.-X., Jiang X.-K., Li Z.-T. (2008), Foldamer Organogels: A Circular Dichroism Study of Glucose-Mediated Dynamic Helicity Induction and Amplification, *J. Am. Chem. Soc.*, 130, 13450-13459 (DOI: 10.1021/ja8043322).
80. Amemiya R., Mizutani M., Yamaguchi M. (2010), Two-Component Gel Formation by Pseudoenantiomeric Ethynylhelicene Oligomers, *Angew. Chem. Int. Ed.*, 49, 1995-1999 (DOI: 10.1002/anie.200906693).
81. Meazza L., Foster J. A., Fucke K., Metrangolo P., Resnati G., Steed J.W. (2013), Halogen-bonding-triggered Supramolecular Gel Formation, *Nat. Chem.*, 5, 42-47 (DOI: 10.1038/nchem.1496).
82. Ichinose W., Ito J., Yamaguchi M. (2013), Tetrameric  $\alpha\beta\beta$  Aggregate Formation by Stereoisomeric Bidomain Helicene Oligomers, *Angew. Chem. Int. Ed.*, 52, 5290-5294 (DOI: 10.1002/anie.201301463).
83. Fichman G., Guterman T., Adler-Abramovich L., Gazit E. (2015), Synergetic Functional Properties of Two-component Single Amino Acid-Based Hydrogels, *CrystEngComm*, 17, 8105-8112 (DOI: 10.1039/C5CE01051A).
84. Hanabusa K., Miki T., Taguchi Y., Koyama T., Shirai H. (1993), Two-Component, Small Molecule Gelling Agents, *J. Chem. Soc., Chem. Commun.* 1382-1384 (DOI: 10.1039/C39930001382).
85. Krishnan B. P., Ramakrishnan S., Sureshan K. M. (2013), Supramolecular Design of a Bicomponent Topochemical Reaction between Two Non-Identical Molecules, *Chem. Commun*, 49, 1494-1496 (DOI: 10.1039/C2CC37067K).

86. Bairi P., Roy B., Nandi A. K. (2010), Bicomponent Hydrogels of Lumichrome and Melamine: Photoluminescence Property and Its Dependency on pH and Temperature, *J. Phys. Chem. B*, 114, 11454-11461 (DOI: 10.1021/jp105378e).
87. Rao K. V., Jayaramulu K., Maji T. K., George S. J. (2010), Supramolecular Hydrogels and High-Aspect-Ratio Nanofibers through Charge-Transfer-Induced Alternate Coassembly, *Angew. Chem., Int. Ed.*, 49, 4218-4222 (DOI: 10.1002/anie.201000527).
88. Biswas S., Rasale D. B., Das A. K. (2016), Blue Light Emitting Self-Healable Graphene Quantum Dot Embedded Hydrogels. *RSC Adv.*, 6, 54793-54800 (DOI: 10.1039/C6RA06587B).
89. Markvoort A. J., ten Eikelder H. M. M., Hilbers P. A. J., de Greef T. F. A., Meijer E. W. (2011), Theoretical Models of Nonlinear Effects in Two-Component Cooperative Supramolecular Copolymerizations. *Nat. Commun.*, 2, 509 (DOI: 10.1038/ncomms1517).
90. Ikeda T., Iijima T., Sekiya R., Takahashi O., Haino T. (2016), Cooperative Self-Assembly of Carbazole Derivatives Driven by Multiple Dipole-Dipole Interactions, *J. Org. Chem.*, 81, 6832-6837 (DOI: 10.1021/acs.joc.6b01169).
91. Rest C., Mayoral M. J., Fucke K., Schellheimer J., Stepanenko V., Fernandez G. (2014), Self-Assembly and (Hydro)gelation Triggered by Cooperative  $\pi$ - $\pi$  and Unconventional C-H $\cdots$ X Hydrogen Bonding Interactions, *Angew. Chem. Int. Ed.*, 53, 700-705 (DOI: 10.1002/anie.201307806).
92. Draper E. R., Eden E. G. B., McDonald T. O., Adams D. J. (2015), Spatially Resolved Multicomponent Gels, *Nat. Chem.*, 7, 848-852 (DOI: 10.1038/nchem.2347).
93. Ardonna H. A. M., Draper E. R., Citossi F., Wallace M., Serpell L. C., Adams D. J. Tovar J. D. (2017), Kinetically Controlled Coassembly of Multichromophoric Peptide Hydrogelators and the Impacts on Energy

- Transport, *J. Am. Chem. Soc.*, 139, 8685-8692 (DOI: 10.1021/jacs.7b04006).
94. Kar H., Ghosh S. (2015), Multicomponent Gels: Remote Control for Self-Assembly, *Nat. Chem.*, 7, 765-767 (DOI: 10.1038/nchem.2351).
95. Brizard A. M., Stuart M. C. A., van Esch J. H. (2009), Self-assembled interpenetrating networks by orthogonal self-assembly of surfactants and hydrogelators, *Faraday Discuss.*, 2009, 143, 345-357 (DOI: 10.1039/B903806J).
96. Brizard A. M., Stuart M. C. A., von Bommel K., Friggeri A., de Jong M., van Esch J. H. (2008), Preparation of Nanostructures by Orthogonal Self-Assembly of Hydrogelators and Surfactants, *Angew. Chem. Int. Ed.*, 47, 2063-2066 (DOI: 10.1002/anie.200704609).
97. Buerkle L. E., Rowan S. J. (2012), Supramolecular Gels Formed from Multi-component Low Molecular Weight Species, *Chem. Soc. Rev.*, 41, 6089-6102 (DOI: 10.1039/C2CS35106D).
98. Wu A, Isaacs L. (2003), Self-sorting: The Exception or the Rule?, *J. Am. Chem. Soc.*, 125, 4831-4835 (DOI: 10.1021/ja028913b).
99. Moffat J. R., Smith D. K. (2009), Controlled Self-sorting in the Assembly of "Multi-gelator" Gels, *Chem. Commun.*, 3, 316-318 (DOI: 10.1039/b818058j).
100. Cornwell D. J., Daubney O. J., Smith D. K. (2015) Photopatterned Multidomain Gels: Multi-component Self-assembled Hydrogels based on Partially Self-sorting 1,3:2,4-dibenzylidene-d-sorbitol Derivatives, *J. Am. Chem. Soc.*, 137, 15486-15492 (DOI: 10.1021/jacs.5b09691).
101. He Z., Jiang W., Schalley C. A. (2015), Integrative Self-sorting: A Versatile Strategy for the Construction of Complex Supramolecular Architecture, *Chem. Soc. Rev.*, 44, 779-789 (DOI: 10.1039/C4CS00305E).
102. Mayoral M. J., Rest C., Schellheimer J., Stepanenko V., Fernandez G. (2012), Narcissistic versus Social Self-Sorting of Oligophenyleneethynylene Derivatives: From Isodesmic Self-

- Assembly to Cooperative Co-Assembly, *Chem. Eur. J.*, 18, 15607-15611 (DOI: 10.1002/chem.201202367).
103. Aratsu K., Prabhu D. D., Iwawaki H., Lin X., Yamauchi M., Karatsu T., Yagai S. (2016), Self-sorting Regioisomers through the Hierarchical Organization of Hydrogen-bonded Rosettes, *Chem. Commun.*, 52, 8211-8214 (DOI: 10.1039/c6cc03419e).
104. South C. R., Burd C., Weck M. (2007), Modular and Dynamic Functionalization of Polymeric Scaffolds, *Acc. Chem. Res.*, 40, 63-74 (DOI: 10.1021/ar0500160).
105. Ikkala O., ten Brinke G. (2002), Functional Materials Based on Self-Assembly of Polymeric Supramolecules, *Science*, 295, 2407-2409 (DOI: 10.1126/science.1067794).
106. Heeres A., van der Pol C., Stuart M., Friggeri A., Feringa B. L., van Esch J. (2003), Orthogonal Self-Assembly of Low Molecular Weight Hydrogelators and Surfactants, *J. Am. Chem. Soc.*, 125, 14252-14253 (DOI: 10.1021/ja036954h).
107. Ward M. D., Raithby P. R., (2013), Functional behaviour from controlled self-assembly: challenges and prospects, *Chem. Soc. Rev.*, 42, 1619 (DOI: 10.1039/C2CS35123D).
108. Xing P., Chu X., Li S., Xin F., Ma M., Hao A. (2013), Switchable and orthogonal self-assemblies of anisotropic fibers, *New J. Chem.*, 37, 3949-3955 (DOI: 10.1039/C3NJ00984J).
109. Xing P., Zhao Y. (2016), Multifunctional Nanoparticles Self-Assembled from Small Organic Building Blocks for Biomedicine. *Adv. Mater.*, 28, 7304-7339 (DOI: 10.1002/adma.201600906).
110. Lei Y. L., Jin Y., Zhou D. Y., Shi X., Liao L., Lee S. T. (2012), White-Light Emitting Microtubes of Mixed Organic Charge-Transfer Complexes, *Adv. Mater.*, 24, 5345-5351 (DOI: 10.1002/adma.201201493).
111. Liu K., Xing R., Zou Q., Ma G., Möhwald H., Yan X. (2016), Simple Peptide-Tuned Self-Assembly of Photosensitizers towards

- Anticancer Photodynamic Therapy, *Angew. Chem. Int. Ed.*, 55, 3036-3039 (DOI: 10.1002/anie.201509810).
112. Coelho J. P., Tardajos G., Stepanenko V., Rodle A., Fernandez G., Guerrero-Martinez A. (2015), Cooperative Self-Assembly Transfer from Hierarchical Supramolecular Polymers to Gold Nanoparticles, *ACS Nano*, 9, 11241-11248 (DOI: 10.1021/acsnano.5b04841).
113. Zhang X., Rehm S., Safont-Sempere M. M., Wurthner F. (2009), Vesicular Perylene Dye Nanocapsules as Supramolecular Fluorescent pH Sensor Systems, *Nat. Chem.*, 1, 623-629 (DOI: 10.1038/nchem.368).
114. Xing P., Zhao Z., Hao A., Zhao Y. (2016), Tailoring Luminescence Color Conversion via Affinitive Co-assembly of Glutamates Appended with Pyrene and Naphthalene Dicarboximide Units, *Chem. Commun.*, 52, 1246-1249 (DOI: 10.1039/C5CC08858E).
115. Abul-Haija Y.M., Roy S., Frederix P.W.J.M., Javid N., Jayawarna V., Ulijn R.V. (2014), Biocatalytically Triggered Co-Assembly of Two-Component Core/Shell Nanofibers, *Small*, 10, 973-979 (DOI: 10.1002/smll.201301668).
116. Okesola B. O., Mata A. (2018), Multicomponent self-assembly as a tool to harness new properties from peptides and proteins in material design, *Chem. Soc. Rev.*, 47, 3721-3736 (DOI: 10.1039/c8cs00121a).
117. Sadownik J. W., Ulijn R. V. (2010), Dynamic Covalent Chemistry in aid of Peptide Self-assembly, *Curr. Opin. Biotechnol.*, 21, 401-411 (DOI: 10.1016/j.copbio.2010.05.010).
118. Lam R. T. S., Belenguer A., Roberts S. L., Naumann C., Jarrosson T., Otto S., Sanders J. K. M. (2005), Amplification of acetylcholine-binding catenanes from dynamic combinatorial libraries, *Science*, 308, 667-669 (DOI: 10.1126/science.1109999).
119. Aprahamian I. (2017), Hydrazone Switches and Things in Between. *Chem. Commun.*, 53, 6674-6684 (DOI: 10.1039/C7CC02879B).

120. Boekhoven J., Poolman J. M., Maity C., Li F., van der Mee L., Minkenberg C. B., Mendes E., van Esch J. H., Eelkema R. (2013), Catalytic Control over Supramolecular Gel Formation, *Nat. Chem.*, 5, 433- 437 (DOI: 10.1038/nchem).
121. Reuther J. F., Dees J. L., Kolesnichenko I. V., Hernandez E. T., Ukraintsev D. V., Guduru R., Whiteley M., Anslyn E. V. (2017), Dynamic Covalent Chemistry Enables Formation of Antimicrobial Peptide Quaternary Assemblies in a Completely Abiotic Manner, *Nat. Chem.*, 10, 45-50 (DOI: 10.1038/nchem.2847).
122. Zhang W.-B., Sun F., Tirrell D. A., Arnold F. H. (2013), Controlling Macromolecular Topology with Genetically Encoded SpyTag–SpyCatcher Chemistry, *J. Am. Chem. Soc.*, 135, 13988-13997 (DOI: 10.1021/ja4076452).
123. Fei L., Perrett S. (2009), Disulfide Bond Formation Significantly Accelerates the Assembly of Ure2p Fibrils because of the Proximity of a Potential Amyloid Stretch, *J. Biol. Chem.*, 284, 11134-11141 (DOI 10.1074/jbc.M809673200).
124. Carnall J. M. A., Waudby C. A., Belenguer A. M., Stuart M. C. A., Peyralans J. J. P., Otto S. (2010), Mechanosensitive Self-Replication Driven by Self-Organization, *Science*, 327, 1502-1506 (DOI: 10.1126/science.1182767).
125. Williams R. J., Smith A. M., Collins R., Hodson N., Das A. K., Ulijn R. V. (2008) Enzyme-assisted Self-assembly under Thermodynamic Control, *Nat. Nanotechnol.*, 4, 19-24 (DOI: 10.1038/nnano.2008.378).
126. Das A. K., Hirst A. R., Ulijn R. V. (2009), Evolving nanomaterials using enzyme-driven dynamic peptide libraries (eDPL). *Faraday Discuss.*, 143, 293–303 (DOI: 10.1039/B902065A).
127. Debnath S., Roy S. Ulijn R.V. (2013), Peptide Nanofibers with Dynamic Instability through Non-Equilibrium Biocatalytic Assembly, *J. Am. Chem. Soc.*, 135, 16789-16792 (DOI: 10.1021/ja4086353).

128. Brochu B. W., Craig S. L., Reichert W. M. (2011), Self-healing Biomaterials, *J. Biomed. Mater. Res. Part A*, 96A, 492-506 (DOI: 10.1002/jbm.a.32987)
129. Tee B. C. K., Wang C., Allen R., Bao Z. (2012), An Electrically and Mechanically Self-healing Composite with Pressure- and Flexion-sensitive Properties for Electronic Skin Applications, *Nat. Nanotechnol.*, 7, 825-832 (DOI: 10.1038/nnano.2012.192).
130. Canadell J., Goossens H., Klumperman B. (2011), Self-Healing Materials Based on Disulfide Links, *Macromolecules*, 44, 2536-2541 (DOI: 10.1021/ma2001492).
131. Liu F., Li F., Deng G., Chen Y., Zhang B., Zhang J., Liu C. Y. (2012), Rheological Images of Dynamic Covalent Polymer Networks and Mechanisms behind Mechanical and Self-Healing Properties. *Macromolecules*, 45, 1636-1645 (DOI: 10.1021/ma202461e).
132. Colquhoun H. M. (2012), Self-repairing Polymers: Materials that Heal Themselves, *Nat. Chem.*, 4, 435-436 (DOI: 10.1038/nchem.1357).
133. Xiao X., Xie T., Cheng Y. T. (2010), Self-healable Graphene Polymer Composites, *J. Mater. Chem.*, 20, 3508-3514 (DOI: 10.1039/C0JM00307G).
134. Fox J., Wie J. J., Greenland B. W., Burattini S., Hayes W., Colquhoun H. M., Mackay M. E., Rowan S. J. (2012), High-Strength, Healable, Supramolecular Polymer Nanocomposites, *J. Am. Chem. Soc.*, 134, 5362-5368 (DOI: 10.1021/ja300050x).
135. Billiet S., Hillewaere X. K. D., Teixeira R. F. A., Du Prez . E. (2013), Chemistry of Crosslinking Processes for Self-Healing Polymers, *Macromol. Rapid Commun.*, 34, 290-309 (DOI: 10.1002/marc.201200689).
136. Herbst F., Döhler D., Michael P., Binder W. H. (2013), Self-Healing Polymers via Supramolecular Forces, *Macromol. Rapid Commun.*, 34, 203-220 (DOI: 10.1002/marc.201200675).

137. Hager M. D., Greil P., Leyens C., van der Zwaag S., Schubert U. S. (2010), Self-Healing Materials, *Adv. Mater.*, 22, 5424-5430 (DOI: 10.1002/adma.201003036).
138. Bergman S. D., Wudl F., (2008), Mendable polymers, *J. Mater. Chem.*, 18, 41-62 (DOI: 10.1039/B713953P).
139. Amamoto Y., Otsuka H., Takahara A., Matyjaszewski K. (2012), Self-Healing of Covalently Cross-Linked Polymers by Reshuffling Thiuram Disulfide Moieties in Air under Visible Light, *Adv. Mater.*, 24, 3975-3980 (DOI: 10.1002/adma.201201928).
140. Imato K., Nishihara M., Kanehara T., Amamoto Y., Takahara A., Otsuka H. (2012), Self-Healing of Chemical Gels Cross-Linked by Diarylbibenzofuranone-Based Trigger-Free Dynamic Covalent Bonds at Room Temperature, *Angew. Chem. Int. Ed.*, 51, 1138-1142 (DOI: 10.1002/anie.201104069).
141. Deng G., Li F., Yu H., Liu F., Liu C., Sun W., Jiang H., Chen Y. (2012), Dynamic Hydrogels with an Environmental Adaptive Self-Healing Ability and Dual Responsive Sol-Gel Transitions, *ACS Macro Lett.* 1, 275-279 (DOI: 10.1021/mz200195n).
142. Wojtecki R. J., Meador M. A., Rowan S. J. (2011), Using the dynamic bond to access macroscopically responsive structurally dynamic polymers, *Nat. Mater.*, 10, 14-27 (DOI: 10.1038/nmat2891).
143. Burattini S., Greenland B. W., Merino D. H., Weng W., Seppala J., Colquhoun H. M., Hayes W., Mackay M. E., Hamley I. W., Rowan S. J. (2010), A Healable Supramolecular Polymer Blend Based on Aromatic  $\pi$ - $\pi$  Stacking and Hydrogen-Bonding Interactions, *J. Am. Chem. Soc.*, 132, 12051-12058 (DOI: 10.1021/ja104446r).
144. Gaharwar A. K., Peppas N. A., Khademhosseini A. (2014), Nanocomposite Hydrogels for Biomedical Applications, *Biotechnol. Bioeng.*, 111, 441-453 (DOI: 10.1002/bit.25160).
145. Roy S., Baral A., Banerjee A. (2013), An Amino-Acid-Based Self-Healing Hydrogel: Modulation of the Self-Healing Properties by

- Incorporating Carbon-Based Nanomaterials, *Chem. Eur. J.*, 19, 14950-14957 (DOI: 10.1002/chem.201301655).
146. Mandal D., Kar T., Das P. K., (2014), Pyrene-Based Fluorescent Ambidextrous Gelators: Scaffolds for Mechanically Robust SWNT-Gel Nanocomposites, *Chem. Eur. J.*, 20, 1349-1358 (DOI: 10.1002/chem.201303401).
147. Shen C., Zhao Y., Liu H., Jiang Y., Li H., Lan S., Bao H., Yang B., Lin Q. (2018), Dynamically Crosslinked Carbon Dots/biopolymer Hydrogels Exhibiting Fluorescence and Multi-stimuli Logic-gate Responses, *Polym. Chem.*, 9, 2478-2483 (DOI: 10.1039/C8PY00165K).
148. Novoselov K. S., Geim A. K., Morozov S. V., Jiang D., Zhang Y., Dubonos S. V., Grigorieva I. V., Firsov A. A. (2004), Electric Field Effect in Atomically Thin Carbon Films, *Science*, 306, 666-669 (DOI: 10.1126/science.1102896).
149. Katsnelson M. I. (2007), Graphene: Carbon in two Dimensions, *Mater. Today*, 10, 20-27 (DOI: 10.1016/S1369-7021(06)71788-6).
150. Stoller M. D., Park S., Zhu Y., An J., Ruoff R. S. (2008), Graphene-Based Ultracapacitors, *Nano Lett.*, 8, 3498-3502 (DOI: 10.1021/nl802558y).
151. Chen H., Meuler M. B., Gilmore K. J., Wallace G. G., Li D. (2008), Mechanically Strong, Electrically Conductive, and Biocompatible Graphene Paper, *Adv. Mater.*, 20, 3557-3561 (DOI: 10.1002/adma.200800757).
152. Agarwal S., Zhou X., Chen P. (2010), Interfacing Live Cells with Nanocarbon Substrates, *Langmuir*, 26, 2244-2247 (DOI: 10.1021/la9048743).
153. Hou C., Zhang Q., Li Y., Wang H. (2012), Graphene-polymer Hydrogels with Stimulus-sensitive Volume Changes, *Carbon*, 50, 1959-1965 (DOI: 10.1016/j.carbon.2011.12.049).

154. Dong Y., Tian W., Ren S., Dai R., Chi Y., Chen G. (2014), Graphene Quantum Dots/l-Cysteine Coreactant Electrochemiluminescence System and Its Application in Sensing Lead(II) Ions, *ACS Appl. Mater. Interfaces*, 6, 1646-1651 (DOI: 10.1021/am404552s).
155. Kwon W., Kim Y.-H., Lee C.-L., Lee M., Choi H.-C., Lee T.-W., Rhee S.-W. (2014), Electroluminescence from Graphene Quantum Dots Prepared by Amidative Cutting of Tattered Graphite, *Nano Lett.*, 14, 1306-1311 (DOI: 10.1021/nl404281h).
156. Dong Y., Chen C., Zheng X., Gao L., Cui Z., Yang H., Guo C., Chi Y., Li C. M. (2012), One-step and High Yield Simultaneous Preparation of Single- and Multi-layer Graphene Quantum Dots from CX-72 Carbon Black, *J. Mater. Chem.*, 22, 8764-8766 (DOI: 10.1039/C2JM30658A).
157. Nurunnabi M., Khatun Z., Huh K. M., Park S. Y., Lee D. Y., Cho K. J., Lee Y.-K. (2013), In Vivo Biodistribution and Toxicology of Carboxylated Graphene Quantum Dots, *ACS Nano*, 7, 6858-6867 (DOI: 10.1021/nn402043c).
158. Jiao T., Zhao H., Zhou J., Zhang Q., Luo X., Hu J., Peng Q., Yan X. (2015), Self-Assembly Reduced Graphene Oxide Nanosheet Hydrogel Fabrication by Anchorage of Chitosan/Silver and Its Potential Efficient Application toward Dye Degradation for Wastewater Treatments, *ACS Sustainable Chem. Eng.*, 3, 3130-3139 (DOI: 10.1021/acssuschemeng.5b00695).
159. Bai H., Li C., Wang X., Shi G. (2010), A pH-sensitive Graphene Oxide Composite Hydrogel, *Chem. Commun.*, 46, 2376-2378 (DOI: 10.1039/C000051E).
160. Xu Y., Wu Q., Sun Y., Bai H., Shi G. (2010), Three-Dimensional Self-Assembly of Graphene Oxide and DNA into Multifunctional Hydrogels, *ACS Nano*, 4, 7358-7362 (DOI: 10.1021/nn1027104).

161. Khabibullin A., Alizadehgiashi M., Khuu N., Prince E., Tebbe M., Kumacheva E. (2017), Injectable Shear-Thinning Fluorescent Hydrogel Formed by Cellulose Nanocrystals and Graphene Quantum Dots, *Langmuir*, 33, 12344-12350 (DOI: 10.1021/acs.langmuir.7b02906).
162. Ramachandran G. N., Kartha G. (1954), Structure of Collagen, *Nature*, 174, 269-270 (DOI: 10.1038/174269c0).
163. Wu H., Zhou Y., Yin L., Hang C., Li X., Agren H., Yi T., Zhang Q., Zhu L. (2017), Helical Self-Assembly-Induced Singlet-Triplet Emissive Switching in a Mechanically Sensitive System, *J. Am. Chem. Soc.*, 139, 785-791 (DOI: 10.1021/jacs.6b10550).
164. Kim C., Kim K. Y., Lee J. H., Ahn J., Sakurai K., Lee S. S., Jung J. H. (2017), Chiral Supramolecular Gels with Lanthanide Ions: Correlation between Luminescence and Helical Pitch, *ACS Appl. Mater. Interfaces*, 9, 3799-3807 (DOI: 10.1021/acsami.6b13916).
165. Jiang J., Meng Y., Zhang L., Liu M. (2016), Self-Assembled Single-Walled Metal-Helical Nanotube (M-HN): Creation of Efficient Supramolecular Catalysts for Asymmetric Reaction, *J. Am. Chem. Soc.*, 138, 15629-15635 (DOI: 10.1021/jacs.6b08808).
166. Kumar M., Brocorens P., Tonnele C., Beljonne D., Surin M., George S. J. (2014), A Dynamic Supramolecular Polymer with Stimuli-responsive Handedness for in situ Probing of Enzymatic ATP Hydrolysis. *Nat. Commun.*, 5, 5793 (DOI: 10.1038/ncomms6793).
167. Ziegler M., Davis A. V., Johnson D. W. Raymond K. N. (2003), Supramolecular Chirality: A Reporter of Structural Memory, *Angew. Chem. Int. Edn.*, 42, 665-668 (DOI: 10.1002/anie.200390183)
168. Yashima E., Ousaka N., Taura D., Shimomura K., Ikai T., Maeda K. (2016), Supramolecular Helical Systems: Helical Assemblies of Small Molecules, Foldamers, and Polymers with Chiral Amplification and Their Functions, *Chem. Rev.*, 116, 13752-13990 (DOI: 10.1021/acs.chemrev.6b00354).

169. Liu M., Zhang L., Wang T. (2015), Supramolecular Chirality in Self-Assembled Systems, *Chem. Rev.* 115, 7304-7397 (DOI: 10.1021/cr500671p).
170. Zhang L., Qin L., Wang X., Cao H., Liu M. (2014), Supramolecular Chirality in Self-Assembled Soft Materials: Regulation of Chiral Nanostructures and Chiral Functions, *Adv. Mater.*, 26, 6959-6964 (DOI: 10.1002/adma.201305422).
171. Xing P., Zhao Y. (2018), Controlling Supramolecular Chirality in Multicomponent Self-Assembled Systems, *Acc. Chem. Res.*, 51, 2324-2334 (DOI: 10.1021/acs.accounts.8b00312).
172. Xing P., Chen H., Bai L., Hao A., Zhao Y. (2016), Superstructure Formation and Topological Evolution Achieved by Self-Organization of a Highly Adaptive Dynamer, *ACS Nano*, 10, 2716-2727 (DOI: 10.1021/acsnano.5b07800).
173. Green M. M., Peterson N. C., Sato T., Teramoto A., Cook R., Lifson S. (1995), A Helical Polymer with a Cooperative Response to Chiral Information, *Science*, 268, 1860-1866 (DOI: 10.1126/science.268.5219.1860).
174. Brunsveld L., Vekemans J., Hirschberg J., Sijbesma R. P., Meijer E. W. (2002), Hierarchical Formation of Helical Supramolecular Polymers via Stacking of Hydrogen-Bonded Pairs in Water, *Proc. Natl. Acad. Sci. U. S. A.* 99, 4977-4982 (DOI: 10.1073/pnas.072659099).
175. Maeda K., Takeyama Y., Sakajiri K., Yashima E. (2004), Nonracemic Dopant-Mediated Hierarchical Amplification of Macromolecular Helicity in a Charged Polyacetylene Leading to a Cholesteric Liquid Crystal in Water, *J. Am. Chem. Soc.* 126, 16284-16285 (DOI: 10.1021/ja044264n).
176. Nakagiri T., Kodama H., Kobayashi K. K. (1971), Helical Twisting Power in Mixtures of Nematic and Cholesteric Liquid

- Crystals, *Phys. Rev. Lett.*, 27, 564-567 (DOI: 10.1103/PhysRevLett.27.564).
177. Herwig P., Kayser C. W., Mullen K., Spiess W. (1996), Columnar Mesophases of Alkylated Hexa-peri-hexabenzocoronenes with Remarkably Large Phase Widths, *Adv. mater.*, 8, 510-513 (DOI: 10.1002/adma.19960080613).
178. Palmans A. R. A., Vekemans J., Havinga E. E., Meijer E. W. (1997), Sergeants-and-Soldiers Principle in Chiral Columnar Stacks of Disc-Shaped Molecules with  $C_3$  Symmetry, *Angew. Chem., Int. Ed.*, 36, 2648-2651 (DOI: 10.1002/anie.199726481).
179. Palmans, A. R. A.; Meijer, E. W. (2007), Amplification of Chirality in Dynamic Supramolecular Aggregates, *Angew. Chem. Int. Ed.*, 46, 8948-8968 (DOI: 10.1002/anie.200701285).
180. Pandeewar M., Avinash M. B., Govindaraju T. (2012), Chiral Transcription and Retentive Helical Memory: Probing Peptide Auxiliaries Appended with Naphthalenediimides for Their One-Dimensional Molecular Organization, *Chem. Eur. J.*, 18, 4818-4822 (DOI: 10.1002/chem.201200197).
181. Liu Y., Chen C., Wang T., Liu M. (2016), Supramolecular Chirality of the Two-Component Supramolecular Copolymer Gels: Who Determines the Handedness? *Langmuir*, 32, 322-328 (DOI: 10.1021/acs.langmuir.5b03938).
182. Oda R., Huc I., Schmutz M., Candau S. J., MacKintosh F. C. (1999), Tuning Bilayer Twist Using Chiral Counterions, *Nature*, 399, 566-569 (DOI: 10.1038/21154).
183. Haedler A. T., Meskers S. C., Zha R. H., Kivala M., Schmidt H. W., Meijer E. W. (2016), Pathway Complexity in the Enantioselective Self-Assembly of Functional Carbonyl-Bridged Triarylamine Trisamides, *J. Am. Chem. Soc.*, 138, 10539-10545 (DOI: 10.1021/jacs.6b05184).

184. Edwards W., Smith D. K. (2014), Enantioselective Component Selection in Multicomponent Supramolecular Gels, *J. Am. Chem. Soc.*, 136, 1116-1124 (DOI: 10.1021/ja411724r).
185. Smith, D. K. (2009), Lost in Translation? Chirality Effects in the Self-assembly of Nanostructured Gel-phase Materials, *Chem. Soc. Rev.* 38, 684-694 (DOI: 10.1039/b800409a).
186. Kim J., Lee J., Kim W. Y., Kim H., Lee S., Lee H. C., Lee Y. S., Seo M., Kim S. Y. (2015), Induction and Control of Supramolecular Chirality by Light in Self-assembled Helical Nanostructures, *Nat. Commun.*, 6, 6959 (DOI: 10.1038/ncomms7959).
187. Yan Y., Yu Z., Huang Y. W., Yuan W. X., Wei Z. X. (2007), Helical Polyaniline Nanofibers Induced by Chiral Dopants by a Polymerization Process, *Adv. Mater.*, 19, 3353-3357 (DOI: 10.1002/adma.200700846).
188. Liu G.-F., Zhu L.-Y., Ji W., Feng C.-L., Wei Z.-X. (2016), Inversion of the Supramolecular Chirality of Nanofibrous Structures through Co-Assembly with Achiral Molecules, *Angew. Chem. Int. Ed.*, 55, 2411-2415 (DOI: 10.1002/anie.201510140).
189. Choi H., Cho K. J., Seo H., Ahn J., Liu J., Lee S. S., Kim H., Feng C., Jung J. H. (2017), Transfer and Dynamic Inversion of Coassembled Supramolecular Chirality through 2D-Sheet to Rolled-Up Tubular Structure, *J. Am. Chem. Soc.*, 139, 17711-17714 (DOI: 10.1021/jacs.7b09760).
190. Wang F., Feng C. L. (2018), Metal-Ion-Mediated Supramolecular Chirality of L-Phenylalanine Based Hydrogels, *Angew. Chem., Int. Ed.*, 57, 5655-5659 (DOI: 10.1002/anie.201800251).
191. Liu G. -F., Ji W., Wang W. -L., Feng C. -L. (2015), Multiresponsive Hydrogel Coassembled from Phenylalanine and Azobenzene Derivatives as 3D Scaffolds for Photoguiding Cell Adhesion and Release, *ACS Appl. Mater. Interfaces*, 7, 301-307 (DOI: 10.1021/am506202s).

192. Liu G., Liu J., Feng C., Zhao Y. (2017), Unexpected Right-handed Helical Nanostructures Co-assembled from L-phenylalanine Derivatives and Achiral Bipyridines, *Chem. Sci.*, 8, 1769-1775 (DOI: 10.1039/C6SC04808K).
193. G. Liu, J. Sheng, H. Wu, C. Yang, G. Yang, Y. Li, R. Ganguly, L. Zhu, Y., Zhao (2018), Controlling Supramolecular Chirality of Two-Component Hydrogels by J- and H- Aggregation of Building Blocks, *J. Am. Chem. Soc.*, 140, 6467-6473 (DOI: 10.1021/jacs.8b03309).
194. Whitesides G. M., Simanek E. E., Mathias J. P., Seto C. T., Chin D. N., Mammen M., Gordon D. M. (1995), Noncovalent Synthesis: Using Physical-Organic Chemistry To Make Aggregates, *Acc. Chem. Res.*, 28, 27-44 (DOI: 10.1021/ar00049a006).
195. Yashima E., Maeda K., Okamoto Y. (1999), Memory of Macromolecular Helicity Assisted by Interaction with Achiral Small Molecules, *Nature*, 399, 449-451 (DOI: 10.1038/20900).
196. Korevaar P. A., George S. J., Markvoort A. J., Smulders M. M., Hilbers P. A., Schenning A. P., De Greef T. F., Meijer E. W. (2012), Pathway Complexity in Supramolecular Polymerization, *Nature*, 481, 492-496 (DOI: 10.1038/nature10720).
197. Shen Z., Jiang Y., Wang T., Liu M. (2015), Symmetry Breaking in the Supramolecular Gels of an Achiral Gelator Exclusively Driven by  $\pi$ - $\pi$  Stacking, *J. Am. Chem. Soc.*, 137, 16109-16115 (DOI: 10.1021/jacs.5b10496).
198. Basak S., Nandaa J., Banerjee A. (2014), Multi-stimuli Responsive Self-healing Metallo-hydrogels: Tuning of the Gel Recovery Property. *Chem. Commun.*, 50, 2356-2359 (DOI: 10.1039/C3CC48896A).
199. Cacialli F., Samori P., Silva C. (2004), Supramolecular Architectures, *Mater. Today*, 7, 24-32 (DOI: 10.1016/S1369-7021(04)00186-5).

200. Naota T., Koori H. (2005), Molecules That Assemble by Sound: An Application to the Instant Gelation of Stable Organic Fluids, *J. Am. Chem. Soc.*, 127, 9324-9325 (DOI: 10.1021/ja050809h).
201. Nelli S. R., Chakravarthy R. D., Mohiuddin M., Lin H. -C. (2018), The Role of Amino Acids on Supramolecular Co-assembly of Naphthalenediimide-pyrene based Hydrogelators, *RSC Adv.*, 8, 14753-14759 (DOI: 10.1039/C8RA00929E).
202. Murata K., Aoki M., Suzuki T., Harada T., Kawabata H., Komori T., Ohseto F., Ueda K., Shinkai S. (1994), Thermal and Light Control of the Sol-Gel Phase Transition in Cholesterol-Based Organic Gels. Novel Helical Aggregation Modes As Detected by Circular Dichroism and Electron Microscopic Observation *J. Am. Chem. Soc.*, 116, 6664-6676 (DOI: 10.1021/ja00094a023).
203. de Loos M., Feringa B. L., van Esch J. H. Eur. (2005), Design and Application of Self-Assembled Low Molecular Weight Hydrogels *J. Org. Chem.*, 17, 3615-3631 (DOI: 10.1002/ejoc.200400723).
204. Estroff L. A., Hamilton A. D. (2004), Water Gelation by Small Organic Molecules *Chem. Rev.*, 104, 1201-1217 (DOI: 10.1021/cr0302049).
205. Dastidar, P. (2008), Supramolecular Gelling Agents: Can they be Designed?, *Chem. Soc. Rev.*, 37, 2699-2715 (DOI: 10.1039/B807346E).
206. Glynn S. A. Albanes D. (1994), Folate and Cancer: A Review of the Literature, *Nutr. Cancer*, 22, 101-119 (DOI: 10.1080/01635589409514336).
207. Tannock I. F., Rotin D. (1989), Acid pH in Tumors and its Potential for Therapeutic Exploitation, *Cancer Res.*, 49, 4373-4384.
208. Lundberg P., Lynd N. A., Zhang Y., Zeng X., Krogstad D. V., Paffen T., Malkoch M., Nystromb A. M., Hawker C. J. (2013), pH-triggered Self-assembly of Biocompatible Histamine-functionalized

- Triblock Copolymers, *Soft Matter*, 9, 82-89 (DOI: 10.1039/C2SM26996A).
209. Colquhoun C., Draper E. R., Eden E. G., Cattoz B. N., Morris K. L., Chen L., McDonald T. O., Terry A. E., Griffiths P. C., Serpell L. C., Adams D. J. (2014), The Effect of Self-sorting and Co-assembly on the Mechanical Properties of Low Molecular Weight Hydrogels, *Nanoscale*, 6, 13719-13725 (DOI: 10.1039/C4NR04039B).
210. Draper E. R., Wallace M., Schweins R., Poole R. J., Adams D. J. (2017), Nonlinear Effects in Multicomponent Supramolecular Hydrogels, *Langmuir*, 33, 2387-2395 (DOI: 10.1021/acs.langmuir.7b00326).
211. Huang Y. F., Chiang W. H., Tsai P. L., Chern C. S., Chiu H. C. (2011), Novel Hybrid Vesicles Co-Assembled from a Cationic Lipid and PAAc-g-mPEG with pH-Triggered Transmembrane Channels for Controlled Drug Release, *Chem. Commun.*, 47, 10978-10980 (DOI: 10.1039/C1CC14793E).
212. Chiang W. H., Ho V. T., Huang W. C., Huang Y. F., Chern C. S., Chiu H. C. (2012), Dual Stimuli-Responsive Polymeric Hollow Nanogels Designed as Carriers for Intracellular Triggered Drug Release, *Langmuir*, 28, 15056-15064 (DOI: 10.1021/la302903v).
213. Seshadri R., Weiss J., Hulbert G. J., Mount, J. (2003), Ultrasonic Processing Influences Rheological and Optical Properties of High-methoxyl Pectin Dispersions, *Food Hydrocolloids*, 17, 191-197 (DOI: 10.1016/S0268-005X(02)00051-6).
214. Massey J., Power K. N., Manners I., Winnik M. A. (1998), Self-Assembly of a Novel Organometallic-Inorganic Block Copolymer in Solution and the Solid State: Nonintrusive Observation of Novel Wormlike Poly(ferrocenyldimethylsilane)-b-Poly(dimethylsiloxane) Micelles, *J. Am. Chem. Soc.*, 120, 9533-9540 (DOI: 10.1021/ja981803d).

215. Deng C., Fang R., Guan Y., Jiang J., Lin C., Wang L. (2012), Sonication-induced Self-assembly of Flexible Tris (ureidobenzyl) Amine: From Dimeric Aggregates to Supramolecular Gels, *Chem. Commun.*, 48, 7973-7975 (DOI: 10.1039/C2CC33408A).
216. Naota T., Koori H. (2005), Molecules That Assemble by Sound: An Application to the Instant Gelation of Stable Organic Fluids, *J. Am. Chem. Soc.*, 127, 9324-9325 (DOI: 10.1021/ja050809h)
217. Malicka, J. M., Sandeep A., Monti F., Bandini E., Gazzano M., Ranjith C., Praveen V. K., Ajayaghosh A., Armaroli N. (2013), Ultrasound Stimulated Nucleation and Growth of a Dye Assembly into Extended Gel Nanostructures, *Chem. Eur. J.*, 19, 12991-13001 (DOI: 10.1002/chem.201301539).
218. Cravotto G., Cintas P. (2009), Molecular Self-assembly and Patterning Induced by Sound Waves. The Case of Gelation, *Chem. Soc. Rev.*, 38, 2684-2697 (DOI: 10.1039/B901840A).
219. Roy B., Bairi P., Chakraborty P., Nandi A. K. (2013), Stimuli-Responsive, Thixotropic Bicomponent Hydrogel of Melamine-Zn(II)-orotate Complex, *Supramolecular Chemistry*, 25, 335-343, (DOI: 10.1080/10610278.2013.782100)
220. Maity I., Rasale D. B., Das A. K. (2012), Sonication Induced Peptide-Appended Bolaamphiphile Hydrogels for in situ Generation and Catalytic Activity of Pt Nanoparticles, *Soft Matter*, 8, 5301-5308 (DOI: 10.1039/C2SM25126D).
221. Anderson K. M., Day G. M., Paterson M. J., Byrne P., Clarke N., Steed J. W. (2008), Structure Calculation of an Elastic Hydrogel from Sonication of Rigid Small Molecule Components, *Angew. Chem. Int. Ed.*, 47, 1058-1062 (DOI: 10.1002/anie.200703785).
222. Afrasiabi R., Kraatz H. -B. (2013), Small-Peptide-Based Organogel Kit: Towards the Development of Multicomponent Self-Sorting Organogels, *Chem. Eur. J.*, 19, 15862-15871 (DOI: 10.1002/chem.201303116).

223. Roy B., Bairi P., Nandi A. K. (2014), Supramolecular Assembly of Melamine and its Derivatives: Nanostructures to Functional Materials, *RSC Adv.*, 4, 1708-1734 (DOI: 10.1039/C3RA44524K).
224. Ye, F., Chen S., Tang G., Wang X. (2014), Sonication Induced Morphological Transformation between 3D Gel network and Globular Structure in a Two-component Gelation System, *Colloids Surf A: Physicochem. Eng. Asp.*, 452, 165-172 (DOI: 10.1016/j.colsurfa.2014.03.084).
225. Wang Y., Ma N., Wang Z., Zhnag X. (2007), Photocontrolled Reversible Supramolecular Assemblies of an Azobenzene-Containing Surfactant with  $\alpha$ -Cyclodextrin, *Angew. Chem. Int. Ed.*, 46, 2823-2826 (DOI: 10.1002/anie.200604982).
226. Zhao Y. L., Stoddart J. F. (2009), Azobenzene-Based Light-Responsive Hydrogel System, *Langmuir*, 25, 8442-8446 (DOI: 10.1021/la804316u).
227. Tomatsu I., Hashidzume A., Harada A. (2005), Photoresponsive Hydrogel System Using Molecular Recognition of  $\alpha$ -Cyclodextrin, *Macromolecules*, 38, 5223-5227 (DOI: 10.1021/ma050670v).
228. Chivers P. R. A., Smith D. K. (2017), Spatially-resolved Soft Materials for Controlled Release-hybrid Hydrogels Combining a Robust Photo-activated Polymer gel with an Interactive Supramolecular Gel, *Chem. Sci.*, 8, 7218-7227 (DOI: 10.1039/c7sc02210g).
229. Zhou Y., Xu M., Yi T., Xiao S., Zhou Z., Li F., Huang C. (2007), Morphology-Tunable and Photoresponsive Properties in a Self-Assembled Two-Component Gel System, *Langmuir*, 23, 202-208 (DOI: 10.1021/la061530x).
230. S., Samai C., Sapsanis S. P., Patil A., Ezzeddine B. A., Moosa H., Omran A.-H., Emwas Salamab K. N., Khashab N. M. (2016), A Light Responsive Two-component Supramolecular Hydrogel: A Sensitive

- Platform for the Fabrication of Humidity Sensors, *Soft Matter*, 12, 2842-2845 (DOI: 10.1039/c6sm00272b).
231. Estroff L. A.; Hamilton, A. D. (2004), Water Gelation by Small Organic Molecules, *Chem. Rev.*, 104, 1201-1217 (DOI: 10.1021/cr0302049).
232. Hirst A. R., Escuder B., Miravet J. F., Smith D. K. (2008), High-tech Applications of Self-assembling Supramolecular Nanostructured Gel-phase Materials: From Regenerative Medicine to Electronic Devices. *Angew. Chem. Int. Ed.*, 47, 8002-8018 (DOI: 10.1002/anie.200800022).
233. Bhuniya S., Park S. M., Kim B. H. (2005), Biotin-Amino Acid Conjugates: An Approach Toward Self-Assembled Hydrogelation, *Org. Lett.*, 7, 1741-1744 (DOI: 10.1021/ol050300r).
234. Yao M. -H., Yang J., Song J. -T., Zhao D. -H., Du M. -S., Zhao Y. -D., Liu B., (2014), Directed Self-assembly of Polypeptide-engineered Physical Microgels for Building Porous Cell-laden Hydrogels, *Chem. Commun.*, 50, 9405-9408 (DOI:10.1039/C4CC04018J).
235. Galler K. M., Aulisa L., Regan K. R., D'Souza R. N., Hartgerink J. D. (2010), Self-Assembling Multidomain Peptide Hydrogels: Designed Susceptibility to Enzymatic Cleavage Allows Enhanced Cell Migration and Spreading, *J. Am. Chem. Soc.*, 132, 3217-3223 (DOI: 10.1021/ja910481t).
236. Wan L., Chen Q., Liu J., Yang X., Huang J., Li L., Guo X., Zhang J., Wang K. (2016), Programmable Self-Assembly of DNA-Protein Hybrid Hydrogel for Enzyme Encapsulation with Enhanced Biological Stability, *Biomacromolecules*, 17, 1543-1550 (DOI: 10.1021/acs.biomac.6b00233).
237. Li P., Yin Z., Dou X. -Q., Zhou G., Feng C. -L. (2014), Convenient Three-Dimensional Cell Culture in Supermolecular Hydrogels, *ACS Appl. Mater. Interfaces*, 6, 7948-7952 (DOI: 10.1021/am501275t).

238. Ghosh K., Ingber D. E. (2007), Micromechanical Control of Cell and Tissue Development: Implications for Tissue Engineering, *Adv. Drug Delivery Rev.*, 59, 1306-1318 (DOI: 10.1016/j.addr.2007.08.014).
239. Adeloew C., Segura T. Hubbell J. A., Frey P. (2008), The Effect of Enzymatically Degradable Poly(Ethylene Glycol) Hydrogels on Smooth Muscle Cell Phenotype, *Biomaterials*, 29, 314-326 (DOI: 10.1016/j.biomaterials.2007.09.036).
240. Jaiswal N., Haynesworth S. E., Caplan A. I. Bruder S. P. (1997), Osteogenic Differentiation of Purified, Culture-Expanded Human Mesenchymal Stem Cells in Vitro, *J. Cell. Biochem.*, 64, 295-312 (DOI: 10.1002/(SICI)1097-4644(199702)64:2<295::AID-JCB12>3.0.CO;2-I).
241. Tibbitt M. W., Anseth K. S. (2009), Hydrogel as Extracellular Matrix Mimics for 3D Cell Culture, *Biotechnol. Bioeng.*, 103, 655-663 (DOI: 10.1002/bit.22361).
242. Lee K. Y., Mooney D. J. (2001), Hydrogels for Tissue Engineering, *Chem. Rev.*, 101, 1869-1879 (DOI: 10.1021/cr000108x).
243. Hoffman, A. S. (2002), Hydrogels for Biomedical Applications, *Adv. Drug Delivery Rev.*, 54, 3-12 (DOI: 10.1016/j.addr.2012.09.010).
244. Liu C., Xia Z., Czernuszka J. T. (2007), Design and Development of Three-Dimensional Scaffolds for Tissue Engineering, *Chem. Eng. Res. Des.*, 85, 1051-1064 (DOI: 10.1205/cherd06196).
245. Szkolar L., Guilbaud J. -B., Miller A. F., Gough J. E., Saiani A. (2014), Enzymatically Triggered Peptide Hydrogels for 3D Cell Encapsulation and Culture, *J. Pept. Sci.*, 20, 578-584 (DOI: 10.1002/psc.2666).
246. Biswas A., Malferrari S., Kalaskar D. M., Das A. K. (2018), Arylboronate Esters Mediated Self-healable and Biocompatible

- Dynamic G-quadruplex Hydrogels as Promising 3D-bioinks, *Chem. Commun.*, 54, 1778-1781 (DOI: 10.1039/c7cc09051j).
247. McConaughy S. D., Kirkland S. E., Treat N. J., Stroud P. A., McCormick C. L. (2008), Tailoring the Network Properties of Ca<sup>2+</sup> Crosslinked Aloe Vera Polysaccharide Hydrogels for in situ Release of Therapeutic Agents, *Biomacromolecules*, 9, 3277-3287 (DOI: 10.1021/bm8008457).
248. Huang R., Qi W., Feng L., Su R., He Z. (2011), Self-assembling Peptide-polysaccharide Hybrid Hydrogel as a Potential Carrier for Drug Delivery, *Soft Matter*, 7, 6222-6230 (DOI: 10.1039/C1SM05375B).
249. Xie Y., Zhao J., Huang R., Qi W., Wang Y., Su R., He Z. (2016), Calcium-Ion-Triggered Co-assembly of Peptide and Polysaccharide into a Hybrid Hydrogel for Drug Delivery, *Nanoscale Res. Lett.*, 11, 184 (DOI 10.1186/s11671-016-1415-8).
250. Lehn J. -M. (1995), *Supramolecular Chemistry: Concepts and Perspectives*, Wiley-VCH, Weinheim, (ISBN: 978-3-527-29311-7).
251. Ballester P., Vidal-Ferran A. (2008), Introduction to Supramolecular Catalysis, In: van Leeuwen P. W. N. M. (ed) *Supramolecular Catalysis*, 1<sup>st</sup> edn, Wiley-VCH, Weinheim, pp 1-27, (ISBN: 978-3-527-32191-9).
252. Wang Q., Yang Z., Wang L., Ma M., Xu B., (2007), Molecular hydrogel-immobilized enzymes exhibit superactivity and high stability in organic solvents, *Chem. Commun.*, 1032-1034 (DOI: 10.1039/B615223F).
253. Escuder B., Rodríguez-Llansola F., Miravet J. F. (2010), Supramolecular Gels as Active Media for Organic Reactions and Catalysis, *New J. Chem.*, 34, 1044-1054 (DOI: 10.1039/B9NJ00764D).

254. Singh N., Zhang K., Angulo-Pachon C. A., Mendes E., van Esch J. H., Escuder B. (2016), Tandem reactions in self-sorted catalytic molecular hydrogels, *Chem. Sci.*, 7, 5568-5572 (DOI: 10.1039/C6SC01268J).
255. Mazzier D., Carraro F., Crisma M., Rancan M., Toniolo C., Moretto A. (2016), A Terminally Protected Dipeptide: From Crystal Structure and Self-assembly, through Co-assembly with Carbon-based Materials, to a Ternary Catalyst for Reduction Chemistry in Water, *Soft Matter*, 12, 238-245 (DOI: 10.1039/C5SM02189H).
256. Guler O., Stupp S. I. (2007), A Self-Assembled Nanofiber Catalyst for Ester Hydrolysis, *J. Am. Chem. Soc.*, 129, 12082-12083 (DOI: 10.1021/ja075044n).



## **Chapter 2**

# **Blue Light Emitting Self-healable Graphene Quantum Dot Embedded Hydrogel**



## 2.1 Introduction

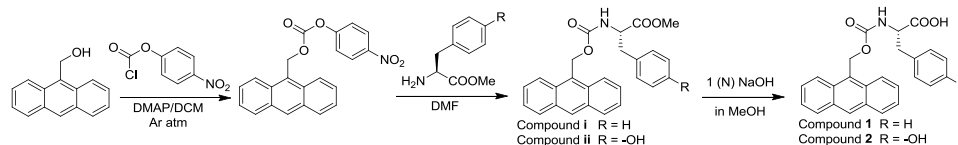
Two dimensional graphene and graphene functionalized derivatives have attracted great attention due to their unique chemical and physical properties such as optical,<sup>[1]</sup> electrochemiluminescent<sup>[2]</sup> and cytotoxic behavior.<sup>[3]</sup> In addition, zero dimensional graphene quantum dots (GQDs) have also attracted researchers over the past few years due to their unique properties such as quantum confinement<sup>[4]</sup> and edge effects.<sup>[5]</sup> As a consequence, GQDs have been used in diverse research fields including photoconductivity,<sup>[6]</sup> optoelectronics,<sup>[7]</sup> bio-imaging,<sup>[8]</sup> light emitting diodes,<sup>[9]</sup> pH sensors<sup>[10]</sup> and solar cell<sup>[11]</sup> applications. Graphene functionalized materials have been used in bioimaging<sup>[8]</sup> and the enhancement of electrical conductivity.<sup>[12]</sup> In nature, self-assembly is driven by hydrogen bonding,  $\pi$ - $\pi$  stacking, hydrophobic and charge-transfer interactions.<sup>[13]</sup> Graphene oxide (GO) embedded biomolecular hydrogels have important features including dye degradation capacity for wastewater treatment.<sup>[14a]</sup> A GO and poly-vinyl alcohol (PVA) composite produced a biocompatible hydrogel which was used for selective drug release application at physiological pH.<sup>[14b]</sup> A self-supported multifunctional hydrogel formed by GO-DNA composite via  $\pi$ - $\pi$  stacking interactions with nearly about 99 percent water content formed an excellent self-healing gel.<sup>[15]</sup> Peptides and amino acids are an interesting class of biomolecules, which can self-assemble to form hydrogels via non-covalent interactions.<sup>[16]</sup> Supramolecular hydrogels were used in drug delivery,<sup>[17]</sup> tissue engineering<sup>[18]</sup> and different fields in biotechnology.<sup>[19]</sup> Xu et al. reported peptide-hydrogel encapsulated hemin as an artificial enzyme to mimic peroxidase.<sup>[20]</sup> Peptide and GO based hybrid hydrogel containing goldnanoparticles was used as efficient catalyst to reduce aromatic nitro to aromatic amino groups.<sup>[21]</sup> Recently, Wang et al. reported that self-assembled oligomers and carbon dots formed fluorescent ultra-long nanoribbons with electrical conductivity.<sup>[22]</sup> Currently, self-

healable materials are envisioned to serve as active materials in drug delivery<sup>[23]</sup> and tissue engineering<sup>[24]</sup> applications. In literature, there are limited reports on amino acid/peptide-based thixotropic hydrogels.<sup>[25]</sup> Self-healing materials can restore its original form by healing the damage caused on it<sup>[26]</sup> and the healing process is driven by thermodynamic parameters<sup>[27a-c]</sup> and also depends on dynamic covalent bond<sup>[27d-f]</sup> and non-covalent<sup>[28]</sup> interactions. Earlier reports give an account on peptide based self-healable multi-stimuli responsive metallo-hydrogel<sup>[29]</sup> and automatic healing by polymer composite.<sup>[30]</sup> Thixotropic and self-healing properties were also achieved from low-molecular-weight hydrogelators.<sup>[31]</sup> Small bioactive molecules in presence of carbon based nanomaterials such as reduced graphene oxide (RGO)<sup>[32,33]</sup> and single-walled carbon nanotubes (SWCNTs)<sup>[34-38]</sup> were used to make hydrogels. It is also reported that SWCNTs weaken the thixotropic property of polysaccharide gels.<sup>[39]</sup> Apart from that GQDs have completely different properties from other carbon based materials.<sup>[40]</sup> Free amino acids are also used to prepare self-healing gels with GO and RGO.<sup>[41]</sup> However, little attention has been paid on the properties of GQDs in presence of small aromatic functionalized molecules.<sup>[22]</sup> To the best of our knowledge, there is no report on the effect of GQDs on gelation and influence on mechanical property of gels composed with N-capped amino acids. N-Protecting groups of amino acids and peptides have the ability to tune the mechanical and physical properties of supramolecular hydrogels.<sup>[42a]</sup> Single amino acid based hydrogels are limited in literature. Fmoc (9-fluorenylmethoxycarbonyl) protected amino acids and peptides were used for different biological application.<sup>[42b]</sup> In this chapter, our objective is to study the interaction between small aromatic functionalized biomolecules and GQDs. Herein; we demonstrate very simple N-terminal protected (Amoc: 9 anthracenemethyloxycarbonyl) amino acids (Amoc-F-OH and Amoc-Y-OH, F: L-phenylalanine; Y: L-tyrosine and -OH represents free acid group) which form self-healable hydrogels upon addition of GQDs at

physiological pH 7.4. To study the interaction of small organic molecules with GQDs using spectroscopic techniques, anthracene moiety is used as good fluorophore. Aromatic amino acids help to exhibit better gelation behaviour due to aromatic  $\pi$ - $\pi$  stacking and hydrophobic interactions.<sup>[42c]</sup> Both aromatic amino acids phenylalanine and tyrosine have structural similarity and main difference is the presence of phenolic -OH group in *p*-position of tyrosine instead of having -H group in case of phenylalanine. Moreover, it is important to study the effect of phenolic -OH on the mechanical property of gels in presence of GQDs. Though there are several reports on self-healing gels embedded with graphene, GO<sup>[32,43]</sup> and also with RGO but hydrogels of biomolecules embedded with GQDs are not studied extensively.<sup>[44,45]</sup> GQDs exhibit solely different properties compare to other graphene based materials.<sup>[40]</sup> So, it is important to study the behavior of the embedded GQDs with biomolecules such as N-protected amino acids. The functionalized GQDs embedded hydrogels are found to exhibit blue light emission, which are analyzed by UV-Vis, fluorescence and electrochemical measurements. The morphological changes and self-healing properties of Amoc amino acids with inclusion of GQDs are also thoroughly assessed.

## 2.2 Experimental

**Scheme 2.1.** Synthetic pathway of Amoc-capped amino acid based amphiphiles



### 2.2.2 Synthesis of Amoc-F-OH (1)

a) Synthesis of compound (i): A stirred solution of *p*-nitrochloroformate (1.259 g, 6.25 mmol) in DCM was cooled in ice bath under argon atmosphere. Dimethylaminopyridine (DMAP) (0.65 g, 5.28



yellow mass was obtained after evaporating the solvent under reduced pressure. Without purification, a solution of Amoc-Phe-OMe (ii) in 5 mL distilled dry methanol was allowed to react with a solution of 5 mL 1 (N) NaOH solution. The reaction progress was monitored by thin layer chromatography. The reaction mixture was stirred upto 4 h. After the completion of the reaction, excess methanol was evaporated to dryness and diluted with 100 mL water. Then the water mixture was taken in a separating funnel and vigorously washed with diethyl ether. The aqueous layer was collected and cooled in an ice bath. Then, the cooled collected water layer was acidified with 1 (N) KHSO<sub>4</sub>. The pH of aqueous layer was adjusted to 2 and the product was extracted with ethyl acetate (3×30 mL). The ethyl acetate layer was dried over anhydrous sodium sulphate and evaporated under reduced pressure to obtain orange-yellow solid compound Amoc-Phe-OH (1).

Yield 1.47 g (3.68 mmol, 92%); FT-IR (KBr):  $\bar{\nu}$  = 3312 (br), 3029 (br), 1688 (s), 1599 (s), 1510 (s), 1441 (s), 1258 (s); <sup>1</sup>H NMR (400 MHz, DMSO-d<sub>6</sub>):  $\delta$  8.60 (s, 1H, Hs of Anth), 8.27-8.24 (d, 2H, *J* = 8.52 Hz, Ar-Hs), 8.06-8.04 (d, 2H, *J* = 8.28 Hz, Ar-Hs), 7.54-7.46 (m, 5H, Ar-Hs), 7.17 (s, 4H, Ar-Hs), 5.99-5.88 (m, 2H, CH<sub>2</sub> of Amoc), 4.17-4.12 (m, 1H, C <sup>$\alpha$</sup> H of Phe), 2.99-2.95 (m, 1H, C <sup>$\beta$</sup> H of Phe), 2.75-2.69 (m, 1H, C <sup>$\beta$</sup> H of Phe) ppm (Figure 2.2). <sup>13</sup>C NMR (100 MHz, DMSO-d<sub>6</sub>):  $\delta$  173.33, 156.20, 137.87, 130.86, 130.41, 129, 128.10, 126.59, 125.22, 124.14, 58.04, 55.60, 36.33 ppm (Figure 2.3). MS (ESI) *m/z* for C<sub>25</sub>H<sub>21</sub>NO<sub>4</sub> (M + H)<sup>+</sup> calcd: 422.1363, found: 422.1385 (Figure 2.4).

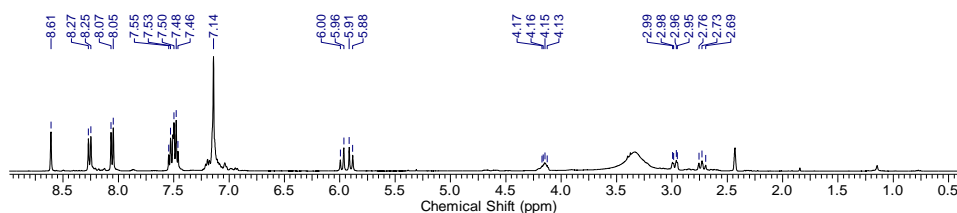


**Figure 2.2.** <sup>1</sup>H NMR spectrum of Amoc-Phe-OH (1) in DMSO-d<sub>6</sub>.

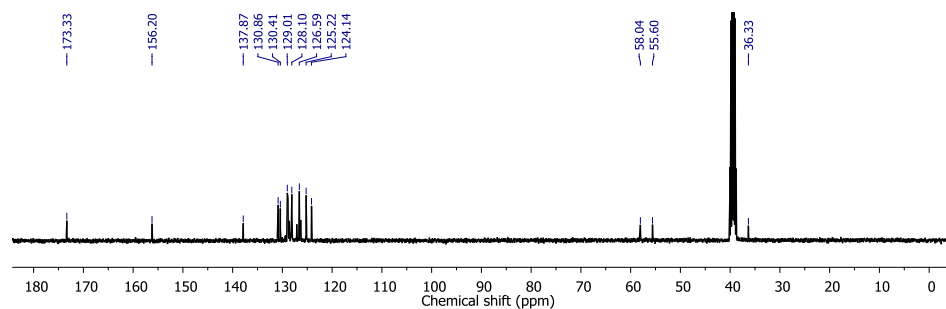


Figure 2.3.  $^{13}\text{C}$  NMR spectrum of Amoc-Phe-OH (1) in  $\text{DMSO-}d_6$ .

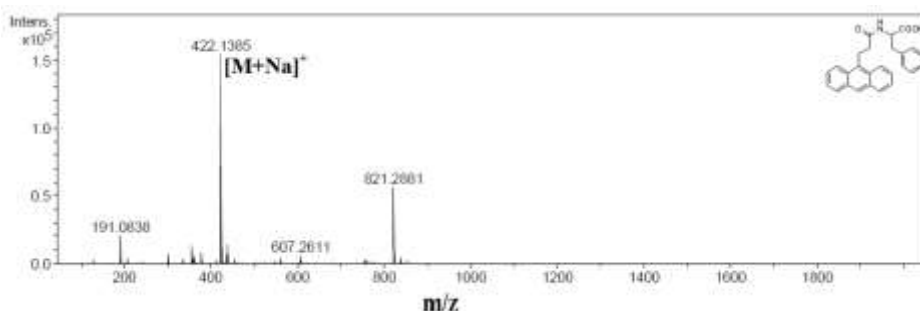


Figure 2.4. ESI-MS spectrum of Amoc-F-OH (1).

### 2.2.3 Preparation of Amoc-Tyr-OH (2)

1.5 g (4.02 mmol) of anthracen-9-ylmethyl (4-nitrophenyl) carbonate (**i**) was dissolved in 3 mL DMF in a 100 mL round bottom flask and cooled it in an ice bath. A neutralized solution of tyrosine methyl ester was extracted from its corresponding hydrochloride salt (1.73 g, 8.04 mmol) and concentrated to add to the reaction mixture. The progress of the reaction was monitored by thin layer chromatography (TLC). The reaction mixture was allowed to stir for 8 h. The reaction mixture was diluted with ethyl acetate and washed with 1 (N) HCl (3×50 mL), saturated  $\text{Na}_2\text{CO}_3$  solution (3×50 mL) and then with brine. Solid yellow mass was obtained after evaporating the solvent under reduced pressure. Without purification, a solution of Amoc-Tyr-OMe (**iii**) in 5 mL distilled dry methanol was allowed to react with a solution of 5 mL 1 (N) NaOH solution. The reaction progress was monitored by thin layer chromatography. The reaction mixture was stirred upto 4 h. After the completion of the reaction,

excess methanol was evaporated to dryness and diluted with 100 mL water. Then the water mixture was taken in a separating funnel and vigorously washed with diethyl ether. The aqueous layer was collected and cooled in an ice bath. Then, the cooled collected water layer was acidified with 1 (N)  $\text{KHSO}_4$ . The pH of aqueous layer was adjusted to 2 and the product was extracted with ethyl acetate (3×30 mL). The ethyl acetate layer was dried over anhydrous sodium sulfate and evaporated under reduced pressure to obtain orange-yellow solid compound Amoc-Tyr-OH **2**.

37 Yield = 0.97 g, (2.34 mmol, 91%), FT-IR (KBr):  $\bar{\nu}$  = 3416 (br), 3198 (br), 1592 (s), 1605 (s), 1510 (s), 1454 (s), 1333 (s);  $^1\text{H}$  NMR (400 MHz,  $\text{DMSO-d}_6$ ):  $\delta$  9.08 (s, 1H), 8.53 (s, 1H, Hs of Anth), 8.19-8.17 (d, 2H,  $J$  = 8.76 Hz, Ar-Hs), 7.99-7.97 (d, 2H,  $J$  = 8.04 Hz, Ar-Hs), 7.47-7.38 (m, 4H, Ar-Hs), 7.31-7.29 (d, 1H,  $J$  = 8.04 Hz, Ar-H), 6.86-6.83 (d, 2H,  $J$  = 8.28 Hz, Ar-Hs), 6.48-6.46 (d, 2H,  $J$  = 8.04 Hz, Ar-Hs), 5.92-5.80 (m, 2H,  $\text{CH}_2$  of Amoc), 4.01-3.95 (m, 1H,  $\text{C}^\alpha\text{H}$  of Tyr), 2.79-2.74 (m, 1H,  $\text{C}^\beta\text{H}$  of Tyr), 2.56-2.50 (m, 1H,  $\text{C}^\beta\text{H}$  of Tyr) ppm (Figure 2.5).  $^{13}\text{C}$  NMR (100 MHz,  $\text{DMSO-d}_6$ ):  $\delta$  173.4, 156.18, 155.79, 130.86, 130.42, 129.93, 128.86, 126.59, 125.22, 124.12, 114.9, 58.06, 55.94, 35.64 ppm (Figure 2.6). MS (ESI)  $m/z$  for  $\text{C}_{25}\text{H}_{21}\text{NO}_5$  ( $\text{M} + \text{H}$ ) $^+$  calcd: 438.1312, found: 438.1333 (Figure 2.7).

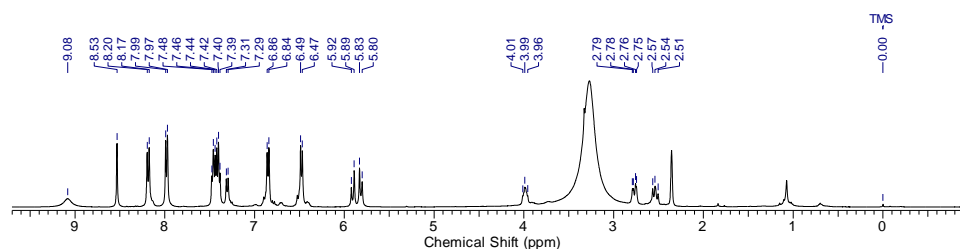


Figure 2.5.  $^1\text{H}$  NMR spectrum of Amoc-Tyr-OH (**2**) in  $\text{DMSO-d}_6$ .

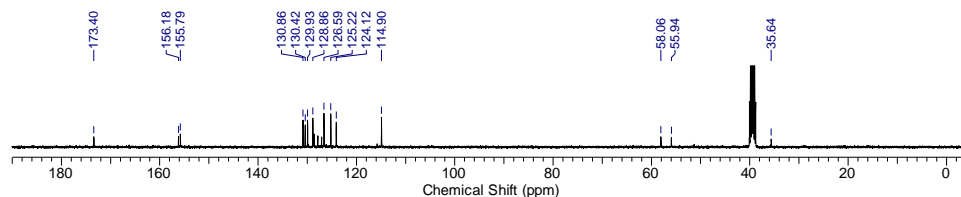


Figure 2.6.  $^{13}\text{C}$  NMR spectrum of Amoc-Tyr-OH (2) in  $\text{DMSO-}d_6$ .

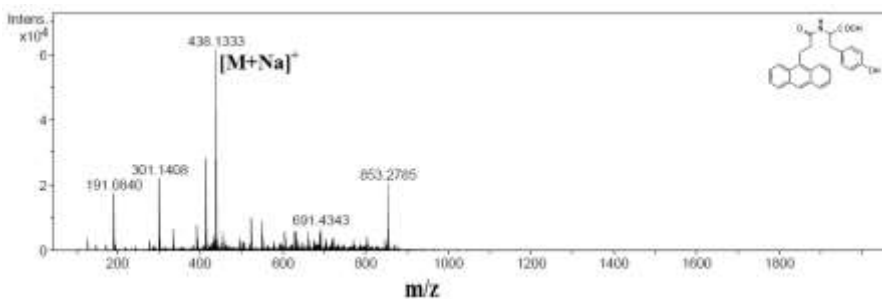


Figure 2.7. ESI-MS spectrum of Amoc-Y-OH (2).

### 2.2.4 Synthesis of graphene quantum dots<sup>[39]</sup>

Commercially available GO (800 mg) was heated in a furnace at 200 °C for two hours to afford graphene sheet and the resultant graphene sheets were mixed with concentrated 40 mL of (3 : 1)  $\text{HNO}_3$  :  $\text{H}_2\text{SO}_4$  mixture. The mixture was heated at 90 °C for 3 h and it was diluted with 250 mL distilled water. Then the mixture was filtered through 0.22 mm microporous syringe filter to remove the acids. Then, the purified (300 mg) oxidized graphene sheets (GSs) were dissolved in 50 mL of millipore water and the pH was adjusted to 8 with NaOH. The mixture was taken in a reaction bomb vessel. Then the reaction bomb vessel was kept into a hot air oven for 12 hours of constant heating at 200 °C. Finally, the solution was dialyzed for 24 hours with a dialysis tube of 3500 K Dalton to remove ions and impurity from solution. The formation of GQDs was confirmed by SEM and TEM images (Figure 2.9).

## 2.3 Gel Preparation and Characterization Techniques

### 2.3.1 Preparation of hydrogels

**2.3.1.1 Preparation of Gel-F and Gel-Y**

5.99 mg (15 mM) of Amoc-F-OH was dissolved in 1 mL of water by drop-wise addition of 0.5 M NaOH. The pH was increased up to 9 for complete dissolution. The elevated pH was then dropped to 7.4 by dropwise addition of 0.1 M HCl solution. The solution was kept rest for 30 min and it was then formed hydrogel (Gel-F). Gel-Y was also prepared as Gel-F was prepared.

**2.3.1.2 Preparation of GQD-F and GQD-Y**

3.99 mg (10 mM) of Amoc-F-OH and 0.5 mg mL<sup>-1</sup> GQDs were dissolved in 1 mL of water by drop-wise addition of 0.5 M NaOH. The pH was increased up to 9 for complete dissolution. Finally the pH was dropped to 7.4 by dropwise addition of 0.1 M HCl solution. The resultant solution was kept rest for 5 min and it was then formed GQD-F (hydrogel 1). GQD-Y (Hydrogel 2) was also prepared by the same procedure.

**2.3.2 Morphological study**

Transmission electron microscopic images were taken using a JEOL electron microscope (model: JEM-2100), operated at an accelerating voltage of 200 kV and Field Emission Gun-Transmission Electron Microscope (model: Tecnai G2, F30), operated on a voltage of 300 kV. 100 mL of gel was dissolved in 200 mL of water and the dilute solution of the hydrogels was dried on carbon-coated copper grids (300 mesh) by slow evaporation in air and then allowed to dry separately in a vacuum at room temperature. GQDs solution in DI water also dried on carbon-coated copper grids. Field emission scanning electron microscope (FE-SEM Supra 55 Zeiss) instrument was used for SEM study. Gels were dried on cover slip and coated with gold for SEM analysis with an operating voltage of 5 kV.

### 2.3.3 UV-Vis spectroscopy

UV-Vis absorption spectra of the hydrogels Gel-F, Gel-Y, GQD-F and GQD-Y were recorded using a Varian Cary100 Bio UV-Vis spectrophotometer at a concentration of 5 mM. UV-Vis absorption spectra of GQD were recorded at a concentration of 0.25 g L<sup>-1</sup>.

### 2.3.4 Fluorescence spectroscopy

Fluorescence spectra of hydrogels (10 mM) were recorded at different excitation wavelength of 390 nm and 380 nm with medium sensitivity on a Horiba Scientific Fluoromax-4 spectrophotometer. The slit width for the excitation and emission was set at 2 nm and a 1 nm data pitch. Samples were prepared in 1 cm<sup>2</sup> quartz cuvette at room temperature.

### 2.3.5 Rheological study

Rheological study was performed to determine the mechanical properties of the hydrogels. These properties were assessed using an Anton Paar Physica Rheometer (MCR 301, Austria) with parallel plate geometry (25 mm in diameter) and temperature was controlled at 25 °C. The dynamic moduli of the hydrogel were measured as a function of frequency in the range of 0.1–100 rad s<sup>-1</sup> with a constant strain value 0.1% and step strain experiment was done at the constant frequency of 10 rad s<sup>-1</sup> and applied strain was changed from 0.1% to 20%. 200 μL of gel was prepared in glass vial and transferred it over the plate using micro-spatula to proceed for rheological measurements.

## 2.4 Results and Discussion

In this chapter, N-terminal protected amino acid based amphiphiles Amoc-F-OH, Amoc-Y-OH (Amoc: 9-anthracenemethyloxycarbonyl) were synthesized by the reported procedure.<sup>[46]</sup> GQDs were synthesized by the simple hydrothermal process from commercially available GO and GQDs were purified by dialysis prior to gelation.<sup>[47]</sup> We prepared hydrogels with

the compounds Amoc-F-OH (Gel-F), Amoc-Y-OH (Gel-Y) with 15 mM of each amphiphilic molecules. GQDs were added into the Amoc-F-OH (GQD-F) and Amoc-Y-OH (GQD-Y). Therefore, the concentration of GQDs (Table 3.1) was optimized for Amoc-F-OH and Amoc-Y-OH using fluorescence spectroscopic technique.

**Table 2.1** Preparation of hydrogels with different conc. of gelators and amount of GQDs

Gelator	Conc. of gelator (mM)	Amount of GQDs (mg mL <sup>-1</sup> )	Property of Gel
Amoc-F-OH	15	0	Gel
	10	0	Sol
	10	0.2	Gel
	10	0.5	Self-healing gel
	7.5	0.2	Gel
	7.5	0.5	Gel
Amoc-Y-OH	15	0	Gel
	10	0	Sol
	10	0.2	Gel
	10	0.5	Self-healing gel
	7.5	0.2	Gel
	7.5	0.5	Gel

Different concentration of Amoc-F-OH/Amoc-Y-OH and GQDs were used to prepare hydrogels (Table 2.1). However, self-healable hydrogels were formed (Figure 2.8) upon mixing of 10 mM Amoc-Y-OH/Amoc-Y-OH and 0.5 mg mL<sup>-1</sup> GQDs (Table 2.1).

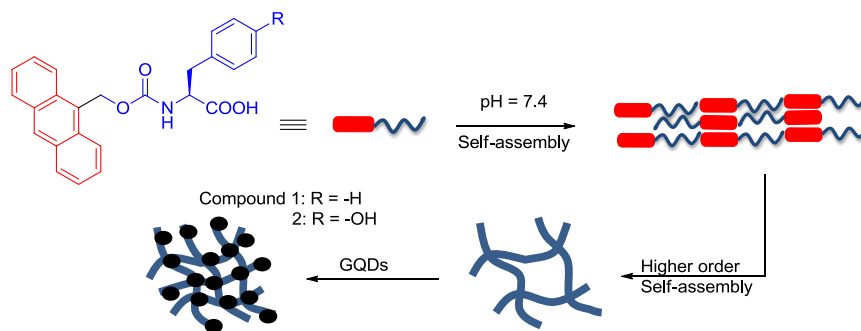


**Figure 3.8.** Schematic representation of gel nanofibers and GQDs embedded gel nanofibers through non-specific molecular co-assembly.

These amphiphilic molecules formed gels using hydrophobic-hydrophilic and other non-covalent interactions at physiological pH.<sup>[48]</sup> Hence, gels were prepared at physiological condition (pH = 7.4) and gelation was initially confirmed by test tube inversion method. For the preparation of self-healable hydrogel GQD-F, 0.449 wt% of Amoc-F-OH and GQDs was used. 0.466 wt% Amoc-Y-OH and GQDs was used for the preparation of hydrogel GQD-Y. Both the cases water content was more than 99.5%. At higher pH (>7.5), the gelator compounds start to dissolve in the water medium and give clear solution of gelator molecules at pH > 8. But at lower pH (pH < 6), the gelator molecules get precipitate from the solution.

### 2.4.1 Microscopic Study

Transmission electron microscopy (TEM) and scanning electron microscopy (SEM) images (Figure 2.9) reveal the size of 7-8 nm of GQDs according to size distribution graph, which was acquired from TEM image (Fig. 2.8). SEM images of Gel-F and Gel-Y exhibit fibrillar networks (Figure 2.9). The SEM images (Figure 2.10) of GQD-F and GQD-Y are consistent with the TEM images (Figure 2.11) of GQD-F and GQD-Y. Both the cases (GQD-F and GQD-Y), GQDs are decorated on the fibers and the average width of the nanofibrillar network is around 20 nm (Figure 2.11 and Figure 2.12).

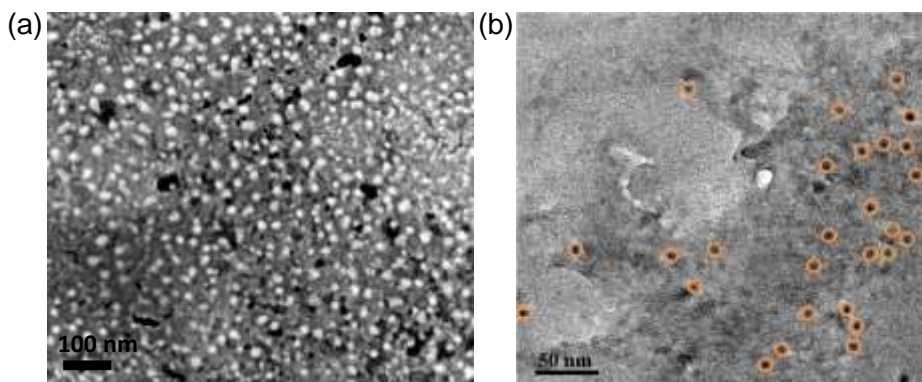


**Figure 2.9.** (a) SEM and (b) TEM images of GQDs show dots are separated and well distributed.

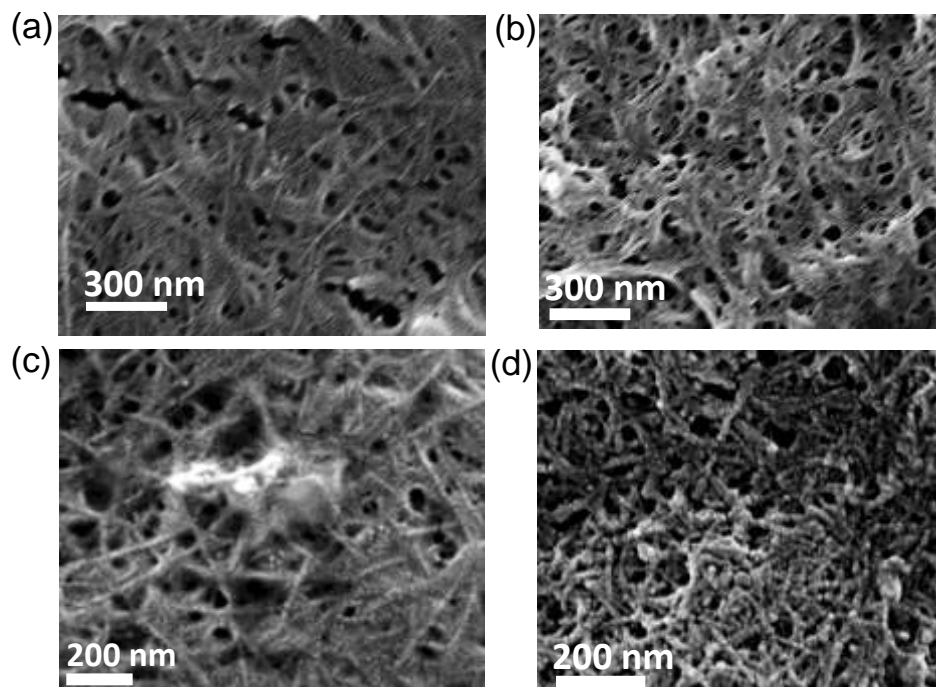


**Figure 2.10.** SEM image of Gel-F (a) shows nanofibrillar network. (b) SEM image of Gel-Y shows nanofibrillar network. (c) describes the GQDs decorated morphology by the SEM image of GQD-F (10 mM of Amoc-F-OH with 0.5 mg mL<sup>-1</sup> GQDs) and (d) SEM image shows GQDs deposited fiber of GQD-Y (10 mM of Amoc-Y-OH with 0.5 mg mL<sup>-1</sup> GQDs).

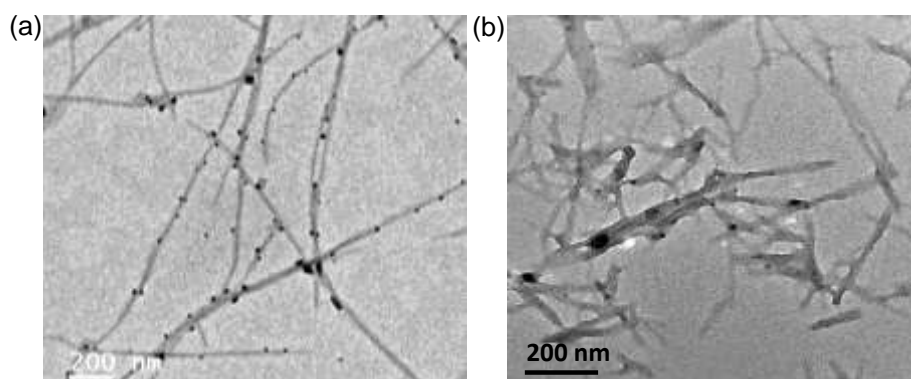


**Figure 2.11.** TEM images of (a) GQD-F (10 mM of Amoc-F-OH with 0.5 mg L<sup>-1</sup> GQDs) and (b) GQD-Y (10 mM of Amoc-Y-OH with 0.5 mg L<sup>-1</sup> GQDs) show GQDs decorated nanofibrillar structures. Both images depict uniform distribution of GQDs on the fibrillar networks.

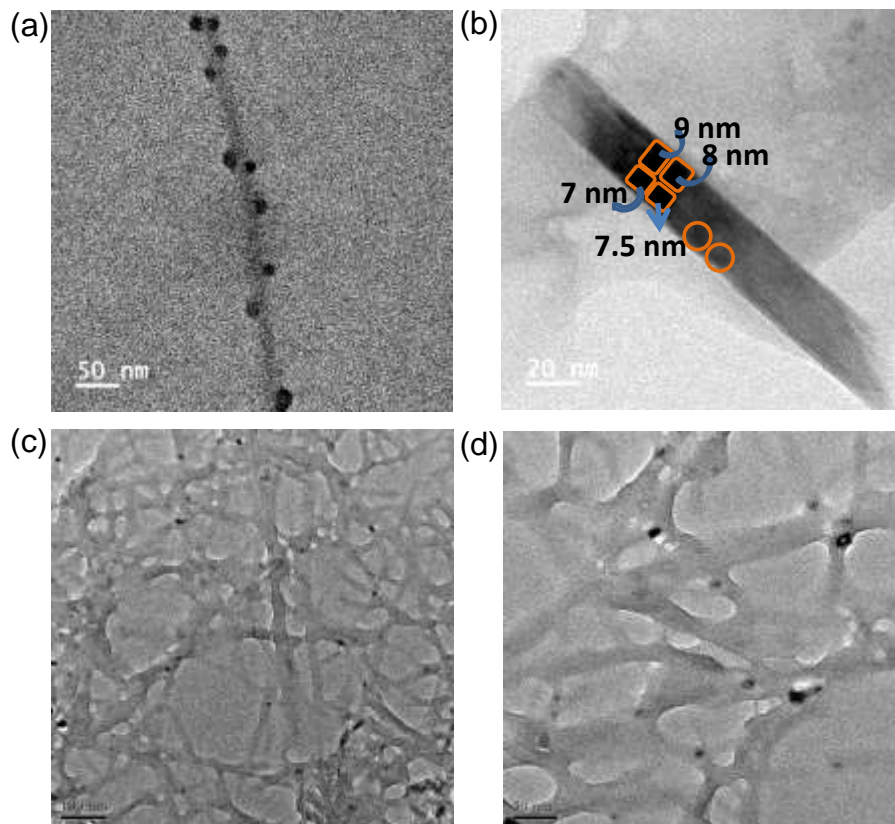


**Figure 2.12.** TEM image of GQD-F (10 mM of Amoc-F-OH with  $0.5 \text{ mg mL}^{-1}$  GQDs) depicts graphene quantum dots are embedded on fibril (a) And at higher magnification it was shown the size of the decorated GQDs are mostly 7-9 nm. (c), (d) TEM images of GQD-Y (10 mM of Amoc-Y-OH with  $0.5 \text{ mg mL}^{-1}$  GQDs) shows random distribution of GQDs on the fibril.

GQD-Y shows straight nanofibrillar network where as GQD-F exhibits nanofibrillar ribbon with sheet type network observed from SEM image (Figure 2.10 c). The morphological difference is attributed to the structural change of gelators. Different concentration of GQDs was used to observe the change in GQDs decorated nanofibrils. TEM images of GQD-F and GQD-Y (Amoc-F-OH/Amoc-Y-OH h 10 mM with  $0.3 \text{ mg L}^{-1}$  GQDs) exhibit nanofibrils decorated with a very less amount of GQDs (Figure 2.13). TEM images of GQD-F and GQD-Y (Amoc-F-OH/Amoc-Y-OH h 10 mM with  $0.7 \text{ mg L}^{-1}$  GQDs) reveal nanofibrils decorated with GQDs (Figure 2.13) which look similar to the distribution of GQDs on nanofibrils (Figure 2.11).

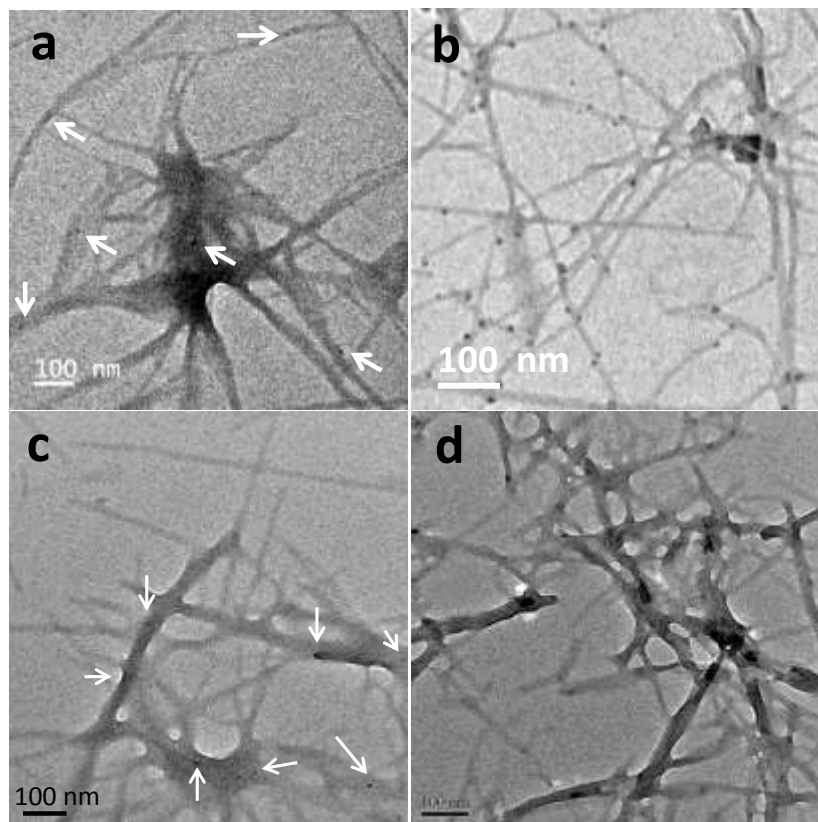


**Figure 2.13.** (a) and (b) represent the TEM images at different concentration of GQDs in GQD-F ( $10 \text{ mmol L}^{-1}$  of Amoc-F-OH). (a) corresponds to  $0.3 \text{ mg mL}^{-1}$  of GQDs which shows less amount of GQDs are deposited on the fibril whereas (b) shows more number of GQDs are deposited on the fiber with  $0.7 \text{ mg mL}^{-1}$  of GQDs. (c) and (d) shows the TEM images for GQD-Y with  $0.3 \text{ mg mL}^{-1}$  and  $0.7 \text{ mg mL}^{-1}$  of GQDs respectively. (c) and (d) also showed similar observation as like (a) and (b).

### 2.4.2 Photophysical Study

UV-Vis absorption spectra of GQDs depict  $\pi-\pi^*$  transition at 206 nm for C=C bond and also  $n-\pi^*$  transition at 260 nm due to the functionalized C=O group (Figure 2.14).<sup>[49]</sup> An absorption band at 251 nm is attributed to the presence of phenylalanine moiety. A broad peak in the region of 380–410 nm was observed for both Gel-F and GQD-F. Absorption spectra of both Gel-Y and GQD-Y show absorption band at 254 nm and similar red shift was observed from 380 nm to 385 nm due to the  $\pi-\pi$  stacking

interaction of Amoc group and GQDs (Figure 2.14). Fluorescence spectra were acquired to know about more insight of GQDs and GQDs embedded Amoc-amino acid based hydrogels (Figure 2.14).<sup>[50]</sup>

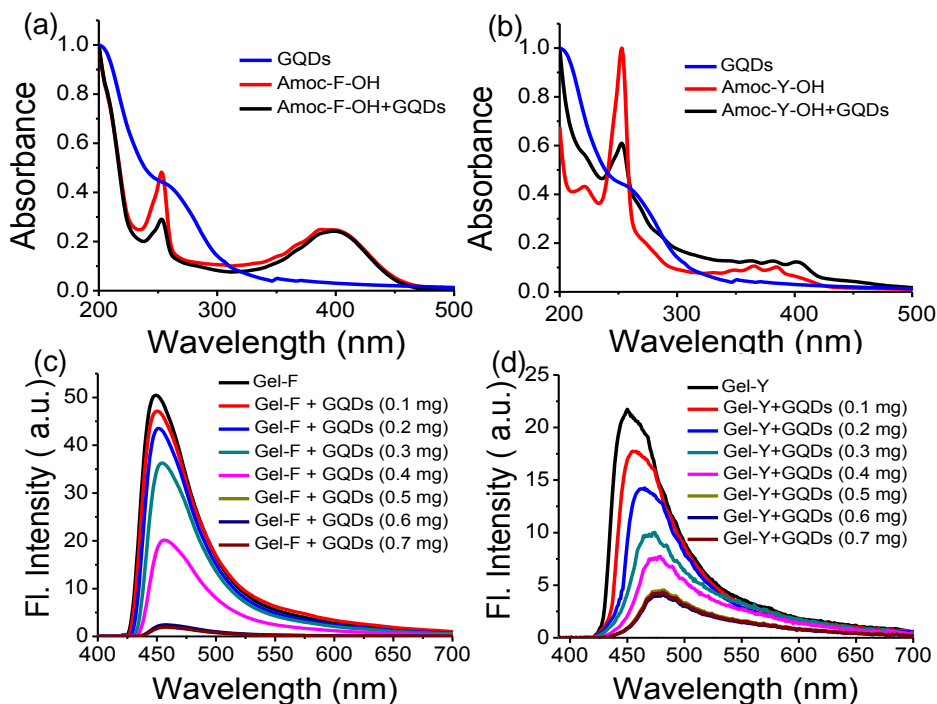


**Figure 2.14.** (a) and (b) show UV-Vis spectra of GQDs, Gel-F, Gel-Y, GQD-F and GQD-Y. Red shift in UV-Vis was observed for both the gels. Fluorescence spectra of (c) Amoc-F-OH (10 mM), GQD-F and (d) Amoc-Y-OH (10 mM), GQD-Y show successive quenching on increasing addition of GQDs.

After the inclusion of GQDs into Amoc-amino acids based hydrogels (GQD-F and GQD-Y), we acquired photoluminescence spectra of Amoc-F-OH and GQD-F at an excitation wavelength of 390 nm and Amoc-Y-OH and GQD-Y at an excitation wavelength of 380 nm (Figure 2.14). Both the gels (GQD-F and GQD-Y) imparted successive fluorescence quenching as compare to the Amoc-F/Y-OH without GQDs. The fluorescence quenching (Figure 2.14) indicates strong  $\pi$ - $\pi$  stacking interactions between aromatic anthracene moieties and GQDs.<sup>[51,52]</sup> Before the inclusion of GQDs, intense emission peak appeared at 450 nm for both Amoc-F-OH and Amoc-Y-OH. With increasing addition of GQDs into

Amoc amino acids, successive fluorescence quenching was observed with red shift. Concentration dependent emission spectra of 10 mM of gelators (Amoc-F-OH/Amoc-Y-OH) were recorded with the varied concentration of GQDs (0 to 0.7 mg L<sup>-1</sup>). The emission intensity gradually decreases with the increase concentration of GQDs up to 0.5 mg mL<sup>-1</sup> for both the gels GQD-F and GQD-Y. However, there is no significant change in emission wavelength and intensity after varying the concentration of GQDs from 0.5 mg L<sup>-1</sup> to 0.7 mg L<sup>-1</sup>. This result signifies that, particular concentration of GQDs (0.5 mg L<sup>-1</sup>) is required for a particular concentration of gelators (10 mM) to achieve maximum interaction with GQDs and the formation of self-healing gel. GQD-F shows quenched emission maxima at 464 nm where as GQD-Y exhibits emission maxima at 480 nm after fluorescence quenching. The red shift signifies stabilization of GQDs on the fibers by non-covalent interaction including  $\pi$ - $\pi$  stacking interaction. The shift is different for two different gels which is attributed to the change in the structural unit of the gelator molecules. The phenolic -OH group of Amoc-Y-OH has affinity over the functionalized GQDs which helps edge-localized  $\pi$ - $\pi$  stacking interaction between Amoc-Y-OH and GQDs. This interaction promotes the composite to shift more towards higher wavelength.<sup>[53]</sup> GQDs exhibit semiconducting property<sup>[54]</sup> and the study of electrochemical property after inclusion of GQDs into gelator molecules is important.

### **2.4.3 Rheological Study**

Rheological experiment reveals more insight about the mechanical and thixotropic properties of hydrogels. Rheological experiments were performed with self-healable hydrogels GQD-F (10 mM of Amoc-F-OH with 0.5 mg L<sup>-1</sup> GQDs) and GQD-Y (10 mM of Amoc-Y-OH with 0.5 mg L<sup>-1</sup> GQDs). In the oscillatory frequency sweep measurements, all the samples show higher storage modulus (G') value with compare to loss modulus (G'') over the entire process (Figure 2.15 and 2.16). Higher

storage modulus compare to loss modulus supports the formation of rigid gels.<sup>[55]</sup> After inclusion of GQDs into hydrogel Gel-F, the hydrogel GQD-F becomes stronger than Gel-F. Similarly GQD-Y becomes stronger than hydrogel Gel-Y. A step strain experiment was performed at constant angular frequency of  $10 \text{ rad s}^{-1}$  to quantify the thixotropic properties of hydrogels (Figure 2.15 and 2.16).

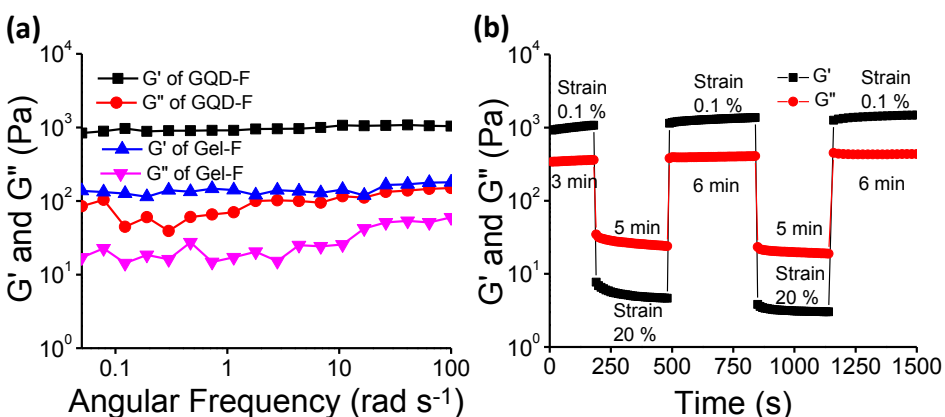


**Figure 2.15.** Dynamic frequency sweep experiment: (a) GQD-F becomes 6 times more rigid than Gel-F due to interaction of GQDs. (b) Step strain experiment signifies thixotropic nature and excellent gel recovery of GQD-F.

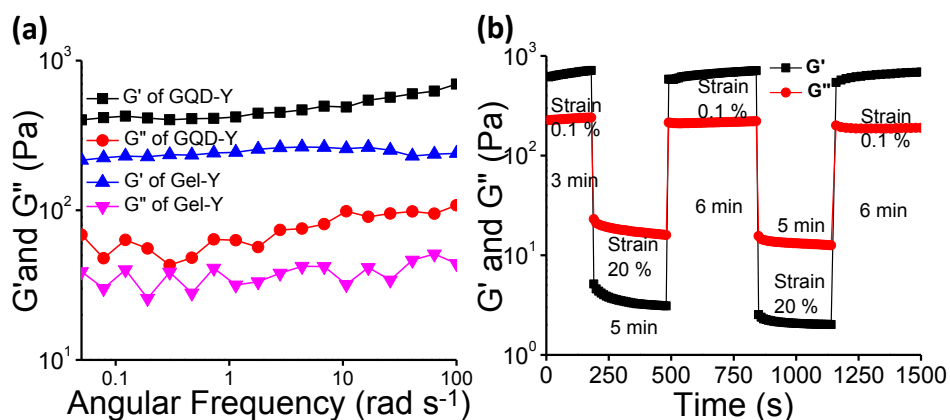


**Figure 2.16.** GQD-Y becomes two times rigid than Gel-Y after inclusion of GQDs represented in dynamic frequency sweep experiment. (b) Step strain experiment describes thixotropic nature and self-healing property of the gel GQD-Y.

A constant strain of 0.1% was applied (step 1) to hydrogels GQD-F and GQD-Y. The fibrillar 3D network completely ruptured when the strain is slowly increased from 0.1% to 20% (step 2) and it took 5 minutes to deliver gel to sol transition ( $G' < G''$ ). Sol to gel transition ( $G' > G''$ ) was observed by applying low strain to 0.1% (step 3) upto 6 min. The storage modulus ( $G'$ ) of GQD-F restored to its present position after 6 min (Figure 2.15) due to reformation of fibrillar 3D networks.<sup>[56]</sup> But the storage modulus of GQD-Y was 710 Pa before applying the strain. GQD-Y recovered upto 98% after removing the strain (step 3). After applying 20% strain (step 4), both the gels attain gel-to-sol property ( $G' < G''$ ). Finally after reduction of strain from 20% to 0.1%, the storage modulus ( $G'$ ) was restored to its present position for GQD-F. However, the storage modulus ( $G'$ ) was restored upto 84% for GQD-Y. Hydrophobicity (expressed as the partition coefficient between water and octanol,  $\log P$ ) of Amoc-F-OH ( $\log P = 5.22$ ) and Amoc-Y-OH ( $\log P = 4.74$ ) is different due to structural difference. Hydrophobicity of the gelator can also tune the mechanical property of the gel<sup>[57]</sup> as a result of this the gel recovery property becomes different for GQD-F and GQD-Y.

#### 2.4.4 Self-healing Property

Due to enhanced non-covalent interaction between gelators and GQDs including  $\pi$ - $\pi$  stacking interaction, the resultant gels become more thixotropic which provide better self-healing property. Though both the above results give an account for the thixotropic nature of the GQDs embedded hydrogel. Autonomous healing upon damage on material is recognized as self-healing property.<sup>[58,59]</sup> This fascinating property was observed during the experiments with the composite of Amocamino acids and GQDs (Figure 2.17). To quantify the self-healing properties of hydrogels, we cut the gel GQD-F with knife into two pieces (Figure 2.17f) and shoved to keep contact with each other for a minute (Figure 2.17g). These two pieces stuck together into a strong self-healable gel which was

capable to make a bridge with two vial caps (Figure 2.17g). Later, we cut the self-healable gel into four small pieces and adhered together to make a self-healable gel (Figure 2.17i). Supramolecular interaction such as  $\pi$ - $\pi$  stacking, hydrophobic and hydrogen bonding interaction<sup>[59]</sup> (Figure 2.8) are responsible for the dynamic property of the formed cross-linking fibrillar networks in gels.

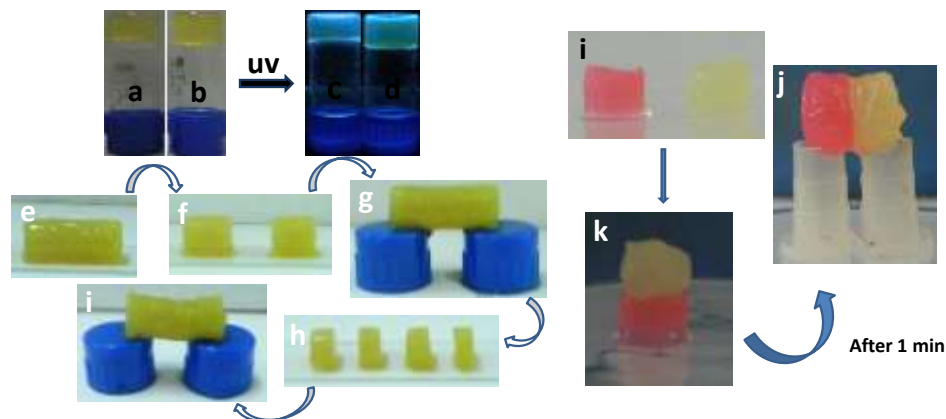


**Figure 2.17.** (a) and (b) are the optical images of GQD-F, GQD-Y respectively under day light. (c) and (d) are the images under UV light irradiation at a wavelength of 365 nm of hydrogels GQD-F and GQD-Y respectively. Optical images (e) to (i) represent the self-healing property of GQD-F. Hydrogel pieces adhere together after keep in contact with each other and regenerate previous shape by crosslinking network by noncovalent interaction. (i), (j) and (k) represent the self-healing property of the gel GQD-Y.

Self-healing property of small amphiphilic molecules is driven by the thermodynamic parameter i.e. entropy. Entropy increases due to the incremental interfacial area with cracking the material by applying the external mechanical forces. With the deformation of the gel composed by small molecules, the number of arrangement increases with increasing entropy in that particular state.<sup>[27a-c]</sup> Increased entropy drives the gelator molecules to come closer to the damaged space by extending the crosslinked 3D network which leads to the formation of the previous shape.

## 2.5 Conclusions

We have demonstrated self-healable GQDs embedded Amoc capped aromatic amino acid based hydrogels at physiological pH. GQDs/Amoc-amino acid based hybrid hydrogels emit blue light under UV light irradiation at 365 nm. Aromatic Amoc amino acids based hydrogels formed nanofibrillar networks. Fluorescence spectroscopic studies of GQDs embedded hydrogels reveal that GQDs are stabilized by nanofibrillar networks. Morphological changes of hydrogel **1** and **2** were observed due to the change in gelator structure and the co-assembly of GQDs in the 3D network of gels. Hydroxyl group in tyrosine affects significantly to the mechanical property of the hydrogel. Aromatic  $\pi$ - $\pi$  stacking interactions within GQDs and Amoc amino acids and hydrogen bonding interactions are the driving force to stabilize the GQDs by the nanofibrillar networks. Fluorescence quenching reveals strong  $\pi$ - $\pi$  stacking interactions<sup>[51,52]</sup> within GQDs and Amoc-amino acids. GQDs embedded Amoc-amino acids based hydrogels afford thixotropic in nature. The hydrogel composites of Amoc-F-OH and GQDs deliver excellent entropy driven self-healable behavior, which can be used in drug delivery, tissue engineering and cell damage repairing in biological systems in future.

## 2.6 References

1. Kwon W., Kim Y.-H., Lee C.-L., Lee M., Choi H.-C., Lee T.-W., Rhee S.-W. (2014), Electroluminescence from Graphene Quantum Dots Prepared by Amidative Cutting of Tattered Graphite, *Nano Lett.*, 14, 1306–1311 (DOI: 10.1021/nl404281h).
2. (a) Zheng L. Y., Chi Y. W., Dong Y. Q., Lin J. P., Wang B. B. (2009), Electrochemiluminescence of Water-Soluble Carbon Nanocrystals Released Electrochemically from Graphite, *J. Am. Chem. Soc.*, 131, 4564–4565 (DOI: 10.1021/ja809073f). (b) Dong Y., Tian W., Ren S.,

- Dai R., Chi Y., Chen G. (2014), Graphene Quantum Dots/l-Cysteine Coreactant Electrochemiluminescence System and Its Application in Sensing Lead(II) Ions, *ACS Appl. Mater. Interfaces*, 6, 1646–1651 (DOI: 10.1021/am404552s).
3. (a) Zhu S., Zhang J., Tang S., Qiao C., Wang L., Wang H., Liu X., Li B., Li Y., Yu W., Wang X., Sun H., Yang B. (2012), Surface Chemistry Routes to Modulate the Photoluminescence of Graphene Quantum Dots: From Fluorescence Mechanism to Up-Conversion Bioimaging Applications, *Adv. Funct. Mater.*, 22, 4732-4740 (DOI: 10.1002/adfm.201201499); (b) Zhu S., Zhang J., Qiao C., Tang S., Li Y., Yuan W., Li B., Tian L., Liu F., Hu R., Gao H., Wei H., Zhang H., Sun H., Yang B. (2011), Strongly green-photoluminescent graphene quantum dots for bioimaging applications, *Chem. Commun.*, 47, 6858-6860 (DOI: 10.1039/C1CC11122A); (c) Dong Y., Chen C., Zheng X., Gao L., Cui Z., Yang H., Guo C., Chi Y., Li C. M. (2012), One-step and High Yield Simultaneous Preparation of Single- and Multi-layer Graphene Quantum Dots from CX-72 Carbon Black, *J. Mater. Chem.*, 22, 8764-8766 (DOI: 10.1039/C2JM30658A).
4. (a) Zhuo S., Shao M., Lee S. T. (2012), Upconversion and Downconversion Fluorescent Graphene Quantum Dots: Ultrasonic Preparation and Photocatalysis, *ACS Nano*, 6, 1059–1064 (DOI: 10.1021/nn2040395); (b) Yan X., Li B., Cui X., Wei Q., Tajima K., Li L. S. (2011), Independent Tuning of the Band Gap and Redox Potential of Graphene Quantum Dots, *J. Phys. Chem. Lett.*, 2, 1119–1124 (DOI: 10.1021/jz200450r).
5. (a) Shen J., Zhu Y., Chen C., Yang X., Li C. (2011), Facile Preparation and Upconversion Luminescence of Graphene Quantum Dots, *Chem. Commun.*, 47, 2580–2582 (DOI:10.1039/C0CC04812G); (b) Liu R., Wu D., Feng X., Muellen K. (2011), Bottom-Up Fabrication of Photoluminescent Graphene Quantum Dots with Uniform Morphology, *J. Am. Chem. Soc.*, 133, 15221–15223 (DOI: 10.1021/ja204953k).

6. (a) Konstantatos G., Badioli M., Gaudreau L., Osmond J., Bernechea M., de Arquer P. G. F., Gatti F., Koppens F. H. L. (2012), Hybrid Graphene–quantum Dot Phototransistors with Ultrahigh Gain, *Nat. Nanotechnol.*, 7, 363–368 (DOI: 10.1038/nnano.2012.60); (b) Gupta V., Chaudhary, N., Srivastava R., Sharma G. D., Bhardwaj R., Chand S. (2011), Luminescent Graphene Quantum Dots for Organic Photovoltaic Devices, *J. Am. Chem. Soc.*, 133, 9960–9963 (DOI: 10.1021/ja2036749); (c) Routh P., Das, S., Shit A., Bairi P., Das P., Nandi A. K. (2013), Graphene Quantum Dots from a Facile Sono-Fenton Reaction and Its Hybrid with a Polythiophene Graft Copolymer toward Photovoltaic Application, *ACS Appl. Mater. Interfaces*, 5, 12672–12680 (DOI: 10.1021/am4040174).
7. Bonaccorso, F., Sun, Z., Hasan T., Ferrari A. C. (2010), Graphene Photonics and Optoelectronics, *Nat. Photonics*, 4, 611-622 (DOI: 10.1038/nphoton.2010.186).
8. Nurunnabi M., Khatun Z., Huh, K. M., Park S. Y., Lee D. Y., Cho K. J., Lee, Y.-K. (2013), In Vivo Biodistribution and Toxicology of Carboxylated Graphene Quantum Dots, *ACS Nano*, 7, 6858-6867 (DOI: 10.1021/nn402043c).
9. Son D. I., Kwon B. W., Park D. H., Seo W.-S., Yi Y., Angadi B., Lee C.-L., Choi W. K. (2012), Emissive ZnO-graphene quantum dots for white-light-emitting diodes, *Nat. Nanotechnol.*, 7, 465-471 (DOI: 10.1038/nnano.2012.71).
10. Paek K., Yang H., Lee J., Park J., Kim B. J. (2014), Efficient Colorimetric pH Sensor Based on Responsive Polymer–Quantum Dot Integrated Graphene Oxide, *ACS Nano*, 8, 2848-2856 (DOI: 10.1021/nn406657b).
11. Kim J. K., Park M. J., Kim S. J., Wang D. H., Cho S. P., Bae S., Park J. H., Hong B. H. (2013), Balancing Light Absorptivity and Carrier Conductivity of Graphene Quantum Dots for High-Efficiency Bulk

- Heterojunction Solar Cells, *ACS Nano*, 7, 7207-7212 (DOI: 10.1021/nn402606v).
12. (a) Eda G., Fanchini G., Chhowalla, M. (2008), Large-area ultrathin films of reduced graphene oxide as a transparent and flexible electronic material, *Nat. Nanotechnol.*, 3, 270–274 (DOI: 10.1038/nnano.2008.83); (b) Worsley M. A., Pauzauskie P. J., Olson T. Y., Biener J., Satcher J. H., Baumann T. F. (2010), Synthesis of Graphene Aerogel with High Electrical Conductivity, *J. Am. Chem. Soc.*, 132, 14067–14069 (DOI: 10.1021/ja1072299).
13. (a) Nalluri S. K. M., Berdugo C., Javid N., Frederix P. W. J. M., Ulijn R. V. (2014), Biocatalytic self-assembly of supramolecular charge-transfer nanostructures based on n-type semiconductor-appended peptides, *Angew. Chem., Int. Ed.*, 53, 5882–5887 (DOI: 10.1002/anie.201311158); (b) Poolman J. M., Boekhoven J., Besselink A., Olive A. G. L., van Esch J. H., Eelkema R. (2014), Variable gelation time and stiffness of low-molecular-weight hydrogels through catalytic control over self-assembly, *Nat. Protoc.*, 9, 977-988 (DOI: 10.1038/nprot.2014.055).
14. (a) Jiao T., Zhao H., Zhou J., Zhang, Q., Luo X., Hu J., Peng Q., Yan X. (2015), Self-Assembly Reduced Graphene Oxide Nanosheet Hydrogel Fabrication by Anchorage of Chitosan/Silver and Its Potential Efficient Application toward Dye Degradation for Wastewater Treatments. *ACS Sustainable Chem. Eng.*, 3, 3130-3139 (DOI: 10.1021/acssuschemeng.5b00695); (b) Bai H., Li C., Wang X., Shi G. (2010), A pH-sensitive Graphene Oxide Composite Hydrogel, *Chem. Commun.*, 46, 2376–2378 (DOI: 10.1039/C000051E).
15. Xu Y., Wu Q., Sun Y., Bai H., Shi G. (2010), Three-Dimensional Self-Assembly of Graphene Oxide and DNA into Multifunctional Hydrogels, *ACS Nano*, 4, 7358-7362 (DOI: 10.1021/nn1027104).
16. (a) Yan X., Cui Y., He Q., Wang K., Li J. (2008), Organogels Based on Self-Assembly of Diphenylalanine Peptide and Their Application To

- Immobilize Quantum Dots, *Chem. Mater.*, 20, 1522-1526 (DOI: 10.1021/cm702931b); (b) Maity I., Rasale D. B., Das A. K. (2012), Sonication Induced Peptide-appended Bolaamphiphile Hydrogels for in situ Generation and Catalytic Activity of Pt Nanoparticles, *Soft Matter*, 8, 5301–5308 (DOI:10.1039/C2SM25126D); (c) Rasale D. B., Maity I., Das A. K. (2012), Emerging  $\pi$ -stacked Dynamic Nanostructured Library, *RSC Adv.*, 2, 9791-9794 (DOI: 10.1039/C2RA21334F); (d) Zou Q., Zhang L., Yan X., Wang A., Ma G., Li J., Mçhwald H., Mann S. (2014), Multifunctional Porous Microspheres Based on Peptide–Porphyrin Hierarchical Co-Assembly, *Angew. Chem., Int. Ed.*, 53, 2366-2370 (DOI: 10.1002/anie.201308792).
17. Bhuniya S., Park S. M., Kim B. H. (2005), Biotin-Amino Acid Conjugates: An Approach Toward Self-Assembled Hydrogelation, *Org. Lett.*, 7, 1741-1744 (DOI: 10.1021/ol050300r).
  18. Yao M.-H., Yang J., Song J.-T., Zhao D.-H., Du M.-S., Zhao Y.-D., Liu B. (2014), Directed Self-assembly of Polypeptide-engineered Physical Microgels for Building Porous Cell-laden Hydrogels, *Chem. Commun.*, 50, 9405-9408 (DOI: 10.1039/C4CC04018J).
  19. Galler K. M., Aulisa L., Regan K. R., D'Souza R. N., Hartgerink J. D. (2010), Self-Assembling Multidomain Peptide Hydrogels: Designed Susceptibility to Enzymatic Cleavage Allows Enhanced Cell Migration and Spreading, *J. Am. Chem. Soc.*, 132, 3217-3223 (DOI: 10.1021/ja910481t).
  20. Wang Q., Yang Z., Zhang X., Xiao X., Chang C. K., Xu B. (2007), A supramolecular-hydrogel-encapsulated hemin as an artificial enzyme to mimic peroxidase, *Angew. Chem., Int. Ed.*, 46, 4285–4289 (DOI: 10.1002/anie.200700404).
  21. Adhikari, B., Biswas A., Banerjee A. (2012), Graphene Oxide-Based Hydrogels to Make Metal Nanoparticle-Containing Reduced Graphene Oxide-Based Functional Hybrid Hydrogels, *ACS Appl. Mater. Interfaces*, 4, 5472-5482 (DOI: 10.1021/am301373n).

22. Zhang G., Yan M., Teng X., Bi H., Han Y., Tian M., Wang M. (2014), Formation of Ultra-long Nanoribbons by Self-assembly of Carbon Dots and Anionic Oligomers for Multi-colored Fluorescence and Electrical Conduction, *Chem. Commun.*, 50, 10244-10247 (DOI: 10.1039/C4CC04835K).
23. (a) Qiu Y., Park K. (2001), Environment-sensitive Hydrogels for Drug Delivery, *Adv. Drug Delivery Rev.*, 53, 321-339 (DOI: 10.1016/S0169-409X(01)00203-4); (b) Knipe J. M., Peppas N. A. (2014), Multi-responsive Hydrogels for Drug Delivery and Tissue Engineering Applications, *Regen. Biomater*, 1, 57-65 (DOI: 10.1093/rb/rbu006); (c) Chang G., Chen Y., Li Y., Li S., Huang F., Shen Y., Xie A. (2015), Self-healable Hydrogel on Tumor Cell as Drug Delivery System for Localized and Effective Therapy, *Carbohydr. Polym.*, 122, 336-342 (DOI: 10.1016/j.carbpol.2014.12.077).
24. (a) Lee K. Y., Mooney D. J. (2001), Hydrogels for Tissue Engineering. *Chem. Rev.*, 101, 1869-1879 (DOI: 10.1021/cr000108x); (b) Zhu J., Marchant R. E. (2011), Design properties of hydrogel tissue-engineering scaffolds, *Expert Rev. Med. Devices*, 8, 607-626 (DOI: 10.1586/erd.11.27); (c) Foo C. T. S. W. P., Lee J. S., Mulyasmita W., Parisi-Amon A., Heilshorn S. C. (2009), Two-component protein-engineered physical hydrogels for cell encapsulation, *Proc. Natl. Acad. Sci. U. S. A.*, 106, 22067-22072 (DOI: 10.1073/pnas.0904851106).
25. (a) Nanda J., Biswas A., Banerjee A. (2013), Single Amino Acid based Thixotropic Hydrogel Formation and pH-dependent Morphological Change of Gel Nanofibers, *Soft Matter*, 9, 4198-4208 (DOI: 10.1039/C3SM27050E); (b) Liu H., Hu Y., Wang H., Wang J., Kong D., Wang L., Chen L., Yang Z. (2011), A Thixotropic Molecular Hydrogel Selectively Enhances Flk1 Expression in Differentiated Murine Embryonic Stem Cells, *Soft Matter*, 7, 5430-5436 (DOI: 10.1039/C1SM05198A); (c) Pasc A., Gizzi P., Dupuy N., Parant S., Ghanbaja J., Gerardin C. (2009), Microscopic and Macroscopic

- Anisotropy in Supramolecular Hydrogels of Histidine-based Surfactants, *Tetrahedron Lett.*, 50, 6183-6186 (DOI: 10.1016/j.tetlet.2009.08.093).
26. Wang Q., Mynar J. L., Yoshida M., Lee E., Lee M., Okuro K., Kinbara K., Aida T. (2010), High-water-content Mouldable Hydrogels by Mixing Clay and a Dendritic Molecular Binder, *Nature*, 463, 339-343 (DOI: 10.1038/nature08693).
27. (a) Nebot V. J., Armengol J., Smets J., Prieto S. F., Escuder B., Miravet J. F. (2012), Molecular Hydrogels from Bolaform Amino Acid Derivatives: A Structure-Properties Study Based on the Thermodynamics of Gel Solubilization, *Chem. Eur. J.*, 18, 4063–4072 (DOI: 10.1002/chem.201103193); (b) Yang Y., Urban M. W. (2013) Self-healing Polymeric Materials, *Chem. Soc. Rev.*, 42, 7446-7467 (DOI: 10.1039/C3CS60109A); (c) Kagan E. (2010), Turing Systems, Entropy, and Kinetic Models for Self-Healing Surfaces, *Entropy*, 12, 554-569 (DOI: 10.3390/e12030554); (d) Lehn J. M. (2007), From Supramolecular Chemistry Towards Constitutional Dynamic Chemistry and Adaptive Chemistry, *Chem. Soc. Rev.*, 36, 151-160 (DOI: 10.1039/B616752G); (e) Rowan S. J., Cantrill S. J., Cousins G. R., Sanders J. K., Stoddart J. F. (2002), Dynamic Covalent Chemistry, *Angew. Chem. Int. Ed.*, 41, 898-952 (DOI: 10.1002/1521-3773(20020315)41:6<898::AID-ANIE898>3.0.CO;2-E); (f) He L., Fullenkamp D. E., Rivera J. G., Messersmith P. B. (2011), pH Responsive Self-healing Hydrogels Formed by Boronate–catechol Complexation, *Chem. Commun.*, 47, 7497-7499 (DOI: 10.1039/C1CC11928A).
28. (a) Greef T. F. A. D., Smulders M. M. J., Wolffs M., Schenning, A. P. H. J., Sijbesma R. P., Meijer E. W. (2009), Supramolecular Polymerization, *Chem. Rev.*, 109, 5687-5754 (DOI: 10.1021/cr900181u); (b) Fox J. D., Rowan S. J. (2009), Supramolecular

- Polymerizations and Main-Chain Supramolecular Polymers, *Macromolecules*, 42, 6823-6835 (DOI: 10.1021/ma901144t).
29. Basak S., Nanda J., Banerjee A. (2014), Multi-stimuli Responsive Self-healing Metallo-hydrogels: Tuning of the Gel Recovery Property, *Chem. Commun.*, 50, 2356-2359 (DOI: 10.1039/C3CC48896A).
30. White S. R., Sottos N. R., Geubelle P. H., Moore J. S., Kessler M. R., Sriram S. R., Brown E. N., Viswanathan S. (2001), Autonomic Healing of Polymer Composites, *Nature*, 409, 794-797 (DOI: 10.1038/35057232).
31. (a) Chen L., Raeburn J., Sutton S., Spiller D. G., Williams J., Sharp J. S., Griffiths P. C., Heenan R. K., King S. M., Paul A., Furzeland S., Atkins D., Adams D. J. (2011), Tuneable Mechanical Properties in Low Molecular Weight Gels, *Soft Matter*, 7, 9721-9727 (DOI: 10.1039/C1SM05827D); (b) Greenfield M. A., Hoffman J. R., de la Cruz M. O., Stupp S. I. (2010), Tunable Mechanics of Peptide Nanofiber Gels, *Langmuir*, 26, 3641-3647 (DOI: 10.1021/la9030969).
32. (a) Zeng X., McCarthy D. T., Deletic A., Zhang X. (2015), Silver/Reduced Graphene Oxide Hydrogel as Novel Bactericidal Filter for Point-of-Use Water Disinfection, *Adv. Funct. Mater.*, 25, 4344-4351 (DOI: 10.1002/adfm.201501454); (b) Ghosh D., Das C. K. (2015), Hydrothermal Growth of Hierarchical Ni<sub>3</sub>S<sub>2</sub> and Co<sub>3</sub>S<sub>4</sub> on a Reduced Graphene Oxide Hydrogel@Ni Foam: A High-Energy-Density Aqueous Asymmetric Supercapacitor, *ACS Appl. Mater. Interfaces*, 7, 1122-1131 (DOI: 10.1021/am506738y); (c) Sui Z., Zhang X., Lei Y., Luo Y. (2011), Easy and Green Synthesis of Reduced Graphite Oxide-based Hydrogels, *Carbon*, 49, 4314-4321 (DOI: 10.1016/j.carbon.2011.06.006).
33. Jiao T., Guo H., Zhang Q., Peng Q., Tang Y., Yan X., Li B. (2015), Reduced Graphene Oxide-Based Silver Nanoparticle-Containing Composite Hydrogel as Highly Efficient Dye Catalysts for Wastewater Treatment, *Sci. Rep.*, 5, 11873 (DOI: 10.1038/srep11873).

34. (a) Roy S., Baral A., Banerjee A. (2013), An Amino-Acid-Based Self-Healing Hydrogel: Modulation of the Self-Healing Properties by Incorporating Carbon-Based Nanomaterials, *Chem. Eur. J.*, 19, 14950-14957 (DOI: 10.1002/chem.201301655); (b) Mandal D., Kar T., Das P. K. (2014), Pyrene-Based Fluorescent Ambidextrous Gelators: Scaffolds for Mechanically Robust SWNT-Gel Nanocomposites, *Chem. Eur. J.*, 20, 1349-1358 (DOI: 10.1002/chem.201303401).
35. (a) Wu B., Hou S., Miao Z., Zhang C., Yanhong J. (2015), Layer-by-Layer Self-Assembling Gold Nanorods and Glucose Oxidase onto Carbon Nanotubes Functionalized Sol-Gel Matrix for an Amperometric Glucose Biosensor. *Nanomaterials*, 5, 1544-1555 (DOI: 10.3390/nano5031544); (b) Zhou M., Liu S., Jiang Y., Ma H., Shi M., Wang Q., Zhong W., Liao W., Xing M. M. Q. (2015), Doxorubicin-Loaded Single Wall Nanotube Thermo-Sensitive Hydrogel for Gastric Cancer Chemo-Photothermal Therapy, *Adv. Funct. Mater.*, 25, 4730-4739 (DOI: 10.1002/adfm.201501434).
36. (a) J. G. Clar, T. Yuan, Y. Zhao, J.-C. J. Bonzongo Ziegler K. J. (2014), Evaluation of Critical Parameters in the Separation of Single-Wall Carbon Nanotubes through Selective Adsorption onto Hydrogels, *J. Phys. Chem. C*, 118, 15495–15505 (DOI: 10.1021/jp503594h); (b) Nabeta M., Sano M. (2005), Nanotube Foam Prepared by Gelatin Gel as a Template. *Langmuir*, 21, 1706-1708 (DOI: 10.1021/la047140x).
37. Yu Y., Pushparaj V. L., Nalamasu O., McGown L. B. (2013), G-Quadruplex Guanosine Gels and Single Walled Carbon Nanotubes. *Molecules*, 18, 15434-15447 (DOI: 10.3390/molecules181215434).
38. Li W., Liu M., Chen H., Xu J., Gao Y., Li H. (2014), Phenylboronate-diol Crosslinked Polymer/SWCNT Hybrid Gels with Reversible Sol-gel Transition, *Polym. Adv. Technol.*, 25, 233–239 (DOI: 10.1002/pat.3228).
39. Goda T., Kurita T., Mitsumata T., Sano M. (2014), Very Small Amounts of Carbon Nanotubes to Weaken Thixotropy of

- Polysaccharide Gels. *Chem. Lett.*, 43, 988–990 (DOI: 10.1246/cl.140205).
40. Cao L., Meziani M. J., Sahu S., Sun Y.-P. (2013), Photoluminescence Properties of Graphene versus Other Carbon Nanomaterials, *Acc. Chem. Res.*, 46, 171–180 (DOI: 10.1021/ar300128j).
41. (a) Liu W., Wang Y., Li Z. (2014), Tuning of Surface Wettability of RGO-based Aerogels for Various Adsorbates in Water Using Different Amino Acids. *Chem. Commun.*, 50, 10311-10314 (DOI:10.1039/C4CC03383C); (b) Heeyoung K. A., Taehoon C., Hoon Y., Cheolsang U., Kiju N., Jaewook A., Kyung H., Lee K. (2014), Gelation of Graphene Oxides Induced by Different Types of Amino Acids. *Carbon*, 71, 229-237 (DOI: 10.1016/j.carbon.2014.01.033).
42. (a) Das A. K., Bose P. P., Drew M. G. B., Banerjee A. (2007), The Role of Protecting Groups in the Formation of Organogels through a Nanofibrillar Network formed by Self-assembling Terminally Protected Tripeptides. *Tetrahedron*, 63, 7432-7442 (DOI: 10.1016/j.tet.2007.05.045); (b) Ulijn R. V., Smith A. M. (2008), Designing Peptide based Nanomaterials, *Chem. Soc. Rev.*, 37, 664–675 (DOI: 10.1039/B609047H); (c) Basak, S., Nanda J., Banerjee A. (2012), A New Aromatic Amino Acid based Organogel for Oil Spill Recovery, *J. Mater. Chem.*, 22, 11658-11664 (DOI: 10.1039/C2JM30711A).
43. (a) Shen J., Xin X., Liu T., Tong L., Xu G., Yuan S. (2016), Manipulation the Properties of Supramolecular Hydrogels of  $\alpha$ -Cyclodextrin/Tyloxapol/carbon-based Nanomaterials, *J. Colloid Interface Sci.*, 468, 78-85 (DOI: 10.1016/j.jcis.2016.01.037); (b) Huang Y., Zeng M., Feng Z., Yin D., Xu Q., Fan L. (2016), Graphene Oxide-based Composite Hydrogels with Self-assembled Macroporous Structures, *RSC Adv.*, 6, 3561-3570 (DOI: 10.1039/C5RA25910J); (c) Cui W., Ji J., Cai Y.-F., Li H., Ran R. (2015), Robust, Anti-fatigue, and Self-healing Graphene Oxide/hydrophobically Associated Composite

- Hydrogels and their Use as Recyclable Adsorbents for Dye Wastewater Treatment, *J. Mater. Chem. A*, 3, 17445-17458 (DOI: 10.1039/C5TA04470G).
44. (a) Hou C., Duan A. Y., Zhang Q., Wang H., Li Y. (2012), Bio-applicable and Electroactive Near-infrared Laser-triggered Self-healing Hydrogels based on Graphene Networks. *J. Mater. Chem.*, 22, 14991-14996 (DOI: 10.1039/C2JM32255B); (b) Peng R., Yu Y., Chen S., Yang Y., Tang Y. (2014), Conductive Nanocomposite Hydrogels with Self-healing Property, *RSC Adv.*, 4, 35149-35155 (DOI: 10.1039/C4RA05381H); (c) Zhong M., Liu Y.-T., Xie X.-M. (2015), Self-healable, Super Tough Graphene Oxide-poly(acrylic acid) Nanocomposite Hydrogels Facilitated by Dual Cross-linking Effects through Dynamic Ionic Interactions, *J. Mater. Chem. B*, 3, 4001-4008 (DOI: 10.1039/C5TB00075K).
45. (a) Cong H.-P., Wang P., Yu S.-H. (2013), Stretchable and Self-Healing Graphene Oxide-Polymer Composite Hydrogels: A Dual-Network Design, *Chem. Mater.*, 25, 3357-3362 (DOI: 10.1021/cm401919c); (b) Liu J., Song G., He C., Wang H. (2013), Self-Healing in Tough Graphene Oxide Composite Hydrogels, *Macromol. Rapid Commun.*, 34, 1002-1007 (DOI: 10.1002/marc.201300242); (c) Han D., Yan L. (2014), Supramolecular Hydrogel of Chitosan in the Presence of Graphene Oxide Nanosheets as 2D Cross-Linkers, *ACS Sustainable Chem. Eng.*, 2, 296-300 (DOI: 10.1021/sc400352a).
46. (a) Kornblum N., Scott A. (1977), A new method for protecting amines. *J. Org. Chem.*, 42, 399-400 (DOI: 10.1021/jo00422a069); (b) Lan, P., Porco J. J. A., South M. S., Parlow J. J. (2003), The Development of a Chromatography-Free Mitsunobu Reaction: Synthesis and Applications of an Anthracene-Tagged Phosphine Reagent, *J. Comb. Chem.*, 5, 660-669 (DOI: 10.1021/cc030028h).

47. Pan D., Zhang J., Li Z., Wu M. (2010), Hydrothermal Route for Cutting Graphene Sheets into Blue-Luminescent Graphene Quantum Dots, *Adv. Mater.*, 22, 734-738 (DOI: 10.1002/adma.200902825).
48. (a) Chassenieux C., Tsitsilianis C. (2016), Recent Trends in pH/thermo-Responsive Self-assembling Hydrogels: from Polyions to Peptide-based Polymeric Gelators, *Soft Matter*, 12, 1344-1359 (DOI: 10.1039/C5SM02710A); (b) Liow S. S., Dou Q., Kai D., Karim A. A., Zhang K., Xu F., Loh X. J. (2016), Thermogels: In Situ Gelling Biomaterial, *ACS Biomater. Sci. Eng.*, 2, 295-316 (DOI: 10.1021/acsbiomaterials.5b00515).
49. Lin L., Zhang S. (2012), Creating High Yield Water Soluble Luminescent Graphene Quantum Dots via Exfoliating and Disintegrating Carbon Nanotubes and Graphite Flakes, *Chem. Commun.*, 48, 10177-10179 (DOI: 10.1039/C2CC35559K).
50. Liu Y., Kim D. Y. (2015), Ultraviolet and Blue Emitting Graphene Quantum Dots Synthesized from Carbon Nano-onions and their Comparison for Metal Ion Sensing, *Chem. Commun.*, 51, 4176-4179 (DOI: 10.1039/C4CC07618D).
51. Tang L., Wang Y., Liu Y., Li J., (2011), DNA-Directed Self-Assembly of Graphene Oxide with Applications to Ultrasensitive Oligonucleotide Assay, *ACS Nano*, 5, 3817-3822 (DOI: 10.1021/nn200147n).
52. Jiao T. F., Gao F. Q., Zhang Q. R., Zhou J. X., Gao F. M. (2013), Spacer Effect on Nanostructures and Self-assembly in Organogels via some Bolaform Cholesteryl Imide Derivatives with Different Spacers, *Nanoscale Res. Lett.*, 8, 406-414 (DOI: 10.1186/1556-276X-8-406).
53. (a) Mallakpour, S., Abdolmaleki A., Borandeh S. (2014), Covalently Functionalized Graphene Sheets with Biocompatible Natural Amino Acids, *Appl. Surf. Sci.*, 307, 533-542 (DOI: 10.1016/j.apsusc.2014.04.070); (b) Wang S., Lemon Z., Cole I. S., Li Q. (2015), Tailoring the Edges of Graphene Quantum Dots to Establish

- Localized  $\pi$ - $\pi$  Interactions with Aromatic Molecules, RSC Adv., 5, 41248-41254 (DOI: 10.1039/C5RA04927J).
54. (a) Lu J., Yeo P. S. E., Gan C. K., Wu P., Loh K. P. (2011), Transforming C<sub>60</sub> Molecules into Graphene Quantum Dots, Nat. Nanotechnol., 6, 247-252 (DOI: 10.1038/nnano.2011.30); (b) Yan X., Cui X., Li B., Li L. S. (2010), Large, Solution-Processable Graphene Quantum Dots as Light Absorbers for Photovoltaics, Nano Lett., 10, 1869-1873 (DOI: 10.1021/nl101060h); (c) Pan D., Xi C., Li Z., Wang L., Chen Z., Luc B., Wu M. (2013), Electrophoretic Fabrication of Highly Robust, Efficient, and Benign Heterojunction Photoelectrocatalysts based on Graphene-Quantum-dot Sensitized TiO<sub>2</sub> Nanotube Arrays, J. Mater. Chem. A, 1, 3551-3555 (DOI: 10.1039/C3TA00059A).
55. Hu Y., Gao W., Wu F., Wu H., He B., He J. (2016), Low Molecular Weight Gels Induced Differentiation of Mesenchymal Stem Cells, J. Mater. Chem. B, 4, 3504-3508 (DOI: 10.1039/C5TB02546J).
56. Das A. K., Maity I., Parmar H. S., McDonald T. O., Konda M. (2015), Lipase-Catalyzed Dissipative Self-Assembly of a Thixotropic Peptide Bolaamphiphile Hydrogel for Human Umbilical Cord Stem-Cell Proliferation, Biomacromolecules, 16, 1157-1168 (DOI: 10.1021/bm501835v).
57. log P was calculated by using online prediction program <http://www.molinspiration.com>.
58. Andersen N. H., Harrington M. J., Birkedal H., Lee B. P., Messersmith P. B., Lee K. Y. C., Wait J. H. (2011), pH-induced Metal-ligand Cross-links Inspired by Mussel Yield Self-healing Polymer Networks with Near-covalent Elastic Moduli, Proc. Natl. Acad. Sci. U. S. A., 108, 2651-2655 (DOI: 10.1073/pnas.1015862108).
59. Zhou C., Gao W., Yang K., Xu L., Ding J., Chen J., Liu M., Huang X., Wang S., Wu H. (2013), A Novel Glucose/pH Responsive Low-

Molecular-Weight Organogel of Easy Recycling, *Langmuir*, 29, 13568-13575 (DOI: 10.1021/la4033578).

60. Nayar V. T., Weiland J. D., Nelson C. S., Hodge A. M. (2012), Elastic and viscoelastic characterization of agar, *J. Mech. Behav. Biomed. Mater.*, 7, 60-68 (DOI: 10.1016/j.jmbbm.2011.05.027).

## **Chapter 3**

# **Tuning the Handedness: Role of Chiral Component in Peptide appended Bolaamphiphile-based Co-assembled Hydrogels**



### 3.1 Introduction

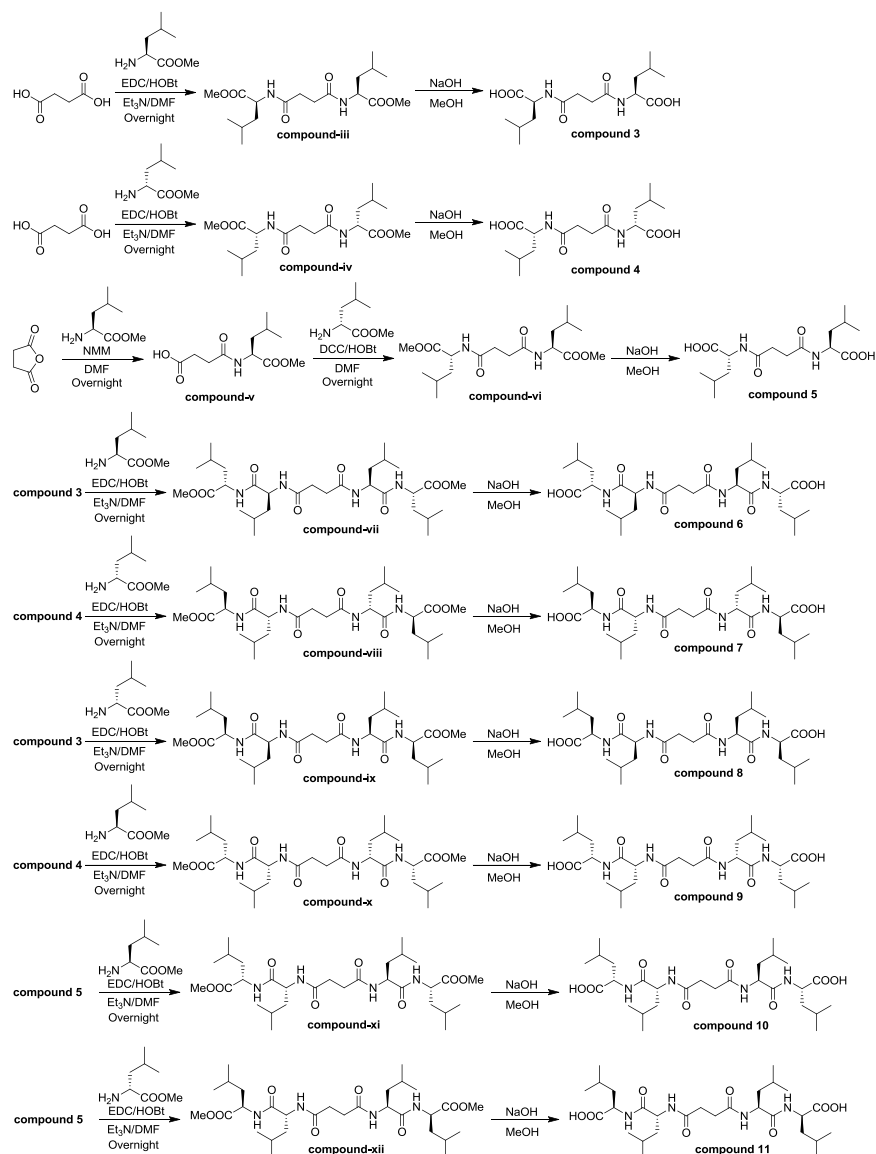
Engineering the chiral nanostructures with a desirable handedness is a great deal of attention due to the various applications in materials science,<sup>[1-5]</sup> chemistry<sup>[6-12]</sup> and biology.<sup>[13-15]</sup> Chiral nanostructures exhibit distinguished photophysical properties and adequate biological effects. Peptides self-assemble and possess both molecular as well as supramolecular chirality.<sup>[16-19]</sup> Therefore, the configuration of amino acids in peptides plays a crucial role to achieve self-assembled chiral nanostructures.<sup>[20-21]</sup> A recent study has shown that configuration of terminal hydrophilic amino acid in peptides plays a significant role to control the overall handedness of the peptide amphiphiles.<sup>[22]</sup> The supramolecular chirality could also be induced or tuned by the amino acid based chiral spacer.<sup>[23]</sup> From a detailed survey of the previous reports, a precise observation is noted that right-handed twist is associated with the amphiphiles of amino acids with L-configuration whereas D-amino acids based amphiphiles assemble to produce left-handed chiral nanostructures.<sup>[24-26]</sup> Moreover, left-handed helical twist is also found for L-amino acids based amphiphiles when  $\beta$ -sheet structure is packed with right-handed  $\beta$ -strands along with the hydrogen bonding direction.<sup>[27-29]</sup> Without alteration of building blocks, the tunability of chiral architecture to a desirable handedness (*i.e.* right-handed: P; left-handed: M) remains a challenge.<sup>[30]</sup> Moreover, the supramolecular chirality is driven by noncovalent interactions and external components as the bicomponent systems work as a remote control for self-assembly and gelation.<sup>[31-37]</sup> Therefore, peptides could rebuild reverse helical nanostructures by interacting with external components (*i.e.* chiral, achiral or asymmetric molecules) without changing the configuration of amino acids.<sup>[38]</sup> The reverse helical nanostructures were acquired through the co-assembly with additives as both shares complementary functionality for hierarchical self-assembly.<sup>[39]</sup>

To date, supramolecular chirality of bolaamphiphiles has attracted the attention of the researchers.<sup>[40-41]</sup> In general, bolaamphiphiles are captivating biomolecules where hydrophobic spacer connects with two polar head groups. Bolaamphiphiles have shown heat sensitive nature to furnish new chiral nanostructures.<sup>[42]</sup> Multiple bolaamphiphiles capped with nucleotides, sugars, amino acids and peptides have been designed to control the helical nanostructures.<sup>[41,43-45]</sup> Bolaamphiphiles self-assembled to form distinct helical nanostructures when it is comprised with an amino acid with different configuration.<sup>[46]</sup> A previous report suggests that aromatic ring-functionalized external component has a profound impact on helical co-assembly with bolaamphiphiles.<sup>[29,47-48]</sup> As a result, controlled nanostructured hydrogel was achieved.<sup>[49]</sup> The bolaamphiphiles composed of aromatic amino acids form twisted nanoscale materials by the influence of aromatic additives through  $\pi$ - $\pi$  stacking interaction.<sup>[29,49]</sup> Indeed few aliphatic peptide bolaamphiphiles have been designed to explore their self-assembled helical architectures, however, helix reversal of aliphatic peptide bolaamphiphiles is interesting in hydrogel state as hydrogels exhibit promising properties.<sup>[50-52]</sup>

In biological systems, an aliphatic amino acid leucine has a profound impact on folding of proteins.<sup>[53-55]</sup> So, a thorough understanding and controlling the chiral self-assembling behavior of leucine-based peptide bolaamphiphiles are necessary. To tune the chiral nanostructures through hydrogen bonding in gel state, bi-component self-assembled systems were developed with tartaric acid.<sup>[56]</sup> It is also necessary to understand how the configuration of amino acids in peptide bolaamphiphiles influences the bicomponent gelation process as well as the supramolecular chirality of amino acid/peptide functionalized bolaamphiphiles.

## 3.2 Experimental

*Scheme 3.1 Synthetic scheme of bolaamphiphiles 3-11*



### 3.2.1 Synthesis of Compound iii

0.5 g (4.23 mmol) of succinic acid in 2 mL of DMF was cooled in an ice-water bath. (L)-Leu-OMe was isolated from 3 g (16.94 mmol) of the corresponding methyl ester hydrochloride by neutralization and subsequent extraction with ethyl acetate and the ethyl acetate extract was concentrated to 8 mL. It was then added to the reaction mixture, followed

immediately by 1.45 g (9.3 mmol) EDC and 1.14 g (8.46 mmol) of HOBt. The reaction mixture was stirred for overnight. The residue was taken up in ethyl acetate (50 mL). The organic layer was washed with 1 M HCl (3 × 50 mL), brine (2 × 50 mL), 1 M sodium carbonate (3 × 50 mL), brine (2 × 50 mL), dried over anhydrous sodium sulfate and evaporated in vacuo to yield **iii** as a white solid. Purification was done by silica gel column (100-200 mesh) using ethylacetate-hexane as eluent. Yield: 1.51 g (96%),  $^1\text{H}$  NMR (400 MHz,  $\text{CDCl}_3$ ):  $\delta$  = 6.52-6.50 (d, 2H,  $J$  = 8 Hz, -NH), 4.53-4.47 (m, 2H,  $\text{C}^\alpha\text{H}$  of Leu), 3.66 (s, 6H, - $\text{OCH}_3$ ), 2.55-2.43 (m, 4H, -Hs of Suc), 1.64-1.54 (m, 4H,  $\text{C}^\beta\text{H}$ s of Leu), 1.09-1.07 (m, 2H,  $\text{C}^\gamma\text{H}$ s of Leu), 0.87-0.85 (m, 12H,  $\text{C}^\delta\text{H}$ s of Leu) ppm. MS (ESI)  $m/z$  for  $\text{C}_{18}\text{H}_{32}\text{N}_2\text{O}_6$  ( $\text{M} + \text{Na}$ ) $^+$  calcd: 395.2158, found: 395.2231.

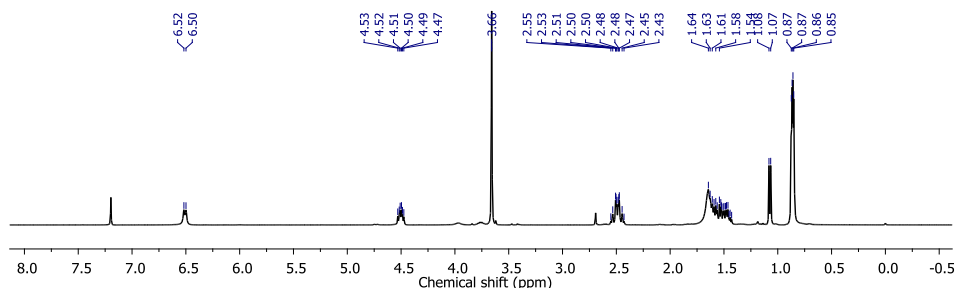


Figure 3.1.  $^1\text{H}$  NMR spectrum of compound **iii** in  $\text{CDCl}_3$ .

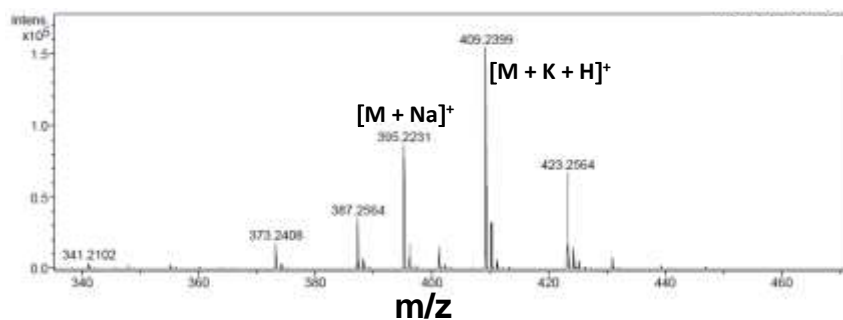
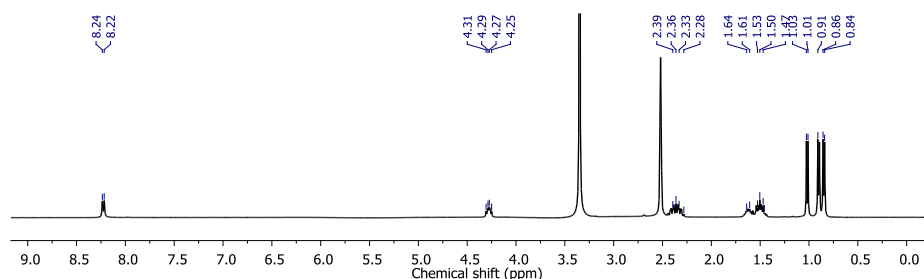


Figure 3.2. Mass spectrum of compound (**iii**).

### 3.2.2 Synthesis of Compound 3

1.4 g (3.76 mmol) of MeO-(L)-Leu-Suc-(L)-Leu-OMe (**iii**) in 10 mL MeOH was taken in a round bottom flask and 1 M NaOH was added to it

dropwise. The reaction mixture was stirred and was continuously monitored by thin layer chromatography (TLC) till the completion of the reaction. The reaction was completed after 6 h. Then MeOH was removed under vacuo and 10 mL of distilled water was added to the reaction. The aqueous part was washed with diethyl ether (2 x 30 mL). Then the collected aqueous layer was cooled under ice-water bath for 10 minute and then pH was adjusted to 1 by drop-wise addition of 1M HCl. It was extracted with ethyl acetate (3 x 50 mL) and then the ethyl acetate part was dried over anhydrous Na<sub>2</sub>SO<sub>4</sub> and evaporated in vacuo to yield **3** as a white solid. Yield = 1.21 g (94%), <sup>1</sup>H NMR (400 MHz, DMSO-d<sub>6</sub>): δ = 8.24-8.22 (d, 2H, *J* = 8 Hz, -NH), 4.31-4.25 (m, 2H, C<sup>α</sup>H of Leu), 2.39-2.28 (m, 4H, -Hs of Suc), 1.53-1.47 (m, 4H, C<sup>β</sup>Hs of Leu), 0.87-0.85 (m, 14H, C<sup>γ</sup> and C<sup>δ</sup>Hs of Leu) ppm. <sup>13</sup>C NMR (100 MHz, DMSO-d<sub>6</sub>): δ = 173.89, 156.72, 52.55, 24.69, 23.24, 21.60, 15.04 ppm. MS (ESI) *m/z* for C<sub>16</sub>H<sub>28</sub>N<sub>2</sub>O<sub>6</sub> (M + Na)<sup>+</sup> calcd: 345.2026, found: 345.2053.



**Figure 3.3.** <sup>1</sup>H NMR spectrum of compound **3** in DMSO-d<sub>6</sub>.

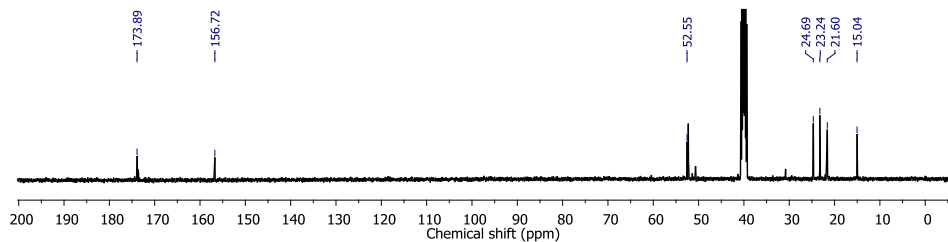


**Figure 3.4.** <sup>13</sup>C NMR spectrum of compound **3** in DMSO-d<sub>6</sub>.

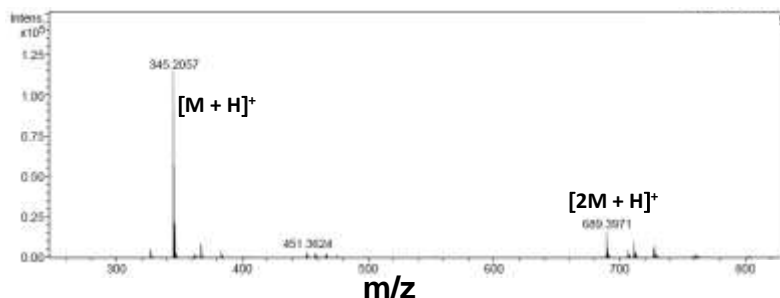
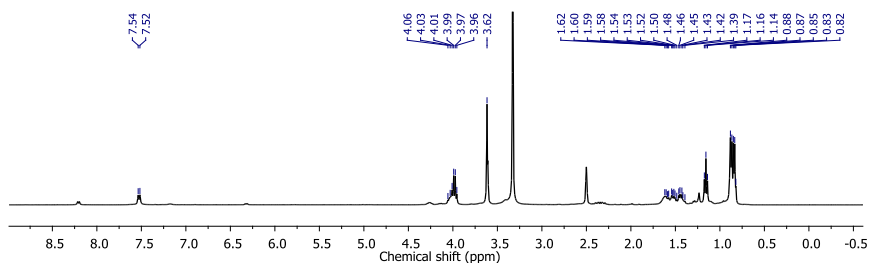


Figure 3.5. Mass spectrum of compound 3.

### 3.2.3 Synthesis of Compound iv

0.5 g (4.23 mmol) of succinic acid in 2 mL of DMF was cooled in an ice-water bath. (D)-Leu-OMe was isolated from 3 g (16.94 mmol) of the corresponding methyl ester hydrochloride by neutralization and subsequent extraction with ethyl acetate and the ethyl acetate extract was concentrated to 8 mL. It was then added to the reaction mixture, followed immediately by 1.45 g (9.3 mmol) of EDC and 1.14 g (8.46 mmol) of HOBT. The reaction mixture was stirred for overnight. The residue was taken up in ethyl acetate (50 mL). The organic layer was washed with 1 M HCl (3 × 50 mL), brine (2 × 50 mL), 1 M Na<sub>2</sub>CO<sub>3</sub> (3 × 50 mL), brine (2 × 50 mL), dried over Na<sub>2</sub>SO<sub>4</sub> and evaporated in vacuo to yield **iv** as a white solid. Purification was done by silica gel column (100-200 mesh) using ethyl acetate - hexane as eluent. Yield: 1.46 g (92%), <sup>1</sup>H NMR (400 MHz, DMSO-d<sub>6</sub>): δ = 7.54-7.52 (d, 2H, *J* = 8 Hz, -NH), 4.05-3.96 (m, 4H, C<sup>α</sup>H of Leu), 3.62 (s, 6H, -OCH<sub>3</sub>), 1.62-1.39 (m, 6H, C<sup>β</sup>Hs of Leu), 1.17-1.14 (m, 4H, -CH<sub>2</sub> of Suc), 0.88-0.82 (m, 14H, C<sup>γ</sup> and C<sup>δ</sup>Hs of Leu) ppm. MS (ESI) *m/z* for C<sub>18</sub>H<sub>32</sub>N<sub>2</sub>O<sub>6</sub> (M + Na)<sup>+</sup> calcd: 395.2158, found: 395.2281.



**Figure 3.6.**  $^1\text{H}$  NMR spectrum of compound **iv** in  $\text{DMSO-}d_6$ .

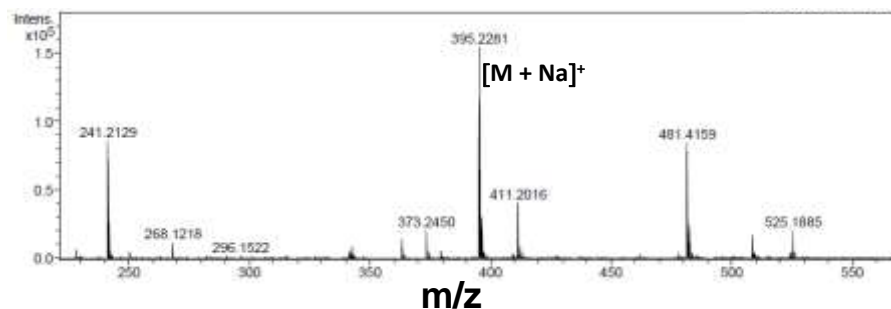


**Figure 3.7.** Mass spectrum of compound **iv**.

### 3.2.4 Synthesis of Compound 4

1.3 g (3.49 mmol) of MeO-(D)-Leu-Suc-(D)-Leu-OMe (**iv**) in 10 mL MeOH was taken in a round bottom flask and 1 M NaOH was added to it dropwise. The reaction mixture was stirred and was continuously monitored by thin layer chromatography (TLC) till the completion of the reaction. The reaction was completed after 6 h. Then MeOH was removed under vacuo and 10 mL of distilled water was added to the reaction. The aqueous part was washed with diethyl ether (2 x 30 mL). Then the collected aqueous layer was cooled under ice-water bath for 10 minute and then pH was adjusted to 1 by dropwise addition of 1M HCl. It was extracted with ethyl acetate (3 x 50 mL) and then the ethyl acetate part was dried over anhydrous  $\text{Na}_2\text{SO}_4$  and evaporated in vacuo to yield **4** as a white solid. Yield: 1.16 g (96%),  $^1\text{H}$  NMR (400 MHz,  $\text{DMSO-}d_6$ ):  $\delta$  = 12.50 (s, 2H, -COOH), 8.12-8.10 (d, 2H, -NH), 4.27-4.21 (m, 2H,  $\text{C}^\alpha\text{H}$  of Leu), 2.43-2.33 (m, 4H,  $-\text{CH}_2$  of Suc), 1.54-1.52 (m, 6H,  $\text{C}^\beta$  and  $\text{C}^\gamma$  Hs of Leu), 0.93-0.86 (m, 12 H,  $\text{C}^\delta\text{Hs}$  of Leu) ppm.  $^{13}\text{C}$  NMR (100 MHz,  $\text{DMSO-}d_6$ ):  $\delta$  = 174.71, 171.86, 50.64, 31.06, 24.78, 23.34, 21.82 ppm. MS (ESI) m/z for  $\text{C}_{16}\text{H}_{28}\text{N}_2\text{O}_6$  ( $\text{M} + \text{Na}$ ) $^+$  calcd: 345.2026, found: 345.2029.

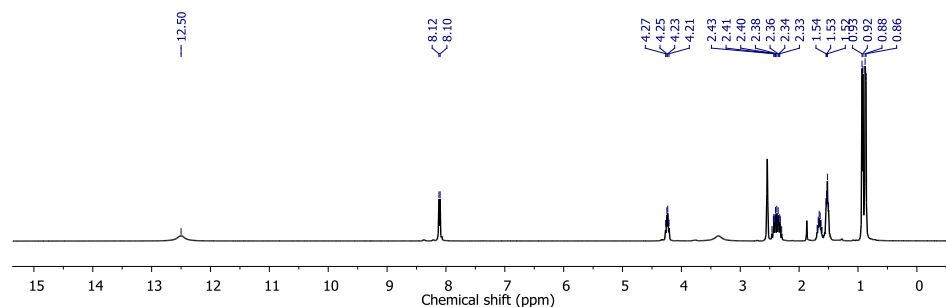


Figure 3.8.  $^1\text{H}$  NMR spectrum of compound **4** in  $\text{DMSO-}d_6$ .

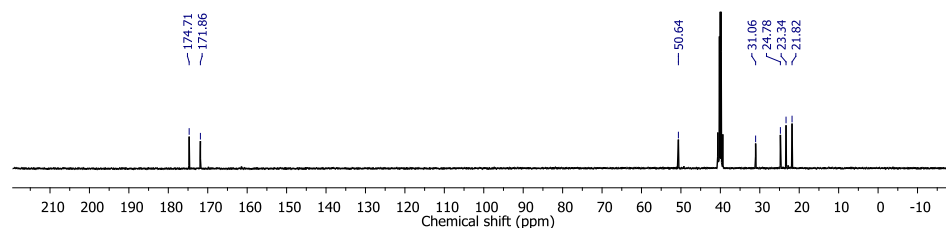


Figure 3.9.  $^{13}\text{C}$  NMR spectrum of compound **4** in  $\text{DMSO-}d_6$ .

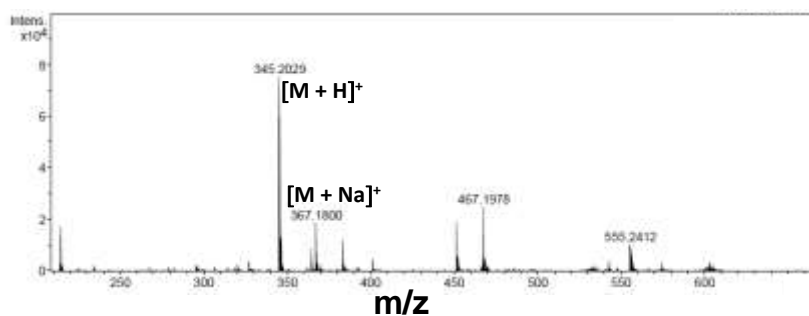


Figure 3.10. Mass spectrum of compound **5**.

### 3.2.5 Synthesis of Compound **v**

1 g (9.99 mmol) succinic anhydride in 2 mL of DMF was cooled in a 100 mL round bottom flask. (L)-Leu-OMe was isolated from 3.6 g (19.98 mmol) of the corresponding methyl ester hydrochloride by extraction with ethyl acetate and the ethyl acetate extract was concentrated to 8 mL. It was then added to the reaction mixture, followed immediately by 1.21 g (11.98 mmol, 1 ml 300  $\mu\text{L}$ ) N-methyl morpholine. The reaction mixture was stirred for overnight. 50 mL ethyl acetate was added to the reaction mixture and the organic layer was washed with 1M HCl (3 x 50 mL.). The ethyl acetate part was dried over anhydrous  $\text{Na}_2\text{SO}_4$ . It was evaporated in

vacuo to yield **v** as sticky solid. Purification was done by silica gel column (100-200 mesh) using chloroform-methanol as eluent. Yield = 2.05 g, 84%,  $^1\text{H}$  NMR (400 MHz,  $\text{DMSO-d}_6$ ):  $\delta$  = 8.12-8.1 (d, 1H,  $J$  = 8 Hz, -NH), 4.26-4.2 (m, 1H,  $\text{C}^\alpha\text{H}$  of Leu), 3.64 (s, 3H,  $-\text{OCH}_3$ ), 2.75-2.73 (d, 2H, -Hs of Suc), 2.56-2.52 (d, 2H, -Hs of Suc), 1.78-1.48 (m, 3H,  $\text{C}^\beta$  and  $\text{C}^\gamma$ -Hs of Leu), 0.91-0.84 (m, 6H,  $\text{C}^\delta\text{Hs}$  of Leu) ppm. MS (ESI)  $m/z$  for  $\text{C}_{11}\text{H}_{19}\text{NO}_5(\text{M} + \text{Na})^+$  calcd: 268.1161, found: 268.1139.

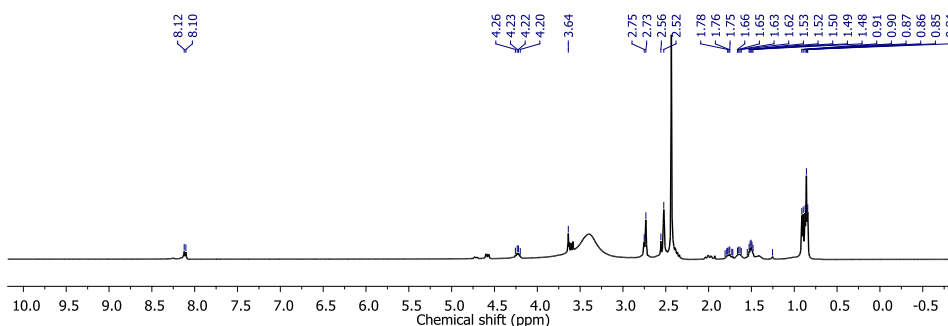


Figure 3.11.  $^1\text{H}$  NMR spectrum of compound **v** in  $\text{DMSO-d}_6$ .

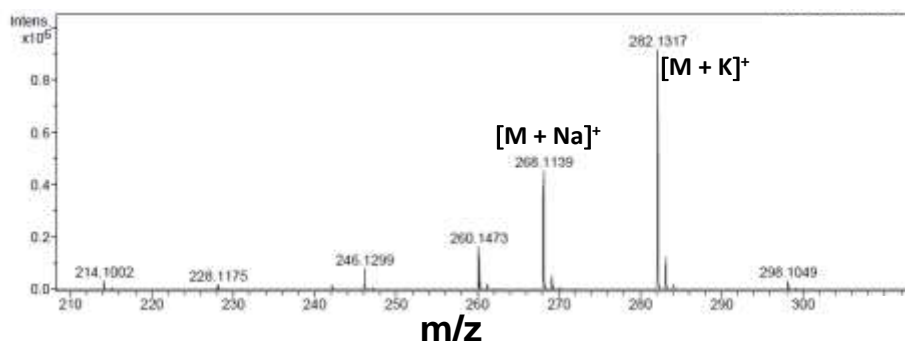
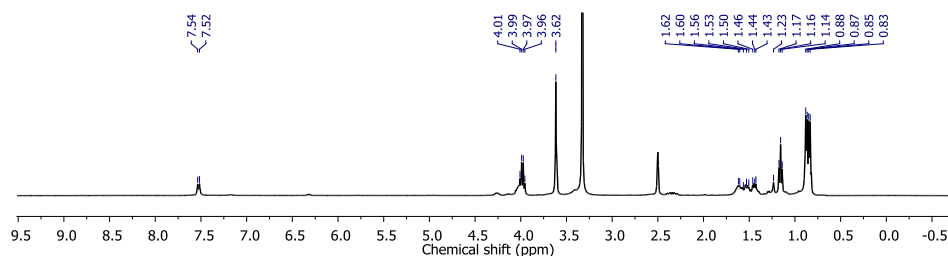


Figure 3.12. Mass spectrum of compound **v**.

### 3.2.6 Synthesis of Compound **vi**

1.52 g (6.19 mmol) of HO-Suc-(L)-Leu-OMe (**v**) in 6 mL of DMF was cooled in an ice-water bath and (D)-Leu-OMe was isolated from 2.24 g (12.39 mmol) of the corresponding methyl ester hydrochloride by neutralization and subsequent extraction with ethyl acetate and the ethyl acetate extract was concentrated to 8 mL. It was then added to the reaction mixture, followed immediately by 1.06 g (6.81 mmol) EDC and 0.83 g (6.19 mmol) of HOBt. The reaction mixture was stirred for overnight. The

residue was taken up in ethyl acetate (50 mL). The organic layer was washed with 1 M HCl (3 × 50 mL), brine (2 × 50 mL), 1 M Na<sub>2</sub>CO<sub>3</sub> (3 × 50 mL), brine (2 × 50 mL), dried over anhydrous Na<sub>2</sub>SO<sub>4</sub> and evaporated in vacuo to yield compound **vi** as a white solid. Purification was done by silica gel column (100-200 mesh) using ethyl acetate-hexane as eluent. Yield = 1.84 g, 81%, <sup>1</sup>H NMR (400 MHz, DMSO-d<sub>6</sub>): δ = 7.54-7.52 (d, 2H, *J* = 8 Hz, -NH), 4.01-3.96 (m, 2H, C<sup>α</sup>H of Leu), 3.66 (s, 6H, -OCH<sub>3</sub>), 1.62-1.43 (m, 6H, C<sup>β</sup> and C<sup>γ</sup> -Hs of Leu), 1.23-1.14 (m, 4H, -Hs of Suc), 0.88-0.83 (m, 12H, C<sup>δ</sup>Hs of Leu) ppm. MS (ESI) *m/z* for C<sub>18</sub>H<sub>32</sub>N<sub>2</sub>O<sub>6</sub> (M + Na)<sup>+</sup> calcd: 395.2158, found: 395.2237.



**Figure 3.13.** <sup>1</sup>H NMR spectrum of compound **vi** in DMSO-d<sub>6</sub>.

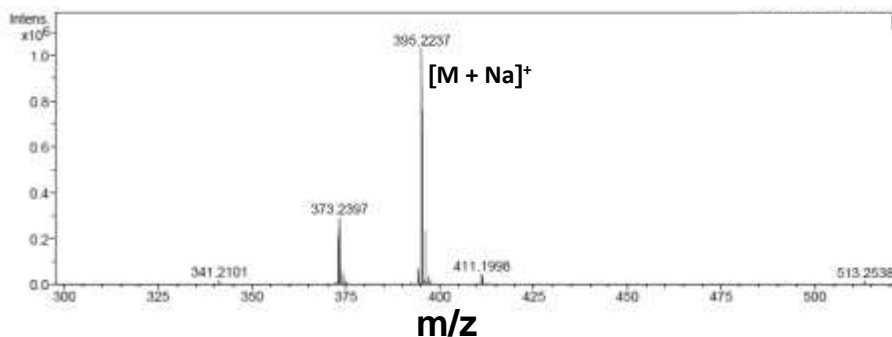


**Figure 3.14.** Mass spectrum of compound **vi**.

### 3.2.7 Synthesis of Compound 5

1.4 g (3.76 mmol) of MeO-(D)-Leu-Suc-(L)-Leu-OMe (**vi**) in 20 mL MeOH was taken in a round bottom flask and 1 M NaOH was added to it dropwise. The reaction mixture was stirred and was continuously monitored by thin layer chromatography (TLC) till the completion of the

reaction. The reaction was completed after 6 hours. Then MeOH was removed under vacuo and 10 mL of distilled water was added to the reaction mixture. The aqueous part was washed with diethyl ether (2 x 30 mL). Then the collected aqueous layer was cooled under ice-water bath for 10 minute and then pH was adjusted to 1 by dropwise addition of 1M HCl. It was extracted with ethyl acetate (3 x 50 mL) and then the ethyl acetate part was dried over anhydrous Na<sub>2</sub>SO<sub>4</sub> and evaporated in vacuo to yield **5** as a white solid. Yield = 1.21 g, 94%, <sup>1</sup>H NMR (400 MHz, DMSO-d<sub>6</sub>): δ = 7.93-7.91 (d, 2H, *J* = 8 Hz -NH), 4.26-4.21 (m, 2H, C<sup>α</sup>Hs of Leu), 2.89-2.82 (m, 4H, -CH<sub>2</sub> of Suc), 1.25-1.17 (m, 6H, C<sup>β</sup> and C<sup>γ</sup>-Hs of Leu), 0.91-0.83 (m, 12 H, C<sup>δ</sup>Hs of Leu) ppm. <sup>13</sup>C NMR (100 MHz, DMSO-d<sub>6</sub>): δ = 173.62, 171.94, 50.68, 30.80, 24.68, 23.77, 21.78 ppm. MS (ESI) *m/z* for C<sub>16</sub>H<sub>28</sub>N<sub>2</sub>O<sub>6</sub> (M + Na)<sup>+</sup> calcd: 345.2026, found: 345.1246.

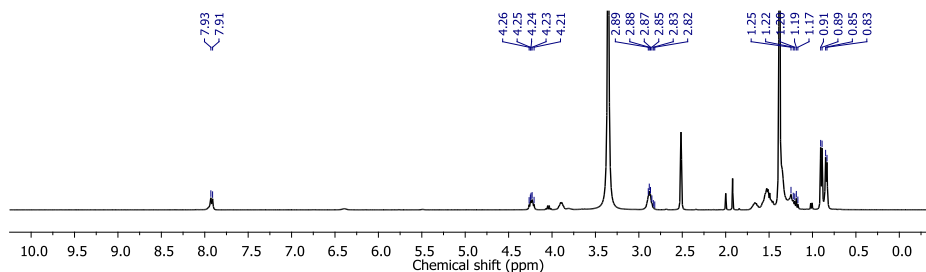


**Figure 3.15.** <sup>1</sup>H NMR spectrum of compound **5** in DMSO-d<sub>6</sub>.

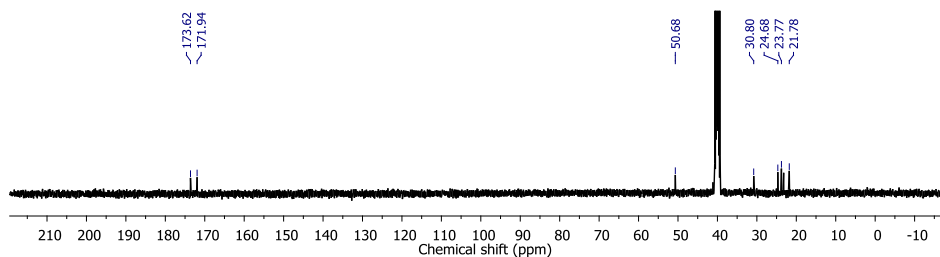


**Figure 3.16.** <sup>13</sup>C NMR spectrum of compound **5** in DMSO-d<sub>6</sub>.

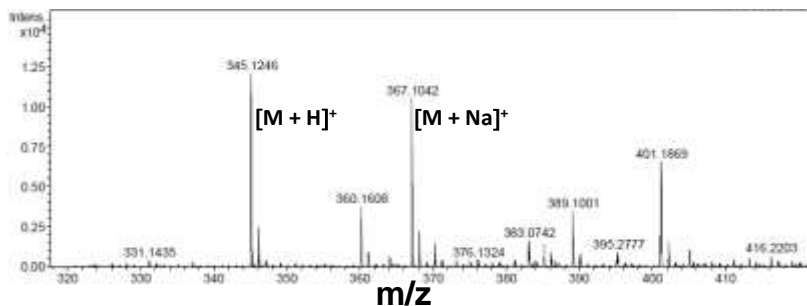


**Figure 3.17.** Mass spectrum of compound 5.

### 3.2.8 Synthesis of Compound vii

0.42 g (1.22 mmol) of HO-(L)Leu-Suc-(L)-Leu-OH (**3**) in 2 mL of DMF was cooled in an ice-water bath. (L)-Leu-OMe was isolated from 0.89 g (4.88 mmol) of the corresponding methyl ester hydrochloride by neutralization and subsequent extraction with ethyl acetate and the extracted ethyl acetate was concentrated to 8 mL. It was then added to the reaction mixture, followed immediately by 0.42 g (2.64 mmol) EDC and 0.33 g (2.44 mmol) of HOBt. The reaction mixture was stirred for overnight. The reaction mixture was diluted to 50 mL with ethyl acetate. The organic layer was washed with 1 M HCl (3 × 50 mL), brine (2 × 50 mL), 1 M Na<sub>2</sub>CO<sub>3</sub> (3 × 50 mL), brine (2 × 50 mL), dried over anhydrous Na<sub>2</sub>SO<sub>4</sub> and evaporated in vacuo to yield **vii** as a white solid. Purification was done by silica gel column (100-200 mesh) using ethyl acetate-hexane as eluent. Yield: 0.65 g (89%), <sup>1</sup>H NMR (400 MHz, CDCl<sub>3</sub>): δ = 6.64-6.62 (m, 2H, -NH), 4.58-4.54 (m, 2H, -NH), 4.21-4.15 (m, 4H, C<sup>α</sup>H of Leu), 3.73 (s, 6H, -OCH<sub>3</sub>), 2.60-2.51 (m, 4H, -CH<sub>2</sub> of Suc), 1.68-1.53 (m, 12H, C<sup>β</sup>Hs of Leu), 1.29-1.26 (m, 4H, -Hs of Leu), 0.94-0.93 (m, 24 H, C<sup>δ</sup>Hs of Leu) ppm. MS (ESI) m/z for C<sub>30</sub>H<sub>54</sub>N<sub>4</sub>O<sub>8</sub> (M + Na)<sup>+</sup> calcd: 621.3839, found: 621.3992.

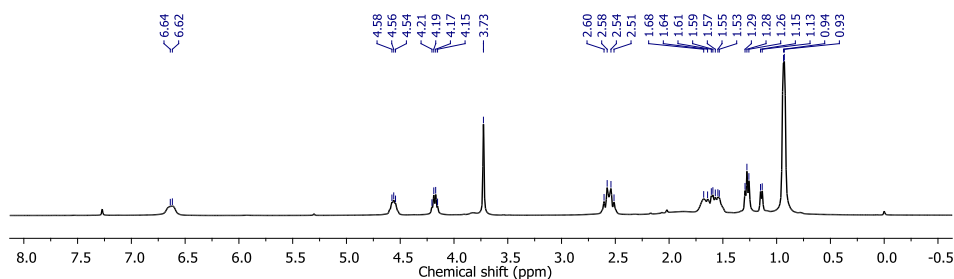


Figure 3.18.  $^1\text{H}$  NMR spectrum of compound **vii** in  $\text{CDCl}_3$ .

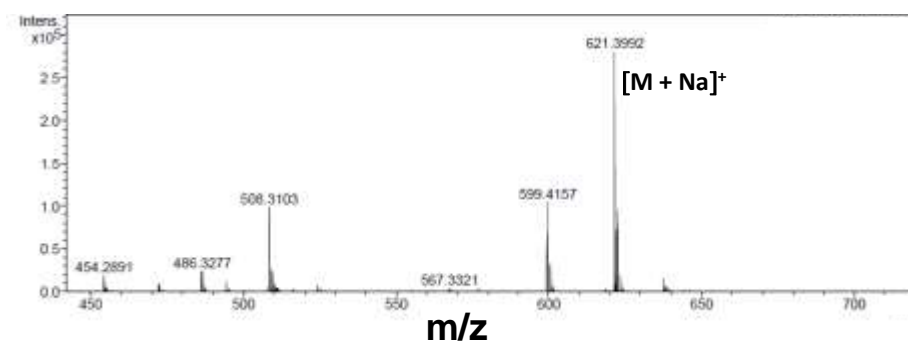
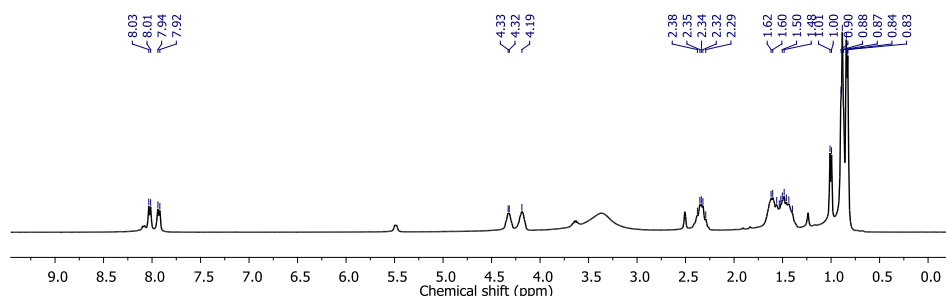


Figure 3.19. Mass spectrum of compound **vii**.

### 3.2.9 Synthesis of Compound 6

0.4 g (0.69 mmol) of MeO-(L)-Leu-(L)-Leu-Suc-(L)-Leu-(L)-Leu-OMe (**vii**) in 10 mL MeOH was taken in a round bottom flask and 1 M NaOH was added to it dropwise. The reaction mixture was stirred and was continuously monitored by thin layer chromatography (TLC) till the completion of the reaction. The reaction was completed after 6 h. Then MeOH was removed under vacuo and 10 mL of distilled water was added to the reaction. The aqueous part was washed with diethyl ether (2 x 30 mL). Then the collected aqueous layer was cooled under ice-water bath for 10 minute and then pH was adjusted to 1 by dropwise addition of 1M HCl. It was extracted with ethyl acetate (3 x 50 mL) and then the ethyl acetate part was dried over anhydrous  $\text{Na}_2\text{SO}_4$  and evaporated in vacuo to yield **6** as a white solid. Yield: 0.36 g (94%),  $^1\text{H}$  NMR (400 MHz,  $\text{DMSO-d}_6$ ):  $\delta$  = 8.03-7.92 (m, 4H, -NH), 4.33-4.19 (m, 4H,  $\text{C}^\alpha\text{H}$  of Leu), 2.38-2.29 (m, 4H,  $-\text{CH}_2$  of Suc), 1.62-1.48 (m, 12H,  $\text{C}^\beta\text{H}$ s of Leu), 1.01-0.83 (m, 28H,  $\text{C}^\gamma\text{H}$ s and  $\text{C}^\delta\text{H}$ s of Leu) ppm.  $^{13}\text{C}$  NMR (100 MHz,  $\text{DMSO-d}_6$ ):  $\delta$  =

174.42, 172.67, 171.73, 51.13, 50.71, 31.34, 24.72, 24.59, 23.79, 23.61, 23.36, 21.85 ppm. MS (ESI)  $m/z$  for  $C_{28}H_{50}N_4O_8$  ( $M + K$ )<sup>+</sup> calcd: 609.3266, found: 609.3260.



**Figure 3.20.** <sup>1</sup>H NMR spectrum of compound **6** in DMSO-*d*<sub>6</sub>.

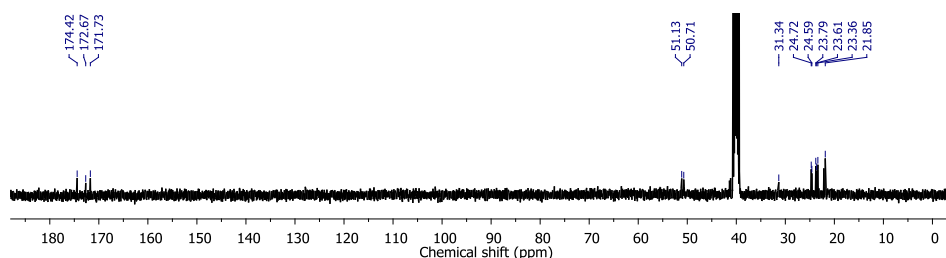


**Figure 3.21.** <sup>13</sup>C NMR spectrum of compound **6** in DMSO-*d*<sub>6</sub>.

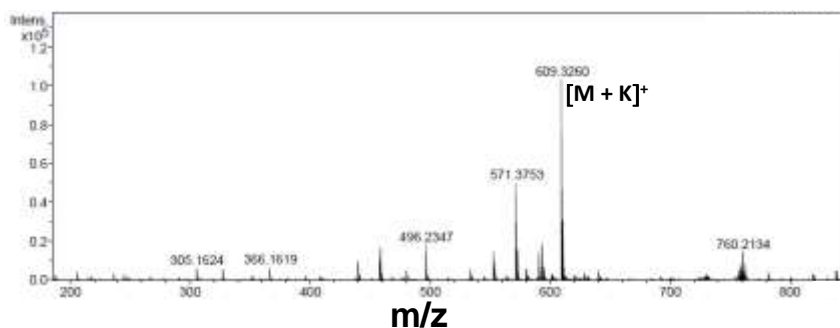


**Figure 3.22.** Mass spectrum of compound **6**.

### 3.2.10 Synthesis of Compound viii

0.41 g (1.19 mmol) of HO-(D)Leu-Suc-(D)-Leu-OH (**4**) in 2 mL of DMF was cooled in an ice-water bath. (D)-Leu-OMe was isolated from 0.86 g (4.76 mmol) of the corresponding methyl ester hydrochloride by neutralization and subsequent extraction with ethyl acetate and the extracted ethyl acetate was concentrated to 8 mL. It was then added to the

reaction mixture, followed immediately by 0.41 g (2.61 mmol) EDC and 0.32 g (2.38 mmol) of HOBT. The reaction mixture was stirred for overnight. The reaction mixture was diluted to 50 mL with ethyl acetate. The organic layer was washed with 1 M HCl (3 × 50 mL), brine (2 × 50 mL), 1 M Na<sub>2</sub>CO<sub>3</sub> (3 × 50 mL), brine (2 × 50 mL), dried over anhydrous Na<sub>2</sub>SO<sub>4</sub> and evaporated in vacuo to yield **viii** as a white solid. Purification was done by silica gel column (100-200 mesh) using ethyl acetate-hexane as eluent. Yield: 0.64 g (90), <sup>1</sup>H NMR (400 MHz, DMSO-d<sub>6</sub>): δ = 8.27-8.25 (d, 2H, *J* = 8 Hz, -NH) 8.03-8.01 (m, 2H, *J* = 8Hz, -NH), 4.40-4.33 (m, 4H, C<sup>α</sup>H of Leu), 3.67 (s, 6H, -OCH<sub>3</sub>), 2.41-2.40 (m, 4H, -CH<sub>2</sub> of Suc), 1.63-1.50 (m, 12H, C<sup>β</sup>Hs of Leu), 0.94-0.96-0.91 (m, 24 H, C<sup>γ</sup> and C<sup>δ</sup>Hs of Leu) ppm. <sup>13</sup>C-NMR (100 MHz, DMSO-d<sub>6</sub>): δ = 173.29, 172.86, 171.76, 52.19, 51.06, 50.68, 33.81, 31.24, 24.62, 24.56, 23.49, 23.22, 22.13, 21.74 ppm. MS (ESI) *m/z* for C<sub>30</sub>H<sub>54</sub>N<sub>4</sub>O<sub>8</sub> (M + H)<sup>+</sup> calcd: 599.4020, found: 599.2282.

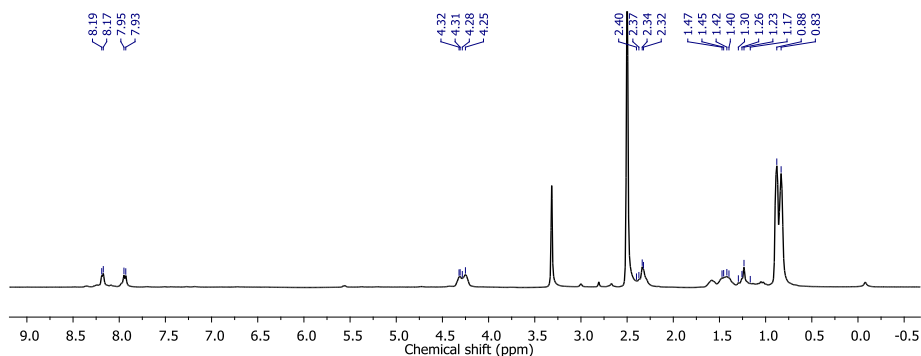


**Figure 3.23.** <sup>1</sup>H NMR spectrum of compound **viii** in DMSO-d<sub>6</sub>.

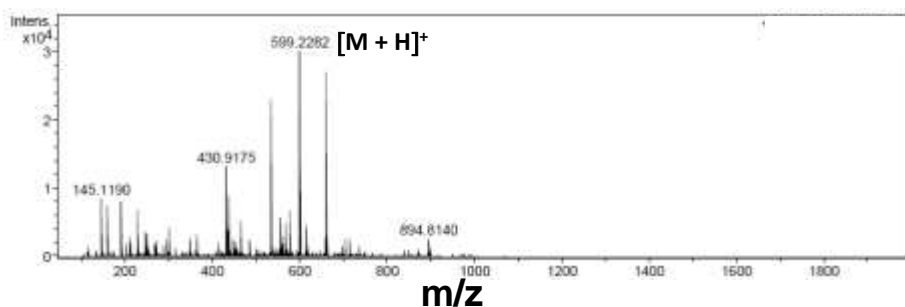


**Figure 3.24.** Mass spectrum of compound **viii**.

### 3.2.11 Synthesis of Compound 7

0.37 g (0.62 mmol) of MeO-(D)-Leu-(D)-Leu-Suc-(D)-Leu-(D)-Leu-OMe (**viii**) in 10 mL MeOH was taken in a round bottom flask and 1 M NaOH was added dropwise to it till the completion of the reaction. The reaction mixture was stirred and was continuously monitored by thin layer chromatography (TLC) till the completion of the reaction. The reaction was completed after 3 hours. Then MeOH was removed under vacuo and 10 mL of distilled water was added to the reaction. The aqueous part was washed with diethyl ether (2 x 30 mL). Then the collected aqueous layer was cooled under ice-water bath for 10 minute and then pH was adjusted to 1 by dropwise addition of 1M HCl. It was extracted with ethyl acetate (3 x 50 mL) and then the ethyl acetate part was dried over anhydrous Na<sub>2</sub>SO<sub>4</sub> and evaporated in vacuo to yield **7** as a white solid. Yield: 0.33 g (94%), <sup>1</sup>H NMR (400 MHz, DMSO-d<sub>6</sub>): δ = 8.19-8.17 (d, 2H, *J* = 8 Hz, -NH) 7.95-7.93 (m, 2H, *J* = 8Hz, -NH), 4.32-4.25 (m, 4H, C<sup>α</sup>H of Leu), 2.4-2.32 (m, 4H, -CH<sub>2</sub> of Suc), 1.47-1.17 (m, 8H, C<sup>β</sup>Hs of Leu), 0.88-0.83 (m, 28 H, C<sup>γ</sup> and C<sup>δ</sup>Hs of Leu) ppm. <sup>13</sup>C NMR (100 MHz, DMSO-d<sub>6</sub>): δ = 173.29, 172.86, 171.76, 52.19, 51.06, 33.81, 31.24, 24.62, 24.56, 23.49, 23.22, 22.13, 21.74 ppm. MS (ESI) *m/z* for C<sub>28</sub>H<sub>50</sub>N<sub>4</sub>O<sub>8</sub> (M + H)<sup>+</sup> calcd: 571.3707, found: 571.3753.

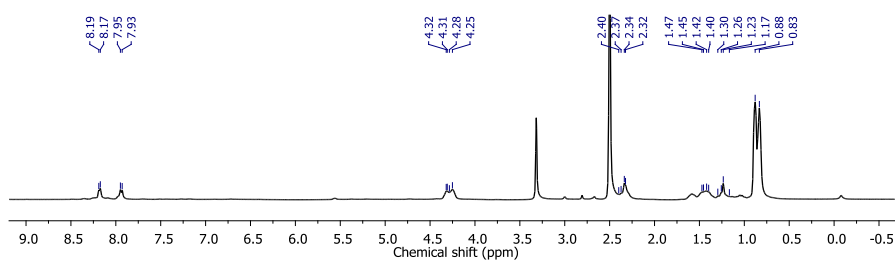


**Figure 3.25.** <sup>1</sup>H NMR spectrum of compound **7** in DMSO-d<sub>6</sub>.

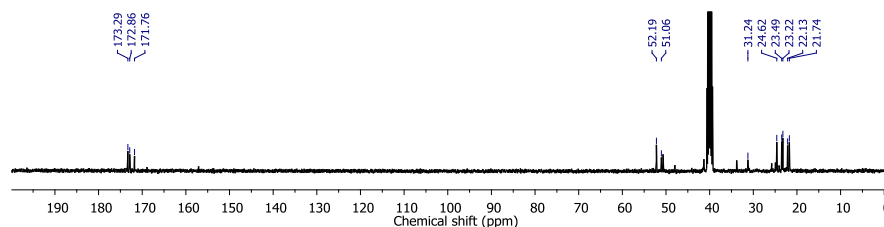


Figure 3.26.  $^{13}\text{C}$  NMR spectrum of compound **7** in  $\text{DMSO-}d_6$ .

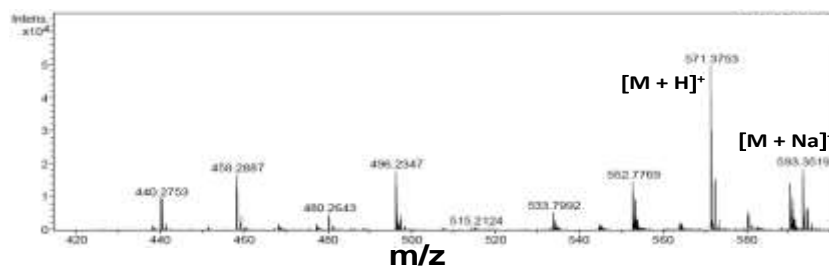


Figure 3.27. Mass spectra of compound **7**.

### 3.2.12 Synthesis of Compound **ix**

0.507 g (1.47 mmol) of HO-(L)Leu-Suc-(L)-Leu-OH (**3**) in 2 mL of DMF was cooled in an ice-water bath. (D)-Leu-OMe was isolated from 1.07 g (5.88 mmol) of the corresponding methyl ester hydrochloride by neutralization and subsequent extraction with ethyl acetate and the extracted ethyl acetate was concentrated to 8 mL. It was then added to the reaction mixture, followed immediately by 0.5 g (3.23 mmol) EDC and 0.39 g (2.94 mmol) of HOBt. The reaction mixture was stirred for overnight. The reaction mixture was diluted to 50 mL with ethyl acetate. The organic layer was washed with 1 M HCl ( $3 \times 50$  mL), brine ( $2 \times 50$  mL), 1 M  $\text{Na}_2\text{CO}_3$  ( $3 \times 50$  mL), brine ( $2 \times 50$  mL), dried over anhydrous  $\text{Na}_2\text{SO}_4$  and evaporated in vacuo to yield **ix** as a white solid. Purification was done by silica gel column (100-200 mesh) using ethyl acetate-hexane as eluent to get **ix** as white solid. Yield: 0.72 g (82%),  $^1\text{H}$  NMR (400 MHz,  $\text{DMSO-}d_6$ ):  $\delta = 7.33$ - $7.31$  (d, 2H,  $J = 8$  Hz, -NH), 6.95 (s, 2H, -NH), 4.57-4.52 (m, 4H,  $\text{C}^\alpha\text{Hs}$  of Leu), 3.69 (s, 6H,  $-\text{OCH}_3$ ), 2.58-2.49 (m, 4H,  $-\text{CH}_2$  of Suc), 1.66-1.56 (m, 12H,  $\text{C}^\beta$  and  $\text{C}^\gamma\text{Hs}$  of Leu), 0.93-0.89 (m, 24H,

$C^{\delta}Hs$  of Leu) ppm. MS (ESI)  $m/z$  for  $C_{30}H_{54}N_4O_8$  ( $M + Na$ ) $^{+}$  calcd: 621.3839, found: 621.3855.

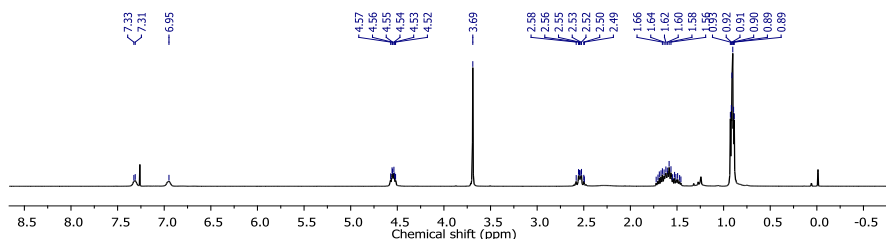


Figure 3.28.  $^1H$  NMR spectrum of compound **ix** in  $CDCl_3$ .

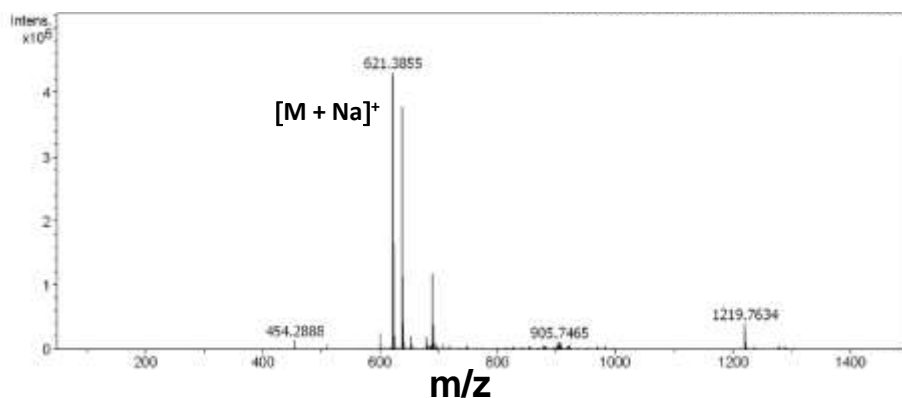


Figure 3.29. Mass spectra of compound **ix**.

### 3.2.13 Synthesis of Compound **8**

0.35 g (0.58 mmol) of MeO-(D)-Leu-(L)-Leu-Suc-(L)-Leu-(D)-Leu-OMe (**ix**) in 10 mL MeOH was taken in a round bottom flask and 1 M NaOH was added to it dropwise. The reaction mixture was stirred and was continuously monitored by thin layer chromatography (TLC) till the completion of the reaction. The reaction was completed after 3 hours. Then MeOH was removed under vacuo and 10 mL of distilled water was added to the reaction. The aqueous part was washed with diethyl ether (2 x 30 mL). Then the collected aqueous layer was cooled under ice-water bath for 10 minute and then pH was adjusted to 1 by dropwise addition of 1M HCl. It was extracted with ethyl acetate (3 x 50 mL) and then the ethyl acetate part was dried over anhydrous  $Na_2SO_4$  and evaporated in vacuo to yield **8** as a white solid. Yield 0.31 g (95%),  $^1H$  NMR (400 MHz,  $DMSO-d_6$ ):  $\delta$  = 8.12-8.1 (d, 2H,  $J$  = 8 Hz, -NH), 7.92-7.9 (d, 2H,  $J$  = 8 Hz, -NH),

4.37-4.15 (m, 4H, C<sup>α</sup>Hs of Leu), 2.38-2.28 (m, 4H, -CH<sub>2</sub> of Suc), 1.56-1.40 (m, 12H, C<sup>β</sup> and C<sup>γ</sup>Hs of Leu), 0.85-0.78 (m, 24 H, C<sup>δ</sup>Hs of Leu) ppm. <sup>13</sup>C NMR (100 MHz, DMSO-d<sub>6</sub>): δ = 174.45, 172.55, 171.77, 51.23, 50.55, 31.26, 24.71, 23.45, 23.30, 22.08, 21.67 ppm. MS (ESI) m/z for C<sub>28</sub>H<sub>50</sub>N<sub>4</sub>O<sub>8</sub> (M + Na)<sup>+</sup> calcd: 593.3526, found: 593.3825.

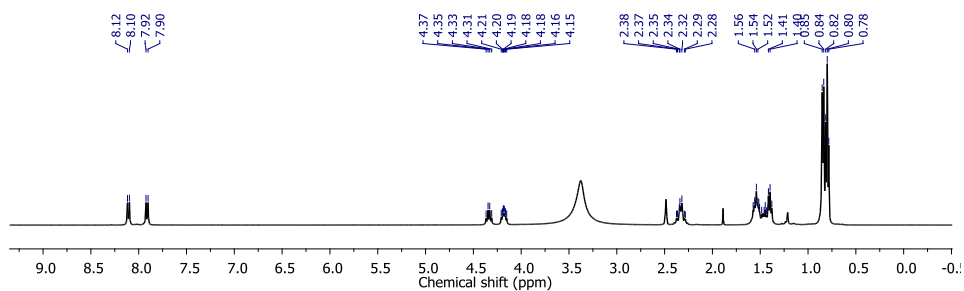


Figure 3.30. <sup>1</sup>H NMR spectrum of compound 8 in DMSO-d<sub>6</sub>.

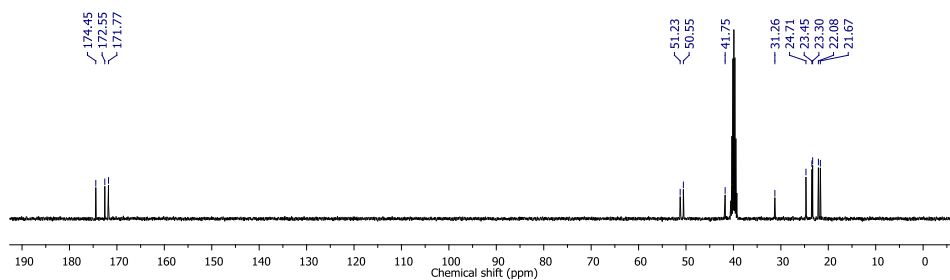


Figure 3.31. <sup>13</sup>C NMR spectrum of compound 8 in DMSO-d<sub>6</sub>.

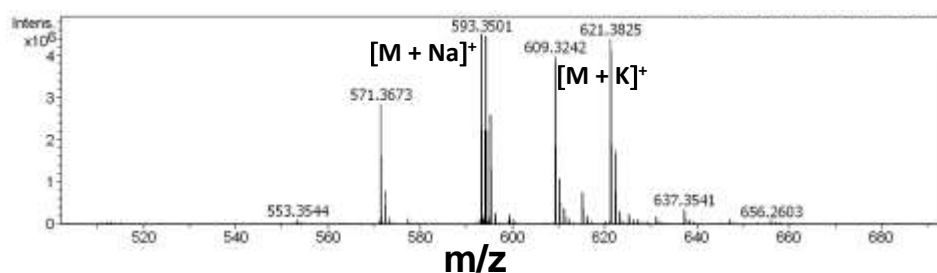


Figure 3.32. Mass spectra of compound 8.

### 3.2.14 Synthesis of Compound x

0.53 g (1.54 mmol) of HO-(D)Leu-Suc-(D)-Leu-OH (**4**) in 2 mL of DMF was cooled in an ice-water bath. (L)-Leu-OMe was isolated from 1.12 g (6.16 mmol) of the corresponding methyl ester hydrochloride by

neutralization and subsequent extraction with ethyl acetate and the extracted ethyl acetate was concentrated to 8 mL. It was then added to the reaction mixture, followed immediately by 0.52 g (3.38 mmol) EDC and 0.42 g (3.08 mmol) of HOBt. The reaction mixture was stirred for overnight. The reaction mixture was diluted to 50 mL with ethyl acetate. The organic layer was washed with 1M HCl (3 × 50 mL), brine (2 × 50 mL), 1M Na<sub>2</sub>CO<sub>3</sub> (3 × 50 mL), brine (2 × 50 mL), dried over anhydrous Na<sub>2</sub>SO<sub>4</sub> and evaporated in vacuo to yield **x** as a white solid. Purification was done by silica gel column (100-200 mesh) using ethyl acetate-hexane as eluent. Yield: 0.8 g (87%), <sup>1</sup>H NMR (400 MHz, DMSO-d<sub>6</sub>): δ = 8.27-8.17 (m, 2H, -NH), 7.97-7.93 (m, 2H, -NH), 4.37-4.23 (m, 4H, C<sup>α</sup>Hs of Leu), 3.61 (s, 6H, -OCH<sub>3</sub>), 2.37-2.32 (m, 4H, -CH<sub>2</sub> of Suc), 1.57-1.41 (m, 12H, C<sup>β</sup> and C<sup>γ</sup>Hs of Leu), 0.89-0.8 (m, 24H, C<sup>δ</sup>Hs of Leu) ppm. MS (ESI) m/z for C<sub>30</sub>H<sub>54</sub>N<sub>4</sub>O<sub>8</sub> (M + Na)<sup>+</sup> calcd: 621.3839, found: 621.3882.

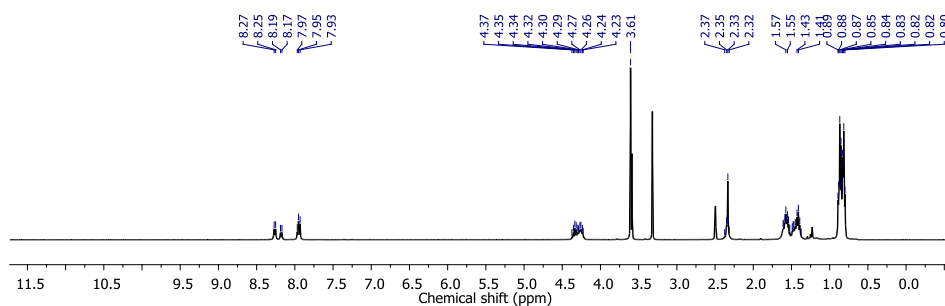


Figure 3.33. <sup>1</sup>H NMR spectrum of compound **x** in DMSO-d<sub>6</sub>.

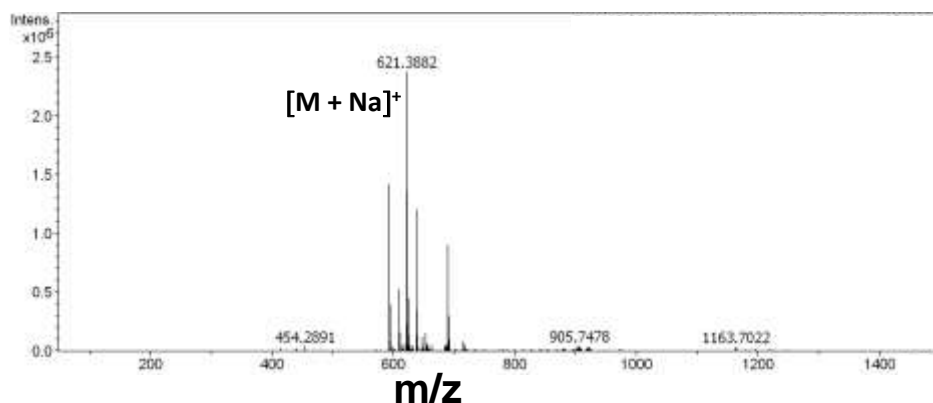


Figure 3.34. Mass spectrum of compound **x**.

## 3.2.15 Synthesis of Compound 9

0.37 g (0.62 mmol) of MeO-(L)-Leu-(D)-Leu-Suc-(D)-Leu-(L)-Leu-OMe (**x**) in 10 mL MeOH was taken in a round bottom flask and 1 M NaOH was added to it dropwise. The reaction mixture was stirred and was continuously monitored by thin layer chromatography (TLC) till the completion of the reaction. The reaction was completed after 3 h. Then MeOH was removed under vacuo and 10 mL of distilled water was added to the reaction. The aqueous part was washed with diethyl ether (2 x 30 mL). Then the collected aqueous layer was cooled under ice-water bath for 10 minute and then pH was adjusted to 1 by dropwise addition of 1M HCl. It was extracted with ethyl acetate (3 x 50 mL) and then the ethyl acetate part was dried over anhydrous Na<sub>2</sub>SO<sub>4</sub> and evaporated in vacuo to yield **9** as a white solid. Yield: 0.34 g (96%), <sup>1</sup>H NMR (400 MHz, DMSO-d<sub>6</sub>): δ = 8.11-7.91 (m, 4H, -NH), 4.36-4.13 (m, 4H, C<sup>α</sup>Hs of Leu), 2.36-2.26 (m, 4H, -CH<sub>2</sub> of Suc), 1.44-1.38 (m, 12 H, C<sup>β</sup> and C<sup>γ</sup>Hs of Leu), 0.89-0.78 (m, 24H, C<sup>δ</sup>Hs of Leu) ppm. <sup>13</sup>C NMR (100 MHz, DMSO-d<sub>6</sub>): δ = 174.36, 172.71, 171.84, 51.17, 50.55, 31.34, 24.70, 23.29, 22.05, 21.65 ppm. MS (ESI) m/z for C<sub>28</sub>H<sub>50</sub>N<sub>4</sub>O<sub>8</sub> (M + H)<sup>+</sup> calcd: 571.3707, found: 571.3697.

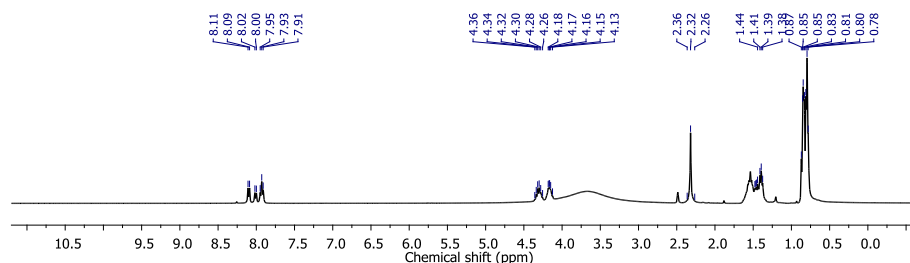


Figure 3.35. <sup>1</sup>H NMR spectrum of compound **9** in DMSO-d<sub>6</sub>.

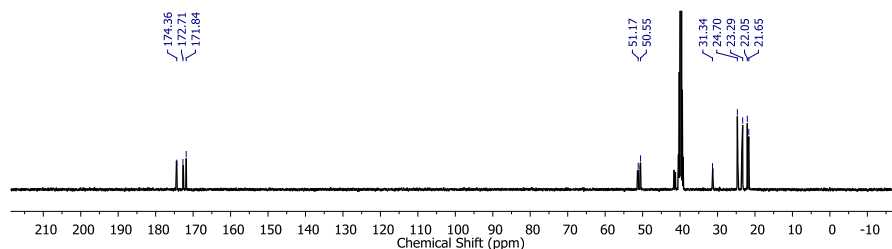


Figure 3.36. <sup>13</sup>C NMR spectrum of compound **9** in DMSO-d<sub>6</sub>.

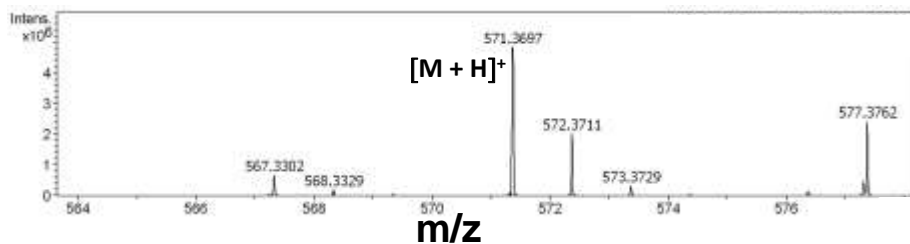


Figure 3.37. Mass spectrum of compound 9.

### 3.2.16 Synthesis of Compound xi

0.45 g (1.31 mmol) of HO-(D)Leu-Suc-(L)-Leu-OH (**5**) in 2 mL of DMF was cooled in an ice-water bath. (L)-Leu-OMe was isolated from 0.95 g (5.23 mmol) of the corresponding methyl ester hydrochloride by neutralization and subsequent extraction with ethyl acetate and the extracted ethyl acetate was concentrated to 8 mL. It was then added to the reaction mixture, followed immediately by 0.45 g (2.88 mmol) EDC and 0.35 g (2.62 mmol) of HOBt. The reaction mixture was stirred for overnight. The reaction mixture was diluted to 50 mL with ethyl acetate. The organic layer was washed with 1 M HCl (3 × 50 mL), brine (2 × 50 mL), 1 M Na<sub>2</sub>CO<sub>3</sub> (3 × 50 mL), brine (2 × 50 mL), dried over anhydrous Na<sub>2</sub>SO<sub>4</sub> and evaporated in vacuo to yield **xi** as a white solid. Purification was done by silica gel column (100-200 mesh) using ethyl acetate-hexane as eluent. Yield: 0.6 g (77%), <sup>1</sup>H NMR (400 MHz, DMSO-d<sub>6</sub>): δ = 8.27-8.17 (m, 2H, -NH), 7.98-7.94 (m, 2H, -NH), 4.33-4.23 (m, 4H, C<sup>α</sup>H of Leu), 3.61 (s, 6H, -OCH<sub>3</sub>), 2.39-2.29 (m, 4H, -Hs of Suc), 1.59-1.41 (m, 12H, C<sup>β</sup> and C<sup>γ</sup>Hs of Leu), 0.89-0.82 (m, 24H, C<sup>δ</sup>Hs of Leu) ppm. MS (ESI) m/z for C<sub>30</sub>H<sub>54</sub>N<sub>4</sub>O<sub>8</sub> (M + Na)<sup>+</sup> calcd: 621.3839, found: 621.3867.

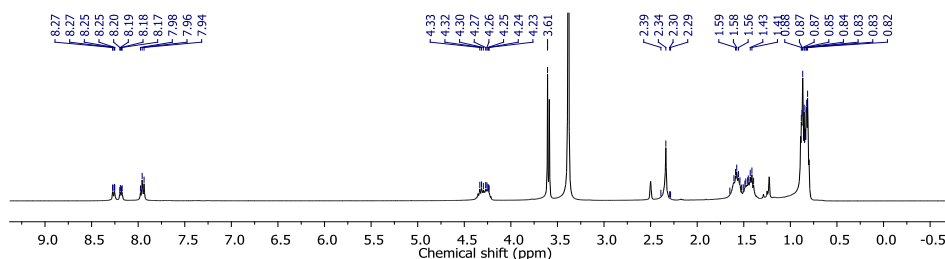
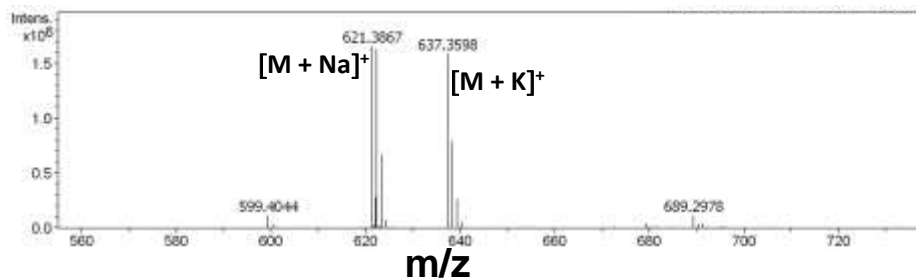


Figure 3.38. <sup>1</sup>H NMR spectrum of compound xi in DMSO-d<sub>6</sub>.



**Figure 3.39.** Mass spectrum of compound **xi**.

### 3.2.17 Synthesis of Compound 10

0.32 g (0.62 mmol) of MeO-(L)-Leu-(D)-Leu-Suc-(L)-Leu-(L)-Leu-OMe (**xi**) in 10 mL MeOH was taken in a round bottom flask and 1 M NaOH was added to it dropwise. The reaction mixture was stirred and was continuously monitored by thin layer chromatography (TLC) till the completion of the reaction. The reaction was completed after 3 h. MeOH was removed under vacuo and 10 mL of distilled water was added to the reaction. The aqueous part was washed with diethyl ether (2 x 30 mL). Then the collected aqueous layer was cooled under ice-water bath for 10 minute and then pH was adjusted to 1 by drop wise addition of 1M HCl. It was extracted with ethyl acetate (3 x 50 mL) and then the ethyl acetate part was dried over anhydrous Na<sub>2</sub>SO<sub>4</sub> and evaporated in vacuo to yield **10** as a white solid. Yield = 0.25 g (82%), <sup>1</sup>H NMR (400 MHz, DMSO-d<sub>6</sub>): δ = 12.44 (s, 2H, -Hs of -COOH) 8.12-7.91 (m, 4H, -NH), 4.36-4.13 (m, 4H, C<sup>α</sup>H of Leu), 2.36-2.29 (m, 4H, -CH<sub>2</sub> of Suc), 1.63-1.36 (m, 12 H, C<sup>β</sup> and C<sup>γ</sup>Hs of Leu), 0.88-0.79 (m, 24H, C<sup>δ</sup>Hs of Leu) ppm. <sup>13</sup>C NMR (100 MHz, DMSO-d<sub>6</sub>): δ = 174.36, 172.66, 171.72, 51.12, 50.65, 31.32, 24.72, 23.32, 22.11, 21.67 ppm. MS (ESI) m/z for C<sub>28</sub>H<sub>50</sub>N<sub>4</sub>O<sub>8</sub> (M + Na)<sup>+</sup> calcd: 593.3526, found: 593.3573.

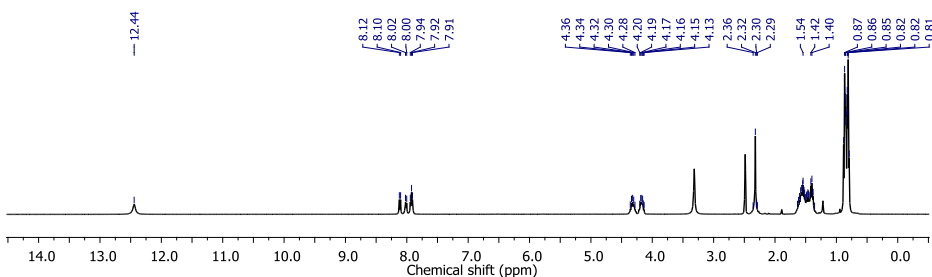


Figure 3.40.  $^1\text{H}$  NMR spectrum of compound **10** in  $\text{DMSO-}d_6$ .

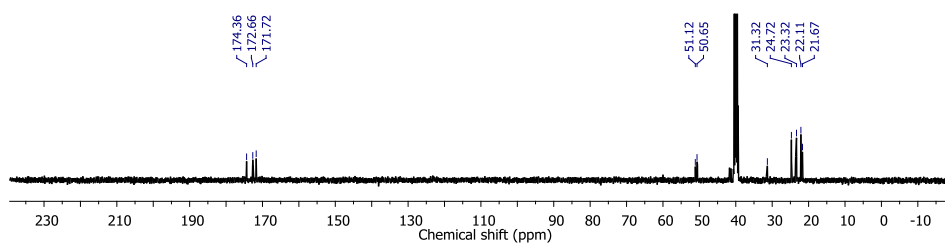


Figure 3.41.  $^{13}\text{C}$  NMR spectrum of compound **10** in  $\text{DMSO-}d_6$ .

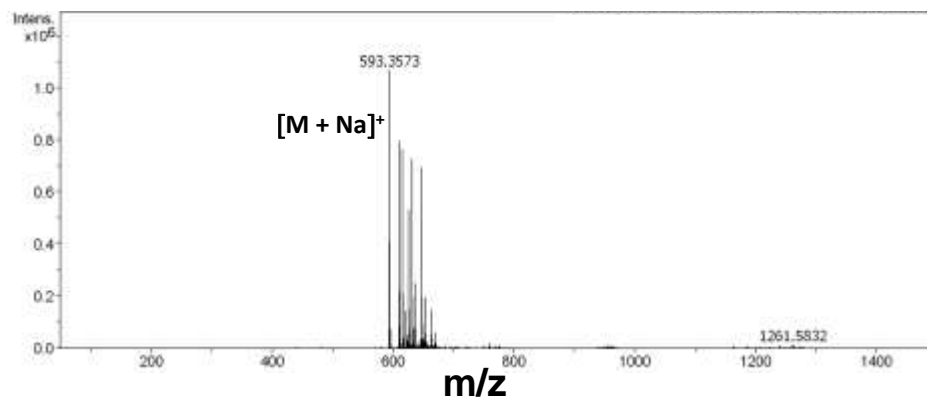
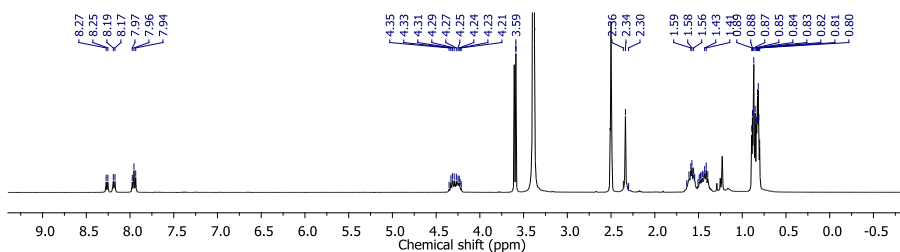


Figure 3.42. Mass spectrum of compound **10**.

### 3.2.18 Synthesis of Compound xii

0.5 g (1.45 mmol) of HO-(D)Leu-Suc-(L)-Leu-OH (**5**) in 2 mL of DMF was cooled in an ice-water bath. (D)-Leu-OMe was isolated from 1.05 g (5.81 mmol) of the corresponding methyl ester hydrochloride by neutralization and subsequent extraction with ethyl acetate and the extracted ethyl acetate was concentrated to 8 mL. It was then added to the reaction mixture, followed immediately by 0.49 g (3.19 mmol) EDC and 0.39 g (2.9 mmol) of HOBt. The reaction mixture was stirred for overnight. The reaction mixture was diluted to 50 mL with ethyl acetate.

The organic layer was washed with 1 M HCl (3 × 50 mL), brine (2 × 50 mL), 1 M Na<sub>2</sub>CO<sub>3</sub> (3 × 50 mL), brine (2 × 50 mL), dried over anhydrous Na<sub>2</sub>SO<sub>4</sub> and evaporated in vacuo to yield **xii** as a white solid. Purification was done by silica gel column (100-200 mesh) using ethyl acetate-hexane as eluent. Yield: 0.7 g (81%), <sup>1</sup>H NMR (400 MHz, DMSO-d<sub>6</sub>): δ = 8.27-8.17 (m, 2H, -NH), 7.97-7.94 (m, 2H, -NH), 4.35-4.21 (m, 4H, C<sup>α</sup>H of Leu), 3.59 (s, 6H, -OCH<sub>3</sub>), 2.36-2.30 (m, 4H, -Hs of Suc), 1.59-1.41 (m, 12H, C<sup>α</sup> and C<sup>β</sup>Hs of Leu), 0.89-0.80 (m, 24H, C<sup>δ</sup>Hs of Leu). MS (ESI) m/z for C<sub>30</sub>H<sub>54</sub>N<sub>4</sub>O<sub>8</sub> (M + Na)<sup>+</sup> calcd: 621.3839, found: 621.3808.



**Figure 3.43.** <sup>1</sup>H NMR spectrum of compound **xii** in DMSO-d<sub>6</sub>.

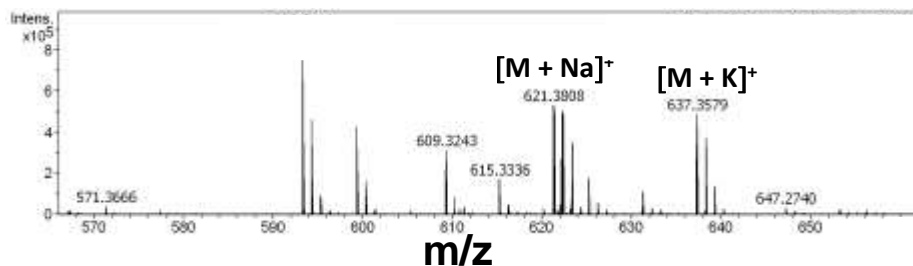


**Figure 3.44.** Mass spectrum of compound **xii**.

### 3.2.18 Synthesis of Compound 11

0.37 g (0.62 mmol) of MeO-(D)-Leu-(D)-Leu-Suc-(L)-Leu-(D)-Leu-OMe (**xii**) in 10 mL MeOH was taken in a round bottom flask and 1 M NaOH was added to it dropwise. The reaction mixture was stirred and was continuously monitored by thin layer chromatography (TLC) till the completion of the reaction. The reaction was completed after 3 h. MeOH was removed under vacuo and 10 mL of distilled water was added to the reaction. The aqueous part was washed with diethyl ether (2 × 30 mL).

Then the collected aqueous layer was cooled under ice-water bath for 10 minute and then pH was adjusted to 1 by dropwise addition of 1M HCl. It was extracted with ethyl acetate (3 x 50 mL) and then the ethyl acetate part was dried over anhydrous  $\text{Na}_2\text{SO}_4$  and evaporated in vacuo to yield **11** as a white solid. Yield = 0.31 g (90%).  $^1\text{H}$  NMR (400 MHz,  $\text{DMSO-d}_6$ ):  $\delta$  = 8.27-8.17 (m, 2H, -NH), 7.95-7.93 (m, 2H, -NH), 4.35-4.21 (m, 4H,  $\text{C}^\alpha\text{H}$  of Leu), 2.39-2.28 (m, 4H, -Hs of Suc), 1.58-1.41 (m, 12H,  $\text{C}^\beta$  and  $\text{C}^\gamma\text{H}$ s of Leu), 0.88-0.81 (m, 24H,  $\text{C}^\delta\text{H}$ s of Leu) ppm.  $^{13}\text{C}$  NMR (100 MHz,  $\text{DMSO-d}_6$ ):  $\delta$  = 173.28, 172.72, 171.81, 52.20, 50.71, 31.25, 24.64, 23.39, 23.23, 22.15, 21.77 ppm. MS (ESI)  $m/z$  for  $\text{C}_{28}\text{H}_{50}\text{N}_4\text{O}_8$  ( $\text{M} + \text{H}$ ) $^+$  calcd: 571.3707, found: 571.3700.

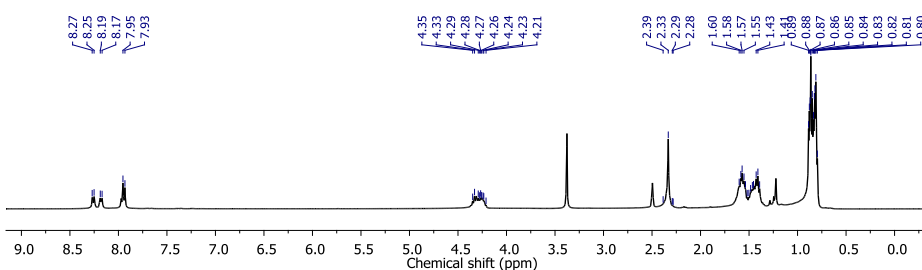


Figure 3.45.  $^1\text{H}$  NMR spectrum of compound **11** in  $\text{DMSO-d}_6$ .

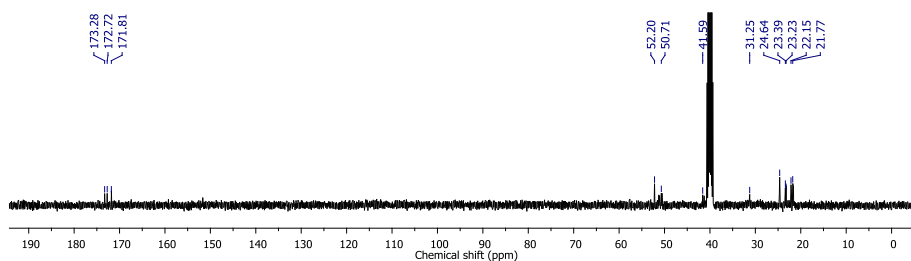


Figure 3.46.  $^{13}\text{C}$  NMR spectrum of compound **11** in  $\text{DMSO-d}_6$ .

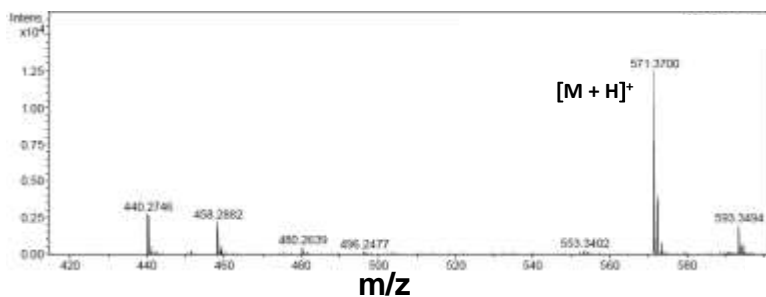


Figure 3.47. Mass spectrum of compound **11**.

## 3.3 Gel Preparation and Characterization Techniques

### 3.3.1 Preparation of hydrogels

11.4 mg (20 mM) of **6** was taken in a clean sample vial and 1 mL of sodium phosphate buffer solution (100 mM, pH = 7.4) was added to it. The resultant mixture was sonicated up to 2 minutes to complete the dissolution of the bolaamphiphile and a transparent solution was obtained. 3 mg (20 mM) of solid D/L-tartaric acid was added with the clear solution. Thereafter to obtain a homogeneous mixture, it was again sonicated for 2 minutes and vortexed well. The resultant mixtures were kept for 5 minutes to achieve self-supporting hydrogels **3**, **4**. Bolaamphiphiles **3**, **4**, **7-11** were also tried with the same method but gelation was not observed. NaOH / HCl method was also used to prepare the hydrogels of **3-11** at different pHs. However, gelation was not observed with bolaamphiphiles **3-11** at different pHs. 11.4 mg (20 mM) of **6** and 3 mg (20 mM) of solid D/L-tartaric acid were taken in a clean sample vial and 700  $\mu$ L of water was added to it. The resultant mixture was basified with 0.5 M NaOH to complete the dissolution of the bolaamphiphile and a transparent solution was obtained. Further, the solution was acidified with 0.1 M HCl solution to maintain the pH 7.4. However, gelation was not observed. Similarly, gelation was tried with **3-11** with the same method but gelation was not observed.

### 3.3.2 Rheological Experiments

Rheological study was performed to determine the mechanical properties of the hydrogels. These properties were assessed using an Anton Paar Physica Rheometer (MCR 301, Austria) with parallel plate geometry (25 mm in diameter) and temperature was controlled at 25 °C. The dynamic

moduli of the hydrogels were measured as a function of frequency in the range of 0.1-100 rad s<sup>-1</sup> with a constant strain value 0.1%.

### 3.3.3 Microscopic Techniques

Field emission scanning electron microscope (FE-SEM Supra 55 Zeiss) was used for morphological analysis. The solutions of bolaamphiphiles (**3-11**), Hydrogels **3**, **4**, **5** and all other co-assembled systems (**7-11**) were directly dried on cover slip and coated with gold for SEM analysis with an operating voltage of 5 kV. Transmission electron microscopic images were taken using a PHILIPS electron microscope (model: CM-200), operated at an accelerating voltage of 200 kV. 100  $\mu$ L of the solution (20 mM) of **6** in phosphate buffer solution (100 mM) was diluted to 200  $\mu$ L of double distilled water. The hydrogels (100  $\mu$ L) were also diluted to 200  $\mu$ L of double distilled water for TEM sample analysis. Dilute solutions of the samples were drop-casted on carbon-coated copper grids (300 mesh) and stained with sodium phosphotungstic acid. Then the grid was dried by slow evaporation in air and then allowed to dry separately in a vacuum at room temperature.

### 3.3.4 FT-IR spectroscopy

All reported FT-IR spectra were recorded with a Bruker (Tensor 27) FT-IR spectrophotometer. The solid-state measurements were performed using the KBr pellet technique with a scan range between 400 and 4000 cm<sup>-1</sup> over 64 scans at a resolution of 4 cm<sup>-1</sup> and an interval of 1 cm<sup>-1</sup>. In FT-IR analysis, **6** was directly used and the hydrogels were dried in vacuum to obtain xerogel prior to the experiment.

### 3.3.5 Wide angle X-ray diffraction

The powder X-ray diffraction (PXRD) measurements were carried out using a Bruker D8 Advance X-ray diffractometer. The X-rays were produced using a sealed tube and the wavelength of the X-rays was 0.154

nm (Cu K $\alpha$ ). The X-rays were detected using a fast counting detector based on silicon strip technology (Bruker LynxEye detector). In PXRD analysis, **6** was used directly and the hydrogels (2 mL, 20 mM) were dried under vacuum prior to the PXRD analysis.

### 3.3.6 Circular Dichroism Spectrometer

CD spectra of **3-11** were analyzed with Jasco J-815 Circular Dichroism (CD) spectrometer. The final concentrations of **3-11** were 400  $\mu$ M for CD experiment. The pH dependent and water medium CD experiments were carried out at pH 6, pH 7.4 by NaOH/HCl pH adjustment method. In each case, the concentrations were 400  $\mu$ M. For concentration dependent CD experiment, different bicomponent systems were developed by varying the concentration of D/L-tartaric acid. In each case, the concentration of bolaamphiphile **6** was same (20 mM). The initial concentration of the composite with a proportion of **6** : D/L-tartaric acids were 20 mM : 0 mM; 20 mM : 4 mM; 20 mM : 8 mM; 20 mM : 12 mM; 20 mM : 16 mM; and 20 mM : 20 mM. The composites (**6**: D/L-tartaric acids) were then diluted in double distilled water to the final concentration of 250  $\mu$ M : 0  $\mu$ M; 250  $\mu$ M : 50  $\mu$ M; 250  $\mu$ M : 100  $\mu$ M; 250  $\mu$ M : 150  $\mu$ M; 250  $\mu$ M : 200  $\mu$ M and 250  $\mu$ M : 250  $\mu$ M for the CD experiments. The other co-assembled systems of **7-11** with D/L-tartaric acid were also carried out at a concentration ratio of 250  $\mu$ M : 250  $\mu$ M. The diluted samples were then measured from 250 to 190 nm with 0.1 data pitch, 20 nm min<sup>-1</sup> scanning speed, 1 nm bandwidth, and 4 s D.I.T.

## 3.4 Results and Discussion

In this chapter, we synthesized a series of dipeptide appended bolaamphiphiles **6-11** which contain D/L-leucine to investigate the effect of peptide sequences with different chirality on bicomponent hydrogelation (Table 3.1).

**Table 3.1.** Molecular structure of bolaamphiphiles **3-11** with absolute configuration of amino acids. CD behavior of **3-11** and physical appearance of **3-11** with addition of D-tartaric acid (DTA) and L-tartaric acid (LTA). CD behaviors of bicomponent systems are also presented.

Compounds	Configuration of amino acids with respect to position				CD spectra	External stimuli	Physical texture	CD Spectra of mixture
	2'	1'	1	2				
<b>3</b>	*	L	L	*	(+)Ve	DTA LTA	Clear Sol Clear Sol	(+) Ve (+) Ve
<b>4</b>	*	D	D	*	(-)Ve	DTA LTA	Clear Sol Clear Sol	(-) Ve (-) Ve
<b>5</b>	*	L	D	*	Silent	DTA LTA	Clear Sol Clear Sol	(+) Ve (-) Ve
<b>6</b>	L	L	L	L	(-)Ve	DTA LTA	Hydrogel 3 Hydrogel 4	(+) Ve (-) Ve
<b>7</b>	D	D	D	D	(+)Ve	DTA LTA	Viscous Sol Viscous Sol	(+) Ve (+) Ve
<b>8</b>	D	L	L	D	(-)Ve	DTA LTA	Viscous Sol Viscous Sol	(-) Ve (-) Ve
<b>9</b>	L	D	D	L	(+)Ve	DTA LTA	Viscous Sol Viscous Sol	(+) Ve (+) Ve
<b>10</b>	L	L	D	L	(+)Ve	DTA LTA	Viscous Sol Viscous Sol	(+) Ve (+) Ve
<b>11</b>	D	L	D	D	(-)Ve	DTA LTA	Viscous Sol Viscous Sol	(-) Ve (-) Ve

\***3-5** contains only two amino acids, and there is no second (2,2') amino acid. Whereas **6-11** each contains four (4) amino acids. “(-)Ve” signifies negative CD signal whereas “(+)Ve” denoted positive CD signal. For compounds **3-11**, the magnitude of CD signals [(-)Ve or (+)Ve] was considered based on the first band from longer wavelength.

L-leucine based dipeptide appended bolaamphiphile **6** (20 mM) does not form hydrogel without the influence of any external component at pH = 7.4.<sup>57</sup> Hydrogelation was also tried in water. The bolaamphiphiles are not sufficiently soluble in water. Therefore, NaOH/HCl method was used to enhance the solubility and maintain the pH 7.4. Bolaamphiphiles didn't

form hydrogel at pH 7.4. The hydrogelation was also tried with other bolaamphiphiles **3-11** at a pH of 6. Bolaamphiphiles **3-11** do not produce any gel and exhibit as clear solution.

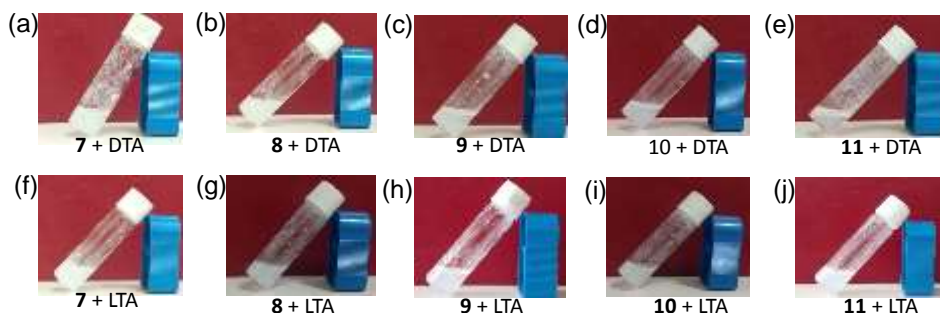


**Figure 3.48.** Images of bolaamphiphiles **7-11** with D/L-tartaric acid.

Therefore, equimolar (20 mM) of D-tartaric acid, L-tartaric acid and meso-tartaric acid was added separately into the sodium phosphate buffer solution (100 mM, pH = 7.4) of **3-11** to develop the supramolecular chiral nanostructure in hydrogel state. Selectively, **6** forms hydrogel (Table 4.1) with L/D-tartaric acid (20 mM) and **9** selectively forms hydrogel with meso-tartaric acid (MTA). At higher concentration (30 mM), only **6** forms hydrogel with D/L-tartaric acid. The hydrogelation was not observed for **7-11**. However, viscous solution was observed (Table 3.1, Figure 3.48). Compounds **3-5** exhibited as transparent solution after addition of L/D-tartaric acid.

### 3.4.1 Rheological Study

The rheological experiments illustrate the mechanical (viscoelastic) properties of the hydrogels.<sup>[58]</sup> A rigid hydrogel is defined in practice of having a storage modulus ( $G'$ ) higher than the loss modulus ( $G''$ ) at variable angular frequency regime. The storage moduli of both hydrogels **3** and **4** are higher than the loss moduli throughout the frequency range (Figure 3.49). The value of the storage modulus ( $G'$ ) of the hydrogel **3** is greater than the storage modulus ( $G'$ ) of hydrogel **4**. The higher storage modulus of hydrogel **3** in comparison to hydrogel **4** signifies that

bolaamphiphile **6** performs better co-assembly with D-tartaric acid in comparison to L-tartaric acid. However, both describe the formation of strong and rigid hydrogels.

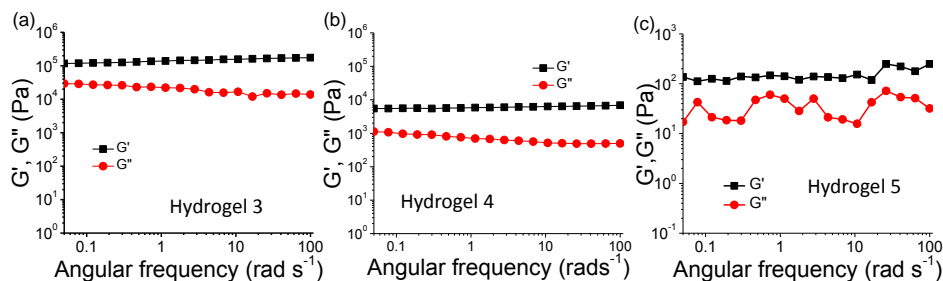


**Figure 3.49.** (a), (b) and (c) represent the frequency sweep experiment data of the hydrogels **3**, **4** and hydrogel **5** (**9** + MTA) respectively. Both signify rigid hydrogel formation.

Hydrogel **3** is also considered as a gel from rheological study. However, hydrogel **3** is comparatively weaker as the storage modulus is less in comparison to hydrogels **3**, **4**. The co-assembled systems of D/L-tartaric acid with bolaamphiphiles **7-11** exhibited as viscous solution or semi gel. Therefore, these co-assembled systems were also studied by rheological experiments. In each case, the storage modulus and loss modulus intersect each other. These data signify that gel was not formed after co-assembly.

### 3.4.2 Morphological Investigation

Scanning electron microscopy (SEM) was performed for clear visualization of the formed morphology in hydrogels **3** and **4** and all other co-assembled systems. Initially, the morphology of the solution of bolaamphiphiles at a pH of 6 was analyzed. Leucine appended bolaamphiphiles **3**, **4**, **5** do not form any specific morphology whereas dipeptide appended bolaamphiphiles (**7-10**) form large spherical aggregates (Figure 3.50). The co-assembled systems (**7-10**) were exhibited as viscous solutions but no crosslinked nanostructures were observed from the SEM experiments (Figure 3.51 a-i). Hydrogel **5** produces nanorods but no chiral twists are developed in the gel state (Figure 3.51 i). SEM image

of hydrogel **3** (**6** + DTA) clearly shows multiple small and narrow P-helical fibers with average diameter of 100 nm. Higher order self-assembly forms large right-handed (P-helical) fibers. Hydrogel **4** (**6** + LTA) forms left-handed fibers (M-helical), which was visualized from SEM (Figure 3.52) study.

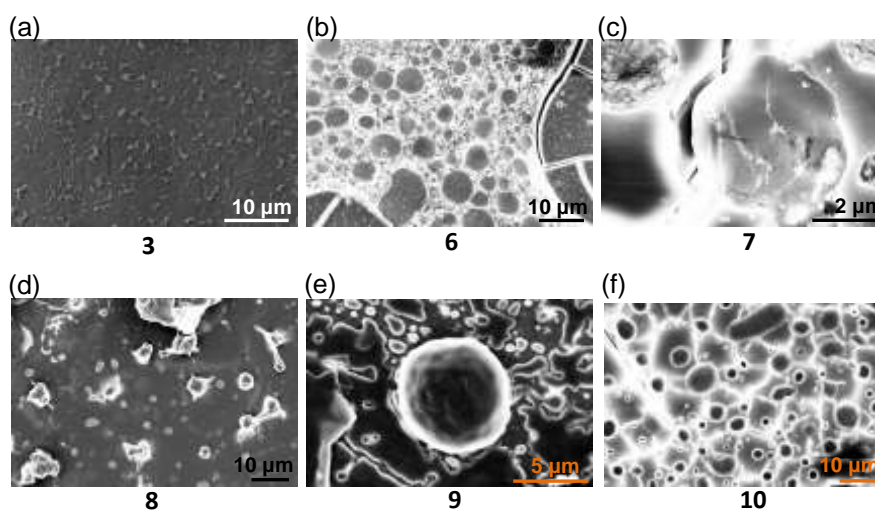


**Figure 3.50.** SEM images of bolaamphiphiles **3** and **6-10** at pH 6.

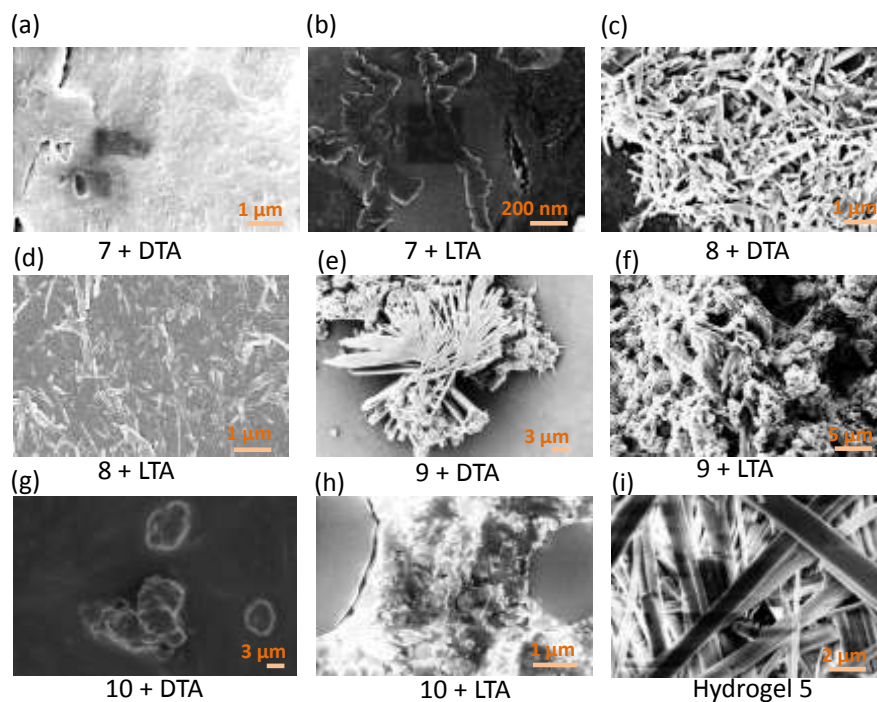


**Figure 3.51.** SEM images of co-assembled systems **7-10** with *L/D*-tartaric acid and hydrogel **5**.

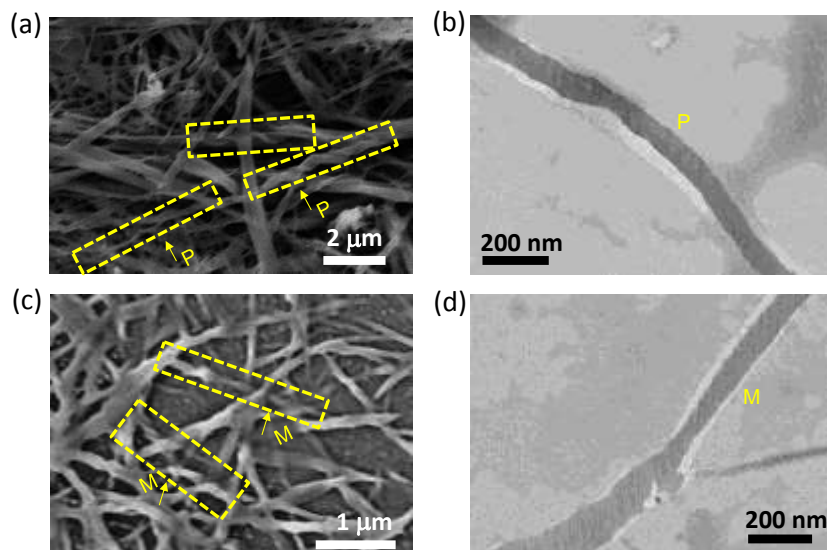


**Figure 3.52.** (a), (b) SEM and TEM images of hydrogel 3 showing right-handed (*P*-helix) nanofiber and (c), (d) are the SEM and TEM images of hydrogel 4 showing left-handed (*M*-helix) nanofiber.

Transmission electron microscopy (TEM) was also performed to know the more insight of the nanostructure of hydrogels. The TEM image of **6** (pH 7.4) shows spherical aggregates with average diameter of 105 nm and the wall thickness is about ~8 nm (Figure 3.53a, Figure 3.54).

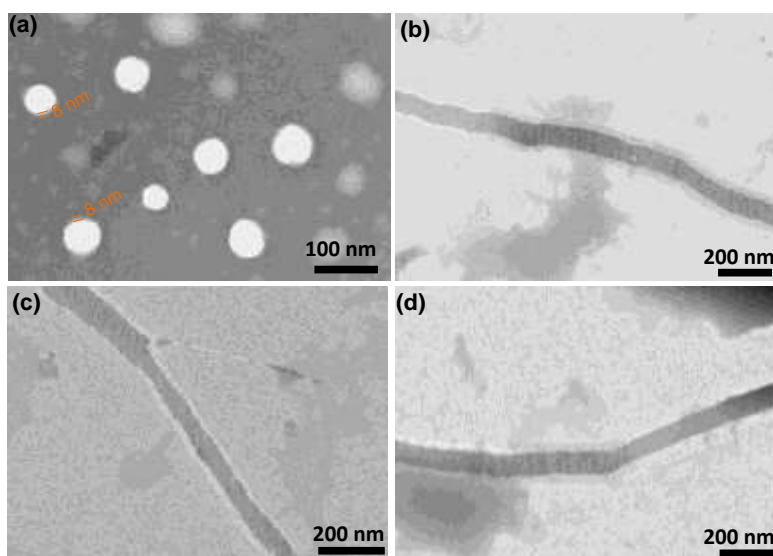


**Figure 3.53.** (a) TEM image of **6** showing vesicles. (b), (c) Show the TEM images of right handed helical fibers of hydrogel 3 (**6** + DTA). (d) The TEM image of hydrogel 4 (**6** + LTA) showing left-handed helical fibers.

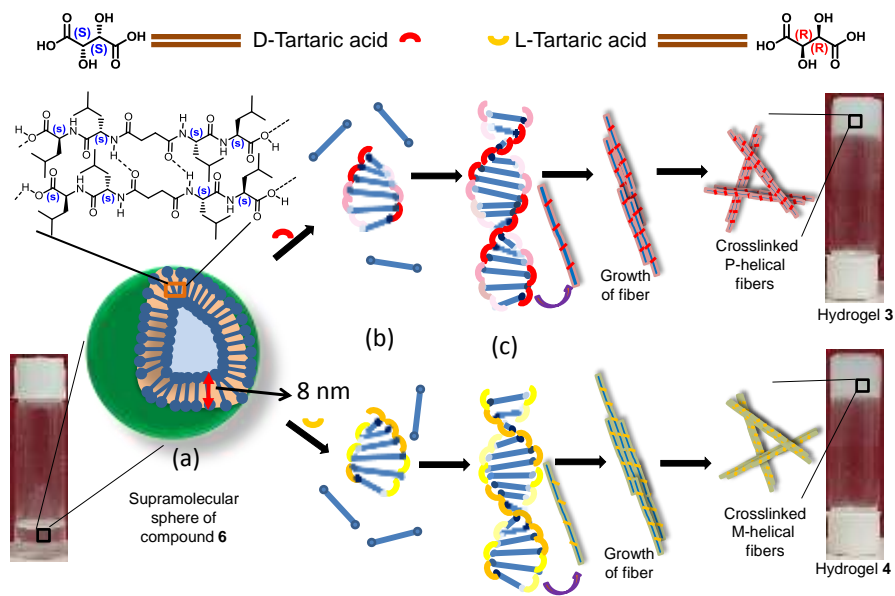


**Figure 3.54.** (a) Showing the formation of spheres comprised with **6**. The spheres ruptured on interaction with D-tartaric acid and L-tartaric acid. (b) Shows the nucleation of the small helical unit with D-tartaric acid and L-tartaric acid. (c) The growth of right-handed helical fiber with D-tartaric acid and left-handed helical fiber with L-tartaric acid. Higher order self-assembly of right-handed and left-handed chiral nanofibers and resulting formation of crosslinked helical nanofibrous hydrogels **3** and **4**.

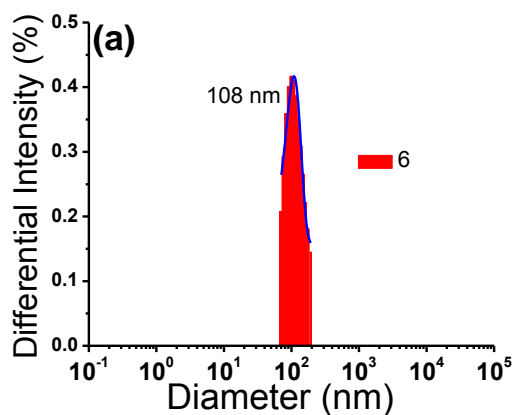


**Figure 3.55.** (a) DLS spectra of formed spherical aggregates of compound **6**.

This is attributed to the self-assembly (Figure 3.54) of **6** without D/L-tartaric acid. Hydrogel **3** forms right-handed (P-helical) nanofibers with average diameter of 45 nm (Figure 3.52, Figure 3.53). Hydrogel **4** forms helical nanofibers with a left-handed (M-helical) twist having average

diameter of 43 nm (Figure 3.52, Figure 3.53). From both SEM and TEM images, it was found that the helical fibers were formed only after the co-assembly (Figure 3.54) of **6** with D/L-tartaric acid. To understand the sphere formation, dynamic light scattering (DLS) experiment was performed with a colloidal suspension of **6** (20 mM) in phosphate buffer solution (pH 7.4). DLS data gives clear evidence for the formation of spherical aggregates by **6** with an average diameter of 109 nm (Figure 3.55).

### 3.4.3 FT-IR Spectroscopy

The mechanistic investigation of the co-assembly in hydrogels was carried out by FT-IR spectroscopy. In native form, **6** shows only amide-II, amide-I band and C=O stretching vibrations of acid at 1550, 1646 and 1730  $\text{cm}^{-1}$  (Figure 3.56).<sup>[59]</sup> The peak at 3312  $\text{cm}^{-1}$  exhibits due to the presence of hydrogen bonded –NH of amide group.

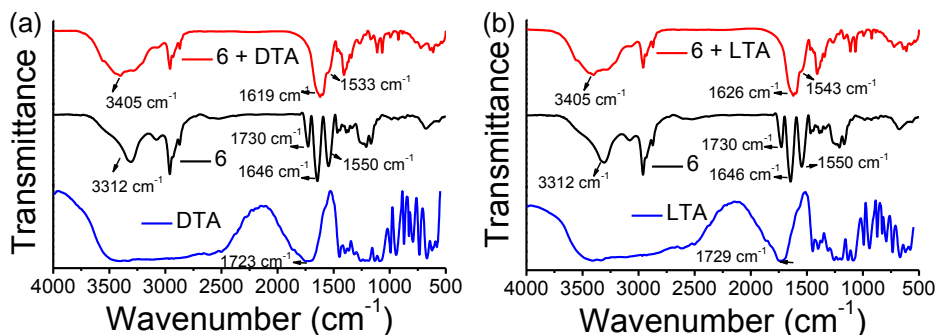


**Figure 3.56.** (a), (b) are the overlaid FTIR spectra of hydrogel **3** (**6** + DTA) and hydrogel **4** (**6** + LTA) respectively.

D-tartaric acid shows peak at 1723  $\text{cm}^{-1}$  for C=O stretching frequency and a broad peak from 2100-4000  $\text{cm}^{-1}$  for –OH and –OH of carboxylic acid group. Hydrogels **3** and **4** show peaks at 1619, 1626 and 1533, 1543  $\text{cm}^{-1}$  for amide-I and amide-II respectively (Figure 3.56a,b). The peaks at ~1619 and 1626  $\text{cm}^{-1}$  correspond to the hydrogen bonded amide stretching frequencies of hydrogels **3** and **4** respectively.<sup>[60]</sup>

Small change in stretching frequencies of amide-I and amide-II was observed in the co-assembled hydrogels **3** and **4**. This signifies better hydrogen bonding between **6** and D-tartaric acid in the hydrogel **3** in comparison to hydrogel **4** (**6** with L-tartaric acid) as the peak shifted more in hydrogel **3**. The presence of hydrogen bonding was also supported by the appearance of new peaks at  $3276$  and  $3405\text{ cm}^{-1}$  for hydrogen bonded  $\text{-NH}$  stretching of amide.<sup>61</sup> Similar terminal hydrogen bonding between bolaamphiphile and D-tartaric acid was also reported by Liu *et. al.*<sup>56</sup>

### 3.4.4 Powder X-ray diffraction Study

The powder X-ray diffraction (PXRD) study was performed to know the detail about the co-assembly occurred between **6** and D/L-tartaric acids in hydrogels (Figure 3.57). In PXRD, **6** exhibits strong characteristic peaks at  $2\theta$  of  $6.86^\circ$ ,  $8.11^\circ$ ,  $12.77^\circ$  and  $19.40^\circ$ .

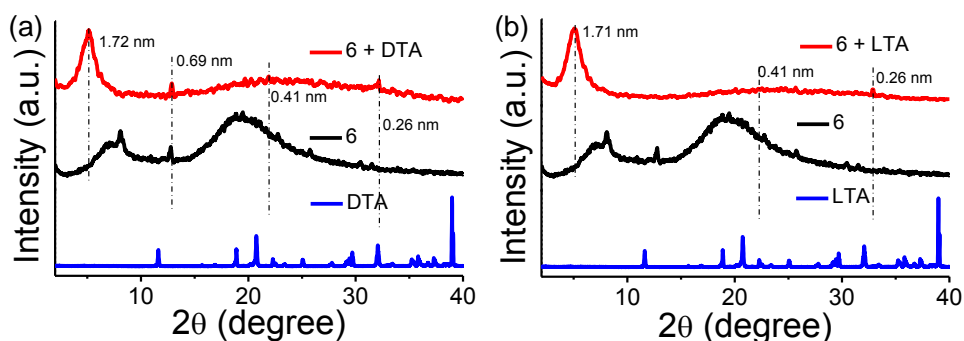


**Figure 3.57.** (a), (b) are the overlaid powder X-ray diffraction spectra of hydrogel **3** (**6** + DTA) and hydrogel **4** (**6** + LTA) respectively.

D/L-tartaric acids both show characteristic peaks which are disappeared after formation of hydrogels **3** and **4** (with L-tartaric acid). The peaks at  $6.86^\circ$  and  $8.11^\circ$  in **6** are exhibited for the d spacing of  $1.28$  and  $1.08$  nm corresponding to the formation of self-assembled monolayer.<sup>62</sup> The hydrogel **3** (with D-tartaric acid) shows peaks at  $2\theta$  of  $5.13^\circ$ ,  $12.85^\circ$ ,  $21.93^\circ$  and  $33.38^\circ$  (Figure 3.57a), which signify the co-assembly in hydrogel state.

The hydrogel **4** (with L-tartaric acid) shows peaks at  $2\theta$  of  $5.16^\circ$ ,  $22.09^\circ$  and  $33.7^\circ$  (Figure 3.57b). The peaks for self-assembled monolayer are disappeared in hydrogels **3** and **4** and new peaks appear at  $5.13^\circ$ ,  $5.16^\circ$  signifying the d spacing of 1.72 nm, 1.71 nm. The d spacing corresponds to the distance between two peptide bolaamphiphiles. In hydrogels **3** and **4**, the d spacing value of 0.41 nm signifies the distance between the alkyl groups present in leucine of two bolaamphiphiles.<sup>[63]</sup> Hydrogels **3** and **4** reveal d spacing of 0.26 nm corresponding to the peak at  $2\theta$  of  $33.45^\circ$  and  $33.7^\circ$  respectively due to the involvement through hydrogen bonding. In hydrogel **3**, one additional peak was found at a d spacing of 0.54 nm which is absent in hydrogel **4**. This suggests different co-assembly pattern in both the hydrogels.

### 3.4.5 $^1\text{H}$ NMR Study

The concentration dependent NMR study shows significant change in the -Hs of D/L-tartaric acid. NH groups of amides of **6** exchanged to ND in presence of  $\text{D}_2\text{O}$ . ND peaks remain silent in  $^1\text{H}$  NMR experiments. The -Hs of tartaric acid significantly shift to up field in  $^1\text{H}$  NMR for both the hydrogels **3**, **4**. This shift signifies that significant interaction occurs in gel state (Figure 3.58).

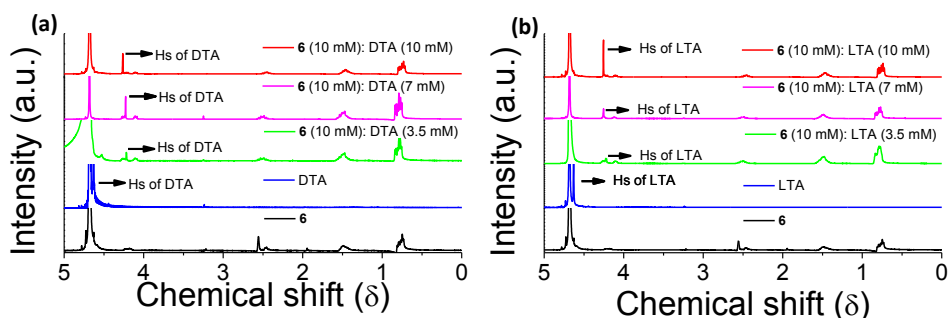


**Figure 3.58.** Concentration dependent NMR spectra of hydrogel **3** with different proportion of D-tartaric acid in  $\text{D}_2\text{O}$ . Concentration dependent NMR spectra of hydrogel **4** with different proportion of L-tartaric acid in  $\text{D}_2\text{O}$ .

## 3.4.6 Investigation of Supramolecular Chirality

To understand the effect of chirality of each amino acid in bolaamphiphile on bicomponent helical nanostructured hydrogel, it is necessary to perform the circular dichroism study. Therefore, the CD experiments, of the synthesized bolaamphiphiles **3-11** were studied thoroughly.

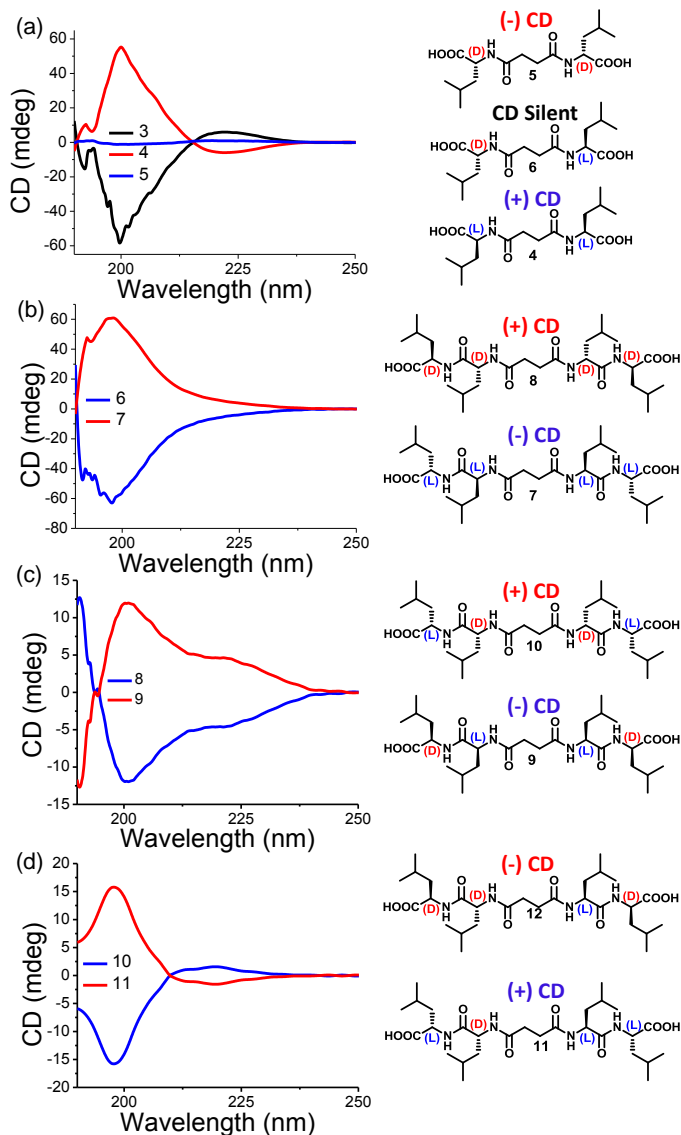


**Figure 3.59.** Circular dichroism spectra of **3-11** showing positive and negative spectra depending upon the configuration of the amino acids present in peptides. In all the cases, the concentrations of the bolaamphiphiles (**3-11**) were 400  $\mu\text{M}$ .

Amino acid functionalized bolaamphiphiles **3-5** are the base unit of dipeptide capped bolaamphiphiles. Therefore, at first **3-5** were taken into consideration for CD study. Bolaamphiphile **3** composed with L-leucine (Table 3.1) exhibits a strong negative peak at 199 nm (Figure 3.59) due to the transition from  $\pi\text{-}\pi^*$  of C=O group of amide and a small positive peak appears at 222 nm corresponding to  $n\text{-}\pi^*$  transition.<sup>[64]</sup> A CD spectrum of **2** shows the mirror image spectra of **1**, as **2** is made of D-leucine (Table 3.1).

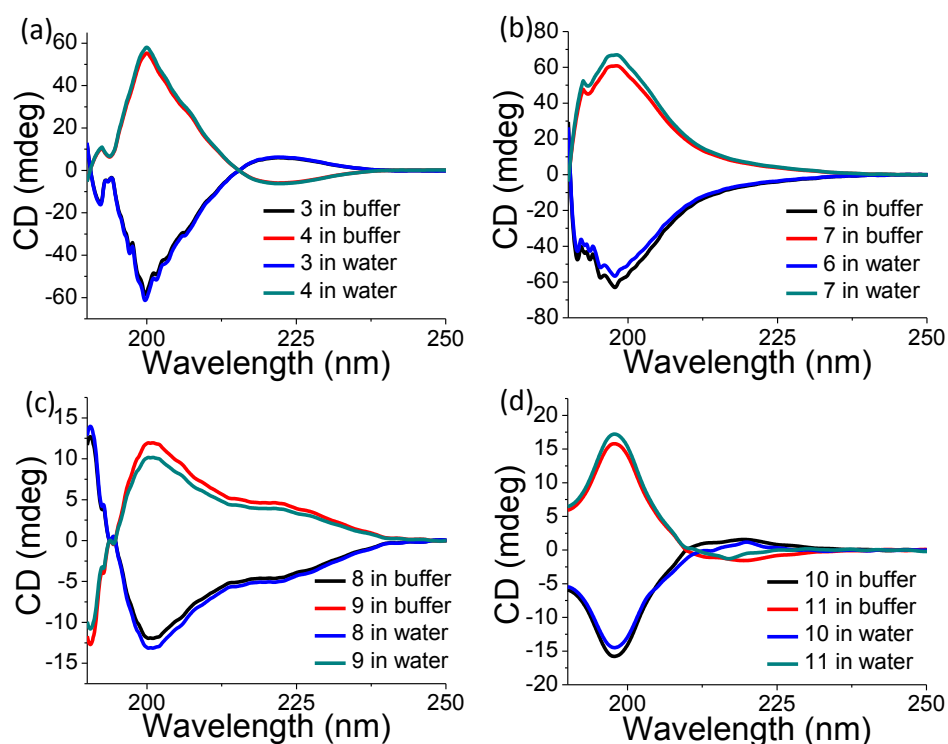


**Figure 3.60.** CD spectra in water and buffer solution of bolaamphiphiles **4-12**. In all the cases, the concentrations of the bolaamphiphiles were 400  $\mu\text{M}$ .

When two end of succinic acid possesses L-leucine and D-leucine (**3**) then it becomes CD silent (Figure 3.59, Table 3.1). A strong negative and positive peak at 197 nm (Figure 3.59) is observed for **6** and **7** respectively due to the  $\pi\text{-}\pi^*$  transition of amide (-CONH) group. Two negative CD bands at 201 nm due to  $\pi\text{-}\pi^*$  transition of carbonyl (C=O) group and 222

nm (Figure 3.59) due to  $n-\pi^*$  transition of amide (-CONH) group are observed for **8**.<sup>[61]</sup>

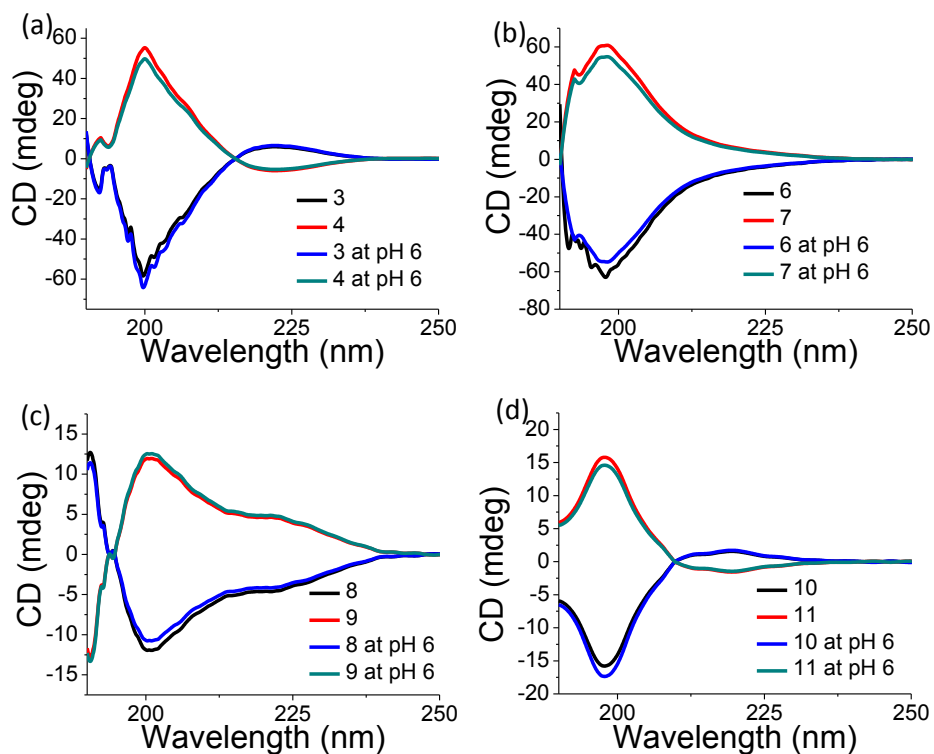


**Figure 3.61.** CD spectra of **3-11** at pH 6 and 7.4. (a) CD spectra of **3, 4**. (b) CD spectra of **6, 7**. (c) CD spectra of **8, 9** and (d) CD spectra of **10, 11**. The concentrations of all compounds were 400  $\mu$ M.

The similar spectra of **8** with opposite magnitude is observed in case of **9**. Bolaamphiphiles **10-11** exhibit L-leucine and D-leucine at first (1,1') position respectively (Table 3.1). A strong negative CD band at 198 nm with a small positive peak appears at 220 nm (Figure 3.59) for **10** as D-leucine at the second (2,2') position. The reverse spectrum of **10** is observed for **11** as the D-leucines are at the second position. The bolaamphiphiles (**6,8**) with L-leucine at first (1,1') position (Table 3.1) show a predominantly negative cotton effect. Similarly, bolaamphiphiles **7,9** consist of D-leucine at first (1,1') position (Table 3.1) give positive spectra. The chirality of leucine at second (2,2') position will be operational for the handedness only if both D-leucine and L-leucine are

present at first (1,1') position respectively. Therefore, the overall chirality of **3-11** depends on the presence of first amino acids whereas the CD band for  $n-\pi^*$  transition is dependent on the second amino acids. The CD spectra of **3-11** were acquired in water medium (Figure 3.60). However, no significant change was observed. The CD experiments were also carried out to know the self-assembly pattern of **3-11** at lower pH. At pH 6, no significant change was observed from the CD spectra (Figure 3.61). D/L-tartaric (20 mM) acid integrates into the solution (20 mM) of dipeptide-appended bolaamphiphiles **6-11**. Bolaamphiphile **6** responds to the chiral stimuli D/L-tartaric acid by forming hydrogels and shows complete inversion of CD spectra with D-tartaric acid (Figure 3.62). Therefore, the concentration dependent CD spectra were performed with bolaamphiphile **6** and D/L-tartaric acid.

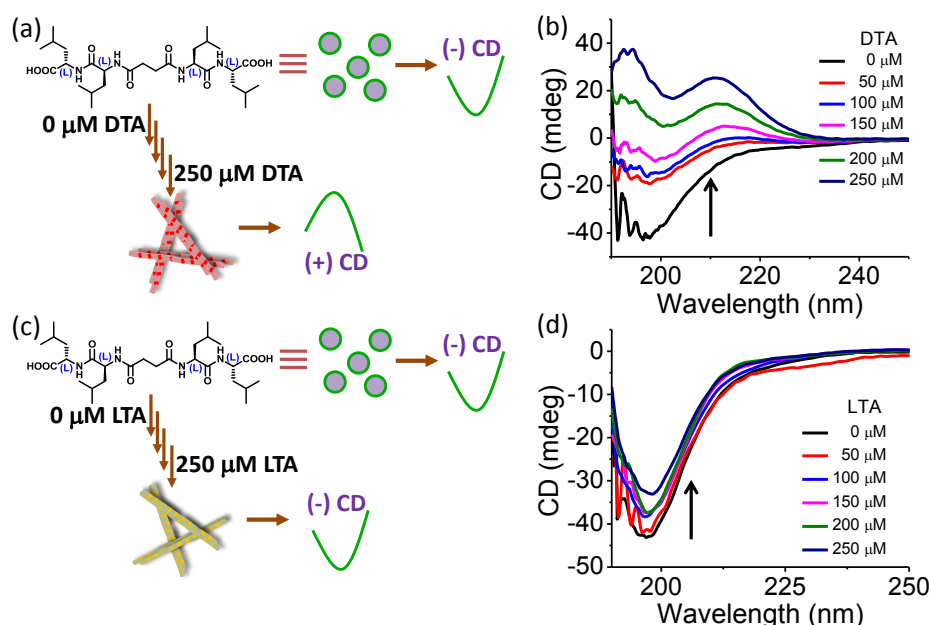


**Figure 3.62.** CD spectra of **7** with variable concentration of D/L-tartaric acid. (a) Shows complete inversion of CD spectra after addition of 250  $\mu\text{M}$  of D-tartaric acid (DTA). (b) Shows small change in CD spectra on addition of L-tartaric acid (LTA). In every case, the concentration of the bolaamphiphile **7** was fixed to 250  $\mu\text{M}$ .

The concentration dependent (0-250  $\mu\text{M}$ ) circular dichroism study of **6** only shows the increment of the peak at 198 nm (Figure 3.63a). Upon addition of different concentration of D/L-tartaric acid into the solution of **6**, the supramolecular chirality changes gradually. The concentration (0-250  $\mu\text{M}$ ) of D-tartaric acid and L-tartaric acid were varied in **6**. Upon addition of 150  $\mu\text{M}$  of D-tartaric acid, a new positive peak generates nearly about 213 nm (Figure 3.62). After addition of equimolar amount (250  $\mu\text{M}$ ) of D-tartaric acid, complete inversion of the CD spectra is observed with the appearance of two peaks at 194 nm and 213 nm. Therefore, the supramolecular chirality dominates at higher concentration (250  $\mu\text{M}$ ) of D-tartaric acid (Figure 3.62). Bolaamphiphile **6** exhibits a peak at 198 with a negative CD on interaction with L-tartaric acid. The gradual increment of L-tartaric acid (0-250  $\mu\text{M}$ ) into the solution of **6** shows small change in CD spectra even after addition of 250  $\mu\text{M}$  of L-tartaric acid. The CD peaks appeared in the co-assembled system are also different for hydrogels **3** and **4**. In case of hydrogel **3**, the  $n-\pi^*$  transition becomes prominent after co-assembly whereas  $\pi-\pi^*$  transition appears prominent for hydrogel **4**. This is attributed to the difference in co-assembly pattern of **6** with D/L-tartaric acid.

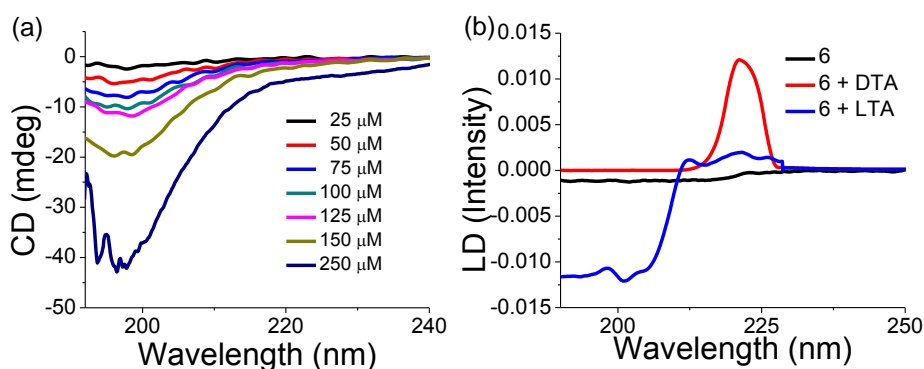


**Figure 3.63.** (a) The concentration dependent CD spectra of bolaamphiphile **6**. (b) Linear dichroism spectra of bolaamphiphile **6**, before and after addition of D/L-tartaric acid.

Therefore it can be concluded that the overall chiral senses of D/L-tartaric acid are transferred to peptide bolaamphiphile **6** to control the supramolecular chirality when the composite forms hydrogels **3** and **4**.<sup>[50,65]</sup> Linear dichroism spectra were recorded to know the detail about induction of supramolecular chirality. In each case, significant change in linear dichroism was observed (Figure 3.63b). Bolaamphiphile **6** shows very less intense negative LD signal.<sup>[66]</sup> After addition of D/L-tartaric acid, supramolecular chirality was induced. The hydrogels **3**, **4** exhibit strong LD signals. Hydrogel **3** shows a positive LD peak at 221 nm due to  $n-\pi^*$  transition. Hydrogel **4** exhibits prominent negative LD signal at 201 nm due to  $\pi-\pi^*$  transition.

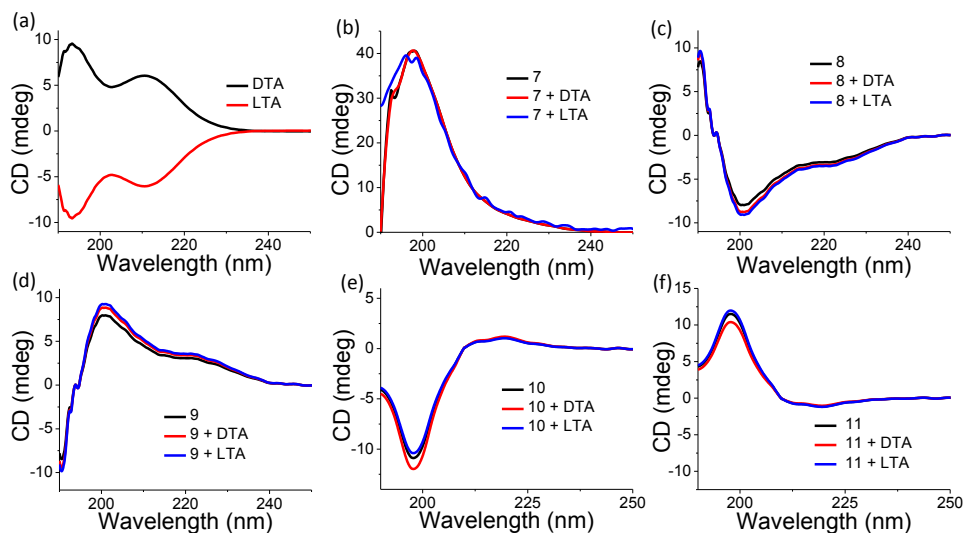


**Figure 3.64.** (a) CD spectra of D/L-tartaric acid. (b), (c), (d), (e) and (f) are the CD spectra of bolaamphiphiles **7-11** with D/L-tartaric acid.

The possible reason behind the selective co-assembly of **6** with D/L-tartaric acid is highly dependent on the synergic chirality. The proper complementary functionality is configurationally more fitted to co-assemble **6** with the D/L-tartaric acid whereas other bolaamphiphiles are not suitably fitted with the D/L-tartaric acid. In this case, chiral-chiral selection of L-leucine appended bolaamphiphile **6** synergistically co-assembles with D/L-tartaric acid using hydrogen bonding interactions. D-

tartaric acid shows positive CD signals whereas L-tartaric acid exhibits negative CD signals. The dipeptide appended bolaamphiphiles, which contain D-leucine (**7-11**), do not form hydrogel with D/L-tartaric acid. Therefore, **7-11** did not show any change in CD spectra after mixing with D/L-tartaric acid (Figure 3.64).

### 3.5 Conclusions

In conclusion, we successfully developed bicomponent hydrogels with controlled right-handed and left-handed twisted fibers. L-leucine based bolaamphiphile **6** co-assembled to form hydrogel. Peptide bolaamphiphiles **7-11** are geometrically not favorable to co-assemble with D-tartaric acid and L-tartaric acids using hydrogen bonding interactions. The overall chiral sense of D/L-tartaric acid was transferred to **6** and nucleation of small chiral unit takes place to control the supramolecular chirality. This nucleation has taken place via the co-assembly between D/L-tartaric acid and **6** through an extensive hydrogen bonding interaction, which was confirmed from FTIR, PXRD and  $^1\text{H}$  NMR experiments. The small nucleated helical unit again integrated to form narrow helical fibers. It was observed that the position of L/D-leucine is the tuning button to control the overall handedness of aliphatic bolaamphiphiles. The tuning ability will transfer to second amino acids only when the first amino acids act neutrally to the bolaamphiphiles. L-leucine based peptide bolaamphiphile and D/L-tartaric acid synergistically stabilize to form co-assembled hydrogels. The nanostructures from sphere to desired left-handed and right-handed nanofibers were successfully tuned in hydrogel state.

### 3.6 References

1. Yang Y., Suzuki M., Fukui H., Shirai H., Hanabusa K., (2006), Preparation of Helical Mesoporous Silica and Hybrid Silica

- Nanofibers Using Hydrogelator, *Chem. Mater.*, 18, 1324-1329 (DOI: 10.1021/cm0519030).
2. Jung J. H., Kobayashi H., van Bommel K. J. C., Shinkai S., Shimizu T. (2002), Creation of Novel Helical Ribbon and Double-Layered Nanotube TiO<sub>2</sub> Structures Using an Organogel Template, *Chem. Mater.*, 14, 1445-1447 (DOI: 10.1021/cm011625e).
  3. Jung J. H., Masuda M., Shimizu T., Shinkai S. (2001), Helical Ribbon Aggregate Composed of a Crown-Appended Cholesterol Derivative Which Acts as an Amphiphilic Gelator of Organic Solvents and as a Template for Chiral Silica Transcription, *J. Am. Chem. Soc.*, 123, 8785-8789 (DOI: 10.1021/ja010508h).
  4. Rodriguez-Llansola F., Escuder B., Miravet J. F. (2009), Switchable Performance of an L-Proline-Derived Basic Catalyst Controlled by Supramolecular Gelation, *J. Am. Chem. Soc.*, 131, 11478-11484 (DOI: 10.1021/ja902589f).
  5. Haldar D., Schmuck C. (2009), Metal-free Double Helices from Abiotic Backbones, *Chem. Soc. Rev.*, 38, 363-371 (DOI: 10.1039/B803553A).
  6. van Dijken D. J., Beierle J. M., Stuart M. C., Szymanski W., Browne W. R., Feringa B. L. (2014), Autoamplification of Molecular Chirality through the Induction of Supramolecular Chirality, *Angew. Chem., Int. Ed.*, 53, 5073-5077 (DOI: 10.1002/anie.201311160).
  7. Haedler A. T., Meskers S. C., Zha R. H., Kivala M., Schmidt H. W., Meijer E. W. (2016), Pathway Complexity in the Enantioselective Self-Assembly of Functional Carbonyl-Bridged Triarylamine Trisamides, *J. Am. Chem. Soc.*, 138, 10539-10545 (DOI: 10.1021/jacs.6b05184).
  8. Smulders M. M. J., Schenning A. P. H. J., Meijer E. W. (2008), Insight into the Mechanisms of Cooperative Self-Assembly: The “Sergeants-and-Soldiers” Principle of Chiral and Achiral C<sub>3</sub>-Symmetrical Discotic

- Triamides, *J. Am. Chem. Soc.*, 130, 606-611 (DOI: 10.1021/ja075987k).
9. van Gestel J., Palmans A. R. A., Titulaer B., Vekemans J. A. J. M., Meijer E. W. (2005), "Majority-Rules" Operative in Chiral Columnar Stacks of  $C_3$ -Symmetrical Molecules, *J. Am. Chem. Soc.*, 127, 5490-5494 (DOI: 10.1021/ja0501666).
  10. Kaiser T. E., Stepanenko V., Wurthner F. (2009), Fluorescent J-Aggregates of Core-Substituted Perylene Bisimides: Studies on Structure–Property Relationship, Nucleation–Elongation Mechanism, and Sergeants-and-Soldiers Principle, *J. Am. Chem. Soc.*, 131, 6719-6732 (DOI: 10.1021/ja900684h).
  11. Ajayaghosh A., George S. J. (2001), First Phenylenevinylene Based Organogels: Self-Assembled Nanostructures via Cooperative Hydrogen Bonding and  $\pi$ -Stacking, *J. Am. Chem. Soc.*, 123, 5148-5149 (DOI: 10.1021/ja005933+).
  12. Yashima E., Ousaka N., Taura D., Shimomura K., Ikai T., Maeda K. (2016), Supramolecular Helical Systems: Helical Assemblies of Small Molecules, Foldamers, and Polymers with Chiral Amplification and Their Functions, *Chem. Rev.*, 116, 22, 13752-13990 (DOI: 10.1021/acs.chemrev.6b00354).
  13. Lv K., Zhang L., Lu W., Liu M. (2014), Control of Supramolecular Chirality of Nanofibers and Its Effect on Protein Adhesion, *ACS Appl. Mater. Interfaces*, 6, 18878-18884 (DOI: 10.1021/am504702p).
  14. Liu G., Zhang D., Feng C. (2014), Control of Three-dimensional Cell Adhesion by the Chirality of Nanofibers in Hydrogels, *Angew. Chem., Int. Ed.*, 53, 7789-7793 (DOI: 10.1002/anie.201403249).
  15. Du X. W., Zhou J., Wang J. Q., Zhou R., Xu B. (2017), Chirality Controls Reaction-Diffusion of Nanoparticles for Inhibiting Cancer Cells, *ChemNanoMat*, 3, 17-21 (DOI: 10.1002/cnma.201600258).

16. Würthner F., Chen Z., Hoeben F. J. M., Osswald P.; You C. C., Jonkheijm P., Herrikhuyzen J. v., Schenning A. P. H. J., van der Schoot P. P. A. M., Meijer E. W., Beckers E. H. A., Meskers S. C. J., Janssen R. A. J. (2004), Supramolecular p-n-Heterojunctions by Co-Self-Organization of Oligo(p-phenylene Vinylene) and Perylene Bisimide Dyes, *J. Am. Chem. Soc.*, 126, 10611-10618 (DOI: 10.1021/ja0475353).
17. Yashima E., Maeda K., Iida H., Furusho Y., Nagai K. (2009), Helical Polymers: Synthesis, Structures, and Functions, *Chem. Rev.*, 109, 6102-6211 (DOI: 10.1021/cr900162q).
18. Cornelissen J. J. L. M., Rowan A. E., Nolte R. J. M., Sommerdijk N. A. J. M. (2001), Chiral Architectures from Macromolecular Building Blocks, *Chem. Rev.*, 101, 4039-4070 (DOI: 10.1021/cr990126i).
19. Ousaka N., Inai Y., Kuroda R. (2008), Chain-Terminus Triggered Chiral Memory in an Optically Inactive  $3_{10}$ -Helical Peptide, *J. Am. Chem. Soc.*, 130, 12266-12267 (DOI: 10.1021/ja805647k).
20. Marchesan S., Easton C. D., Styan K. E., Waddington L. J., Kushkaki F., Goodall L., McLean K. M., Forsythe J. S., Hartley P. G. (2014), Chirality Effects at Each Amino Acid Position on Tripeptide Self-assembly into Hydrogel Biomaterials, *Nanoscale*, 6, 5172-5180 (DOI: 10.1039/C3NR06752A).
21. Basu K., Baral A., Basak S., Dehsorkhi A., Nanda J., Bhunia D., Ghosh S., Castelletto V., Hamley I. W., Banerjee A. (2016), Peptide Based Hydrogels for Cancer Drug Release: Modulation of Stiffness, Drug Release and Proteolytic Stability of Hydrogels by Incorporating D-amino Acid Residue(s), *Chem. Commun.*, 52, 5045-5048 (DOI: 10.1039/C6CC01744D).
22. Wang M., Zhou P., Wang J., Zhao Y., Ma H., Lu J. R., Xu H. (2017), Left or Right: How Does Amino Acid Chirality Affect the Handedness of Nanostructures Self-Assembled from Short Amphiphilic Peptides? *J. Am. Chem. Soc.*, 139, 4185-4194 (DOI: 10.1021/jacs.7b00847).

23. Datta S., Samanta S. K., Bhattacharya S. (2013), Induction of Supramolecular Chirality in the Self-Assemblies of Lipophilic Pyrimidine Derivatives by Choice of the Amino Acid-Based Chiral Spacer, *Chem. Eur. J.* 19, 11364-11373 (DOI: 10.1002/chem.201300605).
24. Richardson J. S. (1981), The Anatomy and Taxonomy of Protein Structure, *Adv. Protein Chem.* 34, 167-229 (DOI: 10.1016/S0065-3233(08)60520-3).
25. Chou K. -C., Nemethy G., Scheraga H. A. (1990), Energetics of Interactions of Regular Structural Elements in Proteins, *Acc. Chem. Res.* 23, 134-141 (DOI: 10.1021/ar00173a003).
26. Shamovsky I. L., Ross G. M., Riopelle R. J. (2000), Theoretical Studies on the Origin of  $\beta$ -sheet Twisting, *J. Phys. Chem. B*, 104, 11296-11307 (DOI: 10.1021/jp002590t).
27. Aggeli A., Nyrkova I. A., Bell M., Harding R., Carrick L., McLeish T. C. B., Semenov A. N., Boden N. (2001), Hierarchical Self-assembly of Chiral Rod-like Molecules as a Model for Peptide  $\beta$ -sheet Tapes, Ribbons, Fibrils, and Fibers, *Proc. Natl. Acad. Sci. U. S. A.* 98, 11857-11862 (DOI: 10.1073/pnas.191250198).
28. Jimenez J. L., Nettleton E. J., Bouchard M., Robinson C. V., Dobson C. M., Saibil H. R. (2002), The Protofilament Structure of Insulin Amyloid Fibrils, *Proc. Natl. Acad. Sci. U. S. A.* 99, 9196-9201 (DOI: 10.1073/pnas.142459399).
29. Wadai H., Yamaguchi K., Takahashi S., Kanno T., Kawai T., Naiki H. Goto Y. (2005), Stereospecific Amyloid-like Fibril Formation by a Peptide Fragment of  $\beta_2$ -Microglobulin, *Biochemistry*, 44, 157-164 (DOI: 10.1021/bi0485880).
30. Liu G.-F., Zhu L.-Y., Ji W., Feng C.-L., Wei Z.-X. (2016), Inversion of the Supramolecular Chirality of Nanofibrous Structures through Co-Assembly with Achiral Molecules, *Angew. Chem. Int. Ed.* 55, 2411-2415 (DOI: 10.1002/anie.201510140).

31. Cameron C. G., Lee C., Meijer E. W., Schenning A. P. H. J. (2009), Preparation and Characterization of Helical Self-assembled Nanofibers, *Chem. Soc. Rev.* 38, 671-683 (DOI: 10.1039/B800407M).
32. Suzuki M., Yumoto M., Shirai H., Hanabusa K. (2008), Supramolecular Gels Formed by Amphiphilic Low-Molecular-Weight Gelators of  $N\alpha, N\epsilon$ -Diacyl-L-Lysine Derivatives, *Chem. Eur. J.* 14, 2133-2144 (DOI: 10.1002/chem.200701111).
33. Verdejo B., Rodríguez-Llansola F., Escuder B., Miravet J. F., Ballester P. (2011), Sodium and pH Responsive Hydrogel Formation by the Supramolecular System Calix[4]pyrrole Derivative/Tetramethylammonium Cation, *Chem. Commun.* 47, 2017-2019 (DOI: 10.1039/C0CC04051G).
34. Biswas S., Jadhav R. G., Das A. K. (2018), Construction of Porous Organic Nanostructures Using Cooperative Self-Assembly for Lipase-Catalyzed Inclusion of Gastrodigenin, *ACS Appl. Nano Mater.*, 1, 175-182 (DOI: 10.1021/acsanm.7b00085).
35. Draper E. R., Eden E. G. B., McDonald T. O., Adams D. J. (2015), Spatially Resolved Multicomponent Gels, *Nat. Chem.* 7, 848-852 (DOI: 10.1038/nchem.2347).
36. Ciesielski A., Palma C.-A., Bonini M., Samori P. (2010), Towards Supramolecular Engineering of Functional Nanomaterials: Pre-Programming Multi-component 2D Self-Assembly at Solid-Liquid Interfaces, *Adv. Mater.*, 22, 3506-3520 (DOI: 10.1002/adma.201001582).
37. Kar H., Ghosh S. (2015), Multicomponent Gels: Remote Control for Self-Assembly, *Nat. Chem.*, 7, 765-767 (DOI:10.1038/nchem.2351).
38. Goto H., Zhang H. Q., Yashima E. (2003), Chiral Stimuli-Responsive Gels: Helicity Induction in Poly(phenylacetylene) Gels Bearing a Carboxyl Group with Chiral Amines, *J. Am. Chem. Soc.*, 125, 2516-2523 (DOI: 10.1021/ja029036c).

39. Lv Z., Chen Z., Shao K., Qing G., Sun T. (2016), Stimuli-Directed Helical Chirality Inversion and Bio-Applications, *Polymers*, 8, 310-329 (DOI: 10.3390/polym8080310).
40. Iwaura R., Yoshida K., Masuda M., Ohnishi-Kameyama M., Yoshida M., Shimizu T. (2003), Oligonucleotide-Templated Self-Assembly of Nucleotide Bolaamphiphiles: DNA-Like Nanofibers Edged by a Double-Helical Arrangement of A-T Base Pairs, *Angew. Chem. Int. Ed.*, 42, 1009-1012 (DOI: 10.1002/anie.200390257).
41. Iwaura R., Shimizu T. (2006), Reversible Photochemical Conversion of Helicity in Self-Assembled Nanofibers from a 1, $\omega$ -Thymidylic Acid Appended Bolaamphiphile, *Angew. Chem. Int. Ed.*, 45, 4601-4604 (DOI: 10.1002/anie.200601173).
42. Ikeda M., Ochi R., Kurita Y. S., Pochan D. J., Hamachi I. (2012), Heat-induced Morphological Transformation of Supramolecular Nanostructures by Retro-Diels-Alder Reaction, *Chem. Eur. J.* 18, 13091-13096 (DOI: 10.1002/chem.201201670).
43. Iwaura R., Yoshida K., Masuda M., Yase K., Shimizu T. (2002), Spontaneous Fiber Formation and Hydrogelation of Nucleotide Bolaamphiphiles, *Chem. Mater.* 14, 3047-3053 (DOI: 10.1021/cm020263n).
44. Jiang J., Wang T., Liu M. (2010), Creating Chirality in the Inner Walls of Silica Nanotubes through a Hydrogel Template: Chiral Transcription and Chiroptical Switch, *Chem. Commun.*, 46, 7178-7180 (DOI: 10.1039/C0CC00891E).
45. Pandeewar M., Avinash M. B., Govindaraju T. (2012), Chiral Transcription and Retentive Helical Memory: Probing Peptide Auxiliaries Appended with Naphthalenediimides for Their One-Dimensional Molecular Organization, *Chem. Eur. J.*, 18, 4818-4822 (DOI: 10.1002/chem.201200197).

46. Chan H. S., Bromberg S., Dill K. A. (1995), Models of Cooperativity in Protein Folding, *Phil. Trans. R. Soc. Lond. B*, 348, 61-70 (DOI: 10.1098/rstb.1995.0046).
47. Zhang L., Qin L., Wang X., Cao H., Liu M. (2014), Supramolecular Chirality in Self-Assembled Soft Materials: Regulation of Chiral Nanostructures and Chiral Functions, *Adv. Mater.*, 26, 6959-6964 (DOI: 10.1002/adma.201305422).
48. Liu M., Zhang L., Wang T. (2015), Supramolecular Chirality in Self-Assembled Systems, *Chem. Rev.*, 115, 7304-7397 (DOI: 10.1021/cr500671p).
49. Liu G., Liu J., Feng C., Zhao Y. (2017), Unexpected Right-handed Helical Nanostructures Co-assembled from L-phenylalanine Derivatives and Achiral Bipyridines, *Chem. Sci.*, 8, 1769-1775 (DOI: 10.1039/C6SC04808K).
50. Duan P., Cao H., Zhang L., Liu M. (2014), Gelation Induced Supramolecular Chirality: Chirality Transfer, Amplification and Application, *Soft Matter*, 10, 5428-5448 (DOI: 10.1039/C4SM00507D).
51. Mandal D., Choudhury P., Sarkar D., Das P. K. (2017), Dissipation of Self-assemblies by Fusion of Complementary Gels: An Elegant Strategy for Programmed Enzymatic Reaction, *Chem. Commun.*, 53, 7844-7847 (DOI: 10.1039/C7CC04269H).
52. Das S., Chakraborty P., Ghosh R., Paul S., Mondal S., Panja A., Nandi A. K. (2017), Folic Acid-Polyaniline Hybrid Hydrogel for Adsorption/Reduction of Chromium (VI) and Selective Adsorption of Anionic Dye from Water, *ACS Sustainable Chemistry & Engineering*, 5, 9325-9337 (DOI: 10.1021/acssuschemeng.7b02342).
53. Zhou P., Deng L., Wang Y., Lu J. R., Xu H. (2016), Interplay between Intrinsic Conformational Propensities and Intermolecular Interactions in the Self-Assembly of Short Surfactant-like Peptides Composed of

- Leucine/Isoleucine, *Langmuir*, 32, 4662-4672 (DOI: 10.1021/acs.langmuir.6b00287).
54. Wendt H., Berger C., Baici A., Thomas R. M., Bosshard H. R. (1995), Kinetics of Folding of Leucine Zipper Domains, *Biochemistry*, 34, 4097–4107 (DOI: 10.1021/bi00012a028).
55. Courtemanche N., Barrick D. (2008), The Leucine-rich Repeat Domain of Internalin B Folds Along a Polarized N-terminal Pathway, *Structure*, 16, 705–714 (DOI: 10.1016/j.str.2008.02.015).
56. Liu Y., Chen C., Wang T., Liu M. (2016), Supramolecular Chirality of the Two-Component Supramolecular Copolymer Gels: Who Determines the Handedness? *Langmuir*, 32, 322-328 (DOI: 10.1021/acs.langmuir.5b03938).
57. Bhattacharya A., Bhowmik S., Singh A. K., Kodgire P., Das A. K. Mukherjee T. K. (2017), Direct Evidence of Intrinsic Blue Fluorescence from Oligomeric Interfaces of Human Serum Albumin, *Langmuir*, 33, 10606-10615 (DOI: 10.1021/acs.langmuir.7b02463).
58. Biswas S., Rasale D. B., Das A. K. (2016), Blue Light Emitting Self-Healable Graphene Quantum Dot Embedded Hydrogels, *RSC Adv*, 6, 54793-54800 (DOI: 10.1039/C6RA06587B).
59. Haris P. I., Chapman D. (1995), The Conformational Analysis of Peptides Using Fourier Transform IR Spectroscopy, *Biopolymers*, 37, 251-63 (DOI: 10.1002/bip.360370404).
60. Naskar J., Palui G., Banerjee A. (2009), Tetrapeptide-Based Hydrogels: for Encapsulation and Slow Release of an Anticancer Drug at Physiological pH, *J. Phys. Chem. B*, 113, 11787-11792 (DOI: 10.1021/jp904251j).
61. Moretto V., Crisma M., Bonora G. M., Toniolo C., Balaram H., Balaram P. (1989), Comparison of the Effect of Five Guest Residues on the  $\beta$ -sheet Conformation of Host (L-val)<sub>n</sub> Oligopeptides, *Macromolecules*, 22, 2939-2944 (DOI: 10.1021/ma00197a010).

62. Banno N., Nakanishi T., Matsunaga M., Asahi T., Osaka T. (2004), Enantioselective Crystal Growth of Leucine on a Self-Assembled Monolayer with Covalently Attached Leucine Molecules, *J. Am. Chem. Soc.*, 126, 428-429 (DOI: 10.1021/ja037942z).
63. Derry M. J., Mykhaylyk O. O., Ryan A. J., Armes S. P. (2018), Thermoreversible Crystallization-driven Aggregation of Diblock Copolymer Nanoparticles in Mineral Oil, *Chem. Sci.*, 9, 4071-4082 (DOI:10.1039/C8SC00762D).
64. Nielsen E. B., Schellman J. A. (1967), The Absorption Spectra of Simple Amides and Peptides, *J. Phys. Chem.*, 71, 2297-2304 (DOI: 10.1021/j100866a051).
65. Oda R., Huc I., Schmutz M., Candau S. J., MacKintosh F. C. (1999), Tuning Bilayer Twist Using Chiral Counterions, *Nature*, 399, 566-569 (DOI: 10.1038/21154).
66. Munye M. M., Ravi J., Tagalakis A. D., McCarthy D., Ryadnov M. G., Hart S. L. (2015), Role of Liposome and Peptide in the Synergistic Enhancement of Transfection with a Lipopolyplex Vector, *Sci. Rep.*, 5, 9292 (DOI: 10.1038/srep09292).

## **Chapter 4**

# **Construction of Porous Organic Nanostructures using Cooperative Self-assembly for Lipase Catalyzed Inclusion of Gastrodigenin**



## 4.1 Introduction

The construction of porous materials with various structural topologies through self-assembly has gained key interest from researchers over the last few decades.<sup>[1-3]</sup> Recently, porous architectures have become the center of attraction for manifold applications including molecular storage, separation, and catalysis.<sup>[4-9]</sup> Scientists are involved in tuning of the pore sizes of organic frameworks through noncovalent interactions to avail supramolecular organic frameworks (SOFs).<sup>[10-12]</sup> Furthermore, functional two-dimensional (2D) SOFs are quite attractive for larger surface area because of the formation of supramolecular organic nanosheets as 2D material, which exhibit properties different from those of their bulk counterparts.<sup>[10]</sup> SOF materials are the simplest multicomponent system because they form porous frameworks through noncovalent interactions using complementary functional groups of two or more different components.<sup>[13,14]</sup> Their flexibility, soft nature, guest selectivity, and specificity toward selective gas molecules make them significantly noticeable.<sup>[15,15]</sup> The loss of porosity of SOFs through structural deformation was perceived upon guest removal, and the modification was materialized with permanent cavity formation by the complementary building blocks.<sup>[16]</sup> Therefore, molecular self-assembly is the perfect tool to achieve SOFs with controlled pore size. Molecular self-assembly integrates molecules through self-organization, which is governed by noncovalent interactions to provide complex architectures.<sup>[17-19]</sup> Different types of amphiphilic molecules impart distinguished supramolecular architectures, which results in the formation of vesicles, toroids, tubes, and other porous architectures.<sup>[20,21]</sup> To enhance the simultaneous multitasking ability, researchers are inspired to expand multimulticomponent self-assembled systems to tune the nanostructures.<sup>[22,23]</sup> Bicomponent materials have been explored as the simplest multicomponent system to acquire controlled molecular self-assembly.<sup>[24-28]</sup> When the specific functionality

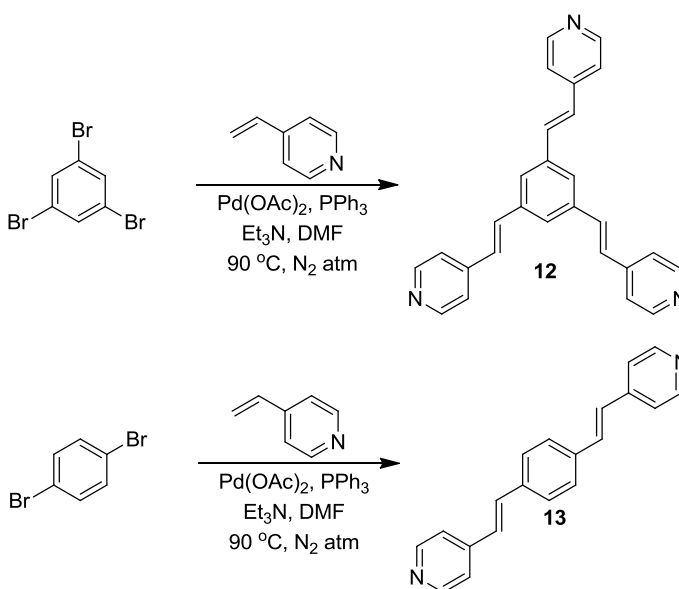
in the bicomponent system is changed, the formation of nanostructures can be tuned by the assistance of cooperative self-assembly.<sup>[29,30]</sup> Cooperative self-assembly is driven by hydrogen-bonding and  $\pi$ - $\pi$ -stacking interactions between two complementary building blocks, which can also form gels.<sup>[24,31]</sup> Therefore, the bicomponent system acts as a remote control for the self-assembly and gelation processes.<sup>[32,33]</sup> However, exploration of the SOF materials with a suitable bicomponent system is still required to tune the pore size and stability toward multiple conditions. Controlling the porosity of SOF materials in the gel state is also a challenge to the researchers, and very few reports have been inscribed in the literature.<sup>[14,34]</sup>

To achieve controlled porous architectures in supramolecular gel, multifunctional (bifunctional and trifunctional) amphiphiles are appropriate because of extended network formation through coordination, ionic, or noncovalent interactions.<sup>[35]</sup> Therefore, multifunctional amphiphiles are suitable building blocks to design supramolecular porous architectures in a gel medium.<sup>[36]</sup> Various functionalized pyridyl amphiphiles have been developed that self-assemble to form distinct nanoarchitectures.<sup>[37]</sup> Therefore, multicoordinating cationic amphiphiles and complementary acids have been chosen for the development of self-supporting gels.<sup>[38]</sup> Bifunctional (BDC) and trifunctional (BTC) acids are well-known for their use in the construction of molecular frameworks.<sup>[39-41]</sup> Multifunctional pyridyl amphiphiles (tpeb and bpeb) also coordinate with metal centers and self-assemble to form various architectures.<sup>[42,43]</sup> Therefore, bifunctional and trifunctional pyridyl amphiphiles were chosen to develop metal-free organic nanostructures. Herein, the objective was to prepare gel-phase supramolecular organic porous nanostructures by the coassembly of the bicomponent system and the use of supramolecular organic nanostructures (SONs) as templates for biocatalysis. Lipase is considered to hydrolyze esters in aqueous and

organic media,<sup>[44]</sup> whereas self-assembly assists the inclusion of gastrodigenin (p-hydroxybenzyl alcohol, p-HBA) via an esterification reaction in the gel phase.<sup>[45]</sup> Gastrodigenin (p-HBA) exhibits a scavenging effect toward free radicals and is currently being considered as a bioactive component of gastrodin.<sup>[46,47]</sup> In this chapter, lipase is used for the incorporation of gastrodigenin in organic-aqueous media-based supramolecular organic porous nanostructures, and it is an incomparably significant way to achieve the goal.

## 4.2 Experimental

*Scheme 4.1* Synthetic scheme of pyridyl amphiphiles **12** and **13**



### 4.2.1 1,3,5-tris[2-(4-pyridyl)ethenyl]benzene (**12**)

2 g (6.43 mmol) of 1,3,5-tribromobenzene was taken in a 100 mL two necked round bottom flask. It was then dissolved in 20 mL DMF. Triphenylphosphine (125 mg, 6 mol%) was added in the resulting mixture and 5 mL triethylamine was also added to the reaction mixture. The resulting solution was made inert using continuous flow of argon gas. After that, 2.43 mL (23.15 mmol) 4-vinylpyridine was added through

another neck of the round bottom flask using syringe. Finally 100 mg (5 mol%) palladium (II) acetate was added to it and it was kept for 72 h under reflux condition at 90 °C. The resultant reaction mixture was then cooled to room temperature and diluted with 50 mL dichloromethane. Diluted solution was washed with 3×50 mL water and the solvent was evaporated under vacuum to yield dark-brown solid. Further, the product was purified by column chromatography using EtOAc : hexane as eluent. Yield: 52%,  $^1\text{H}$  NMR (400 MHz,  $\text{DMSO-d}_6$ )  $\delta$  = 7.47-7.49 (d, 3H,  $J$  = 12 Hz), 7.53-7.55 (d, 3H,  $J$  = 12 Hz), 7.78 (s, 3H), 7.91-7.92 (d, 6H), 8.58-8.60 (d, 6H) ppm.  $^{13}\text{C}$  NMR (100 MHz,  $\text{DMSO-d}_6$ )  $\delta$  = 121.40, 127.37, 129.48, 132.23, 135.96, 144.47, 150.54 ppm. MS (ESI)  $m/z$  for  $\text{C}_{27}\text{H}_{21}\text{N}_3$  (M) $^+$  calcd: 387.1730, found: 387.2626.

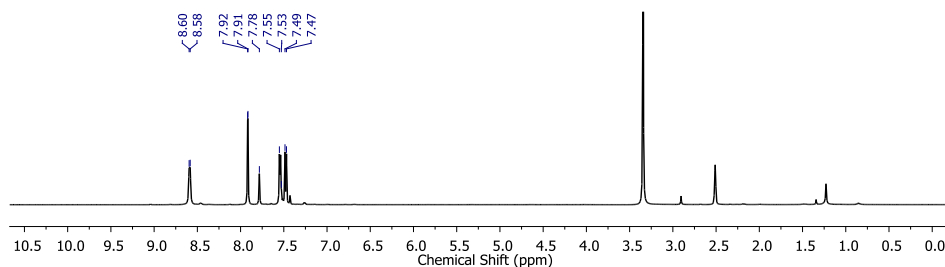


**Figure 4.1.**  $^1\text{H}$  NMR spectrum of 1,3,5-tris[2-(4-pyridyl)ethenyl]benzene (**12**) in  $\text{DMSO-d}_6$ .

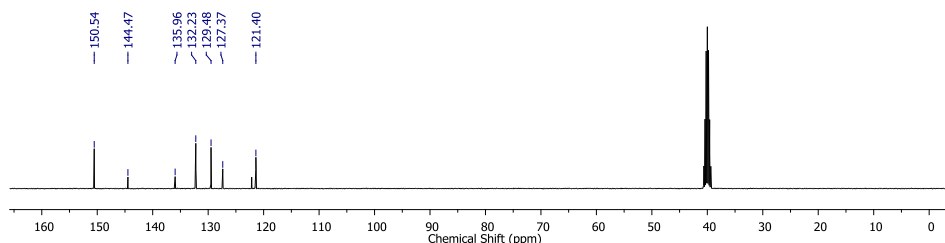


**Figure 4.2.**  $^{13}\text{C}$  NMR spectrum of 1,3,5-tris[2-(4-pyridyl)ethenyl]benzene (**12**) in  $\text{DMSO-d}_6$ .

#### 4.2.2 1,4-bis[2-(4-pyridyl)ethenyl]benzene (**13**)

1,4-bis[2-(4-pyridyl)ethenyl]benzene (**13**) was synthesized using the same procedure. Yield = 53%,  $^1\text{H}$  NMR (400 MHz,  $\text{DMSO-d}_6$ )  $\delta$  = 7.28-7.32 (d,

2H,  $J = 16$  Hz), 7.51-7.57 (m, 6H), 7.62 (4H, s), 8.55-8.57 (d,  $J = 8$  Hz, 4H) ppm.  $^{13}\text{C}$  NMR (100 MHz, DMSO- $d_6$ )  $\delta = 121.53, 123.44, 129.18, 133.33, 141.02, 144.03, 150.63$  ppm. MS (ESI)  $m/z$  for  $\text{C}_{20}\text{H}_{16}\text{N}_2$  ( $\text{M}$ ) $^+$  calcd: 284.1308, found: 284.2203.

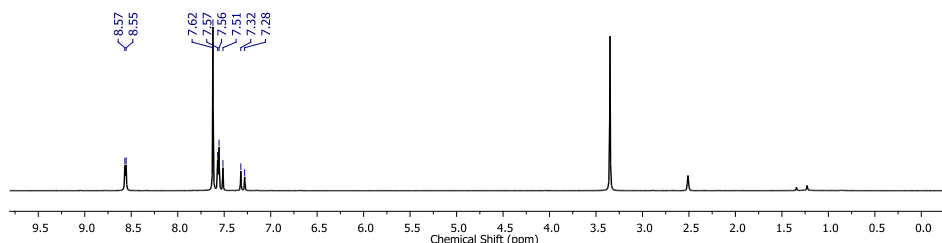


**Figure 4.3.**  $^1\text{H}$  NMR spectrum of 1,4-bis[2-(4-pyridyl)ethenyl]benzene (**13**) in DMSO- $d_6$ .

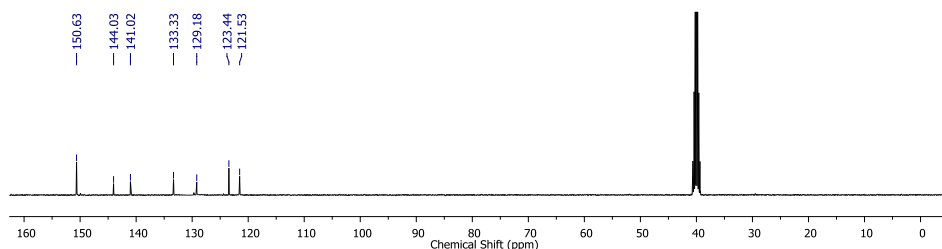


**Figure 4.4.**  $^{13}\text{C}$  NMR spectrum of 1,4-bis[2-(4-pyridyl)ethenyl]benzene (**13**) in DMSO- $d_6$ .

## 4.3 Gel Preparation and Characterization Techniques

### 4.3.1 Preparation of Emulsions Gels

Bicomponent systems were prepared using different ratios of amphiphiles and acids. To prepare the gel, 7.74 mg (20 mM) of tpeb and 4.2 mg (20 mM) of trimesic acid (BTC) were placed in a 5 mL borosilicate vial with a cap containing 700  $\mu\text{L}$  of water and then 300  $\mu\text{L}$  of hexane was added (water/hexane at a ratio of 7:3). The biphasic solution was then stirred (using a 1 cm magnetic bar) for 10 min on a magnetic stirrer at a speed of 480 rpm to make the mixture homogeneous and kept for another 10 min to attain rigidity of tpeb-BTC. Then, a test tube inversion study was performed to visualize the formation of self-supporting gels, which were

further used for rheological experiments. Similarly, a tpeb-BDC (BDC = terephthalic acid) emulsion gel and bpeb-BTC and bpeb-BDC emulsions were prepared using all of the same conditions. In the case of tpeb-BDC, 7.74 mg (20 mM) of tpeb and 9.96 mg (60 mM) of BDC were placed in a vial containing 700  $\mu\text{L}$  of water, and then 300  $\mu\text{L}$  of hexane was added. A total of 8.52 mg (60 mM) of bpeb and 4.2 mg (20 mM) of BTC were placed in a vial containing 700  $\mu\text{L}$  of water, and then 300  $\mu\text{L}$  of hexane was added to prepare the emulsion bpeb-BTC. Similarly, 8.52 mg (30 mM) of bpeb and 4.98 mg (30 mM) of BDC were placed in a vial containing 700  $\mu\text{L}$  of water, and then 300  $\mu\text{L}$  of hexane was added to make the emulsion bpeb-BDC. However, tpeb-BCA, tpeb-SA (SA = succinic acid), bpeb-BCA, and bpeb-SA did not form emulsions under similar conditions. A gelation study was performed with the tpeb-BTC/tpeb-BDC system in only water and hexane individually. However, gelation was not observed.

### 4.3.2 Emulsion Gels for Enzymatic Reaction

The biphasic solutions were stirred for 10 min on a magnetic stirrer to make the mixture. After proper mixing of the two components in the biphasic system, lipase and p-HBA were immobilized in the emulsion gels by simple handshaking for 1 min. The mixture was then incubated at 37  $^{\circ}\text{C}$ , and the progress of the reaction was monitored by high performance liquid chromatography (HPLC).

### 4.3.3 Separation of Product after Esterification

After completion of the esterification reaction, the emulsion gel (tpeb-BDC) was separated into two layers. The organic layer was then collected using a syringe, and it was diluted to 5 mL. The diluted hexane layer was then washed with 1 M HCl, and the organic layer was collected to get the product. The aqueous layer containing lipase and tpeb was recycled up to five times. After the enzymatic reaction, the solution became acidic in

nature (pH 5), and the pH of the aqueous solution was maintained to neutral after each of the reactions with a mild  $\text{NH}_4\text{OH}$  solution before using it for the next reaction. After completion of the fifth reaction cycle, the pyridyl amphiphile tpeb was extracted from the aqueous part. The aqueous part was diluted to 10 mL with a 1 M  $\text{Na}_2\text{CO}_3$  solution and washed with ethyl acetate to obtain 77% tpeb.

#### **4.3.4 Compound Characterization**

All NMR spectra were recorded with 400 MHz Bruker AV spectrometer at 300 K. Compound concentrations were in the range of 1-10 mM in  $\text{DMSO}-d_6$ . Mass spectra were recorded on Bruker micrOTOF-Q II by positive mode electrospray ionization.

#### **4.3.5 Rheological Study**

Rheological study was performed to determine the mechanical properties of emulsion-gels. These properties were assessed using an Anton Paar Physica Rheometer (MCR 301, Austria) with parallel plate geometry (25 mm in diameter, 1 mm gap) and temperature was controlled at 25° C. The dynamic moduli of the gels were measured as a function of frequency in the range of 0.05-100  $\text{rad s}^{-1}$  with a constant strain value 0.1%. The dynamic behavior of emulsions-gel was performed with constant strain of 0.1% and constant angular frequency of 10 Hz during enzymatic reaction. 200  $\mu\text{L}$  of gel was prepared in glass vial and transferred it over the plate using microspatula to proceed for rheological measurements.

#### **4.3.6 FT-IR Spectroscopy**

All reported FT-IR spectra were recorded with a Bruker (Tensor 27) FT-IR spectrophotometer. The solid-state measurements were performed using the KBr pellet technique with a scan range between 400 and 4000  $\text{cm}^{-1}$  over 64 scans at a resolution of 4  $\text{cm}^{-1}$  and an interval of 1  $\text{cm}^{-1}$ .

**4.3.7 UV-Vis Spectroscopy**

UV-Vis absorption spectra of the acids, amphiphiles, emulsions and emulsion gels were recorded using a Varian Cary100 Bio UV-Vis spectrophotometer at a concentration of  $5 \mu\text{mol L}^{-1}$  in 2 mL of water with 0.01% MeOH.

**4.3.8 Wide Angle X-ray Diffraction**

The XRD measurements were carried out using a Bruker D8 Advance X-ray diffractometer. The X-rays were produced using a sealed tube, and the wavelength of the X-rays was 0.154 nm (Cu K $\alpha$ ). The X-rays were detected using a fast counting detector based on silicon strip technology (Bruker LynxEye detector).

**4.3.9 Small Angle X-ray Scattering Study**

A Panalytical X'Pert Pro multipurpose diffraction (MPD) was used for SAXS spectra. The emulsion-gels were dried to obtain solid powder and were used for SAXS experiment.

**4.3.10 Thermogravimetric Analysis**

Thermogravimetric analysis (TGA) was executed using a METTLER TOLEDO TGA instrument. The samples were heated from 25 °C to 500 °C at a constant rate of  $5^\circ\text{C min}^{-1}$  under nitrogen environment.

**4.3.11 Gas Adsorption Measurement**

Gas (N $_2$ ) adsorption/desorption measurements were carried out using a Quantachrome Autosorb IQ2 Automated Gas Sorption System at 77 K (N $_2$  sorption experiments) in the pressure range of 0.025 bar to 1 bar. Before sorption measurements, compounds were degassed for 5 h at 348 K with increasing rate of  $5^\circ\text{C min}^{-1}$ .

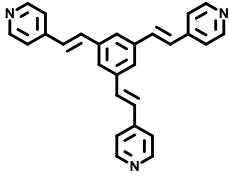
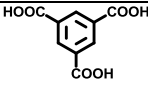
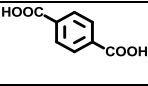
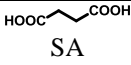
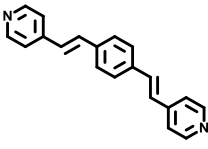
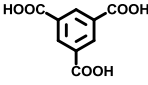
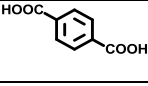
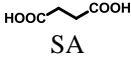
### 4.3.12 HPLC Analysis

A Dionex HPLC-Ultimate 3000 (High Performance Liquid Chromatography) pump was used to analyze products. 20  $\mu\text{L}$  of sample was injected onto a Dionex Acclaim<sup>®</sup> 120 C18 column of 250 mm length with an internal diameter of 4.6 mm and 5  $\mu\text{m}$  fused silica particles at a flow rate of 1  $\text{mL min}^{-1}$  (linear gradient of 40% v/v acetonitrile in water for 35 min, gradually rising to 100% (v/v) acetonitrile in water at 35 min). This concentration was kept constant until 40 min when the gradient was decreased to 40% (v/v) acetonitrile in water at 42 min. The sample preparation involved mixing of 100  $\mu\text{L}$  emulsion-gel in 900  $\mu\text{L}$  acetonitrile-water (50: 50 mixtures) solution containing 0.1% trifluoroacetic acid. The samples were then filtered through a 0.45  $\mu\text{m}$  syringe filter (Whatman, 150 units, 13 mm diameter, 2.7 mm pore size) prior to injection. The products were identified by using Ultimate 3000 RS Variable Wavelength Detector at 280 nm.

## 4.4 Results and Discussion

In this chapter, tri-functional amphiphile 1,3,5-tris[2-(4-pyridyl)ethenyl]benzene (**12**) and di-functional pyridyl 1,4-bis[2-(4-pyridyl)ethenyl]benzene (**13**) have been used to achieve bicomponent SONs through gelation/emulsification. The emulsions are generally dispersion of droplet (composed of tiny fiber, colloidal particle or fibrillar aggregates) of one liquid in another solution.<sup>[48-50]</sup> Further, emulsification can lead to form self-supporting gel which is referred as emulsion-gel.<sup>[51]</sup> This approach suggests the development of distinct supramolecular assemblies through non-covalent interactions of **tpeb** with complementary 1,3,5-benzene tricarboxylic acid (**BTC**) and 1,4-benzene dicarboxylic acid (**BDC**).

Table 4.1. Composition of the bicomponent systems and physical appearance

Amphiphiles	Complementary acids	Physical Appearance
 tpeb (12)	 BTC	Emulsion-gel 6 (tpeb-BTC)
	 BDC	Emulsion-gel 7 (tpeb-BDC)
	 BCA	None
	 SA	None
 bpeb (13)	 BTC	Emulsion (bpeb-BTC)
	 BDC	Emulsion (bpeb-BDC)
	 BCA	None
	 SA	None

Among a series of bicomponent systems (Table 4.1), only **tpeb-BTC** and **tpeb-BDC** form emulsion-gels in water:hexane (7:3) and **bpeb-BTC**, **bpeb-BDC** form emulsions. The gelation was confirmed through test tube inversion study (Figure 4.5) and the rheological experiments depict the mechanical (viscoelastic) properties of the emulsion-gels. Though both emulsion-gels are eminently stable for several days (30 days), acidity and basicity affect the emulsion-gels. **tpeb-BTC** emulsion-gel shows pH ~7 and **tpeb-BDC** emulsion-gel shows pH ~6.5. Both emulsion-gels were deformed with the increase in pH at ~8 (Figure 4.5). Similar observations were also found for lowering the pH to ~5 for both the emulsion-gels. The deformation of the emulsion-gels was also observed on treatment with 100  $\mu\text{L}$  of 100 mM NaCl solution (Figure 4.5).

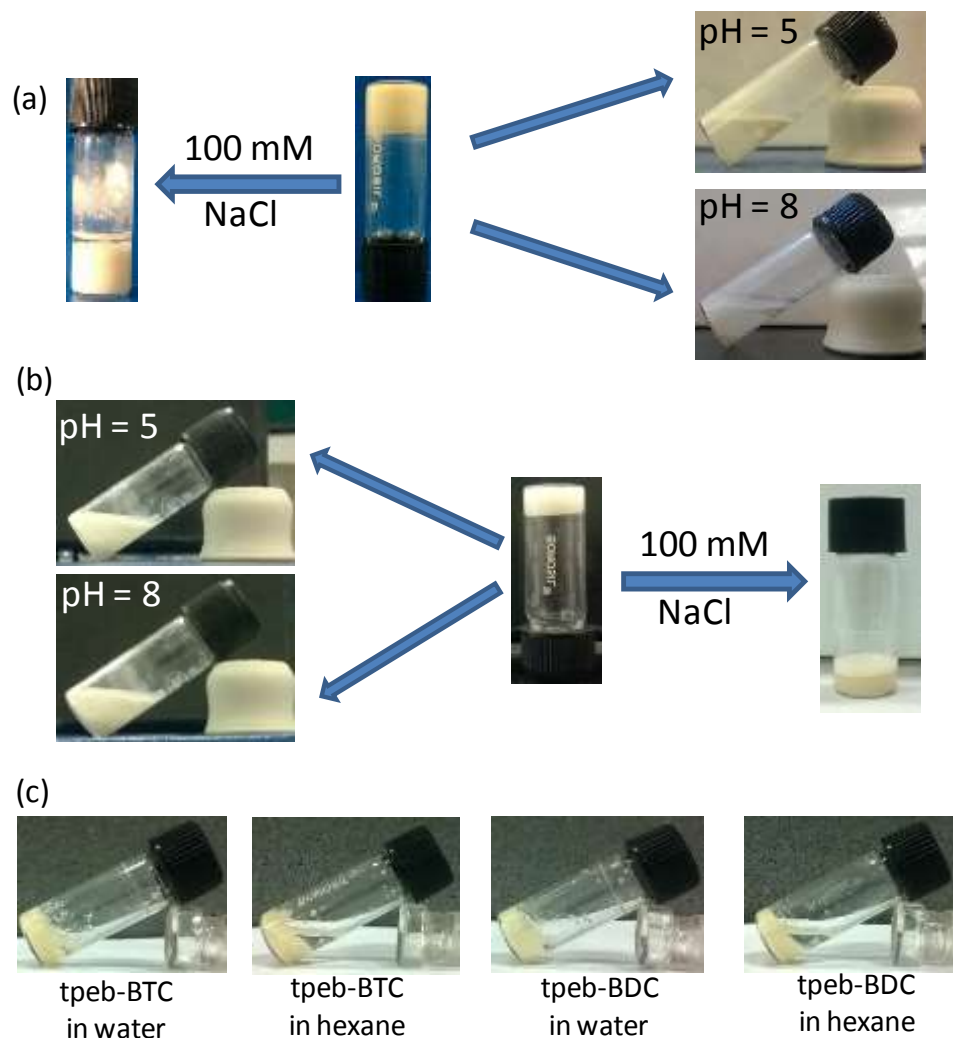


**Figure 4.5.** Optical images of emulsion gels of (a) **tpeb-BTC** at different pHs show deformation of emulsion-gels to emulsions. Addition of 100 mM NaCl, the emulsion-gel turns into two phases. (b) Optical images of **tpeb-BDC** also show the deformation of emulsion-gels to emulsions on variation of pH as well as on the treatment with 100 mM NaCl. (c) Optical images of **tpeb-BTC** and **tpeb-BDC** in hexane or in water. **tpeb-BTC** and **tpeb-BDC** don't produce self-supporting gel in a particular solvent.

#### 4.4.1 Rheological Study

A rigid gel is defined in practice as having a storage modulus ( $G'$ ) that exceeds to the loss modulus ( $G''$ ) by an order of magnitude.<sup>[28]</sup> The storage moduli of both **tpeb-BTC** and **tpeb-BDC** emulsion-gels are higher than

the loss moduli throughout the frequency regime (Figure 4.6). The value of storage modulus ( $G'$ ) of **tpeb-BDC** emulsion-gel exceeds that of loss modulus ( $G''$ ) by a factor of 10 throughout the oscillating frequency, whereas the factor is only about 5 (Figure 4.6) for **tpeb-BTC** emulsion-gel. However, both signify the formation of strong and rigid gels. The **tpeb-BDC** emulsion-gel is much stronger than **tpeb-BTC** emulsion-gel as the storage modulus ( $G' = 8880$  Pa) is much higher for **tpeb-BDC** compare to the storage modulus ( $G' = 872$  Pa) of **tpeb-BTC**.

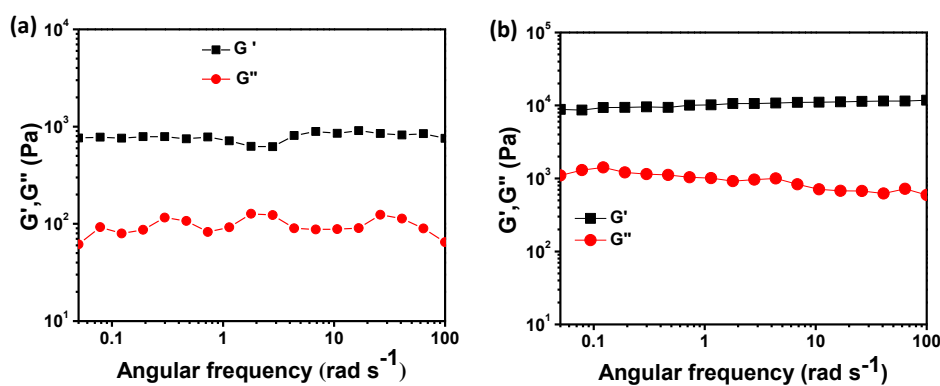


**Figure 4.6.** (a) and (b) represent the frequency sweep experiment of **tpeb-BTC** and **tpeb-BDC** emulsion gels respectively. Both signify rigid gel formation.

#### 4.4.2 Morphological Study

To investigate nanostructural insight of the emulsion-gels and emulsions, transmission electron microscopy experiments were carried out. **tpeb-BTC** shows twisted fibrillar bundle with an average diameter of 200 nm (Figure 4.7a). The fibrillar bundle is composed of small width (25-40 nm) fibers (Figure 4.7a, Figure 4.8a).

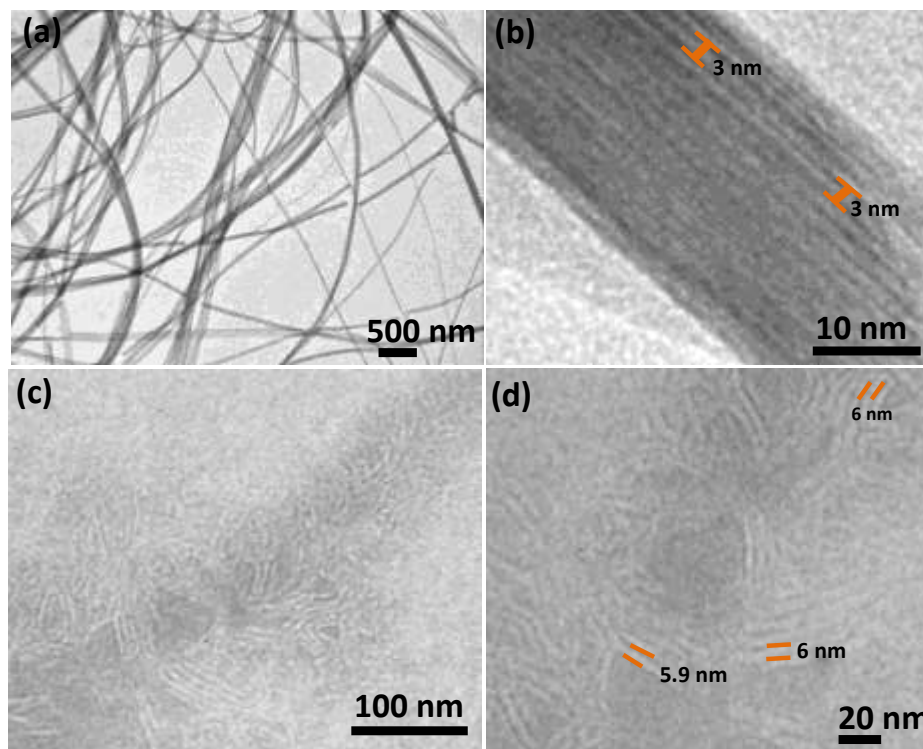


**Figure 4.7.** (a) TEM image of *tpeb-BTC* shows nanofibrillar network structures and (b) HR-TEM image of *tpeb-BTC* shows the supramolecular arrangement of fibers having diameter of 3 nm. (c) Supramolecular organic nanofibers show parallel alignment in the *tpeb-BDC* and (d) higher magnification on the side by side aligned molecular fibers of *tpeb-BDC* shows the average diameter of 6 nm.

The small width fibers are also composed of narrow fibers with an average diameter of 3 nm (Figure 4.7b). *tpeb-BDC* emulsion-gel forms aligned supramolecular organic nanofibers which was observed from TEM image (Figure 4.7c). HR-TEM gives a clear account for side by side alignment of the molecular fibers of diameter ~6 nm (Figure 4.7d).<sup>[52]</sup> Rod structures with an average diameter of 200 nm are responsible for the formation of **bpeb-BTC** emulsion (Figure 4.8c). **bpeb-BDC** forms linear molecular complex that is unable to form any significant nanostructure on aggregation (Figure 4.8d).

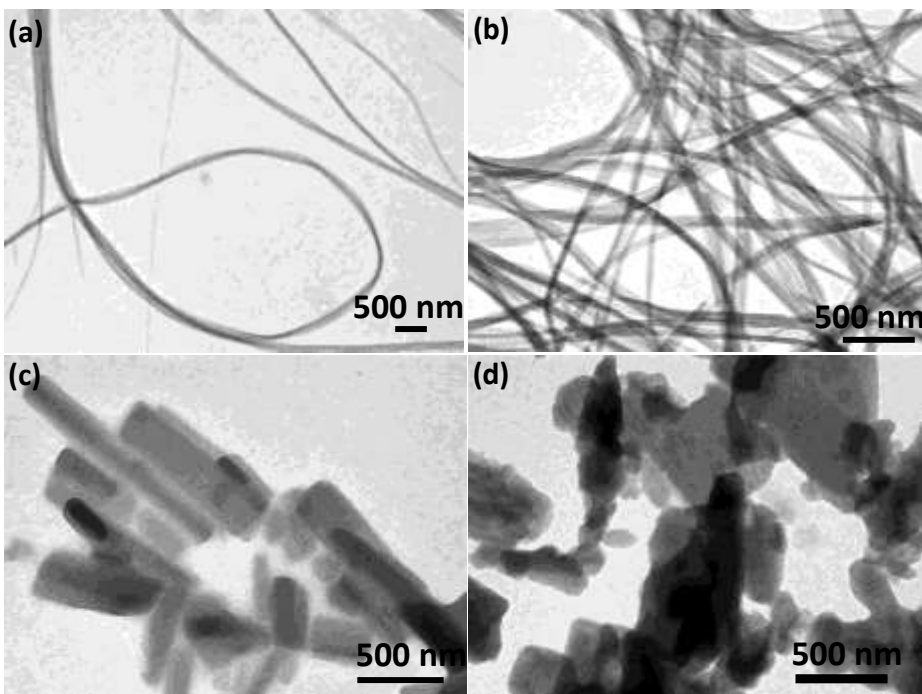


**Figure 4.8.** TEM images (a), (b) show fibrillar bundle formation by *tpeb-BTC* and narrow fibers (diameter 25-40 nm) get separated from bundles. (c) TEM image shows nanorod of *bpeb-BTC* and no significant morphology was observed for *bpeb-BDC* (d).

#### 4.4.3 Mechanistic Study

The mechanistic aspect of supramolecular interactions involved in the formation of the nanostructures was investigated using FT-IR experiments. Both **BTC** and **BDC** exhibited with a broad band at around  $2984\text{ cm}^{-1}$  due to strong intermolecular hydrogen bonded carboxylic acid groups. Strong intense peaks at  $1687\text{ cm}^{-1}$  and  $1700\text{ cm}^{-1}$  are assigned to stretching vibrations of the C=O group of carboxylic acid in more associated state through intermolecular hydrogen bonding in both **BDC** and **BTC** respectively (Figure 4.9).<sup>[53,54]</sup> The peaks at  $1597$ ,  $1544$ , and  $1480\text{ cm}^{-1}$  (Figure 4.9) are attributed to the ring vibration of the pyridine of aromatic pyridyl amphiphiles (**bpeb** and **tpeb**). The pyridinium carboxylate formation was established due to the appearance of a peak at

1634  $\text{cm}^{-1}$  for both **tpeb-BTC** (Figure 4.9a) and **tpeb-BDC** (Figure 4.9b) xerogels.<sup>[55,56]</sup>

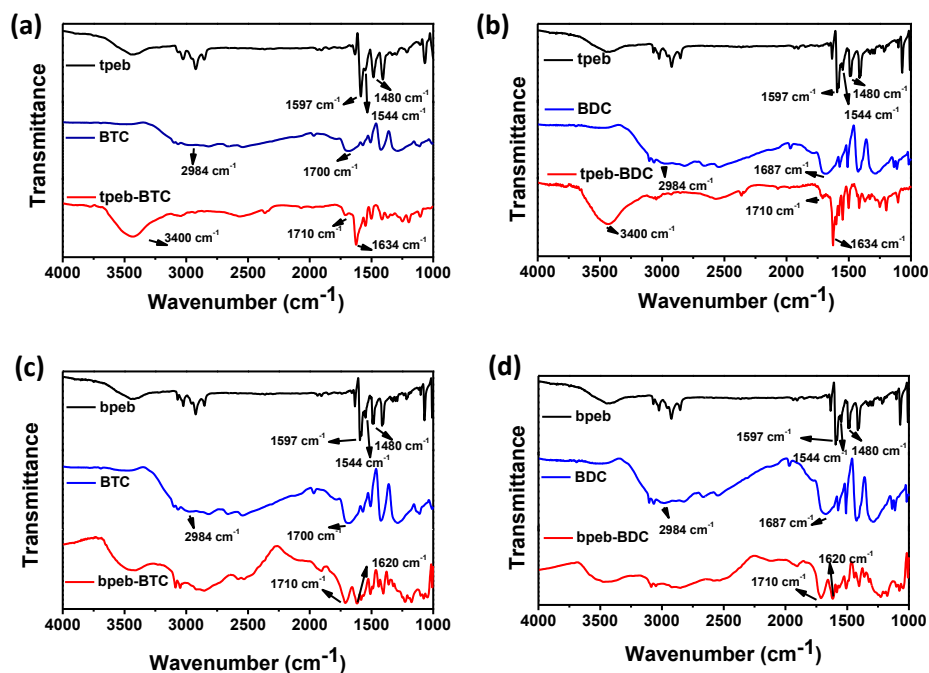


**Figure 4.9.** (a), (b), (c) and (d) show the overlaid plot of the IR spectra of **tpeb-BTC**, **tpeb-BDC**, **bpeb-BTC** and **bpeb-BDC** emulsions respectively.

The protonation of pyridyl N-atom was also supported by the presence of a peak at 3400  $\text{cm}^{-1}$  for N-H of pyridinium carboxylate of the composites of **tpeb-BTC** and **tpeb-BDC** xerogels. Both **tpeb-BTC** and **tpeb-BDC** xerogels show a C=O stretching vibration at 1710  $\text{cm}^{-1}$ , which revealed that the carbonyl group is in a less associated state as compared to the precursor acids (**BTC** and **BDC**). These results suggest that few pyridyl groups are involved in hydrogen bonding interactions with acid groups. Remaining acid groups are involved in intermolecular hydrogen bonding interactions with another **BDC** (in case of **tpeb-BDC**). Here, supramolecular complexes are constructed through protonation of pyridine as well as hydrogen bonding interactions. Both **bpeb-BTC** and **bpeb-BDC** (Figure 4.9c,d) emulsions exhibit two peaks at 1710  $\text{cm}^{-1}$  and 1620  $\text{cm}^{-1}$ . These two peaks with equal intensity signify that complexes which

formed in the emulsions are equilibrated between protonated as well as hydrogen bonded pyridyl group with an equal extent.<sup>[55-57]</sup>

#### 4.4.4 UV-Vis Spectroscopic Study

UV-Vis spectroscopic analyses have been implemented to study the aggregation pattern. **BTC**, **BDC** (Figure 4.10) exhibit peaks at 280 nm, 240 nm respectively and amphiphiles **tpeb** and **bpeb** (Figure 4.10) show broad peaks at 300 nm and 310 nm respectively. UV-Vis spectrum of **tpeb-BTC** (Figure 4.10a) shows two peaks at 293 nm, 313 nm with a shoulder at 325 nm whereas **tpeb-BDC** exhibits a broad peak at 315 nm with a broad shoulder at 359 nm (Figure 4.10b).

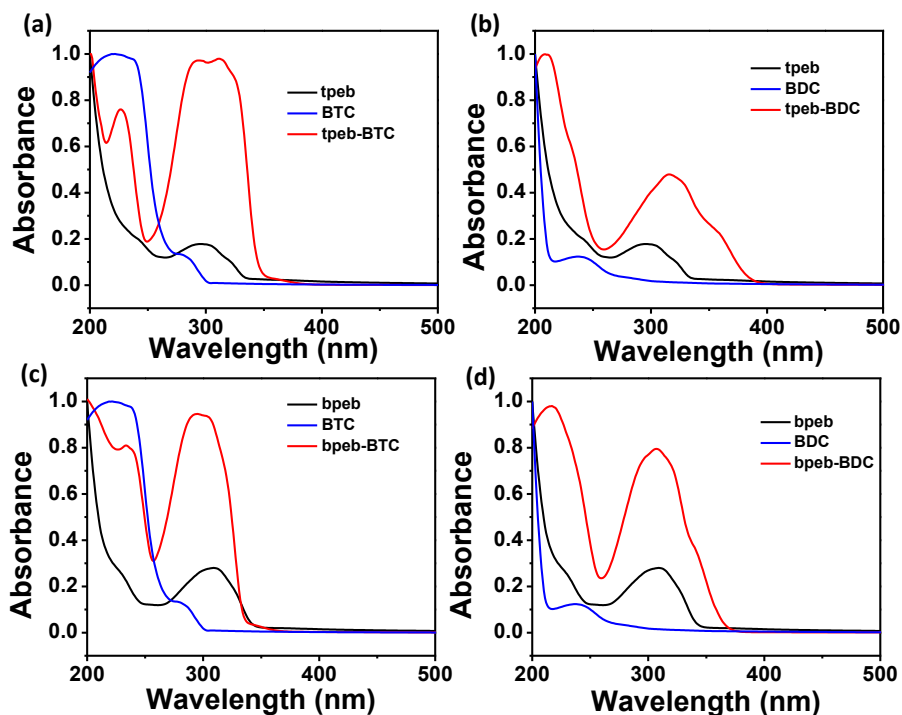


**Figure 4.10.** (a), (b), (c) and (d) describe UV-Vis spectra of **tpeb-BTC**, **tpeb-BDC**, **bpeb-BTC** and **bpeb-BDC** systems.

A concomitant bathochromic shift is noticed after gelation for both **tpeb-BTC** and **tpeb-BDC**. **bpeb-BTC** (Figure 4.10c) complex clearly exhibits a peak at 304 nm whereas a peak is observed at 306 nm for **bpeb-BDC** (Figure 4.10d). No significant red-shift is observed for **bpeb-BTC** and

**bpeb-BDC** emulsions. The red-shift in UV-Vis spectra is attributed to the  $\pi$ - $\pi^*$  transition between aromatic groups in the formed complexes through co-assembly and self-assembly of amphiphiles. According to exciton theory, in-line transition dipole eases to a spectral red-shift for transition in the dimer or complexes formed in the system and higher red-shift in wavelength signifies the higher extent of charge transfer in the aggregated state.<sup>[58]</sup> Bathochromic shift in emulsion-gels indicates that the emulsion-gel is formed through *J*-type of aggregation.<sup>[26,58]</sup>

#### 4.4.5 Powder X-ray Diffraction Study

Powder X-ray diffraction (PXRD) study of **tpeb-BTC** (Figure 4.11a) xerogel reveals the appearance of peaks at  $2\theta$  of  $6.61^\circ$ ,  $18.41^\circ$ ,  $20.31^\circ$  and  $27.88^\circ$  which are different from the parent **tpeb** and **BTC** molecules. These peaks correspond to the *d* spacing of 1.33 nm, 0.48 nm, 0.43 nm and 0.32 nm. The disappearance of the peaks in dried **tpeb-BTC** emulsion-gel within the  $2\theta$  range of  $10^\circ$  to  $15^\circ$  corresponding to **BTC** suggests the formation of new material. The presence of a peak at  $2\theta$  of  $6.61^\circ$  ( $d = 1.33$  nm) indicates the diameter of columnar aggregates of the formed complexes whereas the *d* spacing of 0.48 nm and 0.43 nm indicate inter columnar distances.  $\pi$ - $\pi$  stacking interaction between the complexes was supported by the peak corresponding to the *d* spacing of 0.32 nm. PXRD of **tpeb-BDC** (Figure 4.11b) complex appeared with peaks at  $2\theta$  of  $2.82^\circ$ ,  $5.5^\circ$ ,  $6.76^\circ$ ,  $18.37^\circ$ ,  $19.48^\circ$  and  $26^\circ$  which corroborate to the *d*-spacing of 3.13 nm, 1.6 nm, 1.3 nm, 0.48 nm 0.46 nm and 0.34 nm. The disappearance of sharp peak which were present in both **tpeb** and **BDC** suggested the formation of new material in **tpeb-BDC**. Similar columnar packing is also described for **tpeb-BDC**. A peak at  $2\theta$  of  $26^\circ$  ( $d = 0.34$  nm) indicates the distance between two aromatic groups ( $\pi$ - $\pi$  stacking interaction).<sup>[52]</sup>

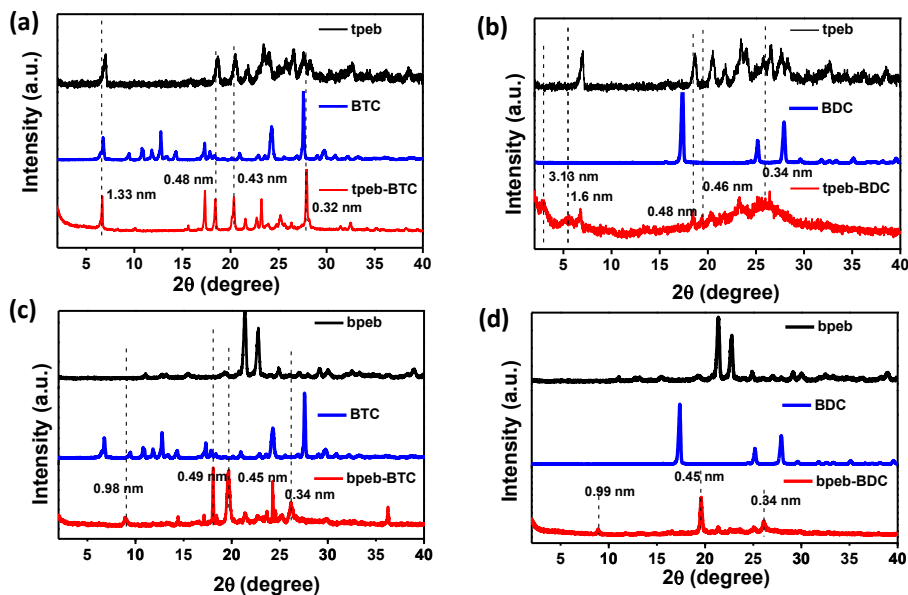


**Figure 4.11.** (a), (b), (c) and (d) show the overlaid plot of the XRD patterns of *tpeb-BTC*, *tpeb-BDC*, *bpeb-BTC* and *bpeb-BDC* systems respectively.

The dried emulsion of **bpeb-BTC** (Figure 4.11c) shows peaks at  $2\theta$  value of  $9^\circ$ ,  $18.07^\circ$ ,  $19.64^\circ$  and  $26.16^\circ$  which correspond to the distance of 0.98 nm, 0.49 nm, 0.45 nm and 0.34 nm. The  $\pi$ - $\pi$  stacking interaction is confirmed by the distance of 0.34 nm. However, the dried emulsion of **bpeb-BDC** (Figure 4.11d) attributes only three peaks at  $2\theta$  value of  $8.9^\circ$  ( $d = 0.99$  nm),  $19.57^\circ$  ( $d = 0.45$  nm) and  $26.16^\circ$  ( $d = 0.34$  nm). The peak at  $2\theta$  of  $26.16^\circ$  ( $d = 0.34$  nm) corresponds to the  $\pi$ - $\pi$  stacking interaction of the linear complexes and the peaks at  $2\theta = 8.9^\circ$  ( $d = 0.99$  nm) and  $19.57^\circ$  ( $d = 0.45$  nm) signify the interlayer distances. The presence of the discotic amphiphiles leads to the formation of a columnar stack.<sup>[60-62]</sup> The combination of linear amphiphile and complementary acids does not form columnar packing.

#### 4.4.6 Porosity Study

Small angle X-ray scattering (SAXS) experiments of the dried emulsion-gels of **tpeb-BTC** (Figure 4.12a) and **tpeb-BDC** (Figure 4.12b) were performed to find out the inner diameter of the nanoarchitectures. **tpeb-**

**BTC** only shows a peak with a calculated  $d$  value of 3.1 nm whereas **tpeb-BDC** shows a peaks at  $d = 5.6$  nm associated with the porous SONs.<sup>[63-68]</sup>

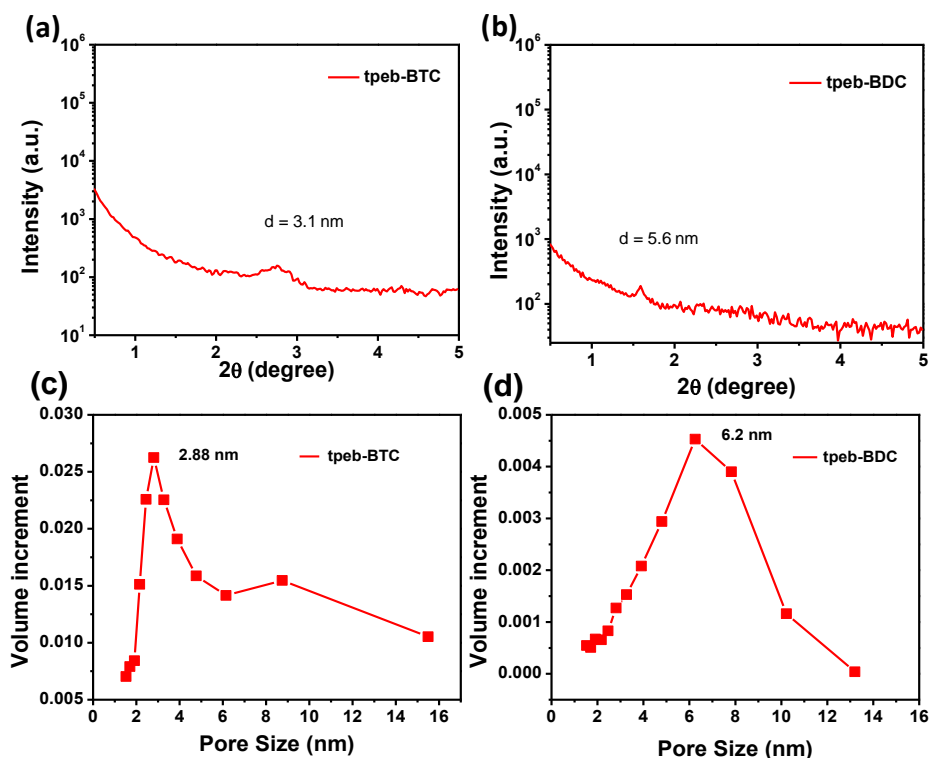


**Figure 4.12.** (a) and (b) are the SAXS spectra of both **tpeb-BTC** and **tpeb-BDC** respectively. Both the data shows the size of the nanostructures formed in the system. (c) and (d) show the pore size distribution obtained from  $N_2$  adsorption of **tpeb-BTC** and **tpeb-BDC** respectively which matches with the calculated data obtained from SAXS.

The thermogravimetric analysis (TGA) was performed to show the thermal stability of **tpeb-BTC** and **tpeb-BDC**. Both **tpeb-BTC** and **tpeb-BDC** were heated at  $10\text{ }^\circ\text{C min}^{-1}$  under nitrogen atmosphere. The **tpeb-BTC** is stable upto  $117\text{ }^\circ\text{C}$  whereas **tpeb-BDC** is stable up to the temperature of  $135\text{ }^\circ\text{C}$  (Figure 4.13). The BET  $N_2$  adsorption gives type IV isotherm plot (Figure 4.13c,d) and both emulsion gels (**tpeb-BTC** and **tpeb-BDC**) dominant with the presence of mesopores.

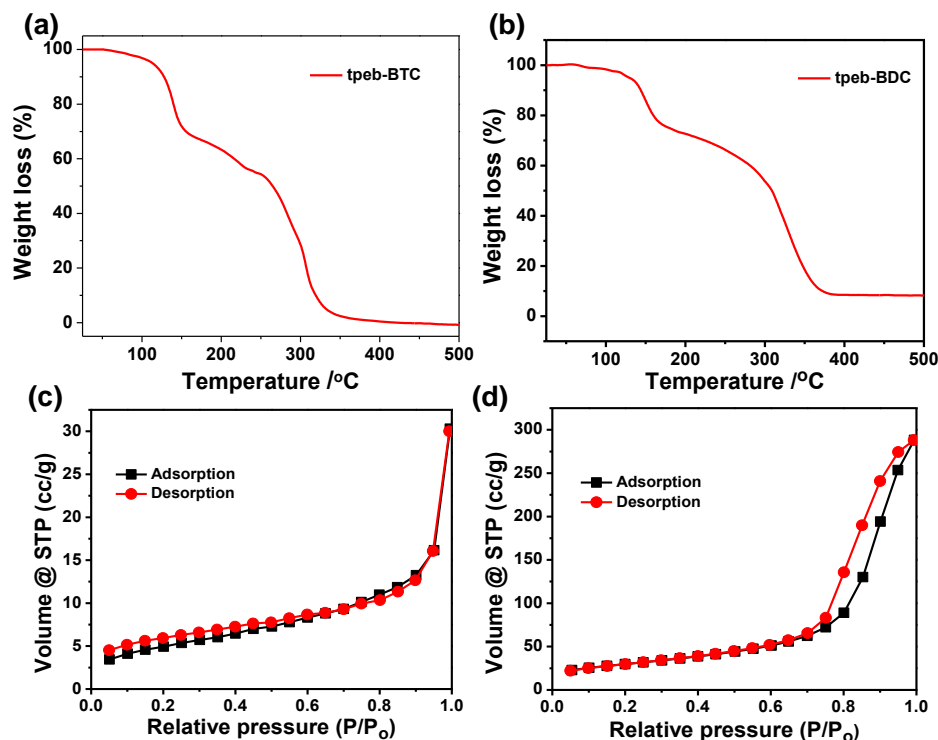


**Figure 4.13.** (a) and (b) show the thermogravimetric analysis (TGA) of **tpeb-BTC** and **tpeb-BDC** respectively.  $N_2$  adsorption in (c) **tpeb-BTC** and (d) **tpeb-BDC** system signify the formation of porous supramolecular organic nanostructures.

The surface area is calculated as  $11 \text{ m}^2/\text{g}$  for **tpeb-BTC** and  $71 \text{ m}^2/\text{g}$  for **tpeb-BDC** from  $N_2$  adsorption isotherm which is a direct consequence of higher  $N_2$  adsorption by **tpeb-BDC**. The large hysteresis loop formation in **tpeb-BDC** is a consequence of capillary condensation. The pore size is calculated on the basis of NLDFT (nonlocal density functional theory) from BET  $N_2$  adsorption (Figure 4.12c,d). The pore sizes are calculated as 2.88 nm for **tpeb-BTC** and 6.2 nm for **tpeb-BDC**.

#### 4.4.7 Mechanism of Nanostructure Formation

UV-Vis analysis suggests aromatic  $\pi$ - $\pi^*$  transition that is responsible for the formation of complexes through the self-assembly and co-assembly of amphiphiles.

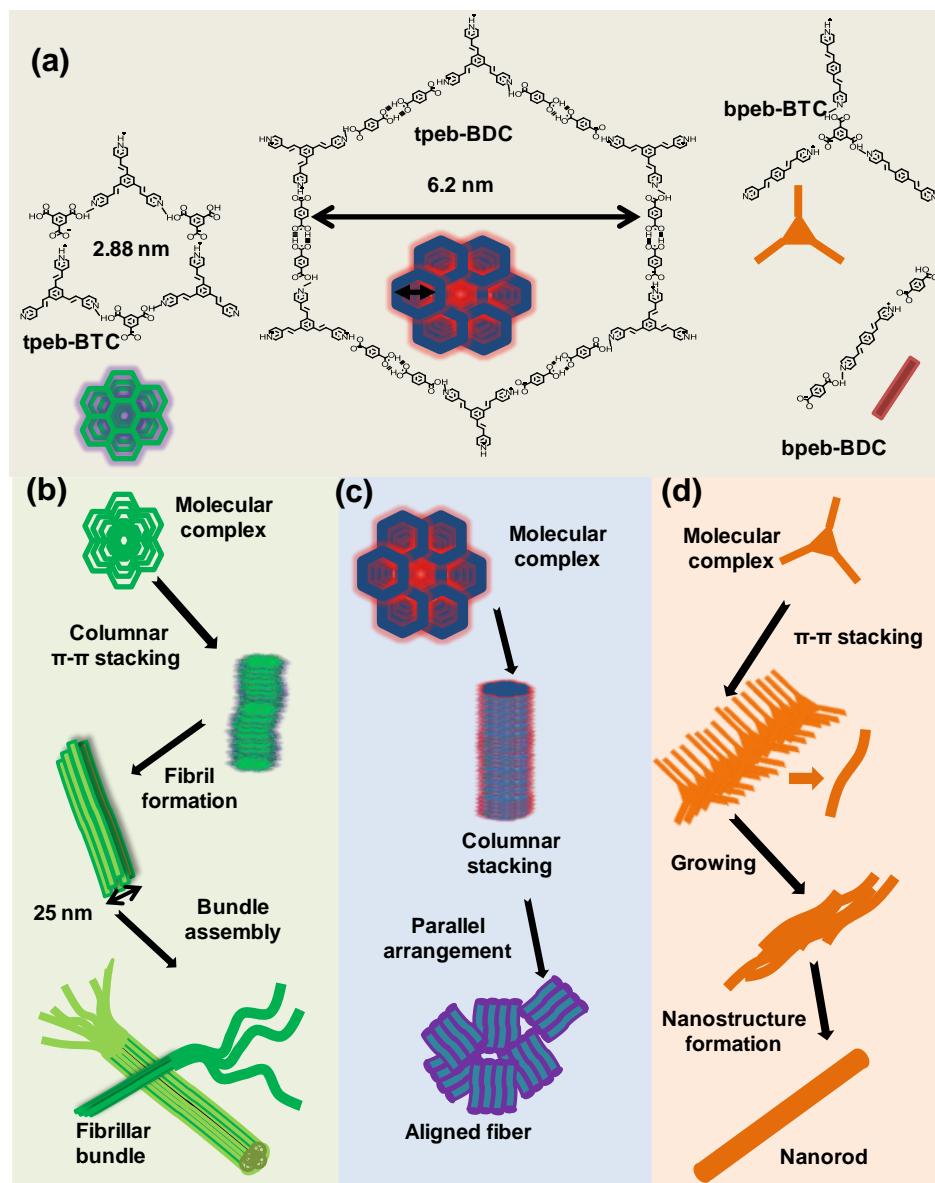


**Figure 4.14.** (a) Cartoon representation of molecular complexes of emulsions-gel **tpeb-BTC**, **tpeb-BDC** and emulsions **bpeb-BTC** and **bpeb-BDC**. (b) The molecular complex of **tpeb-BTC** elongated vertically through columnar  $\pi$ - $\pi$  stacking which forms fibril. Then the fibers composed to form nano-fibrillar bundle. (c) Molecular complex of **tpeb-BDC** with large cavity through columnar stacking forms aligned supramolecular organic nanofibrillar structure. (d) The complex of **bpeb-BTC** elongates through  $\pi$ - $\pi$  stacking interactions forms supramolecular rods.

The extent of hydrogen bonding ( $1710\text{ cm}^{-1}$ ) is characterized by FT-IR spectroscopy, which is responsible for the formation of molecular complexes in **tpeb-BTC** and **tpeb-BDC** emulsion-gels. The PXRD patterns of columnar stacks (d spacing of 1.33 nm, 0.48 nm, 0.43 nm for **tpeb-BTC** and 1.3 nm, 0.48 nm, 0.46 nm for **tpeb-BDC**) suggest the elongation of molecular complexes (Figure 4.14a) and the formation of nanofibers through columnar stacking of molecular complexes. The internal distance of nanofibers for both **tpeb-BTC** ( $\sim 3$  nm) and **tpeb-BDC** ( $\sim 6$  nm) is considered as the distance between two edges of molecular complexes. The distance between two edges is confirmed from SAXS spectra (3.1 nm for **tpeb-BTC** and 5.6 nm for **tpeb-BDC**). However, the extent of protonation is more in case of **tpeb-BDC** emulsion-gel which might have higher aggregation rate compared to **tpeb-BTC** emulsion-gel. **tpeb-BTC** complex forms long fibers with average width of 25-40 nm which are evidenced by HR-TEM (Figure 4.7a, Figure 4.8a). After formation of long fibers with shorter width, they assemble to form twisted fibrillar bundle with an average diameter of 200 nm (Figure 4.8). **tpeb-BDC** molecular complexes ( $\sim 6$  nm) are elongated to form fibers by  $\pi$ - $\pi$  stacking (Figure 4.14c) interactions through *J*-type aggregation which is understood from UV-Vis spectroscopy. Further, the elongated fibers are aligned side by side (Figure 4.14c) with a diameter of  $\sim 6$  nm which is exhibited from HR-TEM (Figure 4.7).<sup>52</sup> FTIR spectra support equal participation (1:1) of hydrogen bonding and protonation for **bpeb-BTC** and **bpeb-BDC** complexes. The molecular complex of **bpeb-BTC** is elongated vertically through  $\pi$ - $\pi$  stacking interaction (Figure 4.14d). Further, elongation led to the formation of supramolecular rods (Figure 4.14d). **bpeb-BDC** forms linear molecular complex (Figure 4.14) and no significant nanostructures were observed.

## 4.4.8 Enzymatic Reaction

Micro or nanoporous architectures were used as templates for various enzymatic reactions.<sup>[69,70]</sup> Due to the presence of large pores in the SOFs, various reactions could be done into the cavity. Enzymatic esterification reaction was performed in supramolecular host-guest system.<sup>[71]</sup> However, porous SONs were not yet used as the template for enzymatic esterification reactions. Here, the porous architectures were used for the enzymatic esterification reactions where lipase was used as a catalyst.

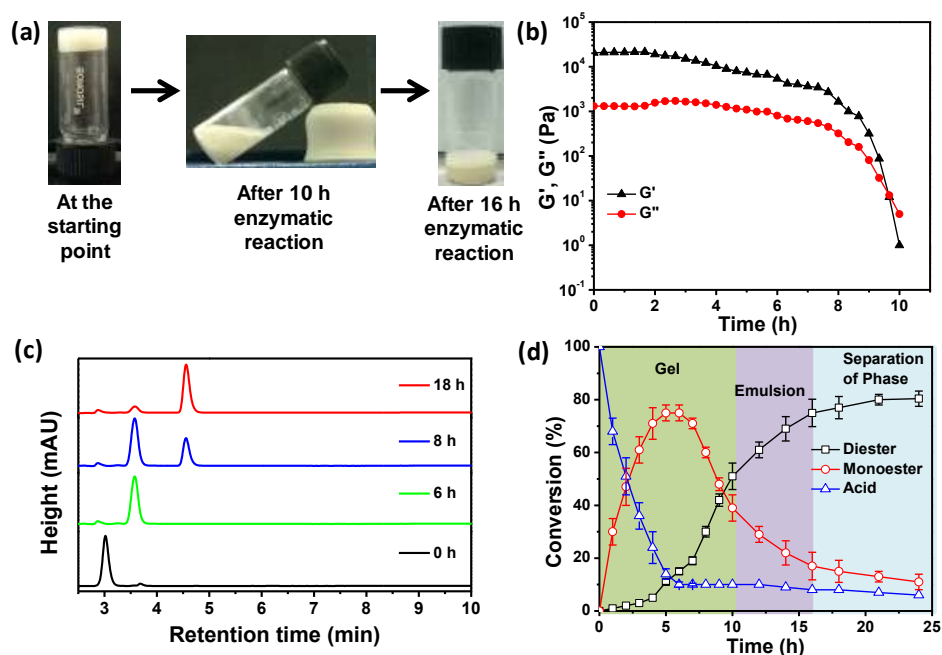


**Figure 4.15.** (a) Real time images of *tpeb*-BDC emulsion-gel for lipase catalyzed esterification reaction. After 10 hours of enzymatic reaction, *tpeb*-BDC emulsion-gel converted to sol-emulsion. At 16 hours of the reaction, the emulsion-gel converted into two phases. (b) Rheological analysis of emulsion-gel to sol-emulsion transition. (c) HPLC chromatograms at different reaction time and (d) real-time enzymatic conversion of mono-ester, di-ester. The colors in the graph signify different physical states (emulsion-gel, emulsion and separation of two phases).

Lipase from *Candida rugosa* (CRL) and *p*-hydroxybenzyl alcohol (*p*-HBA) were dispersed for dissolution into **tpeb-BTC** and **tpeb-BDC** before attending the formation of emulsion-gels. Initially, 4.56 U-45.6 U of lipase was used for esterification reaction (Figure 4.16a). However, an efficient result was obtained with 22.8 U of lipase. Higher amount of *p*-HBA influences the emulsion-gel to deform into sol-emulsion as the emulsion-gel is composed by ionic and hydrogen-bonding interactions. O-H groups of *p*-HBA have a significant impact on hydrogen bonding of the formed complexes, which weaken the network structures. Therefore, an equivalent amount of *p*-HBA offers better conversion. The emulsion-gel started to degrade upon enzymatic esterification reaction as the acid group was gradually converted to *p*-HBA esters. **tpeb-BDC** emulsion-gel was found to be more efficient for the conversion of terephthalate diester from terephthalic acid. The formation of diester leads to the phase separation (Figure 4.15a). **tpeb-BTC** and **tpeb-BDC** complexes were studied by time dependent rheological experiments during the enzymatic reaction.<sup>[72]</sup> **tpeb-BTC** emulsion-gel lost its storage modulus significantly at a reaction time of 7.5 hours (Figure 4.16b) and converted to sol-emulsion whereas **tpeb-BDC** held the gelation property up to 9.75 hours (Figure 4.15b). Initially, **tpeb-BDC** emulsion-gel exhibits 10 times higher storage modulus ( $G'$ ) value than loss modulus ( $G''$ ). As the reaction time increases, the separation between  $G'$  and  $G''$  decreases and finally the emulsion-gel was converted to a solution at 9.75 hours with a loss factor or damping factor ( $\tan \delta$ ) of 0.5. Time sweep rheological experiment for **tpeb-BTC** emulsion-gel shows the crossing of  $G'$  and  $G''$  at 7.5 hours (Figure 4.16b). The reaction was monitored by HPLC analysis (Figure 4.15c).

The **tpeb-BTC** emulsion-gel network yielded monoester, and other two acid groups of **BTC** remain unreacted which were also monitored by HPLC. **tpeb-BTC** emulsion was not separated into two phases. A higher lipase catalyzed esterification reaction within the **tpeb-BDC** complex in

comparison to **tpeb-BTC** complex is concluded as the diameter of the pore is 6.2 nm for **tpeb-BDC** complex and the diameter of lipase is 5 nm.<sup>[73]</sup>

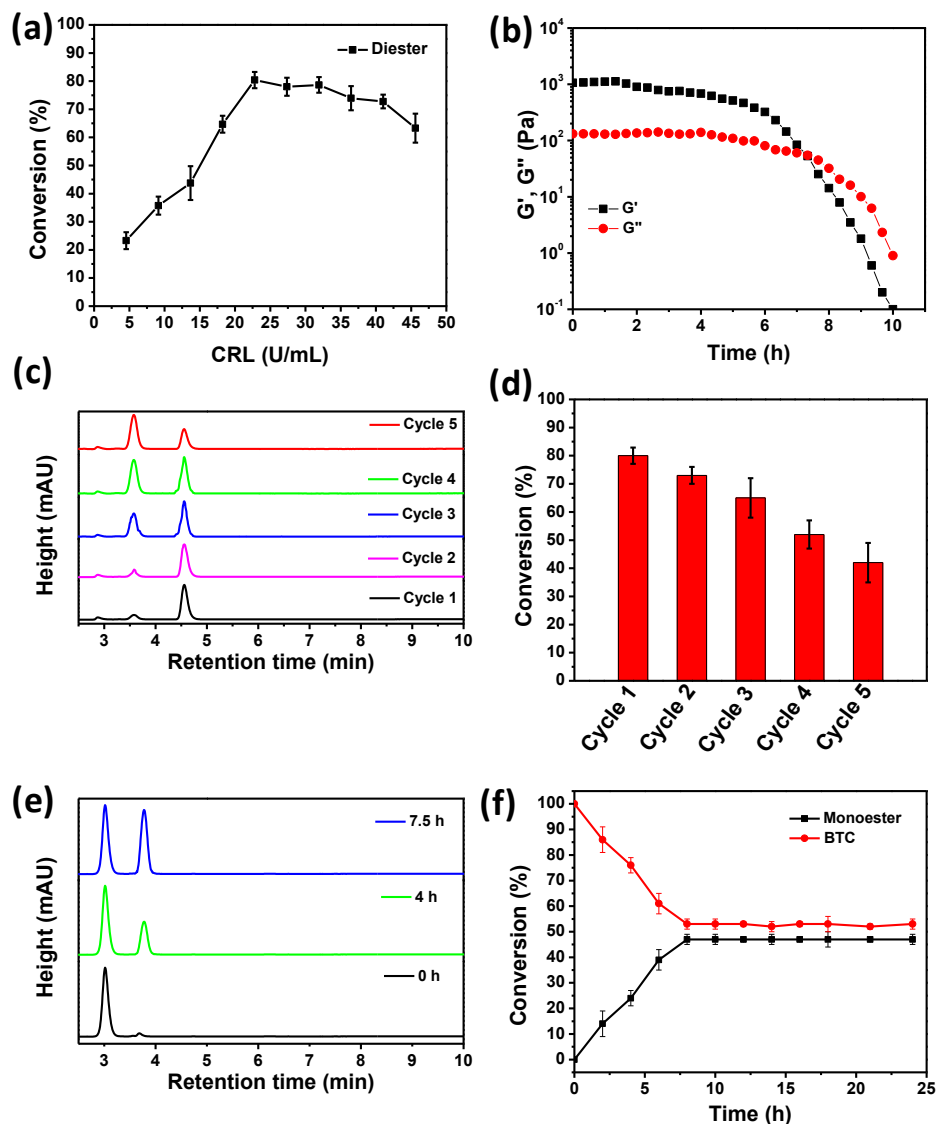


**Figure 4.16.** (a) Standardization of enzyme concentration used for esterification of BDC in tpeb-BDC emulsion gel. (b) Rheological analysis of gel to sol transition of tpeb-BTC. (c), (d) are the HPLC chromatograms of different enzymatic esterification cycles and corresponding histogram plot of the formed BDC-diester. (e) shows the overlaid plot of HPLC chromatograms of BTC monoester formation. (f) Plot of conversion of BTC monoester in tpeb-BTC emulsion-gel.

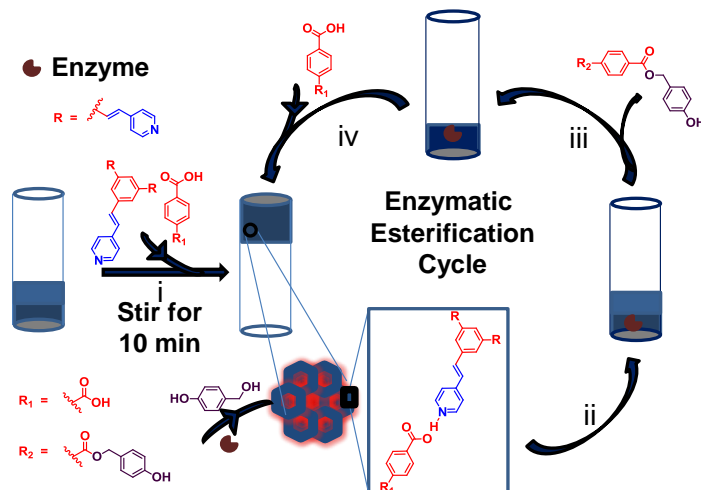


**Figure 4.17.** Overall enzymatic esterification cycle of **BDC** in emulsion-gel (**tpeb-BDC**). (i) Formation of emulsion-gel with lipase and *p*-HBA, (ii) phase separation after esterification, (iii) product isolation and (iv) reformation of emulsion-gel after stirring in presence of additional **BDC**.

Also, SONs formed by the **tpeb-BDC** emulsion-gel have larger surface area to interact with enzyme more as compare to fiber of **tpeb-BTC**. The pore diameter of **tpeb-BTC** complex is 2.88 nm which is found from BET isotherm. The optical images of **tpeb-BDC** complex show emulsion-gel to sol-emulsion transition after completion of 10 hours enzymatic reaction (Figure 4.15a). Further progress of the reaction to 16 hours, **tpeb-BDC** emulsion-gel was separated into biphasic layers (Figure 4.15a) and the conversion of diester was 75%. At 24 hours, the conversion of diester was 80% (Figure 4.15c,d). On esterification reaction, emulsion-gel (**tpeb-BDC**) was separated into two phases and the phase separation led to the excellent recyclability of pyridyl amphiphiles (Figure 4.17) and the enzyme lipase. After 5 reaction cycles, 77% of **tpeb** was recovered. The biocatalyst lipase was also recycled for 5 times. 42% diester of **BDC** was obtained after fifth cycle (Figure 4.16c,d). The turnover frequency (TOF) of lipase is calculated as  $1.24 \times 10^4 \text{ s}^{-1}$ . In contrast, **tpeb-BTC** emulsion-gel turned to emulsion within 7.5 hours with the formation of 47% monoester (Figure 4.16e,f).

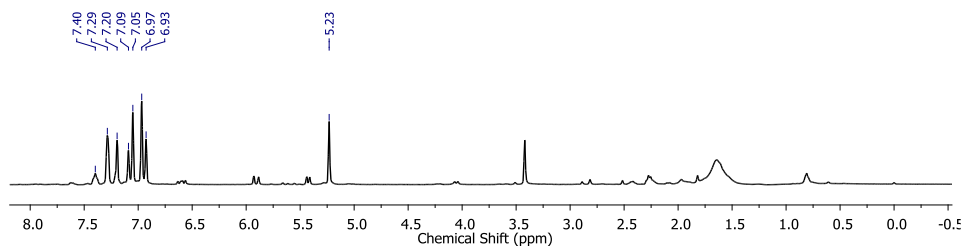


**Figure 4.18.**  $^1\text{H}$  NMR spectrum of **BDC** diester formed after enzymatic reaction in emulsion-gel **tpeb-BDC**. Peak at  $\delta = 5.23$  signifies the formation of ester. To enhance the solubility, 2:1  $\text{CDCl}_3$  and  $\text{DMSO}-d_6$  was used for  $^1\text{H}$  NMR analysis.

The mixture (**tpeb-BTC**/enzyme/*p*-HBA hybrid emulsion) was kept for 30 days. However, the conversion was only increased to 49% monoester formation. The **BDC** diester was also separated and characterized by  $^1\text{H}$  NMR spectroscopy (Figure 4.18). The corresponding peaks at 5.23 ppm signify the esterification of **BDC**. **bpeb-BTC** and **bpeb-BDC** emulsions were unable to give any kind of lipase catalyzed esterified product. Upon addition of *p*-HBA to **bpeb-BTC**, and **bpeb-BDC**, the interaction between the acid and amphiphile gets interrupted due to the involvement of hydrogen bonding (as both don't form strong network like emulsion-gel) interaction using additional hydroxyl group of *p*-HBA.

## 4.5 Conclusion

In conclusion, we have successfully developed different linear and discotic amphiphiles based bicomponent systems with tunable nanostructures and pore sizes. Different architectural building blocks have been formed with significant pore sizes. The pores formed by molecular complexes traps a large amount of immiscible water and organic solvents to form emulsion-gels. Molecular complexes were co-assembled to form emulsion-gels for **tpeb-BTC** and **tpeb-BDC** systems through *J*-type aggregation. **bpeb-BTC** and **bpeb-BDC** emulsions are not strong enough to hold the enzyme and gastrodigenin into the formed microscopic architectures. As a result, the esterification reaction was not observed in emulsions. Whereas, the

emulsion-gels are able to produce esters and the porous architectures in emulsion-gel act as a template for lipase-catalyzed inclusion of gasterodigenin. Larger pore size (**tpeb-BDC**) permits enzyme molecules to insert into the cavity whereas small pores resist the large enzyme to come into the smaller cavity (**tpeb-BTC**). As a result, the enzyme functions on the surface of the smaller porous nanostructures. The enzyme lipase fits into the larger cavity and larger surface area of porous SONs of **tpeb-BDC** to yield the terephthalate diester with an excellent conversion. In contrast, **tpeb-BTC** emulsion-gel forms only monoester during enzymatic esterification as the enzyme come contact to a small area as compare to **tpeb-BDC**. Enzymatic esterification reaction leads to the breakdown of the emulsion-gel **tpeb-BDC** into two phases and phase separation permits for the recyclability of the pyridyl amphiphile. These porous nanostructures open a new path for various enzymatic reactions into the soft material at a mild aqueous-organic condition with a faster rate.

### 4.6 References

1. Kitagawa S., Kitaura R., Noro S. I. (2004), Functional Porous Coordination Polymers, *Angew. Chem., Int. Ed.* 43, 2334-2375 (DOI: 10.1002/anie.200300610).
2. Yaghi O. M., O'Keeffe M., Ockwig N. W., Chae H. K., Eddaoudi M., Kim J. (2003), Reticular Synthesis and the Design of New Materials, *Nature*, 423, 705-714 (DOI: 10.1038/nature01650).
3. Bradshaw D., Claridge J. B., Cussen E. J., Prior T. J., Rosseinsky M. J. (2005), Design, Chirality, and Flexibility in Nanoporous Molecule-Based Materials, *Acc. Chem. Res.*, 38, 273-282 (DOI: 10.1021/ar0401606).
4. Shimomura S., Kitagawa S. (2011), Soft porous crystal meets TCNQ: charge transfer-type porous coordination polymers. *J. Mater. Chem.*, 21, 5537-5546 (DOI: 10.1039/C1JM10208G).

5. Lu J., Perez-Krap C., Suyetin M., Alsmail N. H., Yan Y., Yang S., Lewis W., Bichoutskaia E., Tang C. C., Blake A. J., Cao R., Schröder M. (2014), A Robust Binary Supramolecular Organic Framework (SOF) with High CO<sub>2</sub> Adsorption and Selectivity, *J. Am. Chem. Soc.*, 136, 12828-12831 (DOI: 10.1021/ja506577g).
6. Fu J., Das S., Xing G., Ben T., Valtchev V., Qiu S. (2016), Fabrication of COF-MOF Composite Membranes and Their Highly Selective Separation of H<sub>2</sub>/CO<sub>2</sub>, *J. Am. Chem. Soc.*, 138, 7673-7680 (DOI: 10.1021/jacs.6b03348).
7. Ding S. Y., Gao J., Wang Q., Zhang Y., Song W. G., Su C. Y., Wang W. (2011), Construction of Covalent Organic Framework for Catalysis: Pd/COF-LZU1 in Suzuki-Miyaura Coupling Reaction, *J. Am. Chem. Soc.*, 133, 19816-19822 (DOI: 10.1021/ja206846p).
8. Bhanja P., Mishra S., Manna K., Mallick A., Das Saha K., Bhaumik, A. (2017), Covalent Organic Framework Material Bearing Phloroglucinol Building Units as a Potent Anticancer Agent, *ACS Appl. Mater. Interfaces*, 9, 31411-31423 (DOI: 10.1021/acsami.7b07343).
9. Patra B. C., Khilari S., Manna R. N., Mondal S., Pradhan D., Pradhan A., Bhaumik A. (2017), A Metal-Free Covalent Organic Polymer for Electrocatalytic Hydrogen Evolution, *ACS Catal.*, 7, 6120-6127 (DOI: 10.1021/acscatal.7b01067).
10. Pfeffermann M., Dong R., Graf R., Zajaczkowski W., Gorelik T., Pisula W., Narita A., Müllen K., Feng X. (2015), Free-Standing Monolayer Two-Dimensional Supramolecular Organic Framework with Good Internal Order, *J. Am. Chem. Soc.*, 137, 14525-14532 (DOI: 10.1021/jacs.5b09638).
11. Teyssandier J., Feyter, S. D., Mali K. S. (2016), Host-Guest Chemistry in Two-Dimensional Supramolecular Networks, *Chem. Commun.*, 52, 11465-11487 (DOI: 10.1039/C6CC05256H).

12. Zhang Y., Zhan T. G., Zhou T. Y., Qi Q. Y., Xu X. N., Zhao X. (2016), Fluorescence Enhancement Through the Formation of a Single-Layer Two-dimensional Supramolecular Organic Framework and Its Application in Highly Selective Recognition of Picric Acid, *Chem. Commun.*, 52, 7588-7591 (DOI: 10.1039/C6CC03631G).
13. Yang W., Greenaway A., Lin X., Matsuda R., Blake A. J., Wilson C., Lewis W., Hubberstey P., Kitagawa S., Champness N. R., Schroder M. (2010), Exceptional Thermal Stability in a Supramolecular Organic Framework: Porosity and Gas Storage, *J. Am. Chem. Soc.*, 132, 14457-14469 (DOI: 10.1021/ja1042935).
14. Tian J., Chen L., Zhang D. W., Liu Y., Li Z. T. (2016), Supramolecular Organic Frameworks: Engineering Periodicity in Water Through Host-Guest Chemistry, *Chem. Commun.*, 52, 6351-6362 (DOI: 10.1039/C6CC02331B).
15. Zhang K. D., Tian J., Hanifi D., Zhang Y., Sue A. C. H., Zhou T. Y., Zhang L., Zhao X., Liu Y., Li Z. T. (2013), Toward a Single-Layer Two-Dimensional Honeycomb Supramolecular Organic Framework in Water, *J. Am. Chem. Soc.*, 2013, 135, 17913-17918 (DOI: 10.1021/ja4086935).
16. Maspoch D., Ruiz-Molina D., Veciana J. (2007), Old Materials With New Tricks: Multifunctional Open-Framework Materials, *Chem. Soc. Rev.*, 36, 770-818 (DOI: 10.1039/B501600M).
17. Lehn J. M. (1985), Supramolecular Chemistry: Receptors, Catalysts, and Carriers, *Science*, 227, 849-856 (DOI: 10.1126/science.227.4689.849).
18. Whitesides G. M., Grzybowski B. (2002), Self-Assembly at All Scales, *Science*, 295, 2418-2421 (DOI: 10.1126/science.1070821).
19. Stoddart J. F. (2009), Thither Supramolecular Chemistry? *Nat. Chem.*, 1, 14-15 (DOI: 10.1038/nchem.142).

20. Thota B. N. S., Urner L. H., Haag R. (2016), Supramolecular Architectures of Dendritic Amphiphiles in Water, *Chem. Rev.*, 116, 2079-2102 (DOI: 10.1021/acs.chemrev.5b00417).
21. Cheng C. X., Tian Y., Shi Y. Q., Tang R. P., Xi F. (2005), Porous Polymer Films and Honeycomb Structures Based on Amphiphilic Dendronized Block Copolymers, *Langmuir*, 21, 6576-6581 (DOI: 10.1021/la050187d).
22. Buerkle L. E., Rowan S. J. (2012), Supramolecular Gels Formed from Multi-Component Low Molecular Weight Species, *Chem. Soc. Rev.*, 41, 6089-6102 (DOI: 10.1039/C2CS35106D).
23. Hirst A. R., Smith D. K. (2005), Two-Component Gel-Phase Materials- Highly Tunable Self-Assembling Systems, *Chem. Eur. J.*, 11, 5496-5508 (DOI: 10.1002/chem.200500241).
24. Hanabusa K., Miki T., Taguchi Y., Koyama T., Shirai H. (1993), Two-Component, Small Molecule Gelling Agents, *J. Chem. Soc., Chem. Commun.*, 1382-1384 (DOI: 10.1039/C39930001382).
25. Krishnan B. P., Ramakrishnan S., Sureshan K. M. (2013), Supramolecular Design of a Bicomponent Topochemical Reaction between Two Non-Identical Molecules, *Chem. Commun.*, 49, 1494-1496 (DOI: 10.1039/C2CC37067K).
26. Bairi P., Roy B., Nandi A. K. (2010), Bicomponent Hydrogels of Lumichrome and Melamine: Photoluminescence Property and Its Dependency on pH and Temperature, *J. Phys. Chem. B*, 114, 11454-11461 (DOI: 10.1021/jp105378e).
27. Rao K. V., Jayaramulu K., Maji T. K., George S. J. (2010), Supramolecular Hydrogels and High-Aspect-Ratio Nanofibers through Charge-Transfer-Induced Alternate Coassembly, *Angew. Chem., Int. Ed.*, 49, 4218-4222 (DOI: 10.1002/anie.201000527).
28. Biswas S., Rasale D. B., Das A. K. (2016), Blue Light Emitting Self-Healable Graphene Quantum Dot Embedded Hydrogels, *RSC Adv.*, 6, 54793-54800 (DOI: 10.1039/C6RA06587B).

29. Markvoort A. J., ten Eikelder H. M. M., Hilbers P. A. J., de Greef T. F. A., Meijer E. W. (2011), Theoretical Models of Nonlinear Effects in Two-Component Cooperative Supramolecular Copolymerizations, *Nat. Commun.*, 2, 509 (DOI: 10.1038/ncomms1517).
30. Ikeda T., Iijima T., Sekiya R., Takahashi O., Haino T. (2016), Cooperative Self-Assembly of Carbazole Derivatives Driven by Multiple Dipole-Dipole Interactions, *J. Org. Chem.*, 81, 6832-6837 (DOI: 10.1021/acs.joc.6b01169).
31. Rest C., Mayoral M. J., Fucke K., Schellheimer J., Stepanenko V., Fernandez G. (2014), Self-Assembly and (Hydro)gelation Triggered by Cooperative  $\pi$ - $\pi$  and Unconventional C-H $\cdots$ X Hydrogen Bonding Interactions, *Angew. Chem., Int. Ed.*, 53, 700-705 (DOI: 10.1002/anie.201307806).
32. Draper E. R., Eden E. G. B., McDonald T. O., Adams D. J. (2015), Spatially Resolved Multicomponent Gels, *Nat. Chem.*, 7, 848-852 (DOI: 10.1038/nchem.2347).
33. Kar H., Ghosh S. (2015), Multicomponent Gels: Remote Control for Self-Assembly, *Nat. Chem.*, 7, 765-767 (DOI: 10.1038/nchem.2351).
34. Tian J., Zhou T. Y., Zhang, S. C., Aloni S., Altoe M. V., Xie S. H., Wang H., Zhang D. W., Zhao X., Liu Y., Li Z. T. (2014), Three-Dimensional Periodic Supramolecular Organic Framework Ion Sponge in Water and Microcrystals, *Nat. Commun.*, 5, 5574 (DOI: 10.1038/ncomms6574).
35. Kuehl C. J., Kryschenko Y. K., Radhakrishnan U., Seidel S. R., Huang S. D., Stang P. J. (2002), Self-Assembly of Nanoscopic Coordination Cages of  $D_{3h}$  Symmetry, *Proc. Natl. Acad. Sci. U. S. A.*, 99, 4932-4936 (DOI: 10.1073/pnas.012540799).
36. Wang Q., Wu J., Gong Z., Zou Y., Yi T., Huang C. (2010), From Vesicles to Solid Spheres: Terminal Functional Group Induced Morphology Modification, *Soft Matter*, 6, 2679-2684 (DOI: 10.1039/B927579G).

37. Huang Z., Kang S. K., Banno M., Yamaguchi T., Lee D., Seok C., Yashima E., Lee M. (2012), Pulsating Tubules from Noncovalent Macrocycles, *Science*, 337, 1521-1526 (DOI: 10.1126/science.1224741).
38. Yan X., Xu J. F., Cook T. R., Huang F., Yang Q. Z., Tung C. H., Stang P. J. (2014), Photoinduced Transformations of Stiff-Stilbene-Based Discrete Metallacycles to Metallosupramolecular Polymers, *Proc. Natl. Acad. Sci. U. S. A.*, 111, 8717-8722 (DOI: 10.1073/pnas.1408620111).
39. Nath K., Husain A., Dastidar P. (2015), Metallogels and Silver Nanoparticles Generated from a Series of Transition Metal-Based Coordination Polymers Derived from a New Bis-pyridyl-bis-amide Ligand and Various Carboxylates, *Cryst. Growth Des.*, 15, 4635-4645 (DOI: 10.1021/acs.cgd.5b00911).
40. Horcajada P., Serre C., Vallet-Regi M., Sebba M., Taulelle F., Ferey G. (2006), Metal-Organic Frameworks as Efficient Materials for Drug Delivery, *Angew. Chem., Int. Ed.*, 45, 5974-5978 (DOI: 10.1002/anie.200601878).
41. Streb C., Long D. -L., Cronin L. (2007), Engineering Porosity in a Chiral Heteropolyoxometalate-based Framework: The Supramolecular Effect of Benzenetricarboxylic Acid, *Chem. Commun.*, 471-473 (DOI: 10.1039/B613808J).
42. Balgley R., de Ruiter G., Evmenenko G., Bendikov T., Lahav M., van der Boom M. E. (2016), Light-Induced Conversion of Chemical Permeability to Enhance Electron and Molecular Transfer in Nanoscale Assemblies, *J. Am. Chem. Soc.*, 138, 16398-16406 (DOI: 10.1021/jacs.6b09781).
43. Glavinovic M., Qi F., Katsenis A. D., Friscic T., Lumb J. -P. (2016), Redox-Promoted Associative Assembly of Metal-Organic Materials, *Chem. Sci.*, 7, 707-712 (DOI: 10.1039/C5SC02214B).

44. Mateo C., Palomo J. M., Fernandez-Lorente G., Guisan J. M., Fernandez-Lafuente R. (2007), Improvement of Enzyme Activity, Stability and Selectivity via Immobilization Techniques, *Enzyme Microb. Technol.*, 40, 1451-1463 (DOI: 10.1016/j.enzmictec.2007.01.018).
45. Das A. K., Maity I., Parmar H. S., McDonald T. O., Konda M. (2015), Lipase-Catalyzed Dissipative Self-Assembly of a Thixotropic Peptide Bolaamphiphile Hydrogel for Human Umbilical Cord Stem-Cell Proliferation, *Biomacromolecules*, 16, 1157-1168 (DOI: 10.1021/bm501835v).
46. Rasale D. B., Maity I., Das A. K. (2014), Lipase Catalyzed Inclusion of Gastrodigenin for the Evolution of Blue Light Emitting Peptide Nanofibers, *Chem. Commun.*, 50, 8685-8688 (DOI: 10.1039/C4CC02484B).
47. Zhang W., Sheng Y. X., Zhang J. L. (2008), Determination and Pharmacokinetics of Gastrodin and p-hydroxybenzylalcohol after Oral Administration of *Gastrodia elata* Bl. Extract in Rats by High-Performance Liquid Chromatography-Electrospray Ionization Mass Spectrometric Method, *Phytomedicine*, 15, 844-850 (DOI: 10.1016/j.phymed.2008.02.012).
48. Scott G. G., McKnight P. J., Tuttle T., Ulijn R. V. (2016), Tripeptide Emulsifiers, *Adv. Mater.*, 28, 1381-1386 (DOI: 10.1002/adma.201504697).
49. Harbron R. L., McDonald T. O., Rannard S. P., Findlay P. H., Weaver J. V. M. (2012), One-Pot, Single-Component Synthesis of Functional Emulsion-Templated Hybrid Inorganic-Organic Polymer Capsules, *Chem. Commun.*, 48, 1592-1594 (DOI: 10.1039/C1CC15213K).
50. Moreira I. P., Sasselli I. R., Cannon D., Hughes M., Lamprou D. A., Tuttle T., Ulijn R. V. (2016), Enzymatically Activated Emulsions Stabilised by Interfacial Nanofibre Networks, *Soft Matter*, 12, 2623-2631 (DOI: 10.1039/C5SM02730F).

51. Koenig A., Hébraud P., Perrin P. (2012), Preparation and Rheological Properties of Emulsion Gels, *Langmuir*, 18, 6458-6461 (DOI: 10.1021/la0200663).
52. Smith A. M., Williams R. J., Tang C., Coppo P., Collins R. F., Turner M. L., Saiani A., Ulijn R. V. (2008), Fmoc-Diphenylalanine Self-Assembles to a Hydrogel via a Novel Architecture Based on  $\pi$ - $\pi$  Interlocked  $\beta$ -Sheets, *Adv. Mater.*, 20, 37-41 (DOI: 10.1002/adma.200701221).
53. Tellez C. A., Hollauer S. E., Mondragon M. A., Castano V. M. (2001), Fourier Transform Infrared and Raman Spectra, Vibrational Assignment and Ab Initio Calculations of Terephthalic Acid and Related Compounds, *Spectrochim. Acta, Part A*, 57, 993-1007 (DOI: 10.1016/S1386-1425(00)00428-5).
54. Mahalakshmi G., Balachandran V. (2014), FT-IR and FT-Raman Spectra, Normal Coordinate Analysis and Ab Initio Computations of Trimesic Acid, *Spectrochim. Acta, Part A*, 124, 535-547 (DOI: 10.1016/j.saa.2014.01.061).
55. Dawa B. A., Gowland J. A. (1978), Infrared Studies of Carboxylic Acids and Pyridine in Chloroform and Methanol, *Can. J. Chem.*, 56, 2567-2571 (DOI: 10.1139/v78-421).
56. Johnson S. L., Rumon K. A. (1965), Infrared Spectra of Solid 1:1 Pyridine-Benzoic Acid Complexes; the Nature of the Hydrogen Bond as a Function of the Acid-Base Levels in the Complex, *J. Phys. Chem.*, 69, 74-86 (DOI: 10.1021/j100885a013).
57. Barrow G. M. (1956), The Nature of Hydrogen Bonded Ion-Pairs: The Reaction of Pyridine and Carboxylic Acids in Chloroform, *J. Am. Chem. Soc.*, 78, 5802-5806 (DOI: 10.1021/ja01603a022).
58. Kasha, M.; Rawls, H. R.; Ashraf El-Bayoumi, M. The Exciton Model in Molecular Spectroscopy. *Pure Appl. Chem.* 1965, 11, 371-392 (DOI: 10.1351/pac196511030371).

59. Ajayaghosh A., Praveen V. K. (2007),  $\pi$ -Organogels of Self-Assembled p-Phenylenevinylenes: Soft Materials with Distinct Size, Shape, and Functions, *Acc. Chem. Res.*, 40, 644-656 (DOI: 10.1021/ar7000364).
60. Pisula W., Kastler M., Wasserfallen D., Robertson J. W. F., Nolde F., Kohl C., Mullen K. (2006), Pronounced Supramolecular Order in Discotic Donor-Acceptor Mixtures, *Angew. Chem., Int. Ed.*, 45, 819-823 (DOI: 10.1002/anie.200500669).
61. Paraschiv I., de Lange K., Giesbers M., van Lagen B., Grozema F. C., Abellon R. D., Siebbeles L. D. A., Sudholter E. J. R., Zuilhof H., Marcelis A. T. M. (2008), Hydrogen-Bond Stabilized Columnar Discotic Benzenetrisamides with Pendant Triphenylene Groups, *J. Mater. Chem.*, 18, 5475-5481 (DOI: 10.1039/b805283b).
62. Holst H. C., Pakula T., Meier H. (2004), Liquid Crystals in the Series of 2,4,6-tristyryl-1,3,5-triazines, *Tetrahedron*, 60, 6765-6775 (DOI: 10.1016/j.tet.2004.06.031).
63. Sinha S. K., Sirota E. B., Garoff S., Stanley H. B. (1988), X-Ray and Neutron Scattering from Rough Surfaces, *Phys. Rev. B: Condens. Matter Mater. Phys.*, 38, 2297-2311 (DOI: 10.1103/PhysRevB.38.2297).
64. Xu S. Q., Zhang X., Nie C. B., Pang Z. F., Xu X. N., Zhao X. (2015), The Construction of a Two-Dimensional Supramolecular Organic Framework with Parallelogram Pores and Stepwise Fluorescence Enhancement, *Chem. Commun.*, 51, 16417-16420 (DOI: 10.1039/C5CC05875A).
65. Kuang D., Brezesinski T., Smarsly B. (2004), Hierarchical Porous Silica Materials with a Trimodal Pore System Using Surfactant Templates, *J. Am. Chem. Soc.*, 126, 10534-10535 (DOI: 10.1021/ja0470618).
66. Glatter O., Kratky O. (1982), *Small Angle X-Ray Scattering*; Academic Press: London, 36, 296-296 (ISBN 0-12-286280-5).

67. Kotlarchyk M., Chen S. H. (1983), Analysis of Small Angle Neutron Scattering Spectra from Polydisperse Interacting Colloids, *J. Chem. Phys.*, 79, 2461-2469 (DOI: 10.1063/1.446055).
68. Radlinski A. P., Mastalerz M., Hinde A. L., Hainbuchner M., Rauch R., Baron R., Lin J. S., Fan L., Thiyagarajan P. (2004), Application of SAXS and SANS in Evaluation of Porosity, Pore Size Distribution and Surface Area of Coal, *Int. J. Coal Geol.*, 59, 245-271 (DOI: 10.1016/j.coal.2004.03.002).
69. Guo Z., Ruegger H., Kissner R., Ishikawa T., Willeke M., Walde P. (2009), Vesicles as Soft Templates for the Enzymatic Polymerization of Aniline, *Langmuir*, 25, 11390-11405 (DOI: 10.1021/la901510m).
70. Takahashi H., Li B., Sasaki T., Miyazaki C., Kajino T., Inagaki S. (2000), Catalytic Activity in Organic Solvents and Stability of Immobilized Enzymes Depend on the Pore Size and Surface Characteristics of Mesoporous Silica, *Chem. Mater.*, 12, 3301-3305 (DOI: 10.1021/cm000487a).
71. Wang Z. J., Clary K. N., Bergman R. G., Raymond K. N., Toste F. D. (2013), A Supramolecular Approach to Combining Enzymatic and Transition Metal Catalysis, *Nat. Chem*, 5, 100-103 (DOI: 10.1038/nchem.1531).
72. Boekhoven J., Hendriksen W. E., Koper G. J. M., Eelkema R., van Esch J. H. (2015), Transient Assembly of Active Materials Fueled by a Chemical Reaction, *Science*, 349, 1075-1079 (DOI: 10.1126/science.aac6103).
73. Kim K. K., Song H. K., Shin D. H., Hwang K. Y., Suh S. W. (1997), The Crystal Structure of a Triacylglycerol Lipase from *Pseudomonas Cepacia* Reveals a Highly Open Conformation in the Absence of a Bound Inhibitor, *Structure*, 5, 173-185 (DOI: 10.1016/S0969-2126(97)00177-9).



## **Chapter 5**

# **Bicomponent Co-assembled Nanotubular Hydrogel as Template for Selective Enzymatic Generation of DOPA**



## 5.1 Introduction

Hydrogels are soft materials which can be developed by several ways including inclusion of stimuli,<sup>[1-3]</sup> enzymatic reaction,<sup>[4-7]</sup> photo induced assembly<sup>[8-9]</sup> and also by integration of multiple components. Multicomponent cooperative self-assembly is enlightened as one of the significant tool to design and control such soft materials with distinguishable properties.<sup>[10-13]</sup> The incorporation of multiple components dispenses controlled self-assembly and gelation by self-sorting of the components.<sup>[14-15]</sup> The bicomponent systems are the simplest multicomponent systems, which steer the self-assembling property of the components and to evolve supramolecular hydrogels.<sup>[16-20]</sup> Generally, low molecular weight hydrogelators bearing complementary functionality were integrated to achieve the desired bicomponent cooperative self-assembled system.<sup>[21-26]</sup> The cooperative self-assembly (co-assembly) between two amphiphile changes with the change in complementary functionality and the gelation ability of the composites.<sup>[27-28]</sup> These cooperative self-assembly rely on several non-covalent interactions including hydrogen-bonding and  $\pi$ - $\pi$  stacking interactions,<sup>[29]</sup> Therefore fine tuning of functionality leads to large change in property of bicomponent system. So, it is considered as molecular remote control for self-assembly.<sup>[30-31]</sup> Self-assembled hydrogels are promising materials for several bioapplications due to their eminent biocompatibility having controlled nanoarchitectures.<sup>[32-34]</sup> The bioapplications include cell culture<sup>[35]</sup>, tissue engineering<sup>[36]</sup>, drug delivery<sup>[37]</sup> and several biocatalytic reactions<sup>[38]</sup> inside the gel matrix. Enzymes are the prime candidate as biocatalyst. Immobilization or entrapment into crosslinked fibrillar network of hydrogel is of particular interest.<sup>[39]</sup> Recently, we reported controlled supramolecular organic nanostructured emulsion-gel was developed for biocatalytic inclusion of gastrodigenin using bicomponent co-assembled system.<sup>[40]</sup> The co-assembly between two complementary amphiphile can

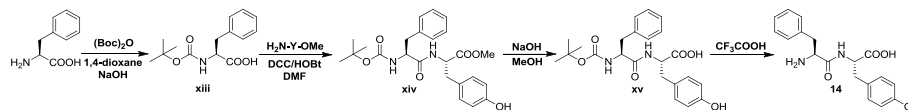
be tuned very easily. This makes the materials more demanding as medium of biocatalytic reaction as the product separation becomes easier subsequent to the enzymatic catalysis. In this work, we focused to evolve bicomponent co-assembled hydrogel as a medium for the selective biocatalytic production of L-DOPA in peptide sequence.

L-DOPA, the precursor of neurotransmitters dopamine and a series of other catecholamines, has important role in neurotrophic factor release in brain and central nervous system. L-DOPA is also known as a drug which is used in the treatment of Parkinson's diseases.<sup>[41]</sup> In living organisms, L-DOPA is produced by the biocatalytic reaction of an amino acid tyrosine with an enzyme tyrosinase. The chemical synthesis of L-DOPA in laboratory involves complicated procedures.<sup>[42]</sup> The metal catalysts and expensive chemicals are used to work under harsh conditions to produce L-DOPA with a low enantiomeric excess and low conversion rate.<sup>[43]</sup> Therefore, enantioselective production of L-DOPA with a high conversion seems necessary and encapsulation of enzyme into supramolecular gel would be a great approach to get the work done.

Development of desired co-assembled bicomponent systems as hydrogel matrix for enzymatic reaction inspired us to choose multifunctional amphiphiles. Amine functionalized multifunctional amphiphiles with complementary group serves maximum interaction to control co-assembly.<sup>[44-45]</sup> Bifunctional (BDC) and trifunctional (BTC) acids are well-known for the co-assembly due to their multiple hydrogen bonding unit.<sup>[46-48]</sup> Therefore, controlled co-assembly can be achieved easily by integrating the multifunctional amphiphiles with their complementary functionalities. Biocatalytic reaction template i.e. bicomponent hydrogel was developed. An hydroxylase enzyme tyrosinase was incorporated into the gel to carry out the synthesis L-DOPA from L-tyrosine. To achieve our goal, L-tyrosine (Y) and Y appended peptide Phe-Tyr (FY) were also taken.

## 5.2 Experimental

*Scheme 5.1 Synthetic scheme of compound 14*



### 5.2.1 Synthesis of Boc-Phe-OH (xiii)

A solution of phenylalanine (2 g, 12.1 mmol) in a mixture of 1,4-dioxane (20 mL), 1(N) sodium hydroxide (20 mL) was stirred and cooled in an ice bath. Bocanhydride (3.06 mL, 13.31 mmol) was added and stirring was continued at room temperature for overnight. The reaction mixture was diluted with 100 mL of water and dioxane was evaporated under vacuum. The aqueous layer was washed with diethyl ether. The aqueous layer was collected the pH was adjusted to 2 with 2(N) hydrochloric acid. The aqueous phase was extracted with ethyl acetate (3 x 50 mL) and dried with  $\text{Na}_2\text{SO}_4$ . The collected ethyl acetate was concentrated in vacuo to obtain product (xiii) as colorless oil. Yield= 3.09 g (11.65 mmol, 96%)  $^1\text{H}$  NMR (400 MHz,  $\text{DMSO-d}_6$ ):  $\delta$  7.28 (m, 5H), 7.11 (d, 1H, NH), 4.09 (q, 1H,  $\text{C}^\alpha\text{H}$  of Phe), 3.00 (d, 2H,  $\text{C}^\beta\text{H}$  of Phe), 1.32 (s, 9H,  $\text{CH}_3$ ) ppm.

### 5.2.2 Synthesis of Boc-Phe-Tyr-OMe (xiv)

0.5 g (1.88 mmol) of Boc-(L)-Phe-OH was dissolved in 2 mL dry DMF in a 100 mL R.B. flask. The (L)-Tyr-OMe was extracted from the corresponding methyl ester hydrochloride salt 0.65 g (2.82 mmol). The extracted (L)-Tyr-OMe was diluted a small volume of ethyl acetate and finally added into Boc-Tyr-OH solution in stirring condition. Then 0.43 g (2.06 mmol) DCC was added followed by the addition of 0.28 g (1.88 mmol) of HOBt and the reaction was kept overnight to stir. The reaction progress was checked by TLC. On completion of the reaction 50 mL ethyl acetate was added into the reaction mixture and then filtered through the suction pump. The filtrate was successively washed with 1 (N) HCl (3x50

mL), saturated  $\text{Na}_2\text{CO}_3$  (3×50 mL) and brine into a separating funnel. The ethyl acetate part was collected, and the dried ethyl acetate (over  $\text{Na}_2\text{SO}_4$ ) was evaporated by rotary evaporator. The product was collected and purified through silica gel column chromatography (100-200 mesh) using hexane: ethyl acetate as eluent. Yield: 0.085 g (1.7 mmol, 89%),  $^1\text{H}$  NMR (400 MHz,  $\text{DMSO-d}_6$ ):  $\delta$  9.24 (s, 1H, -OH of Tyr), 8.24-8.22 (d, 1H, -NH), 7.28-7.20 (m, 5H, aromatic ring Hs of Phe), 7.02-7.00 (d, 2H, aromatic ring Hs of Tyr), 6.88-6.85 (d, 1H, -NH), 6.68-6.66 (d, 2H, aromatic ring Hs of Tyr), 4.46-4.40 (m, 1H,  $\text{C}^\alpha\text{H}$  of Phe), 4.22-4.16 (m, 1H,  $\text{C}^\alpha\text{H}$  of Tyr), 3.59 (s, 3H, Hs of  $-\text{OCH}_3$ ), 2.98-2.65 (m, 4H,  $\text{C}^\beta\text{H}$  of Phe and Tyr), 1.30 (s, 9H, Hs of BOC) ppm. MS (ESI)  $m/z$  for  $\text{C}_{24}\text{H}_{30}\text{N}_2\text{O}_7$   $[\text{M} + \text{Na}]^+$  calcd: 465.2002, found: 465.2153.

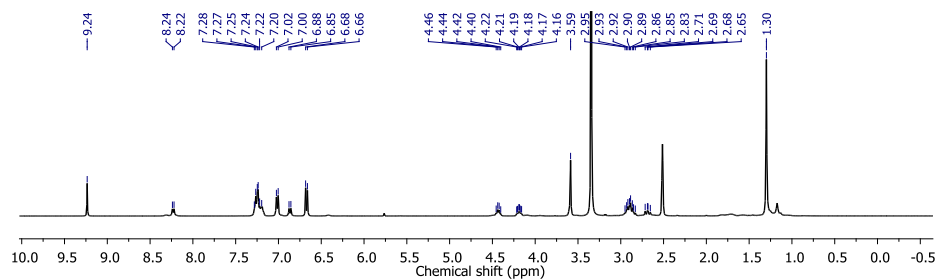


Figure 5.1.  $^1\text{H}$  NMR spectrum of Boc-Phe-Tyr-OMe (xiv) in  $\text{DMSO-d}_6$

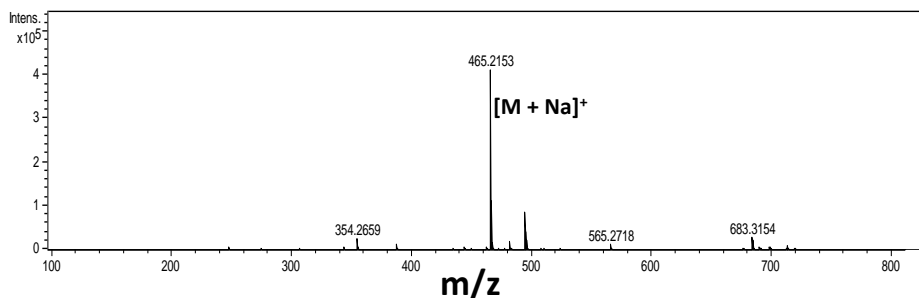


Figure 5.2. Mass spectrum of Boc-Phe-Tyr-OMe (xiv).

### 5.2.3 Synthesis of Boc-Phe-Tyr-OH (xv)

0.6 g (1.35 mmol) of Boc-Phe-Tyr-OMe in 10 mL MeOH was taken in a round bottom flask and 1 M NaOH was added to it dropwise. The reaction mixture was stirred and was continuously monitored by thin layer

chromatography (TLC) till the completion of the reaction. The reaction was completed after 6 hours. Then MeOH was removed under vacuo and 10 mL of distilled water was added to the reaction. The aqueous part was washed with diethyl ether (2 x 30 mL). Then the collected aqueous layer was cooled under ice-water bath for 10 minute and then pH was adjusted to 1 by drop wise addition of 1M HCl. It was extracted with ethyl acetate (3 x 50 mL) and then the ethyl acetate part was dried over anhydrous  $\text{Na}_2\text{SO}_4$  and evaporated in vacuo to yield Boc-FY-OH as a white solid. Yield = 0.54 g (0.13 mmol, 94%),  $^1\text{H}$  NMR (400 MHz,  $\text{DMSO-d}_6$ ):  $\delta$  9.23 (s, 1H, -OH of Tyr), 8.02-8.0 (d, 1H, -NH), 7.28-7.16 (m, 5H, aromatic ring Hs of Phe), 7.05-7.03 (d, 2H, aromatic ring Hs of Tyr), 6.90-6.88 (d, 1H, -NH), 6.69-6.66 (d, 2H, aromatic ring Hs of Tyr), 4.42-4.37 (m, 1H,  $\text{C}^\alpha\text{H}$  of Phe), 4.20-4.14 (m, 1H,  $\text{C}^\alpha\text{H}$  of Tyr), 2.99-2.66 (m, 4H,  $\text{C}^\beta\text{H}$  of Phe and Tyr), 1.30 (s, 9H, Hs of BOC) ppm. MS (ESI)  $m/z$  for  $\text{C}_{23}\text{H}_{28}\text{N}_2\text{O}_6$   $[\text{M} + \text{Na}]^+$  calcd: 451.1845, found: 451.2060.

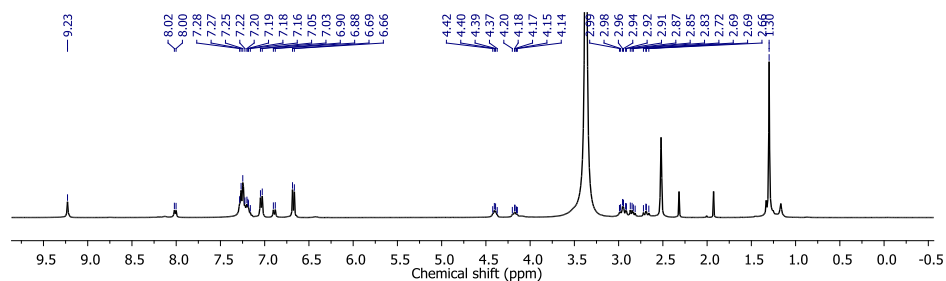


Figure 5.3.  $^1\text{H}$  NMR spectrum of Boc-Phe-Tyr-OH (xv) in  $\text{DMSO-d}_6$

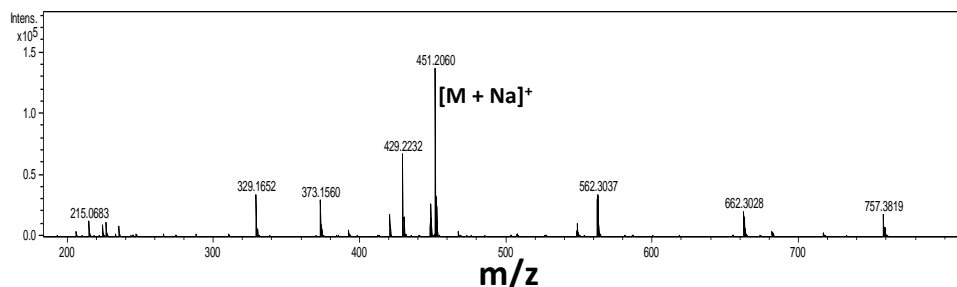


Figure 5.4. Mass spectra of Boc-Phe-Tyr-OH (xv).

### 5.2.4 Synthesis of H<sub>2</sub>N-Phe-Tyr-OH (14)

Boc-Phe-Tyr-OH (0.3 g, 0.7 mmol) was taken in a 100 mL round bottom flask. 2 mL TFA was added into the round bottom flask and stirred for 12 h under argon at room temperature. The excess TFA removed under vacuum and the oily residue was taken in 25 mL of water. The aqueous layer was washed with diethyl ether (2 x 25 mL) white product was obtained after lyophilization. Yield: 0.22 g (96%, 0.67 mmol), <sup>1</sup>H NMR (400 MHz, DMSO-d<sub>6</sub>): δ 9.21 (s, 1H, -OH of Tyr), 8.00-7.98 (d, 1H, -NH), 7.26-7.14 (m, 5H, aromatic ring Hs of Phe), 7.03-7.01 (d, 2H, aromatic ring Hs of Tyr), 6.88-6.86 (d, 1H, -NH), 6.67-6.64 (d, 2H, aromatic ring Hs of Tyr), 4.40-4.35 (m, 1H, C<sup>α</sup>H of Phe), 4.18-4.12 (m, 1H, C<sup>α</sup>H of Tyr), 2.97-2.64 (m, 4H, C<sup>β</sup>H of Phe and Tyr) ppm. <sup>13</sup>C NMR (400 MHz, DMSO-d<sub>6</sub>): 172.55, 170.57, 170.57, 156.36, 130.39, 129.98, 129.85, 127.27, 127.12, 115.12, 114.80, 53.62, 53.22, 36.06, 35.80 δ ppm. MS (ESI) *m/z* for C<sub>18</sub>H<sub>20</sub>N<sub>2</sub>O<sub>4</sub> [M + K]<sup>+</sup> calcd: 367.1055, found: 367.1800.

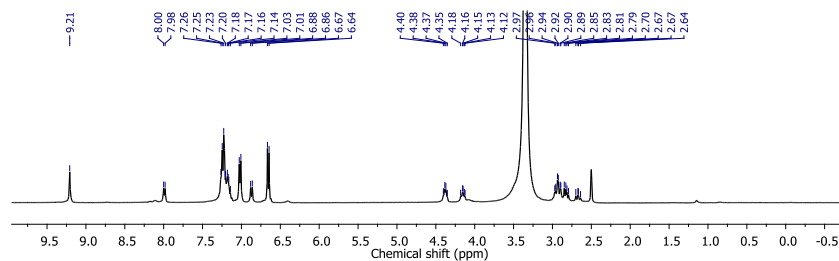


Figure 5.5. <sup>1</sup>H NMR spectrum of H<sub>2</sub>N-Phe-Tyr-OH (14) in DMSO-d<sub>6</sub>.

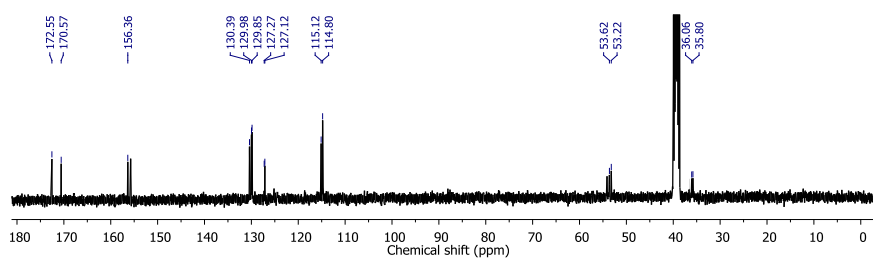


Figure 5.6. <sup>13</sup>C NMR spectrum of H<sub>2</sub>N-Phe-Tyr-OH (14) in DMSO-d<sub>6</sub>.

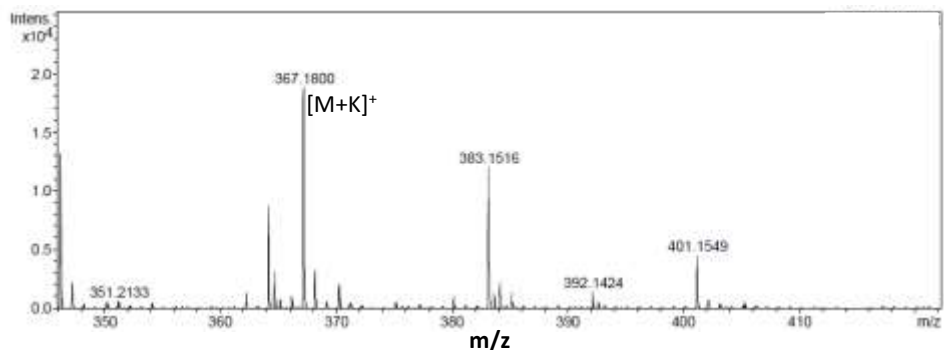


Figure 5.7. Mass spectra of  $H_2N\text{-Phe-Tyr-OH}$  (**14**).

## 5.3 Gel Preparation and Characterization Techniques

### 5.3.1 Preparation of hydrogel

To prepare hydrogel, first 6.2 mg (30 mM) of trimesic acid (**BTC**) was dissolved by sonication in a 5 mL borosilicate vial with a cap containing 1 mL of TNE buffer solution (10 mM, pH = 7.4) and later 7.1 mg (45 mM) of **DAN** was added. The resultant mixture was then sonicated for 5 minutes and vortexed for 30 seconds to obtain a homogeneous mixture. After 1-2 minutes, gelation was observed. Other composites do not form any gel.

### 5.3.2 Preparation of hydrogels for Enzymatic Reaction

The enzyme (5 mg/mL) was dissolved in 1 mL 100 mM TNE buffer (pH = 7.4). Y (14.4 mg, 80 mM) and FY (26.2 mg, 80 mM) were individually dispersed into 400  $\mu\text{L}$  of TNE buffer (25 mM, pH = 7.4). The hydrogel was then prepared with the same amount of **DAN** and **BTC** mentioned above in the hydrogel preparation in 700  $\mu\text{L}$  of TNE buffer. Then 100  $\mu\text{L}$  of Y/FY and 200  $\mu\text{L}$  of tyrosinase solution were added to the gel. The resultant solution was vortexed well and the product conversion was monitored by HPLC.

**5.3.3 Separation of Product after Esterification**

After completion of hydroxylation reaction of Y and FY, the reaction mixture was acidified with 0.5 N HCl. The resultant solution was washed with 20 mL of ethyl acetate into a separating flask. BTC was extracted and aqueous layer was collected. The aqueous layer contains DAN and L-DOPA/F-(L)-DOPA. The aqueous layer was again basified with 0.5 M  $\text{Na}_2\text{CO}_3$  and was washed by ethyl acetate which separates DAN from the mixture. The aqueous layer which contains DOPA/F-(L)-DOPA, was then neutralized by  $\text{KHSO}_4$  solution. The aqueous layer was lyophilized to obtain L-DOPA/F-(L)-DOPA as off-white solid.

**5.3.4 Compound characterization**

All NMR spectra were recorded with 400 MHz Bruker AV spectrometer at 300 K. Compound concentrations were in the range of 1-10 mM in  $\text{DMSO}-d_6$ . Mass spectra were recorded on Bruker micrOTOF-Q II by positive mode electrospray ionization.

**5.3.5 Rheological Study**

Rheological experiment was assessed using an Anton Paar Physica Rheometer (MCR 301, Austria) with parallel plate geometry (25 mm in diameter, 1 mm gap) and temperature was controlled at 25° C. The dynamic modulus of the hydrogel was measured as a function of frequency in the range of 0.05-100  $\text{rad s}^{-1}$  with a constant strain value 0.1%. The dynamic behavior of hydrogel during enzymatic reaction was performed with constant strain of 0.1% and constant angular frequency of 10 Hz. 200  $\mu\text{L}$  of hydrogel was prepared in glass vial and transferred it over the plate using microspatula to proceed for rheological measurements.

### 5.3.6 Morphological study

Field emission scanning electron microscope (FE-SEM Supra 55 Zeiss) instrument was used for SEM study. Gels were dried on cover slip and coated with gold for SEM analysis with an operating voltage of 5 kV. Field Emission Gun-Transmission Electron Microscope (model: Tecnai G2, F30), operated on a voltage of 300 kV. 100  $\mu\text{L}$  of gel was dissolved in 200  $\mu\text{L}$  of water and the dilute solution of the hydrogels was dried on carbon-coated copper grids (300 mesh) by slow evaporation in air and then allowed to dry separately in a vacuum at room temperature.

### 5.3.7 FT-IR Spectroscopy

All reported FT-IR spectra were recorded with a Bruker (Tensor 27) FT-IR spectrophotometer. The solid-state measurements were performed using the KBr pellet technique with a scan range between 400 and 4000  $\text{cm}^{-1}$  over 64 scans at a resolution of 4  $\text{cm}^{-1}$  and an interval of 1  $\text{cm}^{-1}$ . The hydrogel was dried in vacuum prior to the experiment.

### 5.3.8 UV-Vis Spectroscopy

UV-Vis absorption spectra were recorded using a Varian Cary100 Bio UV-Vis spectrophotometer at a concentration of 5  $\mu\text{M}$  of hydrogel **8** in 2 mL of tris buffer solution (10 mM).

### 5.3.9 Powder X-ray Diffraction

The XRD measurements were carried out using a Bruker D8 Advance X-ray diffractometer. The X-rays were produced using a sealed tube, and the wavelength of the X-rays was 0.154 nm (Cu K $\alpha$ ). The X-rays were detected using a fast counting detector based on silicon strip technology (Bruker LynxEye detector).

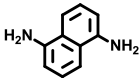
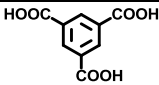
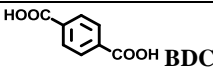
### 5.3.10 HPLC Analysis

A Dionex HPLC-Ultimate 3000 (High Performance Liquid Chromatography) pump was used to analyze products. 20  $\mu\text{L}$  of sample was injected onto a Dionex Acclaim® 120 C18 column of 250 mm length with an internal diameter of 4.6 mm and 5  $\mu\text{m}$  fused silica particles at a flow rate of 1  $\text{mL min}^{-1}$  (linear gradient of 20% v/v acetonitrile in water for 4 minutes, gradually rising to 80% (v/v) acetonitrile in water at 35 min). This concentration was kept constant until 40 min when the gradient was decreased to 20% (v/v) acetonitrile in water at 42 min. The sample preparation involved mixing of 100  $\mu\text{L}$  hydrogel in 900  $\mu\text{L}$  acetonitrile-water (50: 50 mixtures) solution containing 0.1% trifluoroacetic acid. The samples were then filtered through a 0.45  $\mu\text{m}$  syringe filter (Whatman, 150 units, 13 mm diameter, 2.7 mm pore size) prior to injection. The products were identified by using Ultimate 3000 RS Variable Wavelength Detector at 280 nm.

## 5.4 Results and discussion

In this chapter, the bifunctional amphiphile 1,5-diaminonaphthalene (**DAN**) was used to attain bicomponent self-assembly and gelation.

*Table 5.1. Composition of the bicomponent systems and physical appearance*

Amphiphile	Complementary acids	Physical appearance
 <b>DAN</b>	 <b>BTC</b>	Hydrogel <b>8</b> ( <b>DAN-BTC</b> )
	 <b>BDC</b>	Sol
	 <b>BCA</b>	Sol
	 <b>SA</b>	Sol

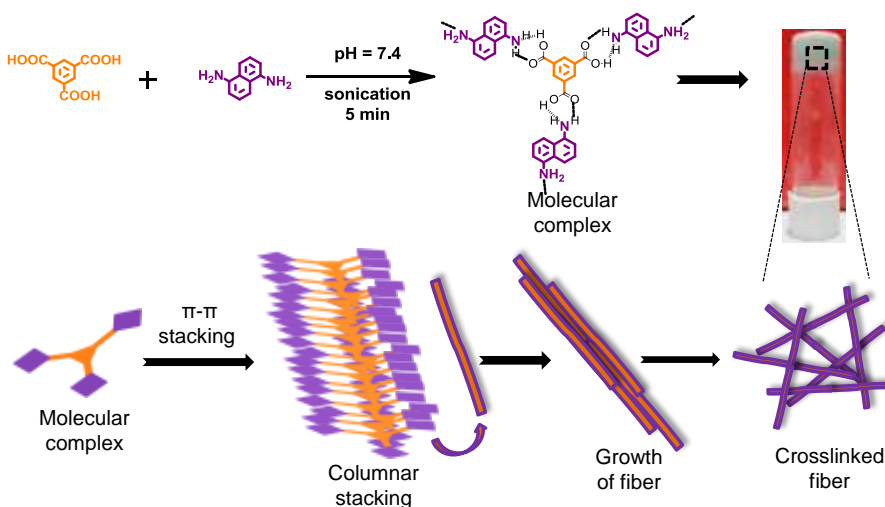


**Figure 5.8.** Schematic representation of molecular complexes of hydrogel **8** (**DAN-BTC**). Molecular complex of **DAN-BTC** elongated vertically through columnar  $\pi$ - $\pi$  stacking interaction, which forms a fibril. Then the fibers on going through higher order self-assembly form a nanofibrillar bundle and finally crosslinked fibrillar network was formed.

Among a series of complementary acids (Table 5.1), only 1,3,5-benzenetricarboxylic acid (**BTC**) co-assembles with **DAN** to produce self-supporting hydrogel **8** (Figure 5.8) in tris-buffer solution (10 mM, pH 7.4). A rigid hydrogel formation was confirmed by test tube inversion study (Figure 5.8).



**Figure 5.9.** Optical imaged of other bicomponent system. **DAN**: 1,5-diaminonaphthalene, **BDC**: 1,4-benzenedicarboxylic acid, **SA**: succinic acid and **BCA**: Benzene carboxylic acid. All are equimolar mixture 30 mM of **DAN** and 30 mM of acid.

The composites DAN-BDC, DAN-SA and DAN-BCA does not form any gel at the same condition (Figure 5.8). The pH becomes 7.22 after attaining the rigidity of the hydrogel **8** (DAN-BTC). The hydrogel **8** is sufficiently stable for several (>30) days. The external ions interfere in co-assembly of the bicomponent system. Therefore, upon exposure with aqueous solution of NaCl (100 mM), 1 (N) HCl and 1 (N) Na<sub>2</sub>CO<sub>3</sub>, gel to sol transition was observed. All other bicomponent system did not form hydrogel (Figure 5.9).

#### 5.4.1 Rheological Study

The rheological experiments illustrate the mechanical (viscoelastic) property of the hydrogel. Amplitude sweep rheological experiments were performed to know the linear viscoelastic region (LVE) and it was found as strain of 0.1% for the hydrogel **8** (Figure 5.10). Then 0.1% strain was used to perform frequency sweep experiment. A rigid hydrogel is defined in practice of having a storage modulus ( $G'$ ) higher than the loss modulus ( $G''$ ) at variable angular frequency regime. The storage modulus of the hydrogel is higher than the loss modulus throughout the frequency range (Figure 5.10) which depicts the formation of strong and rigid hydrogel.

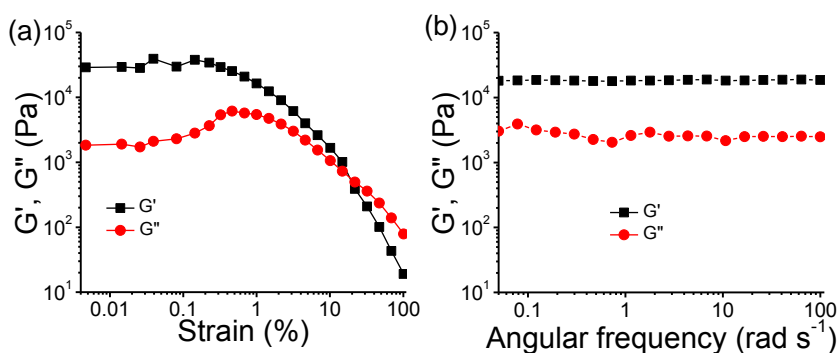


**Figure 5.10.** (a) Amplitude sweep rheological data showing gel deformation after an applied strain 10%. (b) represents the frequency sweep experiment of hydrogel **8** which signifies rigid gel formation.

### 5.4.2 Photophysical Study

UV-vis spectroscopic analyses were carried out to study the aggregation pattern. The **BTC** (Figure 5.11) exhibits peaks at 280 nm and the amphiphile **DAN** (Figure 5.11) shows a peak at 320 nm. The UV-vis spectrum of hydrogel **8** (Figure 5.11) shows more intense peak at 325 nm.

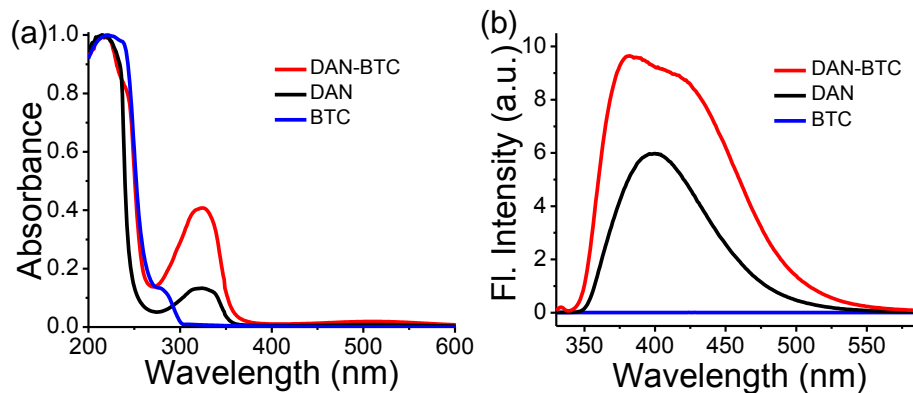


**Figure 5.11.** (a) The comparison of UV-Vis spectra of hydrogel **8** (**DAN-BTC**). (b) Comparative fluorescence spectra of hydrogel **8** (**DAN-BTC**).

A concomitant hyperchromic shift is noticed after gelation. The red shift in UV-vis spectra is attributed to the  $\pi\text{-}\pi^*$  transition between aromatic groups in the formed complexes through the co-assembly and self-assembly of amphiphiles. The hyperchromic shift in the hydrogel implies that the hydrogel **8** is formed by  $\pi\text{-}\pi$  stacking interaction.<sup>[49-51]</sup> Photophysical study gives more insight about the mechanism for the bicomponent hydrogel **8**. The precursor acid **BTC** (Figure 5.11) is unable to show any peak whereas **DAN** (Figure 5.11) exhibits emission maximum at 398 nm. Hydrogel **8** (Figure 5.11) exhibits two peaks at 380 nm and a remarkable red-shifted peak at 419 nm in comparison to the precursor acid and amphiphile. The significant red-shift in emission band is an account for the hybrid complex formation and strong  $\pi\text{-}\pi$  stacking interaction.<sup>[52]</sup>

### 5.4.3 Mechanistic Study

The mechanistic aspect of the co-assembly involved in the formation of hydrogel was investigated using Fourier Transform infrared (FT-IR) experiments. The **BTC** exhibits a broad band at around  $2984\text{ cm}^{-1}$  due to the presence of strong intermolecular hydrogen-bonded carboxylic acid groups. Strong intense peaks at  $1700\text{ cm}^{-1}$  is assigned to stretching vibration of the C=O group of carboxylic acid in associated state through intermolecular hydrogen bonding in **BTC** (Figure 5.12).<sup>[53]</sup>

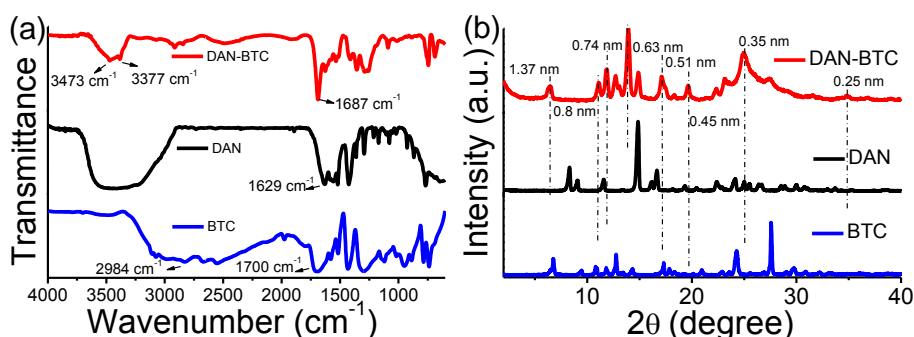


**Figure 5.12.** (a) The overlaid FT-IR spectra of **DAN-BTC** showing significant change in peaks. (b) The overlaid PXRD plot of **DAN-BTC**, **DAN** and **BTC**.

**DAN** exhibits a peak at  $1629\text{ cm}^{-1}$  assigned to  $-\text{NH}$  bending frequency and a broad peak at  $3441\text{ cm}^{-1}$  appeared attributed to  $-\text{NH}$  stretching frequencies. After formation of hydrogel **8** the peak appeared for carboxylic C=O of **BTC** shifted to  $1687\text{ cm}^{-1}$  is due to hydrogen bonding with **DAN** in the composite hydrogel.<sup>[54]</sup> The pattern of  $-\text{NH}$  stretching band of **DAN** is also changed from broad to sharp peak at 3377 and 3473  $\text{cm}^{-1}$  due to hydrogen bonding interactions. A powder X-ray diffraction (PXRD) study of the dried hydrogel **8** (Figure 5.12) reveals the appearance of peaks at  $2\theta$  of  $6.43^\circ$  ( $d = 1.37\text{ nm}$ ),  $11.04^\circ$  ( $d = 0.8\text{ nm}$ ),  $11.91^\circ$  ( $d = 0.74\text{ nm}$ ),  $13.86^\circ$  ( $d = 0.63\text{ nm}$ ),  $17.17^\circ$  ( $d = 0.51\text{ nm}$ ),  $19.69^\circ$  ( $d = 0.45\text{ nm}$ ),  $25.03^\circ$  ( $d = 0.35\text{ nm}$ ) and  $34.82^\circ$  ( $d = 0.25\text{ nm}$ ) which are different from those of the precursors **DAN** and **BTC**. The disappearance of the peaks in the dried hydrogel **8** within the  $2\theta$  range of  $7^\circ$ - $10^\circ$  corresponding

to DAN suggests the formation of a new material. The presence of a peak at  $2\theta$  of  $6.43^\circ$  ( $d = 1.37$  nm) depicts the diameter of columnar aggregates of the molecular complexes, whereas the  $d$  spacing of  $0.51$  and  $0.45$  nm designate the intercolumnar distances.<sup>[55-56]</sup> The  $\pi$ - $\pi$  stacking interaction between the formed complexes is supported by the peak corresponding to the  $d$  spacing of  $0.35$  nm.<sup>[57]</sup> The  $d$  spacing  $0.25$  nm indicates the formation of hydrogen bonding into the hydrogel.<sup>[58-59]</sup>

#### 5.4.4 Microscopic Study

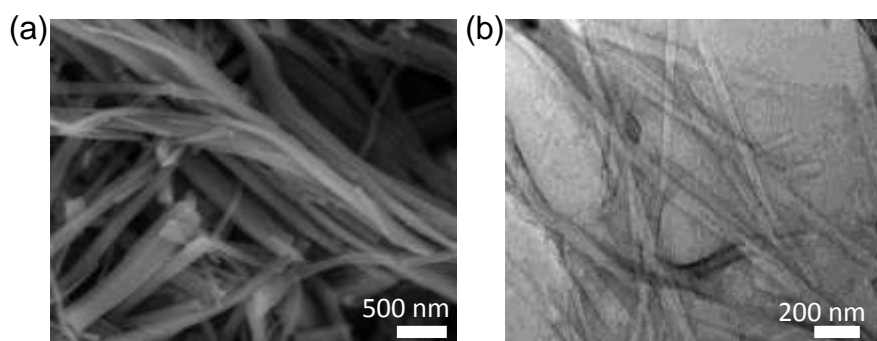


**Figure 5.13.** (a) SEM image of hydrogel **8** showing fibrillar bundle. (b) Fibrillar nanostructures were observed from TEM image of hydrogel **8**.

Morphological insight was investigated by the Scanning electron microscopy (SEM). The SEM image clearly shows the crosslinked fibrillar network formation into the hydrogel **8** (Figure 5.13). Initially narrow fibers in width are formed. On higher order self-assembly it forms wider fibers. Transmission electron microscopy was performed for deeper understanding about the formed morphology. The transmission electron microscopy image shows nanotubular fiber formation in the hydrogel **8** (Figure 5.13).

#### 5.4.5 Enzymatic reaction

Previously, supramolecular system was used as a template for enzymatic reactions.<sup>[60]</sup> The enzymes either entrap into the crosslinked fibrillar

network or into the formed nanostructures.<sup>[61]</sup> In both the cases, the entrapped enzymes shows excellent activity.

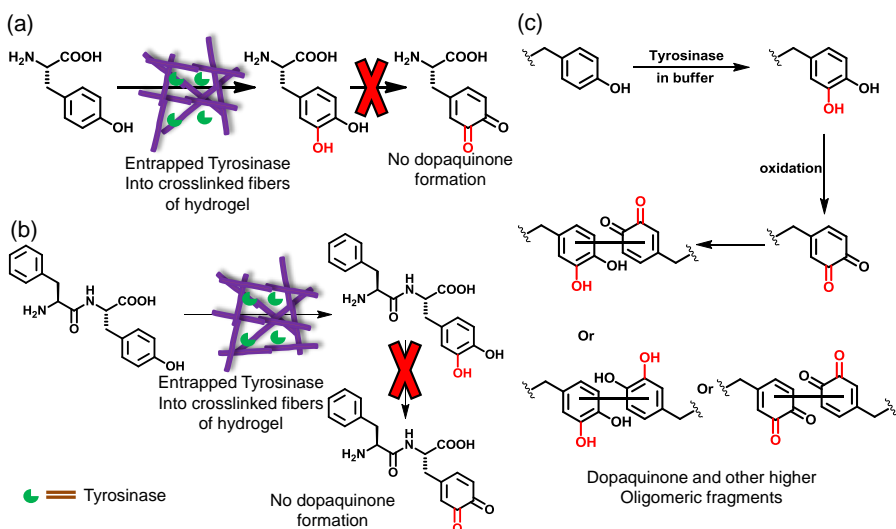


**Figure 5.14.** (a) showing the substrate chosen for the tyrosinase catalyzed DOPA formation. (b) shows the detailed mechanistic aspect of tyrosinase enzyme activity on tyrosine functionalized peptide. Which shows dopaquinone formation and further origomerization occurs to form melanin. (c) Tyrosinase selectively forms L-DOPA functionalized peptide and no further oxidation occurs to form dopaquinone in hydrogel 8.

Here, enzymatic reaction was carried out into the bicomponent co-assembled hydrogel. The hydrogel was not affected by the formation of L-DOPA from tyrosinase. The product conversion (%) was monitored by high performance liquid chromatography (HPLC). The previous methods with inhibitor molecule (ascorbic acid) shows less conversion of L-DOPA with less selectivity and also formation of oxidized dopaquinone is another problem (Figure 5.14).<sup>[63]</sup> The conversion for L-DOPA from Y was 95% whereas in FY peptide the product F-(L)-DOPA conversion was 84% (Figure 5.15). In hydrogel after completion of the reaction oxidized peak was not observed from HPLC chromatogram (Figure 5.16). The HPLC chromatogram shows only a new peak formation at lower retention time in

comparison to Y and FY. No other product was formed in the hydrogel medium.

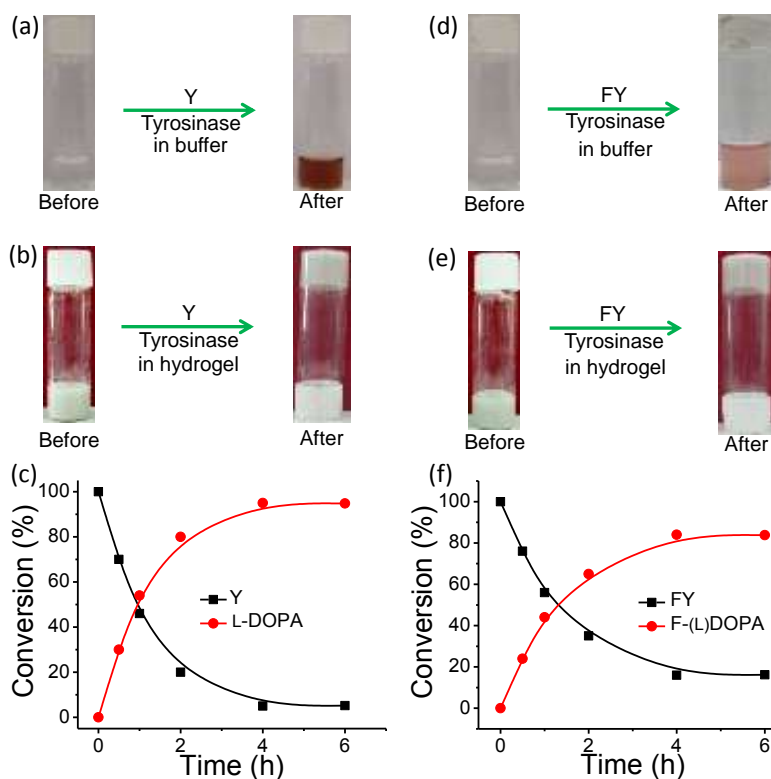


**Figure 5.15.** (a) Shows optical images of Y in buffer before (colourless) and after the reaction (dark brown). (b) Optical images of DAN-BTC hydrogel showing no color change before and after the conversion of L-DOPA from tyrosine. (c) Conversion of L-DOPA from tyrosine in hydrogel observed by HPLC chromatogram. (d) Optical images of FY in buffer solution before and after the reaction showing significant color change due to oxidation and oligomerization of DOPA (e) Optical images of DAN-BTC hydrogel showing no color change before and after the conversion of F-(L)-DOPA from FY. (f) Conversion of F-(L)-DOPA from FY in hydrogel observed by HPLC chromatogram.

The ESI mass spectrometry data confirmed the formation of a new peak having the mass ( $m/z$ ) of  $[M-H]^-$  is 196.1 (Figure 5.17) corresponding to L-DOPA and  $[M+K]^+$  383.1512 (Figure 5.18) due to the formation of F-(L)-DOPA. The whole reaction was completed in a short time range of six hours. In both the cases, the selective formation of L-DOPA in the hydrogel medium is confirmed.

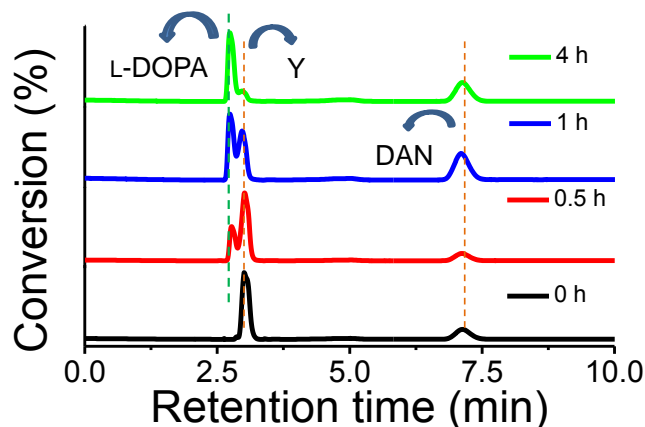


*Figure 5.16. HPLC chromatogram of the formation of L-DOPA in hydrogel.*

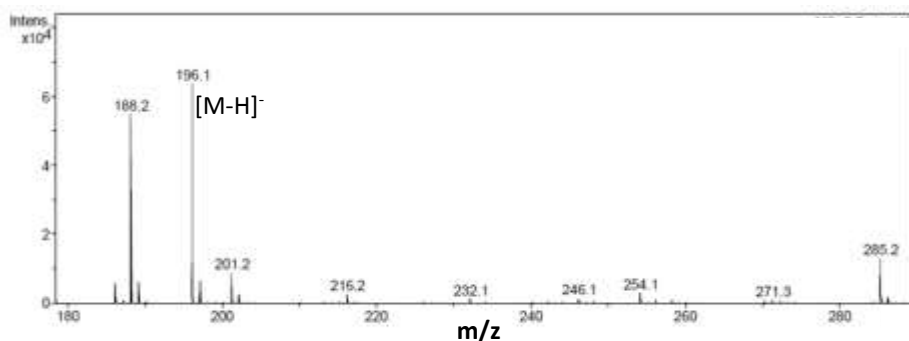


*Figure 5.17. Mass spectrum of L-DOPA synthesized in hydrogel medium.*

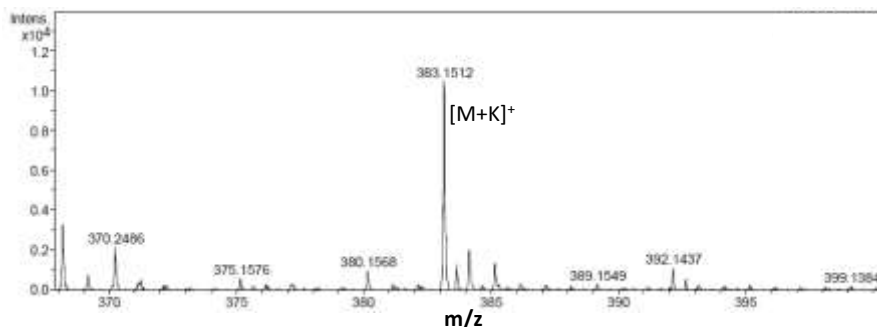


*Figure 5.18. Mass spectrum of F-(L)-DOPA synthesized in hydrogel medium.*

## 5.5 Conclusion

In conclusion, we have successfully integrated small amphiphilic molecules 1,5-DAN and BTC to obtain a self-supporting hydrogel. Small molecular building blocks co-assemble through hydrogen bonding and  $\pi$ - $\pi$  stacking interaction. The FT-IR spectroscopy and PXRD analysis account

for the detail mechanism of the cooperative self-assembly. The co-assembled hydrogel is strong enough to hold tyrosinase enzyme within the crosslinked fibrillar network. Y and FY were immobilized into the hydrogel to obtain L-DOPA and peptide F-(L)-DOPA. This method is very efficient to produce L-DOPA in the gel medium with an excellent conversion (95% for L-DOPA and 84% for F-(L)-DOPA). This hydrogel helps to form tyrosine to L-DOPA without the formation of dopaquinone and other higher oligomeric fragments directly in peptide with an easy separation technique within a short time range.

## 5.6 References

1. Cui H., Webber M. J., Stupp S. I. (2010), Self-assembly of peptide amphiphiles: From molecules to nanostructures to biomaterials, *Biopolymers*, 94, 1-18 (DOI: 10.1002/bip.21328).
2. Pochan D. J., Schneider J. P., Kretsinger J., Ozbas B., Rajagopal K., Haines L. (2003), Thermally Reversible Hydrogels via Intramolecular Folding and Consequent Self-Assembly of a de Novo Designed Peptide, *J. Am. Chem. Soc.*, 125, 11802-11803 (DOI: 10.1021/ja0353154).
3. Rajagopal K., Lamm M. S., Haines-Butterick L. A., Pochan D. J., Schneider J. P. (2009), Tuning the pH Responsiveness of  $\beta$ -Hairpin Peptide Folding, Self-Assembly, and Hydrogel Material Formation, *Biomacromolecules*, 10, 2619-2625 (DOI: 10.1021/bm900544e).
4. Das A. K., Maity I., Parmar H. S., McDonald T. O., Konda, M. (2015), Lipase-Catalyzed Dissipative Self-Assembly of a Thixotropic Peptide Bolaamphiphile Hydrogel for Human Umbilical Cord Stem-Cell Proliferation, *Biomacromolecules* 16, 1157-1168 (DOI: 10.1021/bm501835v).
5. Yang Z., Liang G., Xu B. (2008), Enzymatic Hydrogelation of Small Molecules, *Acc. Chem. Res.*, 41, 315-326 (DOI: 10.1021/ar7001914).

6. Toledano S., Williams R. J., Jayawarna V., Ulijn R. V. (2006), Enzyme-Triggered Self-Assembly of Peptide Hydrogels via Reversed Hydrolysis, *J. Am. Chem. Soc.*, 128, 1070-1071 (DOI: 10.1021/ja056549l).
7. Gao Y., Kuang Y., Guo Z.-F., Guo Z., Krauss I. J., Xu B. (2009), Enzyme-Instructed Molecular Self-assembly Confers Nanofibers and a Supramolecular Hydrogel of Taxol Derivative, *J. Am. Chem. Soc.*, 131, 38, 13576-13577 (DOI: 10.1021/ja904411z).
8. Haines L. A., Rajagopal K., Ozbas B., Salick D. A., Pochan D. J., Schneider J. P. (2005), Light-Activated Hydrogel Formation via the Triggered Folding and Self-Assembly of a Designed Peptide, *J. Am. Chem. Soc.*, 127, 17025-17029 (DOI: 10.1021/ja054719o).
9. Zhang J., Yang Y., Chen Y., Liu X., Guo S., Zhu L., Wang Y. (2016), An in situ phototriggered-imine-crosslink composite hydrogel for bone defect repair, *J. Mater. Chem. B*, 4, 973-981 (DOI: 10.1039/C5TB02377G).
10. Zhang L., Wang X., Wang T., Liu M. (2015), Tuning Soft Nanostructures in Self-assembled Supramolecular Gels: From Morphology Control to Morphology-Dependent Functions, *Small*, 11, 1025-1038 (DOI: 10.1002/sml.201570054).
11. Adhikari B., Nanda J., Banerjee A. (2011), Multicomponent Hydrogels from Enantiomeric Amino Acid Derivatives: Helical Nanofibers, Handedness and Self-sorting, *Soft Matter*, 7, 8913-8922 (DOI: 10.1039/C1SM05907F).
12. Raeburn J., Alston B., Kroeger J., McDonald T. O., Howse J. R., Cameron P. J., Adams D. J. (2014), Electrochemically-triggered spatially and temporally resolved multi-component gels, *Mater. Horiz.*, 1, 241-246 (DOI: 10.1039/C3MH00150D).
13. Palma C.-A., Samori P., Cecchini M. (2010), Atomistic Simulations of 2D Bicomponent Self-Assembly: From Molecular Recognition to Self-

- Healing, J. *Am. Chem. Soc.*, 132, 17880-17885 (DOI: 10.1021/ja107882e).
14. Cafferty B. J., Gallego I., Chen M. C., Farley K. I., Eritja R., Hud N. V. (2013), Efficient Self-Assembly in Water of Long Noncovalent Polymers by Nucleobase Analogues, *J. Am. Chem. Soc.*, 135, 2447-2450 (DOI: 10.1021/ja312155v).
15. Raymond D. M., Nilsson B. L. (2018), Multicomponent peptide assemblies, *Chem. Soc. Rev.*, 47, 3659-3720 (DOI: 10.1039/C8CS00115D).
16. de Loos M., van Esch J., Kellogg R. M., Feringa B. L. (2001), Chiral Recognition in Bis-Urea-Based Aggregates and Organogels through Cooperative Interactions, *Angew. Chem. Int. Ed.*, 40, 613-616 (DOI: 10.1002/1521-3773(20010202)40:3<613::AID-ANIE613>3.0.CO;2-K).
17. Cai W., Wang G.-T., Du P., Wang R.-X., Jiang X.-K., Li Z.-T. (2008), Foldamer Organogels: A Circular Dichroism Study of Glucose-Mediated Dynamic Helicity Induction and Amplification, *J. Am. Chem. Soc.* 130, 13450-13459 (DOI: 10.1021/ja8043322).
18. Amemiya R., Mizutani M., Yamaguchi M. (2010), Two-Component Gel Formation by Pseudoenantiomeric Ethynylhelicene Oligomers, *Angew. Chem. Int. Ed.*, 49, 1995-1999 (DOI: 10.1002/anie.200906693).
19. Meazza L., Foster J. A., Fucke K., Metrangolo P., Resnati G., Steed J. W. (2013), Halogen-bonding-triggered supramolecular gel formation, *Nat. Chem.*, 5, 42-47 (DOI: 10.1038/nchem.1496).
20. Ichinose W., Ito J., Yamaguchi M. (2013), Tetrameric  $\alpha\beta\beta$  Aggregate Formation by Stereoisomeric Bidomain Helicene Oligomers, *Angew. Chem. Int. Ed.*, 52, 5290-5294 (DOI: 10.1002/anie.201301463).
21. Fichman G., Guterman T., Adler-Abramovich L., Gazit E. (2015), Synergetic functional properties of two-component single amino acid-

- based hydrogels, *CrystEngComm*, 17, 8105-8112 (DOI: 10.1039/C5CE01051A).
22. Hanabusa K., Miki T., Taguchi Y., Koyama T., Shirai H. (1993), Two-Component, Small Molecule Gelling Agents, *J. Chem. Soc., Chem. Commun.*, 1382-1384 (DOI: 10.1039/C39930001382).
23. Krishnan B. P., Ramakrishnan S., Sureshan K. M. (2013), Supramolecular Design of a Bicomponent Topochemical Reaction between Two Non-Identical Molecules, *Chem. Commun.*, 49, 1494-1496 (DOI: 10.1039/C2CC37067K).
24. Bairi P., Roy B., Nandi A. K. (2010), Bicomponent Hydrogels of Lumichrome and Melamine: Photoluminescence Property and Its Dependency on pH and Temperature, *J. Phys. Chem. B*, 114, 11454-11461 (DOI: 10.1021/jp105378e).
25. Rao K. V., Jayaramulu K., Maji T. K., George S. J. (2010), Supramolecular Hydrogels and High-Aspect-Ratio Nanofibers through Charge-Transfer-Induced Alternate Coassembly, *Angew. Chem., Int. Ed.*, 49, 4218-4222 (DOI: 10.1002/anie.201000527).
26. Biswas S., Rasale D. B., Das A. K. (2016), Blue Light Emitting Self-Healable Graphene Quantum Dot Embedded Hydrogels, *RSC Adv.*, 6, 54793-54800 (DOI: 10.1039/C6RA06587B).
27. Markvoort A. J., ten Eikelder H. M. M., Hilbers P. A. J., de Greef T. F. A., Meijer E. W. (2011), Theoretical Models of Nonlinear Effects in Two-Component Cooperative Supramolecular Copolymerizations, *Nat. Commun.*, 2, 509 (DOI: 10.1038/ncomms1517).
28. Ikeda T., Iijima T., Sekiya R., Takahashi O., Haino T. (2016), Cooperative Self-Assembly of Carbazole Derivatives Driven by Multiple Dipole-Dipole Interactions, *J. Org. Chem.*, 81, 6832-6837 (DOI: 10.1021/acs.joc.6b01169).
29. Rest C., Mayoral M. J., Fucke K., Schellheimer J., Stepanenko V., Fernandez G. (2014), Self-Assembly and (Hydro)gelation Triggered by Cooperative  $\pi$ - $\pi$  and Unconventional C-H $\cdots$ X Hydrogen Bonding

- Interactions, *Angew. Chem., Int. Ed.*, 53, 700-705 (DOI: 10.1002/anie.201307806).
30. Draper E. R., Eden E. G. B., McDonald T. O., Adams D. J. (2015), Spatially Resolved Multicomponent Gels, *Nat. Chem.*, 7, 848-852 (DOI: 10.1038/nchem.2347).
31. Kar H., Ghosh S. (2015), Multicomponent Gels: Remote Control for Self-Assembly, *Nat. Chem.*, 7, 765-767 (DOI: 10.1038/nchem.2351).
32. Estroff L. A., Hamilton A. D. (2004), Water Gelation by Small Organic Molecules. *Chem. Rev.*, 104, 1201-1217 (DOI: 10.1021/cr0302049).
33. de Loos M., Feringa B. L., van Esch J. H. (2005), Design and Application of Self-Assembled Low Molecular Weight Hydrogels, *Eur. J. Org. Chem.*, 2005, 3615-3631 (DOI: 10.1002/ejoc.200400723).
34. Hirst A. R., Escuder B., Miravet J. F., Smith D. K. (2008), High-tech applications of self-assembling supramolecular nanostructured gel-phase materials: from regenerative medicine to electronic devices, *Angew. Chem., Int. Ed.*, 47, 8002-8018 DOI: 10.1002/anie.200800022.
35. Galler K. M., Aulisa L., Regan K. R., D'Souza R. N., Hartgerink J. D. (2010), Self-Assembling Multidomain Peptide Hydrogels: Designed Susceptibility to Enzymatic Cleavage Allows Enhanced Cell Migration and Spreading, *J. Am. Chem. Soc.*, 132, 3217-3223 (DOI: 10.1021/ja910481t).
36. Yao M.-H., Yang J., Song J.-T., Zhao D.-H., Du M.-S., Zhao Y.-D., Liu B. (2014), Directed Self-assembly of Polypeptide-Engineered Physical Microgels for Building Porous Cell-laden Hydrogels, *Chem. Commun.*, 50, 9405-9408 (DOI: 10.1039/C4CC04018J).
37. Bhuniya S., Park S. M., Kim B. H. (2005), Biotin-Amino Acid Conjugates: An Approach Toward Self-Assembled Hydrogelation, *Org. Lett.*, 7, 1741-1744 (DOI: 10.1021/ol050300r).

38. Wan L., Chen Q., Liu J., Yang X., Huang J., Li L., Guo X., Zhang J., Wang K. (2016), Programmable Self-Assembly of DNA–Protein Hybrid Hydrogel for Enzyme Encapsulation with Enhanced Biological Stability, *Biomacromolecules*, 17, 1543-1550 (DOI: 10.1021/acs.biomac.6b00233).
39. Nykänen, V. P. S., Nykänen A., Puska M. A., Silva G. G., Ruokolainen J. (2011), Dual-responsive and super absorbing thermally cross-linked hydrogel based on methacrylate substituted polyphosphazene, *Soft Matter*, 7, 4414-4424 (DOI: 10.1039/C0SM01000F).
40. Biswas S., Jadhav R. G., Das A. K. (2018), Construction of Porous Organic Nanostructures Using Cooperative Self-Assembly for Lipase-Catalyzed Inclusion of Gastrodigenin, *ACS Appl. Nano Mater.*, 1, 175-182 (DOI: 10.1021/acsanm.7b00085).
41. Nagatsu T., Sawada M. (2009), L-Dopa Therapy for Parkinson's Disease: Past, Present, and Future, *Parkinsonism Relat. Disord.*, 15, S3-S8 (DOI: 10.1016/S1353-8020(09)70004-5).
42. Sayyed I. A., Sudalai A. (2004), Asymmetric synthesis of L-DOPA and (R)-selegiline via, OsO<sub>4</sub>-catalyzed Asymmetric Dihydroxylation, *Tetrahedron: Asymmetr.*, 15, 3111-3116 (DOI: 10.1016/j.tetasy.2004.08.007).
43. Valdes R.H., Puzer L., Gomes Jr. M., Marques C. E. S. J., Aranda D. A. G., Bastos M. L., Gemal A., Antunes O. A. C. (2004), Production of L-DOPA under Heterogeneous Asymmetric Catalysis, *Catal. Commun.*, 5, 631-634 (DOI: 10.1016/j.catcom.2004.07.018).
44. Korshin D. E., Kashapov R. R., Murtazina L. I., Mukhitova R. K., Kharlamov S. V., Latypov S. K., Ryzhkina I. S., Ziganshina A. Y., Kononov A. I. (2009), Self-assembly of an Aminoalkylated Resorcinarene in Aqueous Media: Host-guest Properties, *New J. Chem.*, 33, 2397-2401 (DOI: 10.1039/B9NJ00457B).

45. Hirst A. R., Miravet J. F., Escuder B., Noirez L., Castelletto V., Hamley I. W., Smith D. K. (2009), Self-Assembly of Two-Component Gels: Stoichiometric Control and Component Selection, *Chem. Eur. J.*, 15, 372-379 (DOI: 10.1002/chem.200801475).
46. Nath K., Husain A., Dastidar P. (2015), Metallogels and Silver Nanoparticles Generated from a Series of Transition Metal-Based Coordination Polymers Derived from a New Bis-pyridyl-bis-amide Ligand and Various Carboxylates, *Cryst. Growth Des.*, 15, 4635-4645 (DOI: 10.1021/acs.cgd.5b00911).
47. Horcajada P., Serre C., Vallet-Regi M., Sebban M., Taulelle F., Ferey G. (2006), Metal-Organic Frameworks as Efficient Materials for Drug Delivery, *Angew. Chem., Int. Ed.*, 45, 5974-5978 (DOI: 10.1002/anie.200601878).
48. Streb C., Long D.-L., Cronin L. (2007), Engineering Porosity in a Chiral Heteropolyoxometalate-based Framework: The Supramolecular Effect of Benzenetricarboxylic Acid, *Chem. Commun.*, 471-473 (DOI: 10.1039/B613808J).
49. Wu L. C., Yang J., Kopecek J. (2011), Hybrid Hydrogels Self-assembled from Graft Copolymers Containing Complementary  $\beta$ -sheets as Hydroxyapatite Nucleation Scaffolds, *Biomaterials*, 32, 5341-5353 (DOI: 10.1016/j.biomaterials.2011.04.014).
50. Ramachandran S., Tseng Y., Yu Y. B. (2005), Repeated Rapid Shear-Responsiveness of Peptide Hydrogels with Tunable Shear Modulus, *Biomacromolecules*, 6, 1316-1321 (DOI: 10.1021/bm049284w).
51. Ajayaghosh A., Praveen V. K. (2007),  $\pi$ -Organogels of Self-Assembled p-Phenylenevinylenes: Soft Materials with Distinct Size, Shape, and Functions, *Acc. Chem. Res.*, 40, 644-656 (DOI: 10.1021/ar7000364).
52. Ahn J., Park S., Lee J. H., Jung S. H., Moon S.-J., Jung J. H. (2013), Fluorescent Hydrogels Formed by CH- $\pi$  and  $\pi$ - $\pi$  Interactions as the Main Driving Forces: An Approach Toward Understanding the

- Relationship Between Fluorescence and Structure, *Chem. Commun.*, 49, 2109-2111 (DOI: 10.1039/C2CC37249E).
53. Mahalakshmi G., Balachandran V. (2014), FT-IR and FT-Raman Spectra, Normal Coordinate Analysis and Ab Initio Computations of Trimesic Acid, *Spectrochim. Acta, Part A*, 124, 535-547 (DOI: 10.1016/j.saa.2014.01.061).
54. Edwards W., Smith D. K. (2013), Dynamic Evolving Two-Component Supramolecular Gels-Hierarchical Control over Component Selection in Complex Mixtures, *J. Am. Chem. Soc.* 135, 5911-5920 (DOI: 10.1021/ja4017107).
55. Paraschiv I., de Lange K., Giesbers M., van Lagen B., Grozema F. C., Abellon R. D., Siebbeles L. D. A., Sudholter E. J. R., Zuilhof H., Marcelis A. T. M. (2008), Hydrogen-Bond Stabilized Columnar Discotic Benzenetrisamides with Pendant Triphenylene Groups, *J. Mater. Chem.*, 18, 5475-5481 (DOI: 10.1039/B805283B).
56. Park L. Y., Hamilton D. G., McGehee E. A., McMenimen K. A. (2003), Complementary C<sub>3</sub>-Symmetric Donor-Acceptor Components: Cocystal Structure and Control of Mesophase Stability, *J. Am. Chem. Soc.*, 125, 10586-10590 (DOI: 10.1021/ja036540o).
57. Smith A. M., Williams R. J., Tang C., Coppo P., Collins R. F., Turner M. L., Saiani A., Ulijn R. V. (2008), Fmoc-Diphenylalanine Self Assembles to a Hydrogel via a Novel Architecture Based on  $\pi$ - $\pi$  Interlocked  $\beta$ -Sheets, *Adv. Mater.*, 20, 37-41 (DOI: 10.1002/adma.200701221).
58. Steiner T. (2002), The Hydrogen Bond in the Solid State, *Angew. Chem. Int. Ed.*, 41, 48-76 (DOI: 10.1002/1521-3773(20020104)41:1<48::AID-ANIE48>3.0.CO;2-U).
59. Ikeda M., Tanida T., Yoshii T., Hamachi I. (2011), Rational Molecular Design of Stimulus-Responsive Supramolecular Hydrogels Based on Dipeptides, *Adv. Mater.*, 23, 2819-2822 (DOI: 10.1002/adma.201004658).

60. Wang Z. J., Clary K. N., Bergman R. G., Raymond K. N., Toste F. D. (2013), A Supramolecular Approach to Combining Enzymatic and Transition Metal Catalysis, *Nat. Chem.*, 5, 100-103 (DOI: 10.1038/nchem.1531).
61. Athas J. C., Nguyen C. P., Zarket B. C., Gargava A., Nie Z., Raghavan S. R. (2016), Enzyme-Triggered Folding of Hydrogels: Toward a Mimic of the Venus Flytrap, *ACS Appl. Mater. Interfaces*, 8, 19066-19074 (DOI: 10.1021/acsami.6b05024).
62. Lampel A., McPhee S. A., Park H.-A., Scott G. G., Humagain S., Hekstra D. R., Yoo B., Frederix P. W. J. M., Li T.-D., Abzalimov R. R., Greenbaum S. G., Tuttle T., Hu C., Bettinger C. J., Ulijn R. V. (2017), Polymeric peptide pigments with sequence-encoded properties, *Science*, 356, 1064-1068 (DOI: 10.1126/science.aal5005).
63. Xu D.-Y., Chen J.-Y., Yang Z. (2012), Use of cross-linked tyrosinase aggregates as catalyst for synthesis of L-DOPA, *Biochemical Engineering Journal*, 63, 88-94 (DOI: 10.1016/j.bej.2011.11.009).



## **Chapter 6**

### **General Conclusions and Perspectives**



## 6.1 General Conclusions

The thesis work embodies integration of bicomponent systems to achieve controlled co-assembly and gelation. The bicomponent co-assembled hydrogels exhibit distinguished mechanical property, controlled nanostructures in gel state.<sup>[1-4]</sup> The formed supramolecular gels are very labile to the exposure of chemical as well as physical stimuli such as pH, sonication and light.<sup>[5-7]</sup> Thus the tuning ability was used to explore the nanoarchitectural diversity.<sup>[8-9]</sup> In this thesis, we have exploited the co-assembly of several amphiphilic building blocks. Specific as well as random co-assembly process was used to develop self-supporting supramolecular gel by traditional N-terminal protected amphiphiles, bolaamphiphiles and discotic amphiphile. The co-assembled molecular gels were also utilized for biocatalytic reactions.

Chapter 1 described the general introduction to the co-assembly of various amphiphilic molecules, formed nanoarchitectures in the gel medium and applications of the co-assembled nanostructures.

Chapter 2 demonstrated blue light emitting self-healable GQDs embedded Amoc capped aromatic amino acid based hydrogels at physiological pH. Aromatic Amoc amino acids based hydrogels formed nanofibrillar networks. Morphological changes of hydrogel **1** and **2** were observed due to the change in gelator structure and the random co-assembly of GQDs in the 3D network of gels. Hydroxyl group in tyrosine affects significantly to the mechanical property of the hydrogel. Aromatic  $\pi$ - $\pi$  stacking interactions within GQDs and Amoc amino acids and hydrogen bonding interactions are the driving force to stabilize the GQDs by the nanofibrillar networks. Fluorescence quenching reveals strong  $\pi$ - $\pi$  stacking interactions within GQDs and Amoc-amino acids. GQDs embedded Amoc-amino acids based hydrogels afford thixotropic in nature. The hydrogel composites of Amoc-F-OH and GQDs deliver excellent entropy driven

self-healable behavior, which can be used in drug delivery, tissue engineering and cell damage repairing in biological systems in future.

Chapter 3 depicted the development of bicomponent hydrogels with controlled right-handed and left-handed twisted fibers. L-leucine based bolaamphiphile co-assembled to form hydrogel. The overall chiral sense of D/L-tartaric acid was transferred to bolaamphiphile and nucleation of small chiral unit takes place to control the supramolecular chirality. This nucleation has taken place via the co-assembly of D/L-tartaric acid with the bolaamphiphile through an extensive hydrogen bonding interaction. The small nucleated helical unit again integrated to form narrow helical fibers. L-leucine based peptide bolaamphiphile and D/L-tartaric acid synergistically stabilize to form co-assembled hydrogels. The nanostructures from sphere to desired left-handed and right-handed nanofibers were successfully tuned in hydrogel state.

Chapter 4 revealed the development of different linear and discotic amphiphile based bicomponent systems with tunable nanostructures and pore sizes. The pores formed by molecular complexes traps a large amount of immiscible water and organic solvents to form emulsion-gels. Molecular complexes were co-assembled to form emulsion-gels through *J*-type aggregation. The emulsion-gels are able to produce esters and the porous architectures in emulsion-gel act as a template for lipase-catalyzed inclusion of gastrodigenin. Larger pore size (**tpeb-BDC**) permits enzyme molecules to insert into the cavity whereas small pores resist the large enzyme to come into the smaller cavity (**tpeb-BTC**). As a result, the enzyme functions on the surface of the smaller porous nanostructures. The enzyme lipase fits into the larger cavity and larger surface area of porous SONs of **tpeb-BDC** to yield the terephthalate diester with an excellent conversion. Enzymatic esterification reaction leads to the breakdown of the emulsion-gel **tpeb-BDC** into two phases and phase separation permits for the recyclability of the pyridyl amphiphile.

Chapter 5 describes small molecular building blocks co-assemble to produce self-supporting hydrogel through hydrogen bonding and  $\pi$ - $\pi$  stacking interaction. The co-assembled hydrogel is strong enough to hold tyrosinase enzyme within the crosslinked fibrillar network. Y and FY were immobilized into the hydrogel to obtain L-DOPA and peptide F-(L)-DOPA. This method is very efficient to produce L-DOPA in the gel medium with an excellent conversion (95% for L-DOPA and 84% for F-(L)-DOPA). This hydrogel helps to form tyrosine to L-DOPA without the formation of dopaquinone and other higher oligomeric fragments directly in peptide with an easy separation technique within a short time range.

## 6.2 Perspectives

The bicomponent system could merge in several ways such as self-sorting, covalent conjugation and co-assembly to produce self-supporting gels. Nevertheless, the mechanical, physical and chemical properties of the co-assembled gel are very easy to tune as two components combine through the non-covalent interactions. Multiple stimuli i.e. pH, light or sonication could be used to tune the properties of the co-assembled gels. Finally, co-assembled gel has gained interest for various potential applications including drug delivery and 3D cell culture. Amphiphilic molecules are the building blocks for the self-assembly process to generate distinct nanostructures. These amphiphilic building blocks are perfect for designing self-assembled gels through hydrogen bonding and  $\pi$ - $\pi$  stacking interactions. Meanwhile, integration of two amphiphilic molecules in a same pot could provide co-assembled supramolecular gels. There are countless scopes of such co-assembled systems to exploit the soft biomaterials. The complementary chemical functionality of two amphiphile can be varied to tune the co-assembly behavior of the composite. The bicomponent co-assembly approach was found to be appropriate to tune the mechanical,<sup>[10]</sup> photophysical<sup>[11]</sup> or chemical properties.<sup>[12]</sup> These co-assembled materials are highly active in tuning the

nanostructural morphology. Therefore the co-assembly study could help to study the complexity of natural systems such as cellular machinery.

Recently there is a tremendous interest to develop hydrogels through co-assembly having excellent catalytic activity for multistep reaction as well as used as a template for complex reactions. We have reported co-assembled emulsion-gel having controlled supramolecular organic nanostructure shows excellent recyclable lipase catalyzed inclusion of gatrodigenin. The co-assembled system helps to tune the nanostructures. Therefore, it would apply to study the amyloid fibril inhibition through co-assembly by adding complementary foreign substances. The biocompatible co-assembled hydrogels also have potential applications in biotechnology i.e. tissue engineering, cell culture etc.

### **6.3 References**

1. Zhang L., Wang X., Wang T., Liu M. (2015), Tuning Soft Nanostructures in Self-assembled Supramolecular Gels: From Morphology Control to Morphology-Dependent Functions, *Small*, 11, 1025-1038 (DOI: 10.1002/sml.201570054).
2. Adhikari B., Nanda J., Banerjee A. (2011), Multicomponent Hydrogels from Enantiomeric Amino Acid Derivatives: Helical Nanofibers, Handedness and Self-sorting, *Soft Matter*, 7, 8913-8922 (DOI: 10.1039/C1SM05907F).
3. Raeburn J., Alston B., Kroeger J., McDonald T. O., Howse J. R., Cameron P. J., Adams D. J. (2014), Electrochemically-triggered spatially and temporally resolved multi-component gels, *Mater. Horiz.*, 1, 241-246 (DOI: 10.1039/C3MH00150D).
4. Palma C.-A., Samori P., Cecchini M. (2010), Atomistic Simulations of 2D Bicomponent Self-Assembly: From Molecular Recognition to Self-Healing, *J. Am. Chem. Soc.*, 132, 17880-17885 (DOI: 10.1021/ja107882e).

5. Naota T., Koori H. (2005), Molecules That Assemble by Sound: An Application to the Instant Gelation of Stable Organic Fluids, *J. Am. Chem. Soc.*, 127, 9324-9325 (DOI: 10.1021/ja050809h).
6. Nelli S. R., Chakravarthy R. D., Mohiuddin M., Lin H. -C. (2018), The Role of Amino Acids on Supramolecular Co-assembly of Naphthalenediimide-pyrene based Hydrogelators, *RSC Adv.*, 8, 14753-14759 (DOI: 10.1039/C8RA00929E).
7. Murata K., Aoki M., Suzuki T., Harada T., Kawabata H., Komori T., Ohseto F., Ueda K., Shinkai S. (1994), Thermal and Light Control of the Sol-Gel Phase Transition in Cholesterol-Based Organic Gels. Novel Helical Aggregation Modes As Detected by Circular Dichroism and Electron Microscopic Observation *J. Am. Chem. Soc.*, 116, 6664-6676 (DOI: 10.1021/ja00094a023).
8. Buerkle L. E., Rowan S. J. (2012), Supramolecular Gels Formed from Multi-Component Low Molecular Weight Species, *Chem. Soc. Rev.*, 41, 6089-6102 (DOI: 10.1039/C2CS35106D).
9. Hirst A. R., Smith D. K. (2005), Two-Component Gel-Phase Materials- Highly Tunable Self-Assembling Systems, *Chem. Eur. J.*, 11, 5496-5508 (DOI: 10.1002/chem.200500241).
10. Xu Y., Wu Q., Sun Y., Bai H., Shi G. (2010), Three-Dimensional Self-Assembly of Graphene Oxide and DNA into Multifunctional Hydrogels, *ACS Nano*, 4, 7358-7362 (DOI: 10.1021/nn1027104).
11. Bairi P., Roy B., Chakraborty P., Nandi A. K. (2013), Co-assembled White-Light-Emitting Hydrogel of Melamine, *ACS Appl. Mater. Interfaces*, 5, 5478-5485 (DOI: 10.1021/am4013566).
12. Singh N., Zhang K., Angulo-Pachon C. A., Mendes E., van Esch J. H., Escuder B. (2016), Tandem reactions in self-sorted catalytic molecular hydrogels, *Chem. Sci.*, 7, 5568-5572 (DOI: 10.1039/C6SC01268J).

